Application of Synthetic Jet Actuators for Modification of Separated Boundary Layers

Itimad Dawood Jumaah Azzawi

Submitted in accordance with the requirements for the

degree of Doctor of Philosophy

The University of Leeds

School of Mechanical Engineering

November, 2016

The candidate confirms that the work submitted is his own, except where work has formed jointly-authored publication has been included.

The contribution of the candidate and other authors to this work has been explicitly indicated overleaf. The candidate confirms that appropriate credit has been given within the thesis where reference has been made to the work of others.

Work Formed from Jointly Authored Publication

The candidate has published one paper form woke contained in this thesis. This was submitted with help of the supervisors. The candidate did the CFD modelling, analysis the results, meshing and results presentation for the publication.

Chapter 3 of this thesis is conference paper jointly authored: Azzawi, I, Mao, X and Jaworski, AJ (2016) *Design, Fabrication and Characterization of Low Speed Open-jet Wind Tunnel.* In: Proceeings of World Congress on Engineering 2016. World Congress on Engineering 2016, 29 Jun - 01 Jul 2016, London. IAENG. ISBN 978-988-19253-0-5 (In Press)

The candidate has conducted the majority of the work that appears in the published paper, such as developing the CFD model, presenting and analysing the data. The co-authors provided valuable review and guidance to the candidate.

Acknowledgements

I would like to express my extreme appreciation to my main supervisor, Prof. Artur Jaworski and second supervisor Dr. Xiaon Mao for their invaluable guidance and continual support over the time of my research. They were always willing to make time to see me and their advices were always invaluable.

The PhD student also wants to express his gratitude to Iraqi organizations (HCED and University of Diyala) for their financial support during the PhD study.

I would like to extend my great thanks also to Mr. Ed woodhouse, Dave Instral and Gurdev Bhogal for their help and support, advices and fabrication points of view. You are helped me a lot; thank you very much indeed.

Finally, largest thankful to my, wife and daughters for their help, support, encouragement and patience during the years of my study. She has always supported me and gave a lot of motivation to face the whole challenges during my PhD study.

ABSTRACT

The topic of flow separation control has been extensively studied as a means by which drag can be minimized and lift improved. Such flow control can be either passive or active; the primary focus of this research is on active flow control. This study investigates the use of synthetic jet actuators (SJAs) to control flow separation and recirculation area behind a convex "hump" model. This work is motivated by the need to reduce the separation length, reverse flow width which represents the main source of drag force in commercial aircraft.

A single convex hump model was selected based on experimental and numerical investigations. These models had a fixed height of H =30 mm and two lengths of L = 200 mm and 30 mm respectively. The results further showed that there was a delay in the flow separation due to the decrease in aspect ratio H/L, resulting in the formation of recirculation area nearer to the trailing edge. Moreover, from quiescent flow condition study, it has been noticed that by utilizing the Helmholtz resonance frequency of the cavity and amplitude modulation excitations, the actuator can exhibit more significant blowing velocity with a diminished power input. Therefore, some useful guidelines on the influence of both geometrical and operational parameters on SJA design can be derived from these results. Furthermore, to accommodate the hump model with the SJAs, a low velocity "open-circuit" wind tunnel was developed and built at The University of Leeds using a series of Computational Fluid Dynamics (CFD) and experimental techniques.

The latter experiments were examined the effect of the SJAs on the flow separation initiation and recirculation flow dimensions presented in the region behind the hump model. Un-modulated and modulated sine waves were used to drive the SJAs. These experiments were conducted at U_∞ = 7 m/s so that three velocity ratios (Vr) of values 0.5, 1 and 1.5 could be appraised. When the actuation is carried out using either modulated or un-modulated excitation then as the velocity ratio increased from 0.5 to 1.5, a larger reduction in the recirculation width and separation length was seen. There are however, small differences between the effects seen for modulated and un-modulated excitations. Mainly, it was seen that using amplitude modulation excitation, the maximum decrease in the reverse flow thickness and separation length were 4% and 1% respectively lower than the maximum reduction seen for the single sine actuation case (Un-modulated case).

Table of Contents

List of Tables

List of Figures

Nomenclatures

A	Cross sectional area (m^2)
Ar	Area ratio
CR	Contraction ratio
C	Speed of sound (m/s)
D	Diameter (mm)
F^+	Non-dimensional frequency
f	Frequency (Hz)
H	height (m)
I	Current (A)
K	Loss coefficient
k	Suction duty cycle
L	length (m)
L	Dimensionless stroke length
n	Orifice number
P	Pressure (Pa)
q	Dynamic pressure (Pa)
R	Radius
Re	Reynolds number
rpm	Revelations per minute (r/min)
St	Dimensionless strouhal number
S	Dimensionless stokes number
s	Span length (mm)
T	Time period (s)
U	Velocity (m/s)
U_i	Velocity at point i
u_o	Instant stream-wise velocity (m/s)
$\bar{u}$	Average velocity (m/s)
Vr	Velocity ratio (U_j/U_∞)
$Vp\text{-}p$	Peak to peak voltage (V)
W	Width

Greek letters

β	Angular position of actuation
βs	Porosity of mesh screen
σ_s	Solidity of mesh screen
Δ	Difference
Δ	Displacement (mm)
Cμ	Momentum coefficient
μ	Dynamic viscosity (kg/m·s)
v	Kinematic viscosity (m^2/s)
θ	Angle
π	3.14159
ρ	Density (kg/m^3)
σ$_v$	Standard deviation
Ω	Vortex ring circulation

Subscripts

c	Cavity
c	Carrier
e	Excitation
ex	Expansion
f	Friction
H	Helmholtz
h	Hydraulic
j	Jet
m	Modulation
o	Orifice
s	Shedding
st	Settling chamber
ts	Test section
∞	Freestream

Abbreviations

AFC	Active flow control
BFS	Backward facing step
B.R	Blockage Ratio
CFD	Computational fluid dynamics
CTA	Constant temperature anemometer
FFT	Fast Fourier transform
HWA	Hot wire anemometer
IMPC	Ionic polymer-metal composite
PIV	Particle image velocimetry
PSV	Polytec scan vibrometer
PSD	Power spectral density
RFD	Radial field diaphragm
RMS	Root mean square
RANS	Reynolds-average Navier-Stokes
SJA	Synthetic jet actuator
VFD	Variable frequency driver
T.I	Turbulent intensity

Chapter 1: Introduction

1.1. The Need for Flow Separation Control

Different shapes of bluff bodies, including offshore platforms, power lines and heat exchangers, have recently been explored by researchers in their search for industrial application models. Flow over these models and other bluff bodies is an important research area due to it having been widely used in engineering applications. Although bluff bodies, such as circular cylinder and backward facing step (BFS), demonstrate an uncomplicated geometry, but after a particular Reynolds number value, the flow behind them becomes turbulent. For a Reynolds number greater than a critical value, the main feature displayed by bluff body flows, such as cylinders, is flow separation accompanied by vortex shedding in the near-wake, making the flow unstable with high adverse pressure gradient on the body near the surface. This vortex shedding (see **Figures 1a and b**) occurred over a wide range of Reynolds number, vortex shedding results in structural vibration, mixing, acoustic noise and resonance, as well as substantial aerodynamic drag intensification. Various engineering applications, including hydrodynamic loading on marine pipelines, offshore platform support legs, chemical mixing, and lift fluctuations, manifest the phenomenon of flow over a circular cylinder (Ong et al., 2009). This serves to underline the importance of vortex shedding and flow separation control in engineering applications.

However, Von Karman vortex shedding which occurs on two sides behind a bluff body such as a circular cylinder immersed in free stream flow is different from one side vortex shedding which is produced from a backward facing step (BFS). Separated flow over a Backward Facing Step (BFS) is used widely to evaluate the performance of different models for separated flow and it is well known that a backward facing step exists in cars, buildings and airplanes. A simple geometry of this mechanism can be seen in **Figure 1.2**. The study of flow separation is vital because it is responsible for producing drag and erratic aerodynamic forcing which can cause fatigue. The flow over a backward facing step is considered to be the basic building block for all other separated flows and it has been the subject of academic study in the aerodynamics sector for over sixty years. Spazzini (2001) noted that the BFS is ideal for investigating separated flows due to the fact that whilst the flow will split every time at the step/curve it will reform further downstream.

1

a)

Y

Separated flow and vortices

wake

D

Y

b)

Favourable pressure gradient $\frac{\partial p}{\partial x} < 0$

Adverse pressure gradient $\frac{\partial p}{\partial x} > 0$

U_∞

Boundary layer edge

Y

X

wake

Vortices

Separation location   Reverse flow
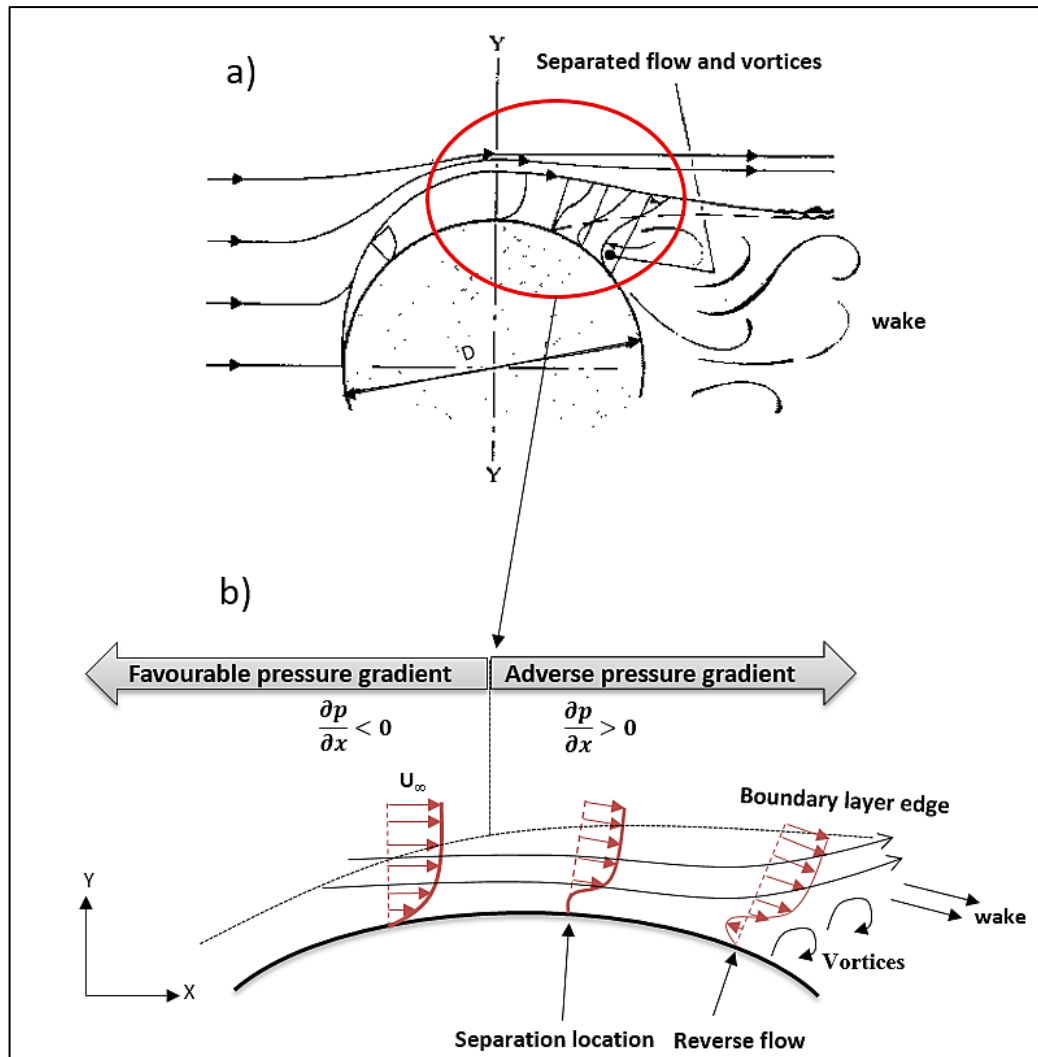
Figure 1.1: a) Boundary layer separation on a cylinder; b) Close-up view boundary layer separation on a cylinder.

Figure 1.2 illustrates the three main regions behind a BFS and these are shear layer zone, the recirculation zone, and the reattachment zone. The shear layer is generated at the separation point and creates a huge amount of instability behind the step and then reattached again to the wall to generate the reattachment point. As can be seen from the figure that the onset of separation location is fixed at the step while the related recirculation area and reattachment point are still preserved. The recirculation area is separated from the new developed flow downstream by the reattachment point which showed highly unstable region.

The potential benefits that flow control can provide have been a focus for research for the last 30 years. The main purpose of flow control can be described as bringing the following characteristics, delay transition, suppression or enhancement of

turbulence and the prevention of separation, so the consequent advantages can include drag reduction, lift enhancement, mixing augmentation, heat transfer enhancement and flow-induced noise suppression.
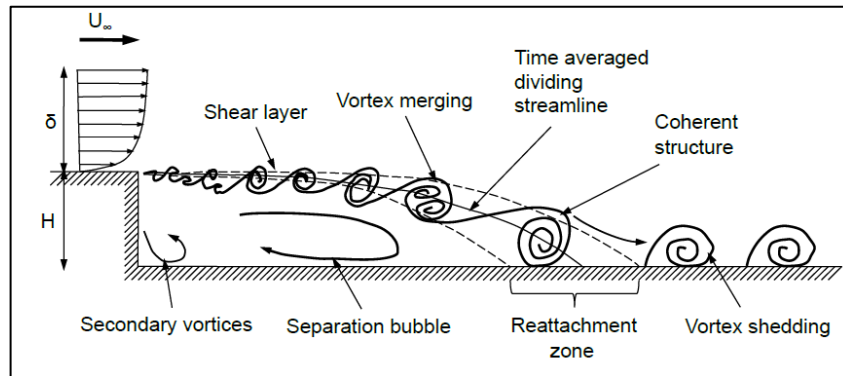
Figure 1.2: Flow over a backward facing step illustrating the associated shed vortices and flow instabilities (Rajasekaran, 2011).

Numerous numerical and empirical studies have addressed the issue of flow separation phenomena and vortex shedding. Flow over a circular cylinder is one of the flow configurations most widely used by researchers and less with BFS. The reason for its extensive use is that it presents flow features of great complexity, even though they have an uncomplicated geometry. There has been an important amount of research carried out over the past fifteen years to investigate the cause, understand the flow physics and the fluid mechanics following the flow separation, vortex shedding and reattachment flow. The existing studies can be classified into two distinct groups. One group of studies is geared towards the modification/elimination of the occurrences of flow separation and reattachment, while the other group of studies is concerned with finding ways in which to control the inception of such occurrence and at the same time to make this control technique as efficient as possible.

Two particular approaches of flow control have been outlined, namely, passive flow control and active flow control. The former is characterized by the fact that the flow can be excited without any power requirement and can be achieved with the use of end plates and splitter plates. The second approach can be achieved through blowing, suction or periodic oscillation via a body surface orifice. Chapter 2 addresses these methods more comprehensively.

The second group of studies is the focus of the present research. The current research is focused mainly on flow control on a convex hump model with respect to

shear layer vorticity and flow separation phenomena in the wake area. Although the convex hump is simple model, but it has been often used in some "domed" roof buildings (Franchini et al, 2005; Lo and Kanda, 2012). Therefore, control the separation and vortex shedding over the hump are important. These vortices can induce a strong vibration even at low wind speed (from 5 -11 m/s) which called vortex induced vibration (VIV) as they caused crucial structure damage (Yaghoui, 1991 and Toy et al, 1983) especially to the nearby buildings. Therefore, the flow control over a convex hump model has been fully studied at free stream velocity of $U_\infty = 7$ m/s and partially investigated at $U_\infty = 10$ m/s which will be explained in Chapter 8 in more details. Moreover, this research is also focused on the examination of geometrical and operating parameters of SJA device when it is applied to a separated boundary layer.

Prior to the flow control tests, a range of measurements have been proposed for the detection of the separated boundary layer as well as for the quantitative and qualitative description of the recirculation area and reattachment point across the convex hump surface. This research is not only trying to eradicate the shedding or modify the separation location at which it occurs, but also tries to reduce the recirculation width and reattachment point and hence reduce the level of the velocity deficit in the wake area behind the hump as a result of such phenomena. Array of synthetic jet actuators were used here as an active flow control technique, which was considered as an efficient and effective method for controlling the flow separation (Watson, et al., 2007). However, despite the extensive use of the synthetic jet actuator, its impact on the flow over a convex hump has not been methodically investigated, and thus further studies should be conducted in the near future. Power spectral density was evaluated from the wake velocity signal using the Matlab program and particle image velocimetry (PIV) techniques are also used in this research to identify any changes to the onset of separation location, reattachment point, shear layer vorticity that occurs because of different actuation parameters.

1.2. Aim and Objectives

The aim of this study is essentially concerned with experimental investigation using an array of synthetic jet actuators to generate vortex rings in order to either eliminate or delay the onset of flow separation over a convex hump model. It was hoped that these vortex rings would be able to interact with the separated boundary layer generating vortical structures that allow a degree of control of the wake area flow field by either reducing the recirculation width and reattachment point behind the convex

hump, or altering the dominant frequency in the power spectral density of the vortex shedding. However, several objectives are set to carry out this study:

➢ A new low-speed open-circuit wind tunnel has been designed and constructed at the University of Leeds. A series of Computational Fluid Dynamic (CFD) and experimental evaluations were conducted to determine the flow quality and to verify the wind tunnel adequacy for aerodynamic studies.

➢ Quantify the onset of separation location, recirculation width, reattachment point and shear layer vorticity over a convex hump model experimentally (baseline tests) without actuation, and this was done while the convex hump undergoes at 7 m/s freestream velocity using numerical simulation, hot-wire anemometer (HWA), flow visualization and PIV techniques.

➢ Develop and study the effect of excitation and geometrical parameters on synthetic jet velocity and circulation under quiescent flow conditions using the hot-wire anemometer technique. This is useful to produce coherent structures which were responsible for the interaction with boundary layer to attempt to alter the wake area behind the convex hump. Therefore, some useful guidelines on the influence of both geometrical and operational parameters on the design of SJAs can be derived from this research.

➢ Investigate whether SJA could be used as a method of flow separation control and to gain better understanding as to what excitation parameters affect this method, such as excitation frequencies, amplitude modulation, angular position of the actuation (β) and velocity ratio (*Vr*).

1.3. Thesis Structure

Chapter 2: This chapter is aimed at providing a comprehensive review of the investigations related to synthetic jets in the context of flow under quiescent flow conditions, uniform cross-flow and boundary layer separation control and to identify the areas where further research is required.

Chapter 3: This chapter pertains to the development of an open-circuit sub-sonic wind tunnel at the University of Leeds. It contains a series of Computational Fluid Dynamics (CFD) and experimental evaluations to determine the flow quality and to verify the wind tunnel suitability for aerodynamic studies.

Chapters 4 & 5: Chapter 4 presents a description of the facilities, convex hump models and the array of synthetic jets used in this research whilst Chapter 5 provides details of the various experimental techniques used throughout this research, with the focus on principle of operation, set-up and measurement techniques given.

Chapter 6: This chapter gives details of the effect which the geometrical and operational parameters had on the flow topology of three scales of synthetic jet actuators under quiet flow conditions. It presents two types of results and discussion; the initial results study the clamping effect on the piezo-ceramic diaphragm displacement using a polytec scan vibrometer (PSV). Moreover, it presents the final geometrical and excitation parameters selected for the purpose of flow separation control. Given that perspective, it was desired to produce the maximum jet strength in the smallest form-factor that was feasible for integration in the convex hump design.

Chapter 7: Chapter 7 gives details of preliminarily investigations of the un-actuated convex hump models at 7 m/s free stream velocity using different qualitative (flow visualization) and quantitative measurements (HWA and PIV). It includes a discussion of these results to select a single hump model with clearer flow separation, recirculation area and reattachment point events occurring in the wake area which will be used in all flow control investigations.

Chapter 8: This chapter presents the results in terms of power spectral density (PSD), flow separation, recirculation area and reattachment point in the wake area behind the convex hump with the synthetic jet actuators operating at different excitation parameters, velocity ratio and angular position of actuation angle (β). These results are then compared to the un-actuated configurations developed in Chapter 7.

Chapter 2: Background and Literature Review

The aim of this chapter is to provide a comprehensive review of the investigations related to the flow separation background and synthetic jets in the context of quiescent flow condition, uniform cross flow as well as the concept and means of flow separation control and to identify the areas where further research is required.

2.1. Flow Separation Phenomena

Pressure distribution along the wall is responsible for flow development within the boundary layer. A decrease in the downstream pressure allows the boundary layer to securely attach to the wall while an increase in pressure in the direction of flow gives rise to separation of the boundary layer from the wall. The separation occurs mainly because the kinetic energy of the fluid particles outside the boundary layer is greater than that of the particles within the boundary layer due to the gradual decrease in velocity towards the solid wall (Prandtl, 1904). Thus, the near wall fluid particles may stop and change direction to form recirculation due to their inability to overcome even the slightest pressure increase that may be experienced within the tenuous region, the behaviour that is characterized as flow separation is induced by an adverse pressure gradient.

Figure 2.1 depicts a schematic illustration of how the velocity profiles in the boundary layer vary in response to the flow behaviour near separation caused by the adverse pressure gradient conducted by the developing flow over a rigid boundary. Because of zero velocity at the wall, the velocity gradient $[\frac{\partial u}{\partial y}]_{y=0}$ has to be zero at the point of separation, positive upstream of separation, and negative in the reverse flow region. The shear layer downstream of the separation point will pass over the recirculation region and reattach to the wall afterwards, or it may form a wake and remain unattached completely. The length scale of region of recirculation can be as large as the body height in the case where the formed wake remains completely unattached. However, the flow separation has one benefit when produced over high speed military and modern civil aircraft (e.g. delta wings) based on the lift which is generated by a pair of counter-rotating leading edge vortices.
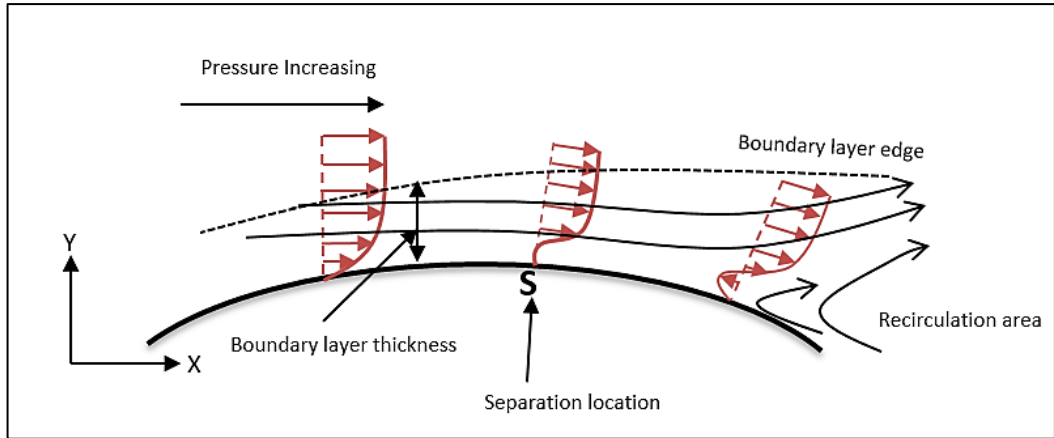
Figure 2.1: Schematic of flow separation 'S' induced by an adverse pressure gradient.

Additionally, there are several computational methods which still can be used to predict separation points into laminar and turbulent boundary layers quite satisfactorily. These methods are clearly explained in **Figure 2.2.**
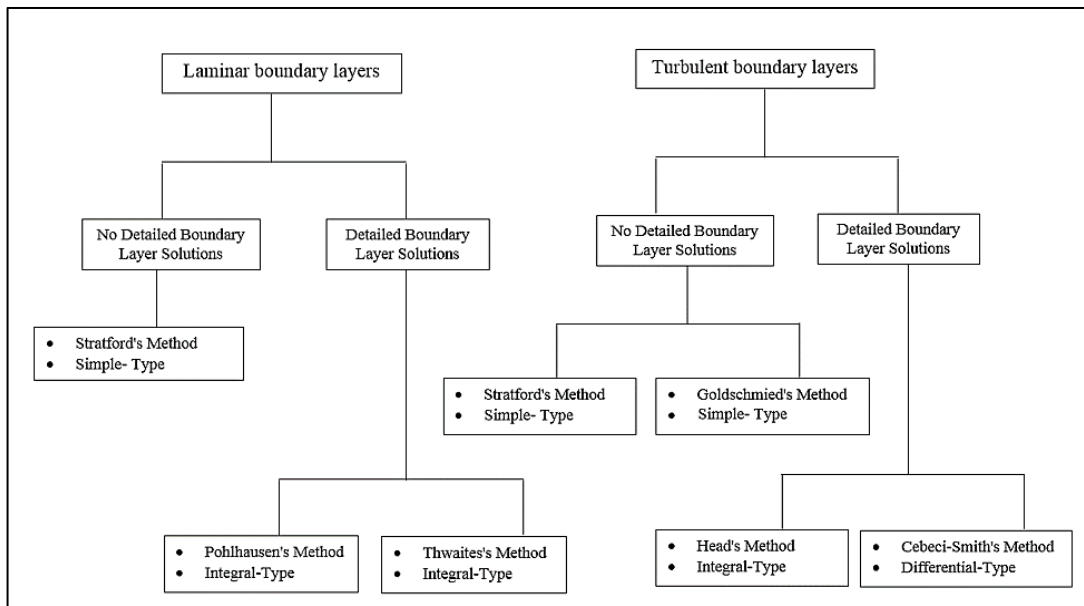
Figure 2.2: The Prediction methods of separation points into laminar and turbulent boundary layers.

These methods can be divided into three main types including, integral-methods, differential-method and simple-methods. For laminar boundary layer, the first general method was named as Pohlhausen's method. In this method, the boundary layer equations are only satisfied at the outer edge and at the wall of the boundary

layer. The displacement thickness δ^*, the skin friction τ_w, and the momentum thickness θ need to be calculated, while the velocity profile within the boundary layer is assumed to yield a polynomial form. However, Pohlhausen's method introduces less accurate results as separation is approached, but becomes more accurate in a favorable pressure gradient region, therefore, the predicted distances to separation are typically 30% too high (Curle, 1962).

In contrast to Pohlhausen's method, Thwaites indicated that once the boundary layer thickness and the skin friction distribution are calculated, it is not necessary to produce clear assumptions concerning detailed velocity profile within the boundary layer. This is the concept on which Thwaites's method is built. A parameter, λ (pressure gradient parameter) was defined in Thwaites method using integral method to solve momentum integral equation. This parameter was related to the separation of the profile as follows:

$$\lambda = \frac{\rho\theta^2}{\mu}\left(\frac{dV_e}{dx}\right) \ldots \ldots \ldots \ldots \ldots \ldots \ldots \ldots \ldots \ldots \ldots \ldots \ldots .2.1$$

Separation was found to occur at $\lambda = -0.0842$ (Kai, 1995).

Additionally, the prediction of the separation point in the turbulent boundary layer is more complex than laminar boundary layer. **Figure 2.1** clearly showed that the separation point prediction for turbulent boundary layer can be divided into two groups, differential and integral types. These types were introduced by Cebeci-Smith's in (1972) and Head's in (1960), the latter used a shape factor ($H = \frac{\delta^*}{\theta}$) in integral methods (Head's method) while a zero wall shear stress is used in Cebeci-Smith's method to predict the separation point in differential methods. The separation is assumed to be occurred when H fall between 1.8 and 2.4 (Cebeci and Smith, 1972).

However, Cebeci-Smith used more exact differential equations than Head's method, therefore, this method is also applicable to axisymmetric flows. Cebeci-Smith's method is the method which is able to handle both laminar and turbulent for incompressible and even compressible flows. This differential method is more complicated compared to other methods and its accurate is lower than integral methods (Head's method) (Cebeci et al 1972). Therefore, most researcher tried to avoid using

the 'complicated' method of Cebeci-Smith, which is no better than an integral-type method in most cases.

The idea of dividing the boundary layer into the inner and outer regions was developed by Stratford (1959) and Goldschmied (1965). These methods do not require detailed boundary layer calculation and with these methods, the point of separation is predicted by simple formula, or by simple differential equations. However, neither Stratford's method nor Goldschmied's method is the correct choice, if any detailed boundary layer information is required. According to Stratford method, the separation point location criterion is predicted based on the following relation:

$$S(x) = \frac{cp\left(x\frac{dcp}{dx}\right)^{0.5}}{(10^{-6}Re)^{0.1}} \dots\dots\dots\dots\dots\dots\dots\dots\dots\dots\dots\dots.2.2$$

The criterion of separation point is occurred when $S(x) = 0.39$-0.5 (Stratford, 1959). Similarly, Goldschmied separation criterion can be considered even simpler than Stratford method. Goldschmied introduced the following separation criterion relation:

$$Cp_{sep} = 200Cf_m \dots\dots\dots\dots\dots\dots\dots\dots\dots\dots\dots\dots.2.3$$

Following an extended period of growth and development, the aviation industry is now confronted with several challenges. It has been identified that the threat of climate change and the contribution of aviation to the production of greenhouse gas emissions are the greatest of these challenges (Lawrence, 2009). Together with the rise in fuel costs and the intensification of aviation traffic, these have prompted interested parties to focus on the development of cleaner, quieter, more effective and eco-friendly aircraft, not only to reduce operational costs, but also to meet the target established by the European (ACARE) Vision for 2020, demanding the minimization of 50% CO_2 emissions, 80% of NO_x emissions, and perceived noise by 50%. Nowadays with the explosive growth of technology, not only the way of increasing the operational efficiency of aircraft, or reducing the effect on the environment is important, but flow control has received a great deal of attention among these new technologies and the potential benefits of flow separation control are the reason why it is still used until today. A good description of "flow control" is "….. any mechanism or process through which the boundary layer of a fluid flow is caused to behave differently than it normally would were the flow developing along a smooth straight surface" (Gad-el-Hak, 2000). However, there are many reasons for using flow control technologies. One of these reasons is that they have been used to control or eliminate separation over the

surface of the wings. In addition, they have brought several benefits to the aviation industry including, drag reduction, lift enhancement and unsteadiness enhancement. Therefore, flow control technologies based on reducing the aerodynamic drag, increasing the lift and improving the system performance which leads to a reduction in fuel consumption hence carbon emission. It has been shown how a 1% reduction in drag may result in a 0.2% reduction in the operation costs of a large aviation industry which corresponds to 10 passengers. Flow control technologies have been applied in an aircraft wing in different ways, as shown in **Figure 2.3** (Reneaux, 2004)**.**
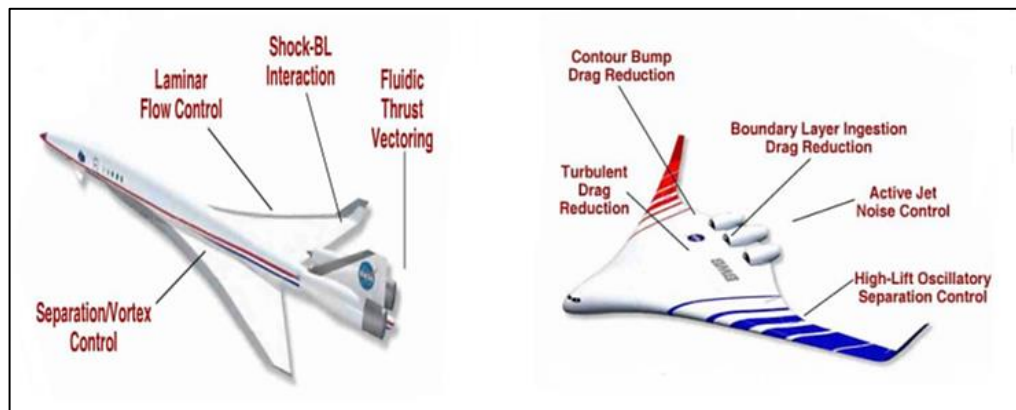
Figure 2.3: Examples of flow control.

Flow control technology can be divided into two main categories: Passive and active flow control. Classic examples of passive flow control could be vortex generators, grooves or any type of passive cavities, which are utilized via geometrical modification, especially on civil transport to delay the separation point. In addition, no extra power would be added during passive flow control. In contrast, the use of blowing, suction or periodic excitation through orifices on the surface of the wing is good example of active flow control technology. Extra power would need to be added during active control to alter the flow in order to produce the desired impact. This might be achieved in several ways, but despite the suction phase having a big impact on delaying the separation, it has been limited because a complex piping system is required which brings a heavy weight. Similarly, it was demonstrated that during the blowing phase effective control can be achieved by using an array of steady jets at the surface of the wing to prevent, or eliminate flow separation and unsteady flow over the wing, through injection of a high momentum jet into the boundary layer, and thus the boundary layer becomes more resistant to the separation flow (Schlichting and Gersten, 2000).

Recently, periodic excitation has shown significant advantages in flow control which has received more attention in comparison to the blowing/suction phases (Greenblatt and Wygnanski, 2000). There are several reasons why osculating blowing is considered to be more efficient in comparison to the blowing/suction phases in terms of flow control. One reason is that the coherent structures are generated and interact with the flow boundary layer, which could make the unsteady flow reattach. Another reason might be that, it is able to produce the same level of control impact of steady blowing and suction, with zero net mass flux. A good example of the periodic excitation flow control technique is the synthetic jet actuator (Tang et al, 2014), which is the main technique used in this research. **Table 2.1** summarized the advantages and disadvantages of both passive and active flow control.

Table 2.1: Aspects of passive and active flow control techniques.

Advantages/Passive flow control	Disadvantages/Passive flow control
Simple installation	Re dependent
External energy source not required	Sensitive to off-design
Mechanical or electro-mechanical components not required	Increased drag
Advantages/Active flow control	**Disadvantages/Active flow control**
Flexible	Greater technological complexity
Adaptable to different flow control conditions	Required external energy source
Manages separation for off-design efficiency	

2.2. Synthetic Jet Actuators

The synthetic jet actuator devices used here have several functions; the most common has been the flow separation control with good success. The next sections outline the theory of SJA, phenomenon of synthetic jets in both quiescent conditions and cross-flow, as well as the concept and means of flow separation control.

2.2.1. Background and Theory of Synthetic Jet Actuators

Ingrad (1950) was the first to discover that the use of a simple cavity with a small orifice at one extremity and generating acoustic waves at high amplitude and frequency at the other extremity would lead to the production of vortex rings from the cavity via

the orifice. Other studies on this topic include the works of Holman et al (2005) and Zhou et al (2009). This concept was developed further once these devices were equipped with smart structure technology. The outcome of this was what is now referred to as a synthetic jet actuator, which is a self-contained and simple device that can operate without complex support systems, such as air supply, an array of hydraulic piping, and connectors.

Zero-net-mass-flux jets which are also known as synthetic jets have been utilised over the last fifteen years as a flexible tool in a wide range of applications, such as active flow control, thrust vectoring, mixing, and heat transfer enhancement. The general functions of synthetic jets include production of large coherent structures in boundary layer flows, reinforcement of transition and introduction of an unstable harmonic or pulsating movement into a turbulent shear layer flow.

A simple schematic representation of a synthetic jet for a round orifice with sharp edges is presented in **Figure 2.4**. The Gaussian cross-stream flow profile peaks at the centreline, while the formation of the vortex pairs can be observed above the exit during the phase of blowing. Synthetic jets have been mostly researched with regard to physics and thresholds of formation, evaluation as well as momentum and impulse development and propagation. It was observed that all vortex pairs formed at the orifice wall, after which they become unsteady during ejection from the exit, eventually become turbulent, losing momentum and coherence in relation to the initial jet flow (Chaudhary et al, 2009).
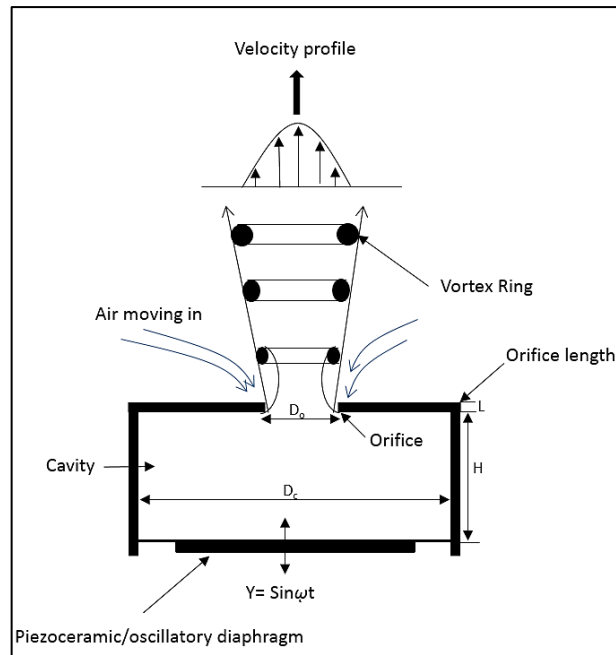
Figure 2.4: Synthetic jet for sharp edges and a round orifice.

2.2.2. The Mechanism of a Synthetic Jet Actuator

Either a cylindrical or rectangular cavity, a slit or round orifice and an oscillating diaphragm are the three basic elements of a standard synthetic jet actuator, as illustrated in **Figure 2.5** (Holman and Utturkar, 2005).
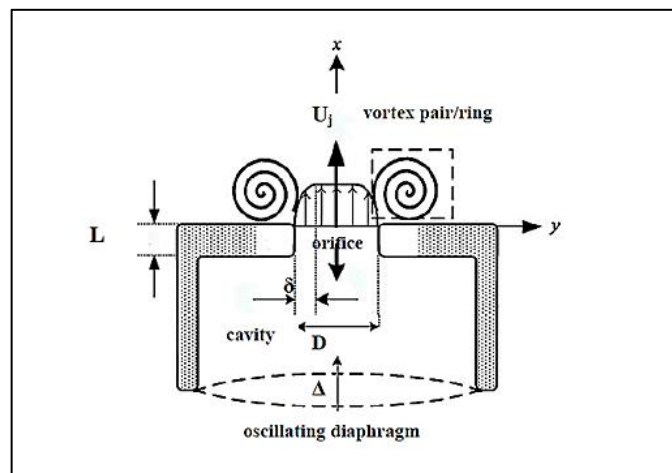
Figure 2.5: Synthetic jet actuator mechanism (Holman and Utturkar, 2005).

The excitation frequency determines the rate of diaphragm deflection, which leads to a gradient pressure discrepancy between the actuator cavity and the external flow. The oscillating diaphragm displays an upward movement during the blowing

phase of the cycle. The separation of the flow from the orifice edge occurs, followed by the formation of the flow into a vortex ring. If the initial impulse from the diaphragm is large enough, the downstream movement of the vortex ring continues, driven by its own velocity and leaving a trailing shear layer. During the suction phase, the external flow is taken by the jet and radially sucked back into the cavity. In the last stage of the cycle, the downward movement of the diaphragm determines the formation of a vortex ring on the internal edge of the orifice. **Figure 2.6** illustrates these processes based on the numerically predicted images Rizzetta et al (1999). Moreover, the flow properties of a single operating cycle of the synthetic jet at four distinct phase angles are clearly indicated in the figure.
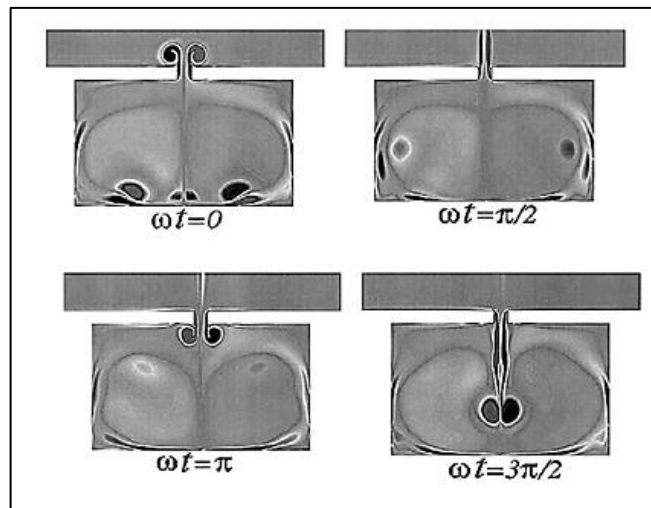
Figure 2.6: Synthetic jet development at four phase angles (Rizzetta, 1999).

The repetition of the diaphragm oscillating cycle initiates the formation of a series of coherent structures which become instable before becoming turbulent, slowing down, and losing their coherence structure and becomes indistinguishable from the mean jet flow.

A unique feature of synthetic jet actuators can be detected from the description of their formation and ability to transmit momentum to the surrounding flow without any additive mass. This ability is essential in adding more energy to the weak flow and enhancing their ability to avoid separation. For instance, the suction phase of the cycle involves the entrainment of low momentum flow into the cavity, as a result of which the high momentum flow is transported from the freestream closer to the jet exit plane.

15

Furthermore, in the blowing phase of the cycle, the low momentum fluid incorporated in the cavity is ejected back in the surrounding flow and re-energized with a higher momentum.

2.2.3. Synthetic Jet Actuator Drivers

The oscillating diaphragm plays an essential role in the synthetic jet actuator. Its displacement gives rise to an alternating pressure gradient which is required to ingest and eject the air from the orifice to form the jet and vortex ring. There are several types of diaphragm, such as motor-driven pistons, an electromagnetic shaker or a camshaft (Crook and Wood, 2001), acoustic loudspeakers (McCormic, 2000), as well as diaphragms underpinned by a fluctuating membrane, which is typically a piezoelectric patch affixed to one part of a metallic shim and excited by a voltage which was used in the current research. Some examples of these devices are shown in **Figure 2.7**.
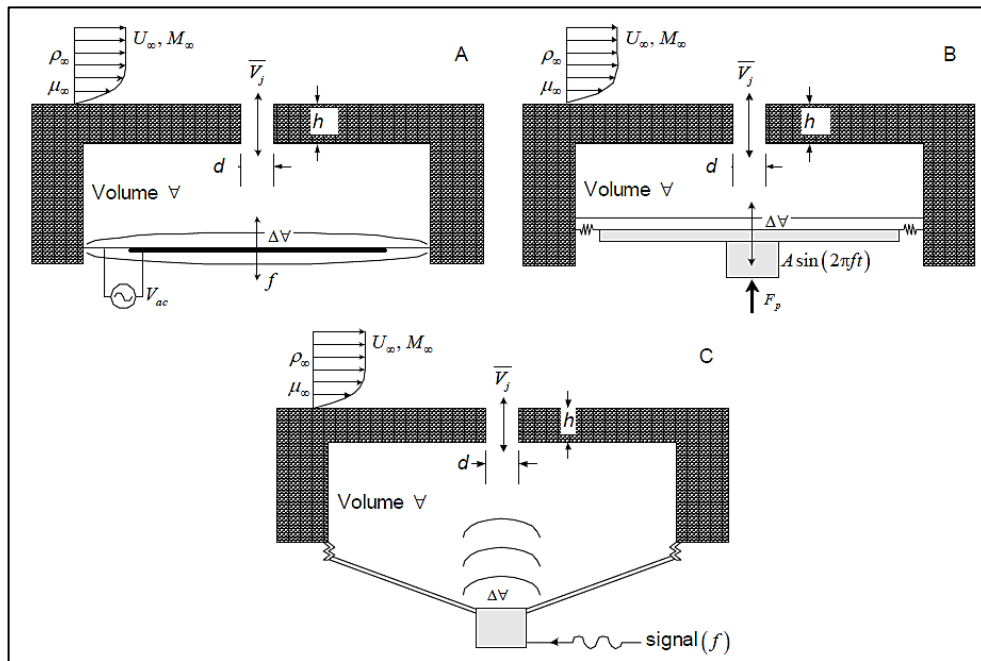
Figure 2.7: Schematic illustration of the three kinds of excitation mechanisms–piezoelectric diaphragm (A); fluctuating piston (B); and acoustic excitation (C), (Gallas, 2005).

2.3. The Parameters Affected by Synthetic Jet Actuators in Quiescent Conditions

To delay flow separation, the synthetic jet actuator parameter design (e.g. diaphragm types, operational and geometrical parameters) that affects the formation of the vortex rings should be investigated. Knowing how such parameters are coupled in the production of a given jet and understanding their contribution towards achieving a given objective of flow control is important when designing actuators which are effective. Even though that is the case, the first vital step is the understanding the synthetic jet fluid mechanics under quiescent conditions, while the second vital step is understanding of the interaction of synthetic jets with uniform cross-flow, which promotes the ability of synthetic jet in flow separation control. Based on the wide range of literature, a typical synthetic actuator parameter design can be categorized into three distinct groups when in quiescent flow which are as follows:

2.3.1. Operation Parameters

The synthetic jet formation and peak jet velocity can be explained via a number of operational parameters, such as excitation frequencies, excitation amplitude, diaphragm types and waveform types and amplitude modulation techniques. In specific regard to the diaphragm types, a comparison was examined between a bimorph, Thunder actuator and Radial Field Diaphragm (RFD) circular bender actuators by Mossi et al (2005), with RFD acknowledged as an innovated technology by NASA, which are known to exploit far stronger d33 coupling mode as opposed to typical actuators, which are based on d31 coupling mode. One of the potential drawback of the method could be identified by the fact that only low frequencies were used for testing. It was found that the Thunder and RFD-based SJA designs were out-performed by the bimorph SJA design. Similarly, Macro Fiber Composite (MFC) actuators demonstrated no aerodynamic behavioural benefits compared to bimorph types, but were stronger and easier to handle than the delicate bimorphs (Ohanian et al 2008). A number of other types of diaphragm were also modelled in the work of Lee et al (2006) which were referred to as Ionic Polymer-Metal Composite (IPMC), with the aim of driving SJA output. This particular type of material has the capacity to achieve greater displacement movements than those achieved through the application of piezoelectric diaphragms; typically, however, these provided much lower levels of force and response time. As one disadvantage following the completion of the analysis,

there was a lack of information pertaining to the frequency actuation limitations that would be expected. In this vein, average jet velocities of approximately 10 m/s were estimated at an approximate driving frequency of 30 Hz. A more innovative method was applied by Liang et al (2006) who utilized Shape Memory Alloy (SMA) diaphragm, along with corresponding iron pads, electromagnetically driven with the aim of achieving notably high jet velocities (190 m/s). Although there was an impressive level of jet output established, nevertheless, there was the need to achieve 200 W (0.27 HP) of electrical power, with the apparatus weight of the SJA amounting to 1.36 kg. Such aspects, alongside the large dimensions, mean that the method would not be as appealing in the case of air vehicle integration; only large aircraft would have the propensity to sustain the power and weight impact, and potentially achieve enhanced vehicle performance through the utilization of such flow control actuators.

Previous studies showed that some parameters could be dependent on other parameters such as the waveform type which has two dependent parameters, amplitude of the waveform which dictates the peak displacement of the diaphragm, in conjunction with the excitation frequency to characterize the jet peak meam velocity. The synthetic jet formation and vortex ring parameter effect studies showed that the operational parameters including the waveform type, have a significant effect on SJA which provide a direction for future research in this field on both quiescent and flow control applications.

To understand how different operational parameters affected the behaviour of the peak mean velocity of synthetic jets, Mane (2005) and Mane et al (2007) investigated four oscillatory types, namely, Bimorph, Thunder, Lipca, and RFD. For each type, the two driving waveforms of sine and sawtooth were examined at various frequencies and amplitudes (dependent variables), while a third waveform, square, was investigated solely for the RFD actuator. According to the findings obtained, the peak jet velocity was significantly affected by the excitation waveform. Furthermore, by comparison with the sine waveform, the sawtooth waveform generated a higher peak jet velocity. The reason for this was that, because of the single pulse effect, only one peak jet velocity was generated by the sawtooth waveform. On the other hand, due to the ejection and ingestion phases, two velocity peaks of different magnitude were produced by the sine and square waveforms. Compared to the sine waveform, the square waveform generated a higher velocity, but it presented a shortcoming, in that it

could not be applied at low frequencies, where the dielectric disintegration could be harmful to the actuator. In general, an increase in the amplitude voltage determined an increase in the velocity of the synthetic jets as well, irrespective of the type of signal. Nonetheless, in order to prevent damage to the actuator, the operation of synthetic jets should be undertaken at voltages lower than the highest voltage permissible for every diaphragm. In addition, in the case where the actuator was driven with the sine waveform, the increase in the peak mean velocity of the synthetic jets was directly proportional to the increase in the excitation frequency. By contrast, in the case of the sawtooth waveform, the velocity profile exhibited significant differences and remained fixed at about 10 Hz for every actuator. The author considered that the choking condition was the cause of the behaviour observed with the sawtooth waveform. Therefore, in the current study the sine waveform was used.

Similarly, sine waveform and square waveform were also examined by Ohanian (2011). It has been found that, by comparison to the excitation parameters generated by the sine waveform and square wave, the square waveform excitation produced a peak jet velocity that was 20% higher. In cases where the square waveform was used to drive a capacitive load, extremely high peak and RMS current were generated, exciting the harmonic frequency which may be harmful to the actuator. When sine excitation is applied, the driving amplifier constraints that are conducive to optimal excitation should be used to produce maximum current and voltage as well as to prevent piezo-ceramic element longevity.

To address the narrow band frequencies of the piezo-ceramic diaphragm (Helmholtz frequency and resonant frequency), an amplitude modulation technique was introduced by Watson (2004). The effect of three different waveform types with the amplitude modulation technique on the synthetic jet velocity at fixed geometrical parameters, named sine waveform, summed waveform and pulse waveform was studied. The results showed that the amplitude modulation and sine waveforms produced the highest peak jet velocity of about 9.6 and 9.4 m/s respectively as shown in **Figure 2.8**. Overall the amplitude modulation excitation generated the maximum jet velocity at the comparatively low frequency (100 Hz) with a peak-to-peak amplitude of 80V, while sine wave excitation at a higher frequency (1200 Hz) and peak-to-peak amplitude of 120V generated a lower jet velocity. The amplitude modulation excitation technique has been used to operate synthetic jet actuators at

different types of frequency other than just resonance frequency. The motivation for using amplitude modulation excitation in SJAs is that the carrier wave has a resonant frequency equal to resonant frequency of the diaphragm, while the low modulation frequency is equal to that of the flow vortex shedding frequency. (Hong, 2006; Arwatz et al, 2007; Qayoum et al 2010).
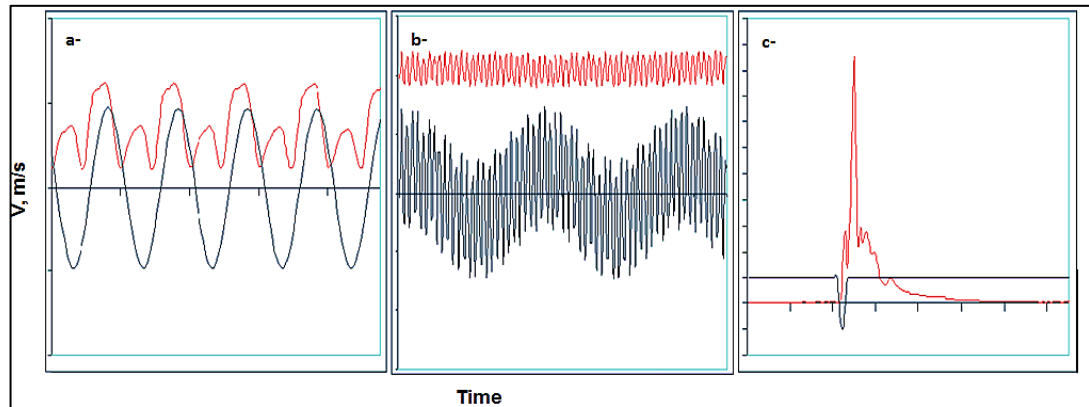
Figure 2.8: Sample velocity time series for: a) sine wave excitation; b) amplitude modulation technique; and c) pulsed waveform. (Red line shows velocity, black line the applied waveform; scales are not comparable between the 3 plots) (Watson, 2004).

The literature showed a wide range of using excitation parameters (e.g. frequency, amplitude and amplitude modulation) to characterize synthetic jets in quiescent flow, active flow control, jet vectoring, heat transfer enhancement and flow mixing. However, most of the studies have been limited to the un-modulated operating parameters, and no systematic study was available in the literature on the effect of the amplitude modulation technique on the synthetic jet formation and velocity profile. Until Qayoum et al (2009 & 2010) studied the influence of the amplitude modulation excitation on a synthetic jet actuator in quiescent flow using a hot-wire anemometer and Schlieren visualization to characterize the jet spread and velocity profile. The carrier frequency was set to 951 Hz which represents the diaphragm resonant frequency, whereas the modulating frequencies were set to 10, 25 and 50 Hz and the excitation voltages in the range 5-50 volts. The results showed that the maximum displacement of the diaphragm was obtained only at its resonant frequency. An additional displacement was achieved by applying amplitude modulation excitation which provided a mechanism by which additional frequency can be introduced as a control parameter of the SJA. The significant observations were that firstly, the amplitude modulation has a vital effect on the spatial and temporal evaluation of the

synthetic jet actuator and these characteristics were dependent on the modulation parameters selected. Secondly, the vortex rings formation and time-average velocity were increased when operating the synthetic jet actuator at amplitude modulation, especially at low modulated frequencies. Finally, flow visualization showed that the vortex rings strength was strongly affected by the amplitude modulation excitation.

Generally, the operational parameter effect studies regarding the excitation frequency, excitation amplitude with amplitude modulation are vital operational parameters that dictate the synthetic jets peak velocities in quiescent flow. Therefore, for a specific flow control application the flow has distinct spectral profiles in which certain frequency ranges dominate, so the actuation operation parameters chosen possibilities will also be important in determining the effectiveness of the devices in altering the surface flow. For the first possibility, most research especially in the 80's and 90's used the exciting frequency of the synthetic jet, which corresponds or is lower than the natural vortex shedding frequency ($F^+ \leq 1$). Another possibility is the application of a high frequency synthetic jet with amplitude modulation, many recent researchers utilised the exciting frequency of synthetic jets much higher than the natural vortex shedding frequency ($F^+ > 1$) (Glezer et al, 2005; Koopmans and Hoeijmakers, 2014).

2.3.2. Geometrical Parameters

The effect of the operational parameters has not answered all questions relating to the fundamental fluid mechanics of synthetic jets and vortex rings. Therefore, to complete another part of the image, the parametric studies of the geometrical parameter effects on the synthetic jet formation and vortex rings will be reviewed in the next sections, these geometrical parameters include:

    A. Diameter of the orifice (D_o)

    B. Thickness of the orifice (L)

    C. Diameter of the cavity (D_c)

    D. Height of the cavity (H)

The near-orifice flow field of an axisymmetric synthetic jet was firstly carried out by Crook and Wood (2000) who utilize smoke and laser light sheet visualization to perform a parametric investigation of the properties of the individual vortex rings

produced by a SJA with a 5 mm diameter orifice operating at 50Hz. Their work attempted to try and define a single parameter that could be used to describe the flow. They were unable to reach a conclusion regarding a single defining parameter but they clearly demonstrated that the form of the structures produced by an actuator is not only dependent on the frequency and level of diaphragm displacement, as may have been expected by the author, but also on the cavity geometry and the depth of the orifice plate.

Later, Mane (2005) agreed with Crook and Wood (2000) who showed that no specific parameter had a great impact on the jet velocity. A derived relation has been introduced to characterize the jet velocity related to the cavity height and orifice diameter as follows:

$$U_j \propto \frac{H}{D_o^2} \dots \dots \dots \dots \dots \dots \dots \dots \dots \dots \dots \dots \dots \dots \dots \dots \dots . . \dots \dots \dots \dots \dots .2.4$$

The relation clearly shows that the time-averaged velocity is affected more by the orifice diameter than the cavity height; therefore, the orifice diameter effect has to be considered in any study on cavity volume. Different orifice size effects on the jet velocity profile were studied by Mane (2005) at fixed cavity volume. The jet velocity was increased rapidly by about 58% for higher orifice diameter compared to the lower orifice diameter.

The orifice diameter and, in the case of actuators with multiple orifices, the spacing between them are the two dominant parameters which were also numerically studied by Razi (2012). The purpose of these studies was to determine the behaviour patterns of vortex rings in actuators with two and three orifices, and the effect on such behaviour of orifice diameter and orifice proximity. It was found that two separate and independent vortex rings were generated, with their characteristics determined by the spacing between the orifices. It is necessary that the vortex rings be entirely independent in order to avoid the effects of circulation cancellation. Experiments were conducted using actuator simulations with between one and five orifices, sufficient distance between them and standard diaphragm displacement and frequency, with the aim of achieving optimum circulation production. Three types of flow were noticed as a function to the space between orifices and stroke length. A complicated coherent structure with low circulation was seen from the first type of flow due to an immediate

interaction between the vortex rings. Therefore, the spacing of the first flow types can be named as "too close". When the space between the orifices increased, a single vortex ring is seen due to the interaction between two vortex rings which are drawn towards each other rapidly. However, when the space between the orifices increased further, the vortex rings were generated separately without any interaction and hence propagate far from the orifice on a straight line, which can produced higher circulation compared to the other type of structures. Therefore, the outcomes of these simulations are encouraging, and demonstrate enhanced levels of circulation production when adequate space between orifices is used.

Moreover, the author found that as the number of orifices increased from one to five at fixed operating conditions, the vortex ring circulation also increased such that a linear relationship was produced between the number of the orifices and total circulation. Similarly, the results of the flow visualisation by (Watson et al 2003) showed that the circulation of the exiting fluid is directly related to the orifice internal area (Watson et al 2003). As a result, the well-known findings of this experiment were indicated that a higher total circulation of vortex ring can be produced by two-orifice actuator having a total area equal to an area of large, single orifice. Therefore, the efficiency of synthetic jet actuators can be increased significantly by a simple change in the orifice plate design and the number of orifices. Finally, in order to have an actuator with a specific jet velocity and total circulation, the number and diameter of the orifices need to be defined. Therefore, an experimental study was conducted on the SJA developed here to validate this feature. Therefore, the overall conclusion that can be drawn from their study is that optimal and efficient synthetic jets can be designed to achieve the required circulation and momentum for a specific application using multiple orifice actuators with minimum input energy. The number of orifice effect was also studied in the current research experimentally to ensure that the highest efficiency of SJA was being produced.

Different types of interactions were seen between the jets from adjacent axisymmetric orifices. Three different flow regimes have been identified, depending on the strength of the jet and the orifice separation and examples of these are shown in **Figure 2.9** (Watson et al 2003a). Each of these separation regimes resulted in very

different jets being produced with varying levels of interactions between the individual trains of structures from each orifice.
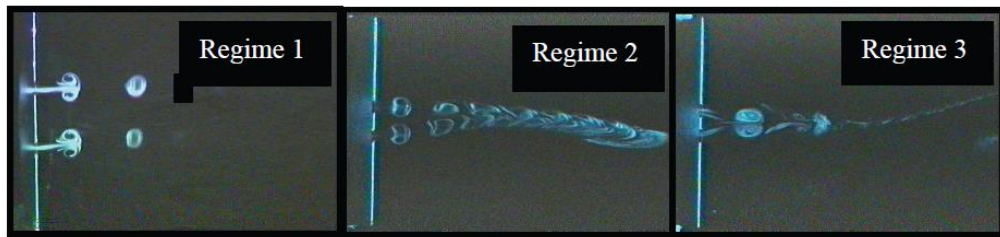
Figure 2.9: The three regimes of adjacent synthetic jet interaction as the orifice spacing varies (Watson et al, 2003a).

More recently, a comparison study between a single jet and the jet array on the jet structure under the same operating parameters has been made by Gue (2010). It has been found that the structure from the jet array travels slower due to the induced velocity produced by the adjacent rings, which to a certain degree depends on the dimensionless stroke length. It has been shown that the trajectory of vortical structures from single jet and jet array are different due to the interaction between the adjacent synthetic jets and the interaction between the jets and the boundary layer. However, apart from numerical and qualitative information, quantitative measurements are not available. This has been encouraging for the SJA array developed in the current research to examine the benefits of multiple circular orifice synthetic jets over a single one for higher circulation production. Moreover, the spacing between the orifices is also another vital parameter which needs to be considered in the design. In this regard the flow structure of synthetic jets with one, two and three orifices are examined and compared in the current study.

It has also been proven that the cavity and orifice shapes have a significant effect on the jet strength and jet velocity (Feero et al, 2015 and Milanovic et al, 2002). A largest momentum was attained by the cylindrical cavity and reduced from the conical to the contraction cavity (Feero et al, 2015). In contrast, the study by Jain et al, (2011) showed that the peak jet velocity produced from three different cavity shapes named; conical, parabola and cylindrical was almost the same. Moreover, it was found that the pitched orifice shape had a lower jet penetration length compared to the straight and tapered configurations (Milanovic et al, 2002).

An investigation was also undertaken into the effect of orifice shape utlising PIV and a range of sharp edge circular and non-circular orifices. In the near field close to the centreline it was better to select the circular nozzle because of the simple creation of the vortex rings in the circular nozzle and their significant movements downstream in comparison to other jets (Hashiehbaf et al, 2014). On the other hand, Oren et al (2009) showed that high coherent structures of the vortex ring were produced from both circular and square configurations with high spreading rate and mixing which makes it the most preferable configuration.

2.3.3. Non-dimensional Parameters

The stroke length and Reynolds number based on the blowing stroke have been suggested by Smith and Glezer (1998); Glezer and Amitay (2002) and Zhong et al (2005), with the purpose of simplifying the non-dimensional parameters that determine the properties of synthetic jet actuators in quiescent flow. Furthermore, Glezer (1988) proposed a straightforward 'slug' model for the development of a vortex ring, in which the zero-net mass flux jet stroke length was equivalent to the length of a fluid column that consisted of the fluid which is issued from the orifice during the blowing stroke:

$$L_o = U_o\,T \ldots\ldots\ldots\ldots\ldots\ldots\ldots\ldots\ldots\ldots\ldots\ldots\ldots\ldots\ldots\ldots\ldots 2.5$$

In the above equation, T and U_o respectively represent the time frame of actuator excitation and the time-averaged blowing velocity throughout the complete cycle. U_o is expressed as:

$$U_o = \frac{1}{T} \int_0^{\frac{T}{2}} \tilde{u}_o\,(t)\,dt \ldots\ldots\ldots\ldots\ldots\ldots\ldots\ldots\ldots\ldots\ldots\ldots\ldots .2.6$$

In the above equation, $\tilde{u}_o$ refers to the instant stream-wise, space-averaged velocity across a section of the orifice. The non-dimensional parameter of stroke length (L) was also submitted by Smith and Glezer (2002) in order to define the zero-net mass flux jet and enable comparisons of its characteristics with those of continuous jets. The expression of the stroke length ratio (L) is:

$$L = \frac{L_o}{D_o} \ldots\ldots\ldots\ldots\ldots\ldots\ldots\ldots\ldots . .\ldots\ldots\ldots\ldots\ldots\ldots .\ldots\ldots 2.7$$

Strouhal number (St) is the second non-dimensional parameter associated with the interval that separates sequential vortices developed regularly via an orifice. The

Strouhal number has been proven to be connected with the stroke length, representing primarily the ratio of inertial forces induced as a result of the unstable acceleration at a point and the convective acceleration caused across a particular area close to the same point. The main application of the Strouhal number is in comparison of the excitation frequency in terms of the duration needed by an element of the fluid to go through the orifice. The Strouhal number takes the following expression:

$$St = \frac{fD_o}{U_o} \dots\dots\dots\dots\dots\dots\dots\dots\dots\dots\dots\dots\dots\dots\dots\dots.2.8$$

where f, D_o and U_o are the disturbance frequency, the diameter of the orifice, and the avarage jet velocity, respectively (Wu and Breuer, 2003).

The Stokes number (S) is the third non-dimensional parameter and describes the vortex ring roll-up. Based on Equation 2.5, Tang (2006) provided the following definition of the Stokes number for a fluctuating pipe flow:

$$S = \sqrt{\frac{2\pi f D_o^2}{v}} \dots\dots\dots\dots\dots\dots\dots.\dots\dots\dots\dots\dots\dots\dots\dots\dots.2.9$$

The Reynolds number represents the fourth non-dimensional parameter and is expressed in terms of the actuator orifice (D_o) and the time-averaged blowing velocity (U_o) across the whole interval:

$$Re_{U_o} = \frac{U_o\,D_o}{v} \dots\dots\dots\dots\dots\dots\dots\dots\dots\dots\dots\dots\dots\dots\dots\dots 2.10$$

In addition to the diameter of the actuator orifice (D_o) and the time-averaged jet velocity (U_o), the Reynolds number is expressed based on a spatial dimension as well during the occurrence of the ejection stroke (Utturkar et al, 2003). Thus:

$$Re = \frac{U_o\,D_o}{v} = \frac{U_o\,L}{v} \dots\dots\dots\dots\dots\dots\dots\dots.\dots\dots.\dots\dots\dots\dots.2.11$$

This parameter indicates the level of suitability of the produced vortex strength for the detachment of the fluid from the orifice. A high Reynolds number enhances the capacity of vortex rings to deviate farther from the orifice, thus diminishing the effect of the suction phase. However, when the Reynolds number is around 50 or lower, it causes flow reversal and delays separation of the jet from the orifice edge. Consequently, despite being in opposite directions, the suction phase and the blowing phase have the same value (Wu and Breuer, 2003).

The time average velocity of synthetic jet actuator was examined at a range of Re number from 1000 to 10000 by Urgina (2007) using hot-wire anemometer technique at fixed Strouhal number (Str = 0.9). Wu and Breuer (2003) and Urgina (2007) agreed that at a low Reynolds number the suction phase of the oscillating cycle is more conspicuous, meaning that synthetic jets with higher Reynolds number are capable of operating over a more extensive range. Thus, an increase in the Reynolds number caused the average vertical velocity to increase as well, as was expected by the authors. On the other hand, the shift from reversible flow to synthetic jet is suppressed by a low Reynolds number.

Among the parameters described, the Reynolds number is one of the most important parameters, as it denotes not only the vortex ring circulation and assessment, but also the nature of the flow (i.e. laminar or turbulent). To confirm that four distinct flow patterns were observed by Cater and Soria (2002), they applied the method of dye flow visualization in a water tank and employed a circular synthetic jet with an orifice that measured 2 mm in diameter that was driven by a piston cylinder. As illustrated in **Figure 2.10**, increases in the initially low Reynolds number gave rise to four different patterns of flow. A laminar-like flow was the first pattern observed **(Figure 2.10a)**, which did not exhibit any mixture with the surrounding fluid. A separate laminar vortex ring was the second pattern (**Figure 2.10b**), which then mixed with the fluid and produced a transitional-like flow which represents the third pattern **(Figure 2.10c)**. Finally, a complete turbulent jet formed at the maximum Reynolds number and this constituted the fourth pattern (**Figure 2.10d**). This jet was very similar in form to a standard continuous turbulent jet.

The effect of varying Reynolds number between 230 - 2300 on the structure of vortex rings was also examined by Crook and Wood (2001) as shown in **Figure 2.11**. The increase in the diameter of the vortex rings was directly proportional to the rise in the Reynolds number. Furthermore, a restrictive Reynolds number was also documented, which suppressed the formation of vortex rings that were substituted with tail-like structures emerging at the rear of the vortex ring inception. Secondary vortices also appeared in the wake of the primary vortex rings at Reynolds numbers over 2300. It has been concluded that a tail or secondary vortices generated when the vortex ring is saturated of excess circulation.
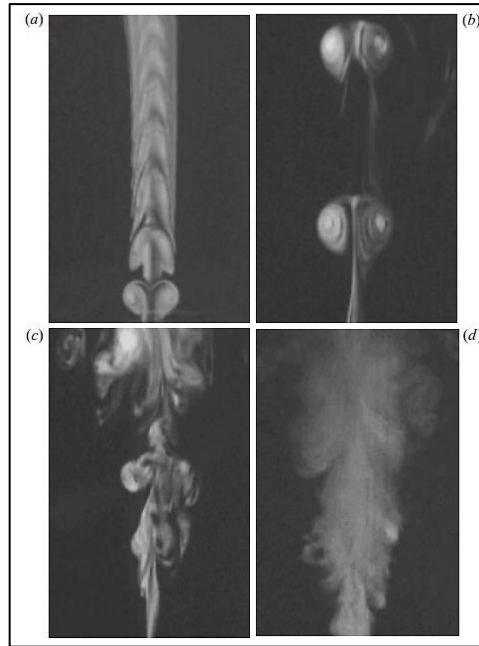
Figure 2.10: The flow patterns determined by the Reynolds number: a) laminar jet; b) laminar rings; c) transitional jet; d) turbulent jet (Cater and Soria, 2002).
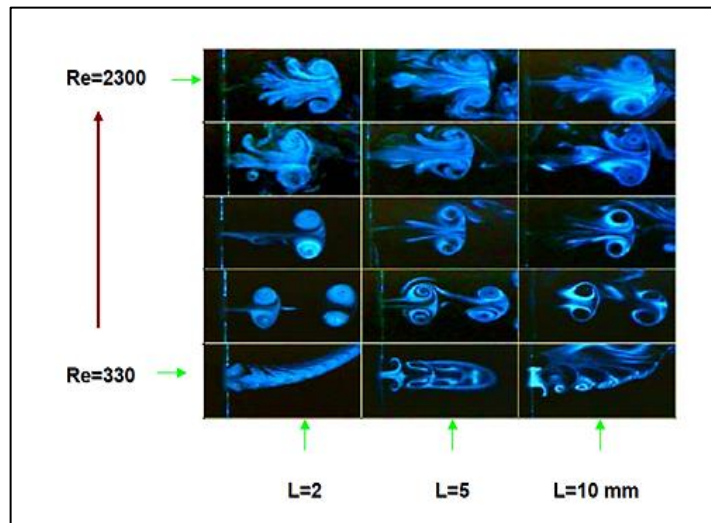
Figure 2.11: The effect of the Reynolds number and orifice length on the structure of vortex rings (Crook and Wood, 2001).

Furthermore, laminar and turbulent synthetic jets have been clearly distinguished, the former having received considerably less attention than the latter. However, different studies have relied on distinct characteristic velocity and length scale to define the Reynolds number. For example, on the basis of the stroke length, Glezer (1988) reported that the vortex ring circulation and the Reynolds number were correlated. The strength of a vortex ring can be quantified by the Reynolds number which is equivalent to the vortex circulation.

With regard to the stroke length in synthetic jets, which is equivalent to the distance between a vortex ring and the orifice exit, an insufficiently large stroke length makes the vortex ring unable to distance itself enough from the orifice before the following suction phase starts and it will become re-entrained into the orifice to the actuator cavity as a result of the suction. Hence, the vortex ring should overcome the suction velocity during the ingestion phase for a synthetic jet to develop. According to the theoretical analysis conducted by Holman et al. (2005), the formation of a vortex ring from 2D slot actuator occurs only when the stroke length is higher than 0.50, threshold which differs somewhat for various orifice structures. The PIV experiments carried out by Shuster and Smith (2007) produced identical results. However, Didden (1979) reported that the formation of vortex rings from an impulsively-started piston did not happen for stroke length values lower than 0.4. Likewise, in the case of synthetic jets, newly-formed vortices require a certain stroke length to move away from the orifice and thus determine the formation of synthetic jets.

The Reynolds number and stroke length have been clearly demonstrated to have a decisive influence on the strength and position of vortex rings. The PIV experiment findings obtained by Shuster and Smith (2007) revealed that an increase in the stroke length caused the distance between the vortex ring and the orifice to increase too (**see Figures 2.12a, b and c**). Moreover, the Reynolds number was also found to have an effect on the strength of the vortex ring, but not on its position (**see Figures 2.12d and e**). Similarly, the same two key parameters were varied in a larger range based on investigation made by Smith and Swift (2001) to analyse the trajectory of a pair of vortices. They noted that, despite the close distance between the trajectories that had been normalised by stroke length, the trajectories also exhibited discrepancies due to the effect of the extremely high Reynolds number on the transition of the vortex pair.
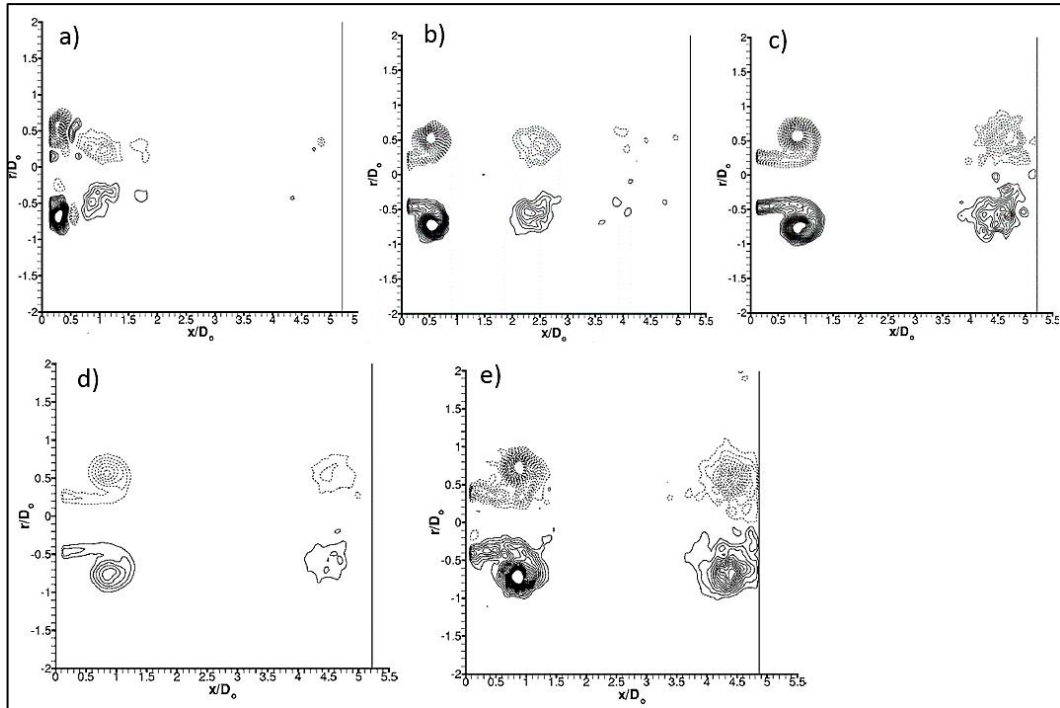
Figure 2.12: The outline of phase-averaged vorticity generated by the jet at phase angle 162°, a) L=1.0, Re_{U_o} =2500; b) L=2.0, Re_{U_o} =2500; c) L=3.0, Re_{U_o} =2500; d) Re_{U_o}=2500, L=3.0D_o; e) Re_{U_o}=10000, (Shuster and Smith, 2007).

The increase in the circulation of the vortex ring generated during the blowing stroke is directly proportional to the stroke length until the latter reaches a value of 4, after which the primary vortex circulation becomes fixed and the excess vorticity is eliminated as a secondary vortex that follows the primary vortex (**see Figure 2.13**). Gharib et al (1998) and Rosenfeld et al (1998) provided a comprehensive discussion of this phenomenon, whilst also establishing an upper threshold for laminar vortex rings. Additionally, the authors designated a non-dimensional parameter of time, referred to as the formation number, which resulted from the average discharge velocity, the discharge time, and the opposite of the orifice diameter. In keeping with flow conditions, when the value of this number became larger than the range of 3.6 - 4.5, the formed vortex rings started to exhibit a tail. It was proposed that the reason for this was the fact that the level of circulation in the ring was determined by the discharge time and velocity. The increase in the ring diameter was directly proportional to the increase in circulation up to a point when stability concerns delayed any further increase in the ring diameter. This caused the shedding of any additional circulation into the ring tail, where it could determine the formation of a secondary vortex ring.

Crook and Wood (2001) and Jabbal et al (2006) obtained the same threshold value for the beginning of the secondary vortex shedding from the primary vortex, corroborating the results of Gharib et al (1998) who demonstrated that the increase in the circulation of the vortex rings stopped when the formation number (given by the piston stroke to diameter ratio which corresponds to *L*) reached a value of 4. Likewise, the experimental work conducted by Crook and Wood (2000), Milanovic et al (2005) and Jabbal et al (2006) produced a formation number for synthetic jets too. Just as in the case of vortex rings, a limiting stroke length value of 4 was distinguished by Jabbal et al (2006) for circular synthetic jets in quiescent conditions; the vortex circulation in the primary vortex became saturated above this value, giving rise to secondary vortices. Based on the PIV method, Zhong et al (2007) investigated how the variation in the stroke length over the range of 0.81 to 4.455 affected jet formation and velocity, and found that a secondary vortex formed in the wake of the primary vortex at a stroke length of 7.1. The authors deduced that variation of the stroke length within the established range had no impact on the form of the velocity profile.
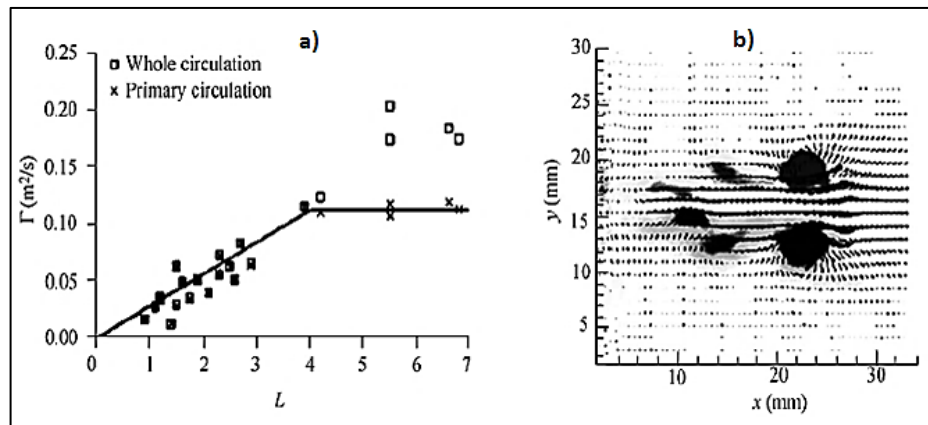
Figure 2.13: The overall circulation of: a) the primary vortex ring circulation (as function of stroke length ratio; b) PIV visualisation of the secondary vortex (Zhong et al, 2007).

On the other hand, when the stroke length was too small, the vortex ring that was formed lacked sufficient velocity to distance itself from the orifice prior to the beginning of the ingestion phase and therefore was re-absorbed (**see Figure 2.14f**) (Broučková et al, 2012). As a result, a stroke length of less than 0.5 was not conducive to the formation of vortex rings. However, when the stroke length had a large value, secondary vortices formed in the rear of the primary vortices, being the outcome of the vorticity that exceeded the capacity of the primary vortex rings, as was explained by

Zhong et al. (2007). A stroke length value of more than 4 induced the shift from a single vortex ring to secondary vortex shedding. In line with the results obtained by Gharib et al (1998) for pulsed jets.
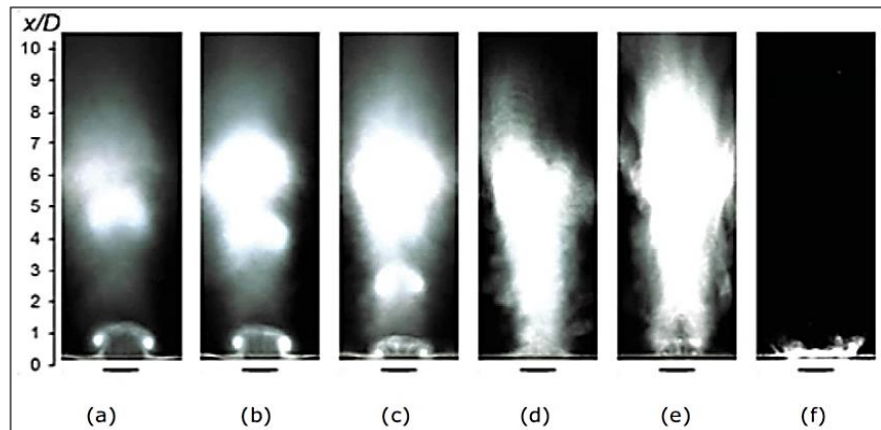
Figure 2.14: Flow visualisation of SJs at: a) L = 2.97; b) L = 2.73; c) L=1.68; d) L = 0.76; e) L = 0.55, f) L = 0.48) (Broučková et al, 2012)

Recent numerical and experimental studies done by Gue (2010) and Zhou (2010) on a series of synthetic jets with the purpose of investigating the manner in which synthetic jets acted in quiescent conditions and interacted with a boundary layer, as well as how efficient they were in controlling flow separation. Each study has been reviewed separately in the relevant sections. Regarding the research carried out on a synthetic jet in quiescent conditions, Gue (2010) conducted quantitative PIV measurements and applied smoke-wire visualization to examine the effect of the non-dimensional parameters of stroke length, Reynolds number and Stokes number on the properties of the synthetic jets and vortex roll-up. The author observed that, similarly, at a low stroke length value, the suction phase had an effect on the vortex ring, leading to the formation of an asymmetrical vortical structure. Furthermore, both the profile of the velocity exiting the orifice and vortex ring strength was found to be determined by a minimum Stokes number value of 9.4 at a stroke length of 2. Another important finding of this study was that, when the three non-dimensional parameters were identical, the synthetic jets of varying scales had the same properties. Based on these scaling parameters, it was possible to extend the results of research on macro-scale actuators to micro-scale actuators, the measurement of which poses considerable challenges. The author considers a parameter map to show the different patterns of synthetic jets with and without vortex roll-up, as illustrated in **Figure 2.15.**
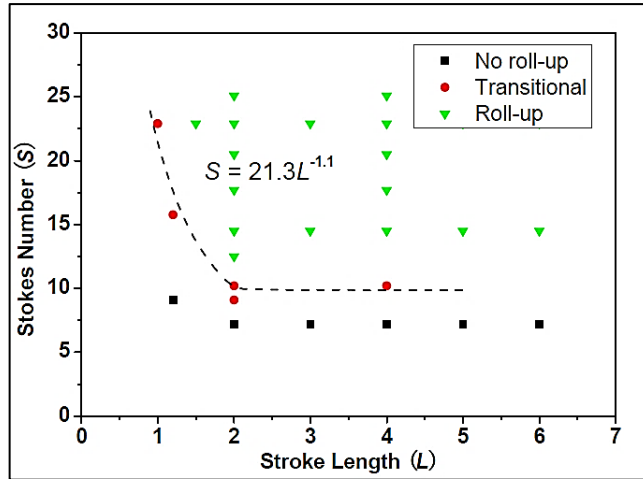
Figure 2.15: Parameter map indicating the roll-up formation patterns associated with synthetic jets (Gue, 2010).

Similar to Gue's (2010) study, Zhou (2010) found that the strength of the vortex roll-up of the synthetic jet emitted from an orifice of limited depth was dictated by the Stokes number. The results of the numerical simulations were also used to create a parameter map illustrating the three distinct synthetic jet regimes, namely, no jet and jet formation with and without vortex roll-up. This parameter map is presented in the following **Figure 2.16.**
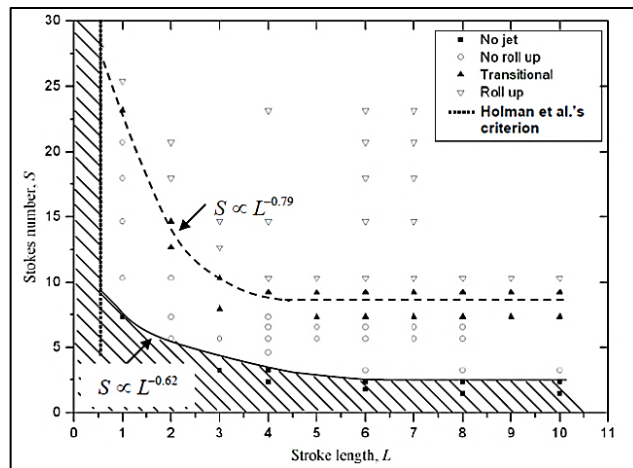
Figure 2.16: Parameter map indicating the various formation regimes of synthetic jets (Zhou, 2010).

However, there are some differences between the parameter maps produced by Zhou (2010) and Gue (2010). For instance, the Stokes number and stroke length values that Zhong (2010) found to be necessary for the formation of a substantial vortex roll-up was 8.5 and 4, respectively, whereas Gue (2010) obtained the values of 9.4 and 2.

Furthermore, when the stroke length was lower than 4, Zhou (2010) observed that the limit of the Stokes number for vortex roll-up and jet formation increased. At a high stroke length, on the other hand, synthetic jet formation could be inhibited even by an extremely low Stokes number. Two parameter maps for circular synthetic jet in quiescent conditions at low Reynolds number were also proposed by Xia and Zhong (2012) on the basis of the PIV method. Such maps could prove useful in cases where consistent vortex rings are needed, as they facilitate the selection of operational parameters for a particular applications. In contrast to Zhou (2010) and Gue (2010), Xia and Zhong (2012) did not include jet transition, but jet instability (denoting vortex structure collapse) alongside the three flow regimes of the synthetic jet, namely, no jet and jet formation with and without vortex roll-up as shown in **Figure 2.17**. Furthermore, the minimum values of the Stokes number and Reynolds number required for the formation of vortex ring roll-up were found to be 5 and 30 or 100, respectively.
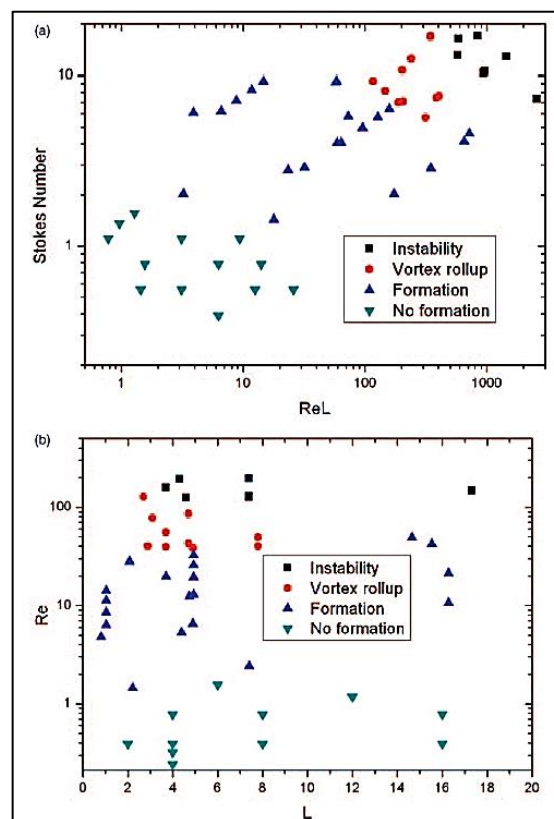
Figure 2.17: Parameter maps for flow regimes of synthetic jets; a) Reynolds number versus Stokes number; b) stroke length versus Reynolds number (Xia and Zhong, 2012).

2.4. Interaction of Synthetic Jet Actuators with a Uniform Cross-Flow

The previous section has shown the effect of non-dimensional parameters in quiescent flow, in this section, the effect of the same parameters on the synthetic jets with uniform cross-flow boundary layer is reviewed. To understand the behaviour and the interplay between synthetic jets and uniform cross-flow boundary layer, the examination of synthetic jets in a cross-flow is necessary. As it is capable of promoting flow separation control, the effect of synthetic jets on the boundary layer has been the focus of much research.

In the case of a synthetic jet actuator with fixed geometry, the freestream velocity, U_∞, and the diaphragm operating conditions need to be included in the range of variables which influence the behaviour of the synthetic jet.

The jet-to freestream velocity ratio, $Vr = U_j/U_\infty$ …..2.12

Strouhal number, $St = f\ D/\ U_\infty$ …………………………………………….2.13

Therefore, U_∞ should be taken into account alongside the main dimensionless jet parameters in quiescent conditions. Therefore, the SJA effect on uniform cross-flow boundary layer has been reviewed in the next sections.

The majority of researchers have indicated that the jet-to-freestream velocity ratio, Vr, was the most vital dimensionless parameter which affects the trajectory of the synthetic jet and vortex ring in uniform boundary layer cross-flow. This was characterised by Pratte and Baines (1967); Crook et al (2000); Mittal and Rampunggoon (2001); Gordon and Soria (2002); Schaeffler (2003); Gordon et al (2004); Milanovic et al (2005); Zhong et al (2005); Ugrina (2007); Jabbal and Zhong (2007, 2008); Ishtiaq (2012, 2013).

Pratte and Baines (1967) applied the power law relationship:

$$\frac{y}{V_r D_o} = A(\frac{x}{V_r D_o})^B \text{ … … … … … … … … … … … … … … … … … … … . … … 2.14}$$

In the above expression, Vr and D represent the velocity ratio and the orifice scale, respectively, while A and B represent the fit constants. These constants can be adjusted to determine the best fit curve in order to estimate the jet trajectories. This equation has also been employed by Gordon et al (2004) to adjust the trajectory of the

synthetic jet in cross-flow, the highest dye concentration and maximum velocity points being used to approximate the velocity ratios Vr = 4.6 and 7.0. A similarity exists between the trajectory of the synthetic jet in cross-flow and the trajectory of the continuous jet because there is a consistency between the region of constant variation and the region of the continuous jet in cross-flow. **Table 2.2** gives some examples of the jet trajectory coefficients of both synthetic jet and continuous jet in a cross-flow boundary layer.

Table 2.2: The jet trajectory coefficients for synthetic jet actuator and continuous jet in cross-flow analysis.

Literature Constants		
Pratte and Baines (1967)	continuous jet,	A = 2.05, B = 0.28
Ugrina (2007)	synthetic jet actuator, Vr = 1.5	A = -, B = -
Gordon et al (2004)	synthetic jet actuator, Vr=4.6	A = 2.08, B = 0.28
		A = 2.16, B = 0.27
Gordon et al (2004)	synthetic jet actuator, Vr = 7	A = 1.51, B = 0.37
		A = 1.74, B = 0.34
Xia and Mohseni (2010)	synthetic jet actuator, Vr = 4.5	A = -, B = -

The instant velocity of the synthetic jet during interaction with the cross-flow boundary layer was determined by Ugrina (2007) with the help of the hot-wire measurement technique. **Figure 2.18b** shows the outlines of the time-averaged velocity in the plane along the orifice centreline. In this figure, a correlation exists between the curves of the maximum velocity points and the trajectory of the vortex ring of the synthetic jet in cross-flow. Furthermore, the author proposed a simplified model that could be applied to assess the effect of jet velocity, location and jet diameter on the flow field generated by the synthetic jet actuator in cross-flow. The universal quantities along the centreline of the jet were monitored with control volume concept and integral methods.

The use of the proposed model demanded the formulation of several assumptions regarding the cross-sectional shape of the jet, the suction rate, and the surface force coefficients. **Figure 2.18b** illustrates the trajectory of the vortex ring of the synthetic jet in cross-flow which has been determined with the analysis model and which is consistent with the trajectory obtained on the basis of the experimental data derived from the hot-wire. A further indication of the acceptable predictability of the trajectory of the vortex ring of the synthetic jet in cross-flow is the fact that the trajectory was estimated using the analysis model and hot-wire measurement by Xia

and Mohseni (2010) (**Figure 2.18c**) is similar to the trajectory determined by Gordon et al (2004) using PIV measurement **(see Figure 2.18a)**.
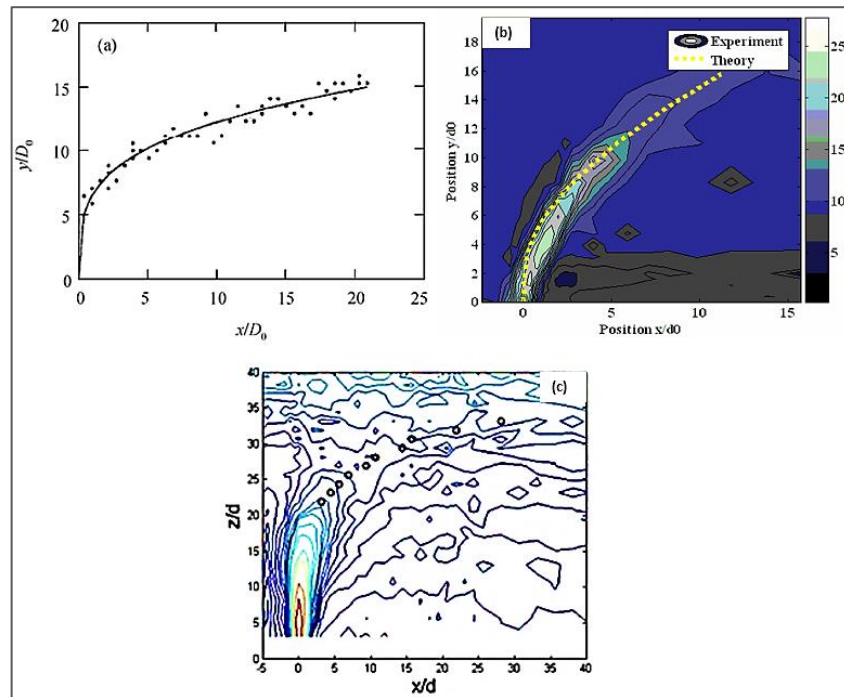
Figure 2.18: The trajectory of the synthetic jet in uniform boundary layer: a) $Vr = 4.6$, A= 2.16, B = 0.27 (Gordon et al, 2004); b) Vr =1.5, (Ugrina, 2007); c) Vr = 4.5 (Xia and Mohseni, 2010).

To determine the threshold that would facilitate the penetration of the synthetic jet actuator into the boundary layer, a range of velocity ratio cases were explored by the same author, Ugrina (2007) who observed that the occurrence of this penetration was associated with the critical velocity ratio of 1.0. When Vr was less than 1.0 and in keeping with the self-induced velocity and strength of the vortex ring, it was anticipated that the boundary layer would be obstructed by the synthetic jet actuator, resulting in the diversion of the cross-flow. On the other hand, the orifice is subjected to enough pressure by the cross-flow at low velocity ratios and no significant vertical jet momentum can be observed. It appears that the jet is rapidly diverted, the superior effect of the external cross-flow causing it to lose its structure. By contrast, the near-wall flow is only slightly disrupted by the effect of the synthetic jet actuator, which is fully embedded within the boundary layer. The flow becomes turbulent when the synthetic jet is swept along with the cross-flow, whilst at the same time the minor elevation triggered in the on-coming flow just above and some distance downstream from the orifice causes the boundary layer to be thicken slightly. The synthetic jet has

greater power to push the boundary layer from the wall as the velocity ratio rises. Therefore, given that the velocity ratio is lower than 1.0, the degree of control of the actuator can be determined based on the level of disruption of these stream-lines. The strength of the synthetic jet is greater when the velocity ratio exceeds 1.0, enabling it to change the momentum of the external flow. Moreover, there is a greater depth of penetration of the synthetic jet in the cross-flow and outside the limits of the boundary layer. The boundary layer flow seems to be completely obstructed by the vortex ring formation, resulting in a reduced momentum and partial deflection of the external streamlines, which are to some extent incorporated in the developed vortex ring. The strength of the synthetic jet, vortex rings, as well as its trajectory slope increases with a rise in the velocity ratio. What is more, the synthetic jet adopted an almost vertical position in the cross-flow at a velocity ratio of 6. Every case was associated with the development of an area of separated flow with low pressure downstream of the orifice of the jet. Thus, the effect of the actuator induced a change in the local pressure distribution on the wall.

Similarly, Mittal and Rampunggoon (2001) showed that at a velocity ratio less than one, about 0.67, the boundary layer consisting of clockwise vorticity neutralised the counter-clockwise rotating vortex. On the other hand, the clockwise vortex sucked fluid from the boundary layer and external flow and underwent a size growth during downstream convection.

A distinction may also arise from a discrepancy in incoming flow, such as the thickness of the boundary layer. However, at a very low velocity ratio of about 0.3, Mittal and Rampunggoon (2001) noted that the counter-clockwise vorticity was immediately terminated. Additionally, no penetration of the free stream part of the boundary layer by the clockwise vortices was observed, and therefore, the entrainment of high momentum external flow was not happened. Moreover at a high velocity ratio $Vr = 3.0$, penetration of the flat plate boundary layer was created by the synthetic jet and vortex pair during the blowing stroke and begins to convect downstream. Milanovic et al (2005) demonstrated that, at an established stream-wise location, the jet penetration height of a synthetic jet in cross-flow is defined exclusively by the momentum flux ratio which, in their study, corresponds to the velocity ratio Vr. As such, the synthetic jet will remain within the boundary layer for a protracted interval at low values, which enhances its potential efficiency where the overall objective is

flow control. By contrast to the accumulating knowledge regarding the flow behaviour of isolated SJAs in a cross-flow, less attention and research has been dedicated to the interplay between multiple synthetic jets.

A preliminary examination of flow interaction among two circular synthetic jets in three contexts – quiet air, laminar boundary layer, and turbulent boundary layer was conducted by Watson et al (2003). Based on flow visualisation, a reduction in orifice spacing was observed to trigger a change in the trajectory of adjoining synthetic jets, causing the jets to move towards each other. In the case of extremely small orifice spacing, there would be immediate interaction between the two adjoining synthetic jets when they emerge from the orifice, producing a single large vortex ring. In the case of fixed spacing, the decrease of yaw angle was noted to change the interaction between rings. Thus, it was proposed that the yaw angle and the orifice spacing together would increase or decrease the vorticity amount in the flow. However, delineating the fluctuation of vorticity required quantitative data. Liddle and Wood (2005) applied oil flow visualisation and stream-wise velocity contour mapping and indicated that the yaw angle could be used to control the interaction mode between two circular synthetic jets and a turbulent boundary layer.

Crook et al (2000) was observed of what probably indicated as hairpin vortical structure when the synthetic jets interacting with cross-flow boundary layer. To establish this, Zhong et al (2005) studied the interaction between circular synthetic jets and cross-flow boundary layer using dye flow visualisation at different operating conditions. When Re number and velocity ratio, *Vr* was altered, different types of vortical structures were seen with the hairpin vortices being attached to the wall (see **Figure 2.19a**). When the Re and *Vr* was increased, the circulation of the vortex ring was also increased with essential amount of tilting and stretching and hence stretching vortical structures with a weak branch were formed (see **Figure 2.19b**). This stretching feature was disappeared when Re and *Vr* increased further and only tilting is appeared which penetrate the boundary layer edge in short time (see **Figure 2.19c**). To conclude, the author suggested that the vorticity in the boundary layer was able to suppress the upstream branch of the synthetic jet vortex rings when they interact, while enhance the downstream branch to generate the hairpin vortical structures. However, when the *Vr* increased, the vortex rings become strong and travel far from the orifice to penetrate the boundary layer at a certain distance downstream and hence the effect on the near-

wall flow is found to be limited. Based on that, the author suggested that for effective flow control application with minimum power expenditure, the hairpin vortical structures could be the desirable one.
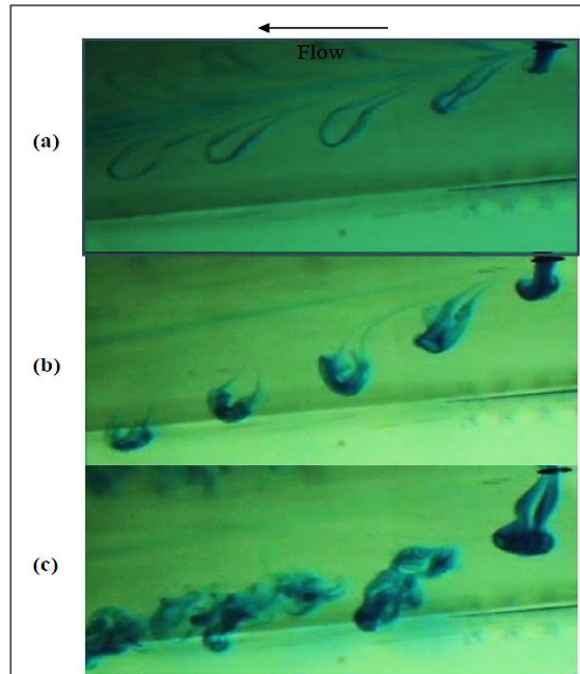
Figure 2.19: Dye visualisation of vortex structures formed by synthetic jets in a laminar boundary layer: a) hairpin vortices; b) stretched and tilted vortex rings; and c) distorted vortex rings (Zhong et al, 2005).

To make this structure more visible, dye was injected into the flow by Zhong et al (2007) in a water tunnel and thus illustrate the interaction between the vortex structure of the circular synthetic jet and the cross-flow, as indicated in **Figure 2.20**. The boundary layer vorticity weakens the strength of the upstream section of the vortex ring developed close to the actuator orifice, while the interplay between the circular synthetic jet and the cross-flow gave rise to the hairpin vortex structure. This hairpin vortex was elevated and the vortex head and actuator orifice were linked by the vortex legs. Furthermore, the hairpin vortex structure of the synthetic jet in cross-flow has been the focus of numerous numerical simulation studies: Milanovic et al (2005); Schaettler (2004) and Rumsey (2004) observed that the stimulation of the hairpin caused the injection of the high speed fluid from the outer area into the near wake area of the boundary layer, while the moderately fluids of low speed were elevated in the external flow. This process improves the boundary layer momentum, thus enabling the

flow to surmount the negative pressure gradient and delay boundary layer separation. Moreover, similar to the findings of Ugrina (2007), Milanovic et al (2005) reported that as the velocity ratio increased, the trajectory steepness of the structures during their downstream propagation. They also maintained that the distance between consecutive structures is given by the Strouhal number *St* which was defined on the basis of the freestream velocity. The graph in **Figure 2.20b** shows the velocity ratio range, the Strouhal number and the stroke length. It can be observed that the hairpin vortices are anticipated to occur in the velocity ratio range of 0.1-0.5 within the range of the Strouhal number used in the empirical work, while the stretched vortex rings are anticipated to occur in the stroke length range of 1.0-5.0.
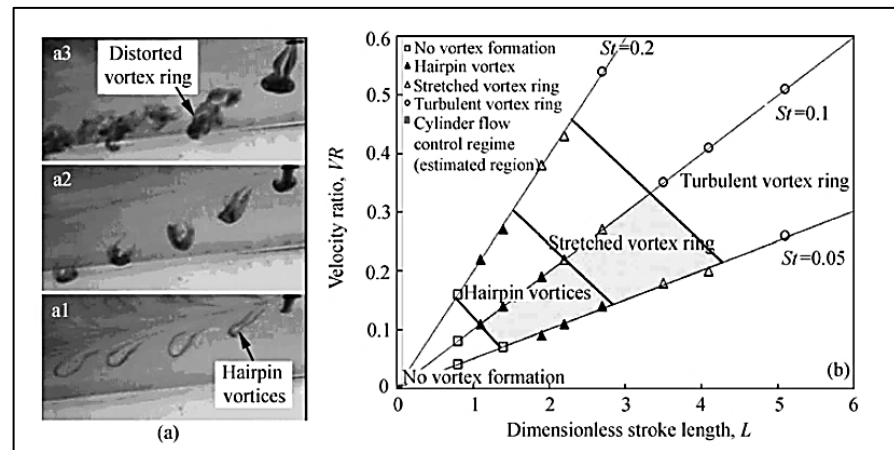
Figure 2.20: Dye-based visualisation with different parameters of the flow structures created by the synthetic jet in cross-flow; a) the three major vortex structures; b) the response of the flow structure to the velocity ratio and the stroke length ratio (Zhong et al, 2007).

Similarly, Jabbal and Zhong, (2007, 2008) showed that hairpin, stretched and tilted vortical structures are seen due to the interaction between circular synthetic jet and laminar boundary layer using PIV and liquid crystal visualisation. **Figures 2.21a to c** clearly show that as marked by the thermal footprint of what can be named as "stream-wise vortex pair" embedded in the boundary layer which is quite similar to the characteristic as both hairpin and stretched vortical structures. However, a tertiary vortex pair in the near-wall region is clearly induced by the trailing edge associated with tilted vortex ring. This tertiary vortex ring could be able to produce a common momentum towards the wall and therefore, the thermal foot print is marked by a single streak line along the centerline (**see Figure 2.21c**).

Finally, the authors introduced a parameter maps based on *Vr* vs L and Re vs *Vr* to identify the formation of the three types of vortical structures at different flow conditions as shoen in **Figures 2.21d and e.** The figure clearly show that at approximately *Vr* < 0.4, both hairpin vortices and stretched vortex rings is generated. Furthermore, for flow control application, Crook et al (2000) found that both hairpin vortices and stretched vortex rings seem potentially useful, which also suggested that the interaction of vortex rings with laminar boundary layer is somewhat same to that with turbulent boundary layer. However, Jabbal and Zhong (2010) argued that and provide different idea for flow control application and they found that compared to other types of vortical structures, stretched vortex rings produce higher impact due to wall shear stress enhancement.
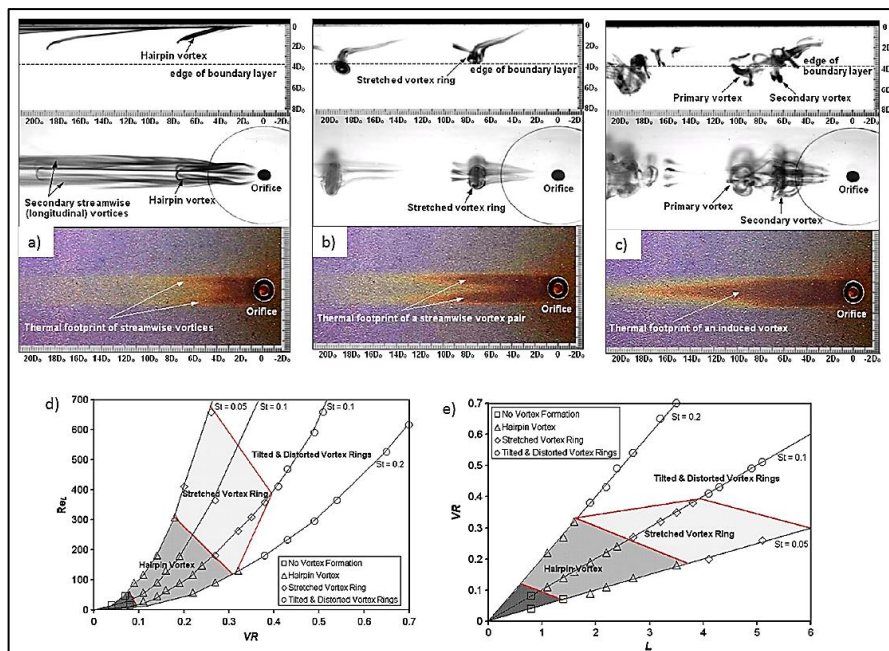
Figure 2.21: Dye and surface liquid crystal images of a synthetic jet showing; a) hairpin vortices at *Vr* = 0.14, Re_L = 46 and L = 1.4; b) stretched vortex rings, *Vr* = 0.27, Re_L = 182 and L = 2.7; and c) distorted vortex rings, *Vr* = 0.51, Re_L = 658 and L = 5.1; Parameter space of the different vortical structures; d) Re_L- *Vr* and e) *Vr* -L (Jabbal and Zhong, 2008).

More recently, the characteristics of the vortical structures generated from the interplay with a laminar boundary layer and synthetic jets were analyzed by Gue (2010) and Zhou (2010) experimentally and numerically. Gue (2010) identified the same vortical structure mentioned above, hairpin vortices, stretched vortex rings and tilted vortex rings as the three kinds of vortical structures emerging from the interplay

between a synthetic jet and a laminar boundary layer. The vorticity in the boundary layer reduces the strength of the upstream vortex branches, causing the hairpin vortices and stretched vortex rings to develop asymmetrically. On the other hand, a rise in jet strength helps the tilted and distorted vortex rings to develop symmetrically.

Likewise, Zhou (2010) found that the interplay between a single synthetic jet and a uniform cross-flow laminar boundary layer gave rise to two kinds of vortical structures – hairpin vortices and tilted vortex rings. As in previous studies, it was demonstrated that the hairpin vortices that develop at lower velocity ratio become lodged in the boundary layer for a significant period of time. Consequently, they develop asymmetrically because the effect of the resident shear in the boundary layer counteracts the upstream vortex branch. Furthermore, two stream-wise streaks of high surface shear stress are generated downstream on both sides of the orifice by the counter-rotating hairpin vortex legs and the associated induced stream-wise vortices. By contrast, following release from the orifice aperture, the tilted vortex rings created at higher velocity ratio embed the boundary layer rapidly. As such, the resident vorticity of the boundary layer has no effect on the upstream branch of the original vortex ring, which enables the vortex ring to maintain its form and develop symmetrically.

It was recognized that synthetic jet interaction with a laminar boundary layer is somewhat similar to that a turbulent boundary layer; however, further review was carried out in order to establish this. Accordingly, hot-wire and PIV measurement was applied by Garcillan et al (2006) in an effort to examine synthetic jet evolution in a turbulent boundary layer. It was found that, for low velocity ratio, the stream-wise velocity contours on the stream-wise central plane established a small distance from the vortical structures to the near-wall region; therefore, the lower boundary layer impact is seen to increase, which is advantageous in relation to flow control. Moreover, the presence of a pair of stream-wise counter - rotating vortices - notably the hairpin vortices' legs - was implied by the patterns of the span-wise flow. Such quantitative findings for the synthetic jets in the turbulent boundary layer are agreed to some extent with those documented by other scholars, who examined laminar boundary (Zhong et al, 2005; Jabbal and Zhong, (2007, 2008); Gue, 2010; Zhou, 2010).

In addition to the effect of SJA in laminar boundary layer, Ishtiaq and Zhong (2014) studied the behaviour of the synthetic jet in both laminar and turbulent boundary layers at a similar freestream and SJA operating conditions using flow visualisation and PIV techniques. It has been shown that in both types of boundary layers, the vortical structures of hairpin vortices, stretched vortex rings and tilted vortices have been reported to develop under different synthetic jet operating conditions as has been shown previously by Zhou (2010); Gue (2010). The formation of hairpin vortices occurs at minimum velocity ratio, stroke length and Reynolds number on the basis of stroke length. Among existing vortical structures, hairpin vortices are best suited for efficient separation control because they are embedded in the boundary layer for a more extensive range of stroke length values. Nevertheless, this assumption is credible, since the hairpin vortices need reduced velocity ratio and stroke length to develop and therefore they are able to manage active flow control using minimum power. When the stroke length is higher but velocity ratio remains low, the vortices experience stiff stretching because they are trapped in the boundary layer, thus giving rise to stretched vortex rings. When both the stroke length and velocity ratio are high, stretched vortex rings give way to tilted and distorted vortices. These latter structures are generally deemed inadequate for control of flow separation because they are unlikely to stay embedded in the boundary layer. In spite of this, at high Reynolds number, trailing secondary and tertiary vortices develop from the tilted vortices and are efficient in controlling flow separation due to the fact that they do stay embedded in the boundary layer. Each one of the assessed cases is classified for parameter space plotting with the purpose of producing information that is relevant with regard to the development of vortical structures under various operating conditions. However, it is vital to consider the level of power that the SJA consumes, in order to make it an acceptable option from a practical viewpoint. Efficient SJA operation is ensured by the parameter scale which affords enough relevant information about the economical operating parameters as shown in **Figure 2.22.**
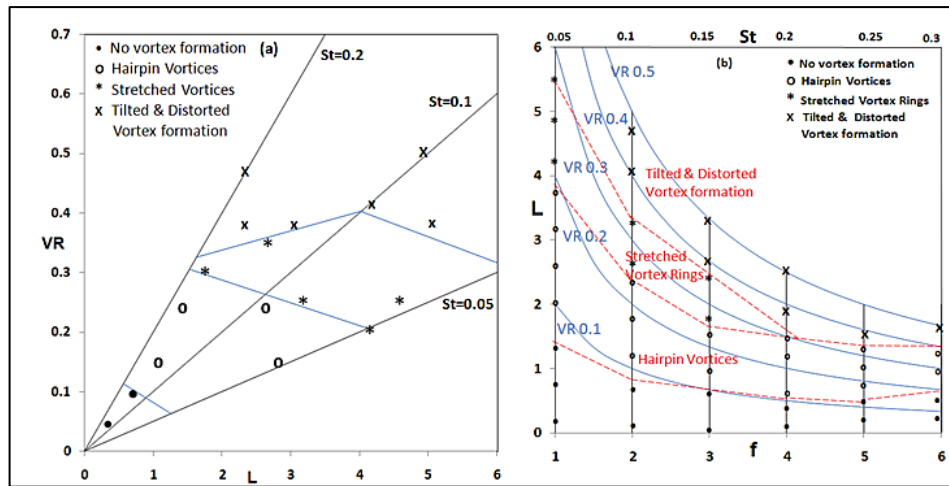
Figure 2.22: The parameter map integrates the operating frequency within the parameter space (Ishtiaq and Zhong, 2012).

Following the completion of the aforementioned study, it was found by Ishtiaq and Zhong (2014) that, in the turbulent boundary layer, the vortical structure is seen to resist turbulence to a larger degree and behave in a similar way to the laminar boundary layer counterparts, as a result of a higher velocity ratio and stroke length. Previously, it was suggested by Zhong et al (2005) that it was far more likely for hairpins to be positioned as the more preferential vortical structure necessary for effective separation control as a result of their inclination to remain within the boundary layer. In supporting this hypothesis, however, there has been a lack of quantitative data, with only the two counter- rotating hairpin legs recognized as proficient in bringing the fluid towards the wall. Moreover, as a result of lower velocity ratio values and the stroke length required for the formation, the active flow control device is operated through minimum consumption by the hairpins. Nevertheless, in more recent work, PIV results were garnered by Ishtiaq et al (2013); Ishtiaq (2013), who show that there is a greater effectiveness of flow separation delay on the surface, achieved through tilted vortices, as a result of their tendency to create trailing secondary and tertiary vortices which, in principle, remain in the boundary layer. At higher velocity ratio and stroke length, distorted and tilted vortices are created beyond stretched vortex rings, and then are believed likely to stay within the boundary layer. This means that, in flow separation control primary vortices are recognized as not being as advantageous. Nonetheless, the secondary and tertiary vortices have been recognized as efficient, hence the need for the SJA to operate at approximately $0.3 < Vr < 0.5$ in order to achieve the greatest possible degree of effectiveness.

2.5. Active Flow Separation Control Using SJA

The effectiveness of the resulting synthetic jet arises from the net injection of vorticity in the form of a train of vortex rings (Smith and Glezer, 1998; Glezer and Amitay, 2002). The ability to generate coherent vortices that can provide a favorable control effect without the need for a net mass flux makes SJAs very attractive for flow separation control on high-lift systems.

As well as the advantages of utilizing SJAs for controlling flow separation on high-lift systems, there are also some potential drawbacks. A notable one is that of debris ingestion, which can cause orifice blockage, especially during the suction stroke. This, however, may be offset by the fact that blowing constitutes half the total cyclic motion, unlike pure suction.

Amitay et al (2001) used an unconventional symmetric airfoil to show that synthetic jet actuators are able to inhibit separation. As illustrated in **Figure 2.23**, the symmetric airfoil consists of the aft section of a NACA four-digit airfoil and a leading edge section half the size of a round cylinder. The assembled airfoil is 62.2 mm thick while the combined cylinder-fairing chord is 25.4 cm, which means that t/c = 0.24. The Reynolds numbers (Re_c) range between 3.1×10^5 and 7.25×10^5 based on the chord length. A pair of rectangular SJAs, aligned along their long span-wise dimension and separated by a distance of 2.5 mm in the freestream direction, is responsible for synthesizing the control jet. The jet actuators were extended in a 140 mm over the middle of the cylinder, at an azimuthal angle γ ranging from -90 to +90 (at $\alpha = 0$) with regard to the direction of the incoming flow through rotation of the cylinder separately from the fairing. The level to which the flow becomes reattached was demonstrated to depend on control input location and jet strength. The lift was significantly enhanced and the pressure drag reduced by around 45% due to the SJA; however, when α exceeds 17.5°, the increase in lift is associated with a rise in drag.
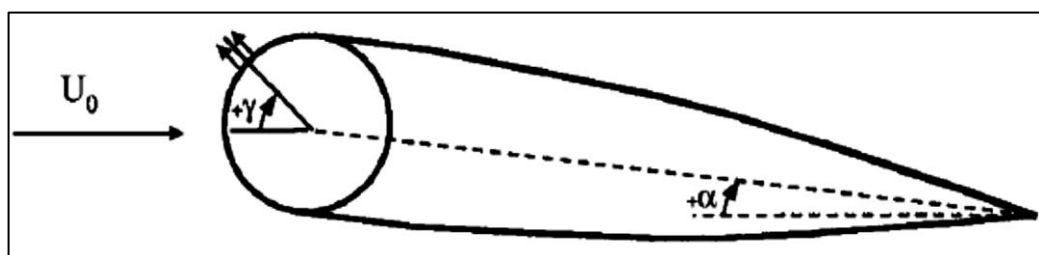
Figure 2.23: Cross sectional representation of an airfoil model created on the basis of NACA four-digit airfoil and circular cylinder (Amitay et al, 2001).

Regarding the flow reattachment across a NACA 0012 airfoil, Donovan et al (1998) employed zero mass flux blowing at $St = 1$. Using numerical simulation proved that the attached flow, as well as the restored lift, is sensitive to the excitation frequency. The simulation revealed that, at α of 22° and in the post-stall region, the lift increased by 29%. Likewise, the manipulation of a separated flow via low-level intermittent blowing/suction in the proximity of the leading edge was demonstrated by Wu et al (1998) in a series of numerical simulations. The development of vortical structures in the separated shear layer is modified by the forcing which also induces the creation of concentrated lifting vortices, the latter changing the global stalled flow through their interplay with trailing-edge vortices. The flow acquires periodicity and is associated with a substantial increase in lift within a specific range of post-stall attack angles and actuation frequencies.

Internal acoustic excitation was developed by McCormick (2000) who created directed synthetic jets and a slot in the stream-wise direction. The technique was exemplified with the use of a two-dimensional diffuser and an airfoil. The diffuser had a half angle of 13° and therefore it was at the flow separation limit. Furthermore, the power of the loudspeaker varied from 0.2 W to 20 W. By increasing the power from 1 W to 5 W, it was possible to achieve flow recovery. However, the separation on the upper surface of the diffuser wall did not permit an increase beyond 5 W. As observed by the author, the active flow control was not associated with drag and therefore its performance was greater than that of a vortex generator that was previously investigated (unpublished). Moreover, around unity was found to be the most efficient non-dimensional actuation frequency, which was accompanied by a common feature of this type of actuator – a reduction in the fluctuation magnitude of the synthetic jet caused by a rise in frequency. In the second experiment, a slot was placed at 4% of the chord of an airfoil, just before the point of separation as shown in **Figure 2.24**. The lift was increased by 25% and the stall angle of attack is shifted by 5° -6°.
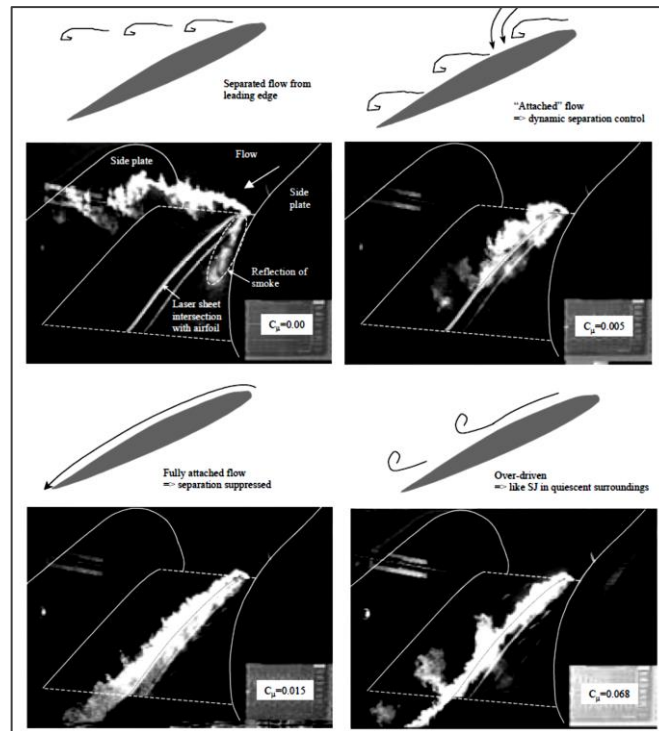
Figure 2.24: Flow visualisation of flow separation control under different conditions (McCormick, 2000).

The usefulness of a synthetic jet actuator in controlling flow separation across the NACA 0015 airfoil was investigated by You and Moin (2008) with the help of a large-eddy simulation. The airfoil was associated with angles of attack ranging from 12° to 18°, with a 375 mm long chord and slot actuation of 2 mm along the entire span length at 12% of the leading edge. On the basis of the wind tunnel freestream velocity and chord length of the airfoil, a high Reynolds number (896000) was used to conduct the simulation. The authors confirm their findings to those obtained by Gilarranz et al (2005) and they found that the delay in the onset of flow separation caused the lift to increase by around 70%. Last but not least, the authors documented the ability of the SJA to add or eliminate momentum to/or from the boundary layer as well as the ability of mixing enhancement between the internal and external sections of the boundary layer.

A micro SJA was also developed by Tuck and Soria (2008) who studied the effect that an internal micro synthetic jet actuator produced on flow separation control and lift increase over the NACA 0015 airfoil leading edge. Tests were carried out in a water tunnel 5 m in length and 500 x 500 mm in cross section at Reynolds numbers of

3.08×10^4 and 1.54×10^4 using particle image velocimetry (PIV) measurements and flow visualisation, respectively. By comparison to the case without control as shown in **Figure 2.25**, the case with control displayed a 46% increase in lift as a results of the actuation effect. Furthermore, the exciting frequency $F^+ = 1.3$ and momentum coefficient of 0.0014 were found to have the highest efficiency, delaying the stall angles by 8°, from 10° to 18°. Bunchmann *et al.* (2013) followed the same excitation parameter $F^+ = 1.3$ in conducting PIV measurements for the assessment of the impact of the SJA of the same airfoil type on the features of the flow structure at the Reynolds number 3×10^4. They reported that flow reattachment and delayed separation were achieved due to the train of vortices produced by the SJA and hence 45% increase in the lift was achieved compered to un-actuated case.
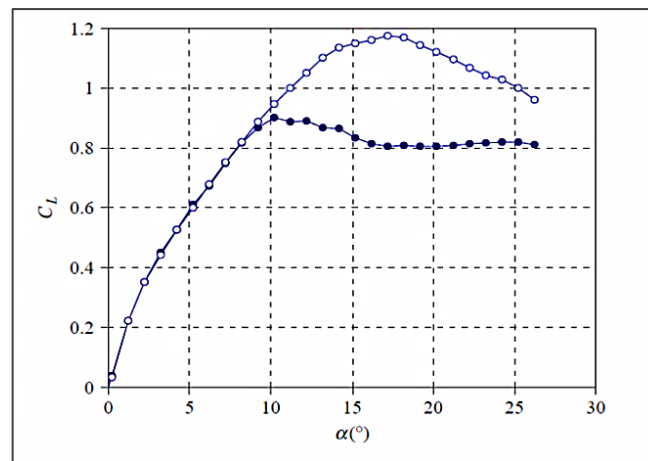
Figure 2.25: Airfoil with and without control, denoted by open and closed circles, respectively ((F$^+$ = 1.3, Cμ=0.0014) (Tuck and Soria, 2008)).

A major issue of aerodynamics is flow around a circular cylinder and backward facing step (BFS). Both have received ample attention due to their use in a multitude of engineering applications and accompanying problems, such as flow-triggered vibration, wake turbulence, acoustic noise, and drag forces on bodies. Williamson (1996), Zdravkovich (2003) and Greenblatt and Wygnanski (2000) provide detailed studies of the flow around a circular cylinder and BFS control.

From a technical viewpoint, control of vortex shedding behind a circular cylinder and BFS is a significant issue. Attempts to control the vortex shedding have been made by many researchers and have encompassed vortex shedding control and

separation control. Controlling vortex shedding is important as it leads to drag reduction, lift improvement, noise suppression, vibration reduction, and mixing.

As previously discussed, the interaction between the flow from SJAs and the separation line on a circular cylinder was investigated by Crook and Wood (2001). A similar study was conducted by Amitay et al (1997) as well, with the exception that they focused on the effect of actuation of the global aerodynamic properties of the cylinder. To this end, the authors relied on smoke visualisation of the flow around a cylinder measuring 62.2 mm in diameter, while the Reynolds number was 4000. The cylinder surface contained two SJAs had a distance between them of 2.5 mm (azimuthal separation). It was possible to adjust the azimuth location of the actuators on the cylinder in relation to the azimuth location of the flow separation line, due to the fact that the cylinder permitted rotation with regard to the freestream direction of flow. It was observed that, compared to the jet length scales, the boundary layer over length scales was almost two orders of magnitude greater as a result of the introduction of momentum in the flow. Consequently, the jets could induce considerable modifications to the recirculating area at the back of the cylinder, giving rise to closed recirculating zones aft of the separation line as well as changing the front stagnation point. **Figure 2.26** illustrates these transformations.
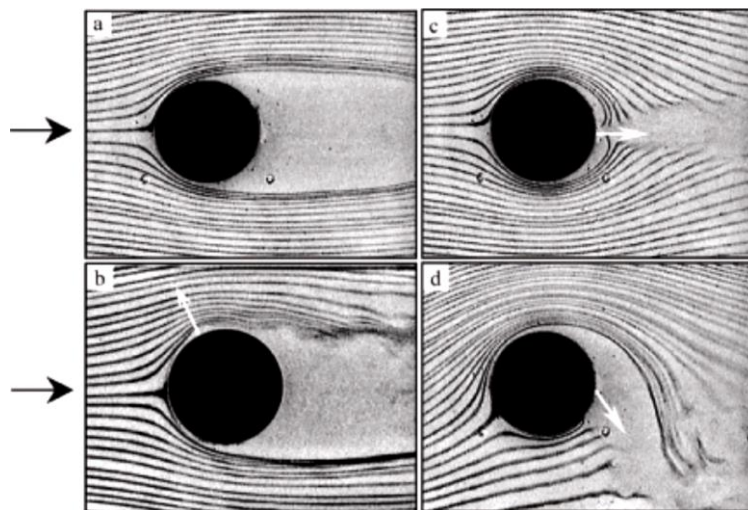
Figure 2.26: Visualisation of flow around circular cylinder with the use of two SJAs; a) no jets; b) jets positioned at azimuth 60°; c) jets positioned at 180°; d) jets positioned at 180°, out of phase by 120° (Amitay et al, 1997).

By comparison to the baseline case, considerable aerodynamic discrepancies were generated by the modifications to the flow, the cylinder lift and drag undergoing drastic changes. This study was among the first to demonstrate that SJAs are able to generate notable control moments and forces, whilst also emphasizing that the type of control depended on the location of the actuators. The same cylinder was used by Amitay et al (1998) who conducted surface pressure and hot wire measurements of the flow around the cylinder. The authors used Reynolds numbers of up to 131000. Results revealed that the system was capable of producing not only a considerable lift when the actuators were located between 0 and 120°, but also the jets were capable of minimizing the related velocity deficit and turbulent quantity level in the wake at the rear of the cylinder.

The alteration in the flow field around a circular cylinder was studied by Fujisawa and Takeda (2003) in wind tunnel investigation. The flow control was excited with acoustic excitation provided internally via a slit of 0.4 mm in width and 400 mm in length to the flow across the cylinder as shown in **Figure 2.27a**. Both PIV and pressure distributions measurements across the cylinder were conducted to permit assessment of the drag and lift force and flow field exerted on the cylinder. Results showed that a 30% decrease in drag was elicited at optimum control parameters including slit angle $\beta = 90^{\circ}$, velocity ratio $Vr = 1.5$ and forcing Strouhal number St = 2. Furthermore, particle image velocimetry was used to measure the flow field surrounding the cylinder under controlled and uncontrolled conditions as shown in **Figures 2.27b and c**. The effect of acoustic excitation caused the downstream elongation of the wake of the circular cylinder and the acceleration of the stream-wise average velocity on each side of the cylinder. Moreover, the figures clearly show how the two recirculation zones are disappeared due to the excitation compared to the un-actuated case and only small area of reverse flow is seen close to the separated shear layer behind the cylinder.
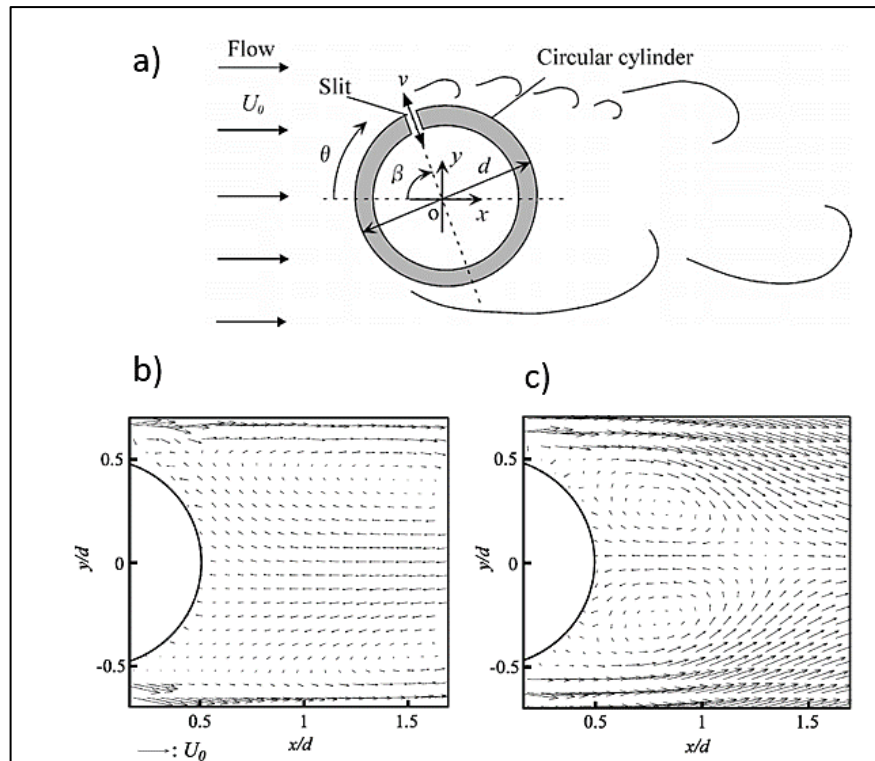
Figure 2.27: a) Diagrammatic representation of flow geometry and illustration of velocity vectors in the near-wake area: b) optimum acoustic control and c) no control (Fujisawa and Takeda, 2003).

A novel actuator signal was achieved by Feng et al (2010) who modified the ratio of suction duty cycle to blowing duty cycle in order to afford the synthetic jet better control over the flow around a circular cylinder. The determining parameters were the momentum coefficient Cμ and factor k of the suction duty cycle, which was given by the ratio of the time duration of the suction cycle and the blowing cycle. Symmetric perturbations were introduced into the flow field by locating the synthetic jet at the stagnation point at the back. Furthermore, the span-wise vorticity field was investigated with the method of proper orthogonal decomposition (POD). A pair of synthetic jet vortices of greater strength and larger scale and with a higher convection velocity was developed as a result of an increase in the factor of the suction duty cycle, which in turn increased the momentum coefficient. The outcome of the interplay between this pair and the span-wise vorticity shear layers behind each side of the cylinder was fluctuation in the wake vortex shedding modes at Reynolds number 950. More specifically, for k and Cμ values of 0.25 and 0.148, respectively, vortex synchronisation occurred at sub-harmonic excitation frequency associated with the anti-symmetric shedding mode. For a k between 0.50 and 1.00 and Cμ between 0.213 and 0.378, vortex synchronisation occurred at the excitation frequency associated with

either symmetric or anti-symmetric shedding mode. For a k between 2.00 and 4.00 and Cµ between 0.850 and 2.362, vortex synchronisation occurred at an excitation frequency in conjunction with the symmetric shedding mode. Thus, an increase in the factor of suction duty cycle, which in turn elevates the momentum coefficient, is conducive to an improvement in the ability of the synthetic jet to control the wake vortex of a circular cylinder. Due to the alternative influences of blowing and suction obtained with synthetic jets, unsteady blowing offers good efficiency in delaying flow separation and reducing drag force compared to steady blowing over the circular cylinder as indicated by Tensi et al (2002) who used a single slot on the wall model as shown in **Figure 2.28c**. The results showed that a 28% of drag reduction was achieved when the synthetic jet actuator is activated, therefore, using zero-net mass flux actuator technique is very promising technique for flow control around several bodies including cylinders with little energy expenditure.
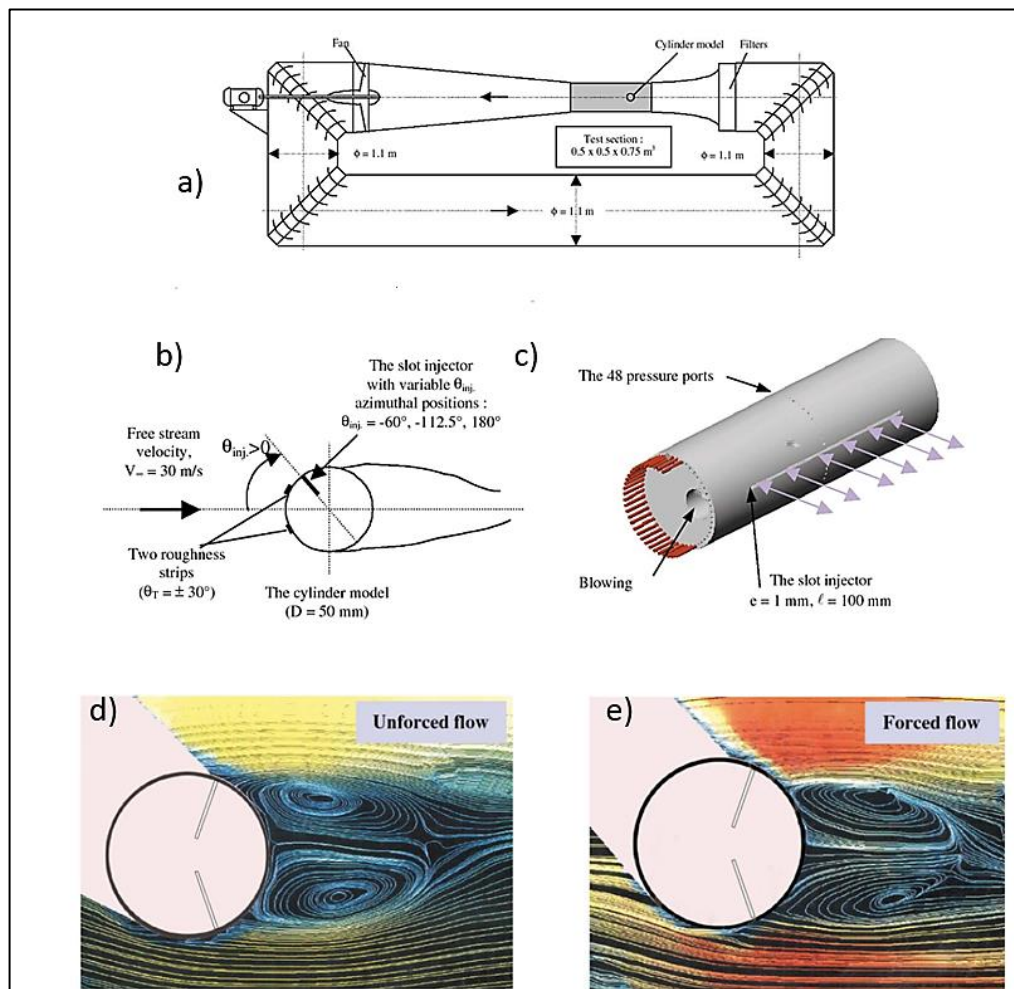
Figure 2.28: A- a) The low speed wind tunnel with a velocity of 30 m/s; b) the cylinder model dimensions; c) the elementary structure of the flow; effect of synthetic jet on the near wake d) Un-actuated case; e) Actuated case (Tensi et al, 2002).

Similarly, proper orthogonal decomposition (POD) in addition to power spectral density techniques was used by Li Qun and Li Hao (2013) to study the effect of synthetic jets on the flow around a circular cylinder in a water tunnel. The location of the synthetic jets was at the front and back stagnation points (**see Figure 2.29**). Data were processed with tools such as power spectrum analysis and proper orthogonal decomposition (POD). The main focus was on the control of the vortical structures surrounding the circular cylinder, where the excitation frequency f_e was up to three times as high as the natural frequency f_o, while the Reynolds number and excitation amplitude were constant. The synthetic jet progressively came to control the whole flow field as the increase in excitation frequency caused the expansion of the influence of the synthetic jet. The properties of natural shedding with anti-symmetric mode were manifested by the distributions of the first two POD modes, as well as by the power spectra associated with their POD coefficients in both the natural and control cases at $f_e/f_o = 1$. However, the wake vortex shedding mode underwent alterations and the dominant frequency was transformed into the excitation frequency, as denoted by the fluctuations in the third and fourth POD modes and related power spectra at $f_e/f_o = 2$ and $f_e/f_o = 3$. Furthermore, with both anti-symmetric and symmetric modes, wake vortex shedding occurred downstream, at $f_e/f_o = 2$. Finally, at $f_e/f_o = 3$, the interaction between the pair of synthetic jet vortices and the near wake layers gave rise to a symmetric wake vortex pair which progressively became anti-symmetric during downstream shedding.
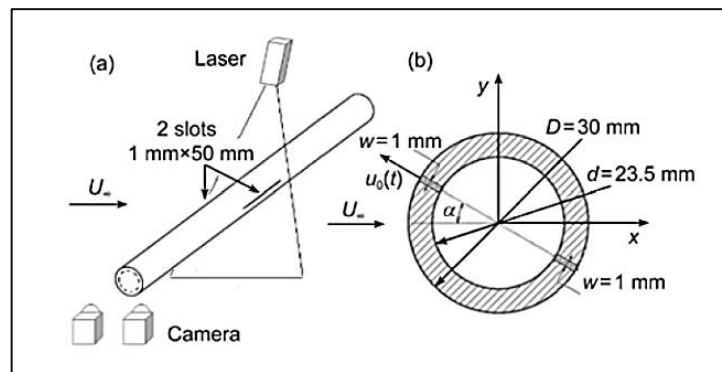
Figure 2.29: The organisation of the experiment and the model (Li Qun and Li Hao, 2013).

In different study, a non-sinusoidal waveform was employed by Feng and Wang (2012) with the purpose of controlling flow separation around a circular cylinder at a Reynolds number with a value of 950. The location of the synthetic jet was the

stagnation point at the back. The determining parameter was chosen to be the factor of the suction duty cycle which stands for the ratio of the time duration of the suction cycle to the blowing cycle. An increase in this factor determined a rise in the exit jet velocity and improved the impact of the synthetic jet, a delaying in flow separation, as well as a 29% decrease in drag. It was observed that separation can be controlled during the blowing and suction cycles with the use of distinct mechanisms. The most effective control was achieved in the blowing cycle.

Furthermore, the same authors Feng and Wang (2014) used another synthetic jet placed at the front stagnation point to alter the wake at the rear of the circular cylinder. The method of particle image velocimetry (PIV) was used to measure the flow field, while the vortex dynamics were studied with the proper orthogonal decomposition (POD) technique. The pair of synthetic jet vortices was activated at intervals in the proximity of the exit orifice and exhibited upstream movement. Due to interaction between the synthetic jet and the cross flow, an envelope upstream of the circular cylinder was produced, which served as a virtual aerodynamic form. Two different types of envelope were identified, namely, periodic-closed envelope and quasi-steady open envelope, each of which was associated with distinct modes of shedding for the wake surrounding the circular cylinder. The modes of vortex shedding under synthetic jet control were six in number: natural Karman vortex mode, bi-stable state mode I, symmetric mode, bi-stable state mode II, anti-symmetric mode accompanied by reduced length of vortex formation, and vortex triggered in the proximity of the stagnation point at the back. According to the results of the vortex dynamics analysis, regular fluctuations for all these shedding modes were displayed by the wake vortex trajectory, vortex circulation, and convection velocity at the vortex core. Moreover, unlike the natural Karman vortex sheet, the outlined shedding modes were reported to be formed through new and different processes. Additionally, a comparison was undertaken between the effects of the momentum coefficient and excitation frequency of the controlling synthetic jet, revealing that the highest importance for the vortex shedding modes was possessed by the front envelope type.

The effect of a single synthetic jet on the flow field around a finite span cylinder of low-aspect ratio (AR = 3) was investigated by DeMauro et al (2012). The jet was positioned normal to the cylinder axis, while surface-mounted pressure taps, stereoscopic particle image velocimetry (SPIV) and constant-temperature anemometry

were the tools employed in the investigation. The flow around the cylinder was disrupted by the synthetic jet which also gave rise to a span-wise modification in the surface pressure that exceeded the size of its orifice. As revealed by the SPIV measurements conducted in the near wake that a mixing enhancement was promoted by the synthetic jet between the downwash from the cylinder free-end and the wake deficit and, as a result, the wake was vectored and narrowed. Moreover, the stream-wise vorticity was penetrated by the synthetic jet and improved mixing inside the wake area and hence diminished the power related to the shedding frequency (St = 0.155), but not below the vortex dislocation of St = 0.22 due to the quasi-two-dimensional cylinder.

Wang et al (2007) have conducted experiments in a water channel to examine the effect of the synthetic jet on separation control and flow configuration in a circular cylinder. The synthetic jet was injected upstream from the cylinder front stagnation point. Despite using a different mechanism of control, this configuration of synthetic jet was demonstrated to be effective in controlling flow separation of the circular cylinder as the standard synthetic jet which is located close to the separation point or within the separation zone. The novel synthetic jet configuration caused the front stagnation point to become displaced upstream and a pair of vortices to be developed adjacent to each side of the exit orifice. During the blowing cycle, when the value of Re_U, denoted by the mean exit orifice velocity of the synthetic jet, was less than 43, a closed envelope developed, which contained the vortex rings inside. An acceptably high value of Re_U was accompanied by the formation of an open envelope upstream of the cylinder with vortex pair being still appeared. This proved that the synthetic jet was capable of enhancing flow separation in a circular cylinder, irrespective of Re_U. As regards the leeward side, there was a progressive disappearance of the flow separation zone behind the cylinder directly proportional to the increase in Re_U. Therefore, when Re_U exceeded 344, the formation of the open envelope upstream of the cylinder caused the complete attachment of the flow. Consequently, the flow over the cylinder was concentrated close to the stagnation point at the rear, where the high shear layer induced the regular development of a new vortex pair shedding.

Watson et al, (2007) presented an experimental study of SJA application to control the unsteadiness level caused by vortex breakdown over a 60° sweep angle delta wing by using an array of synthetic jet actuators along the rounded leading edge.

A steady and unsteady pressure measurement has been performed over the lifting surface of a half delta wing. They have made use of an array of synthetic jet actuators that had 1.2 mm diameter orifices, and operated at three values of frequencies 800, 1000 and 1200 Hz which were chosen from the power spectral density (PSD) in the burst flow during un-actuated experiments. This study used flow visualisation and PIV techniques to find the impact of actuation on the magnitude of unsteadiness based on the RMS of the pressure fluctuation on the delta wing surface as shown in **Figure 2.30** below. They have concluded that during the actuation, the unsteadiness has reduced significantly by up to 40% over the delta wing in the post breakdown region.
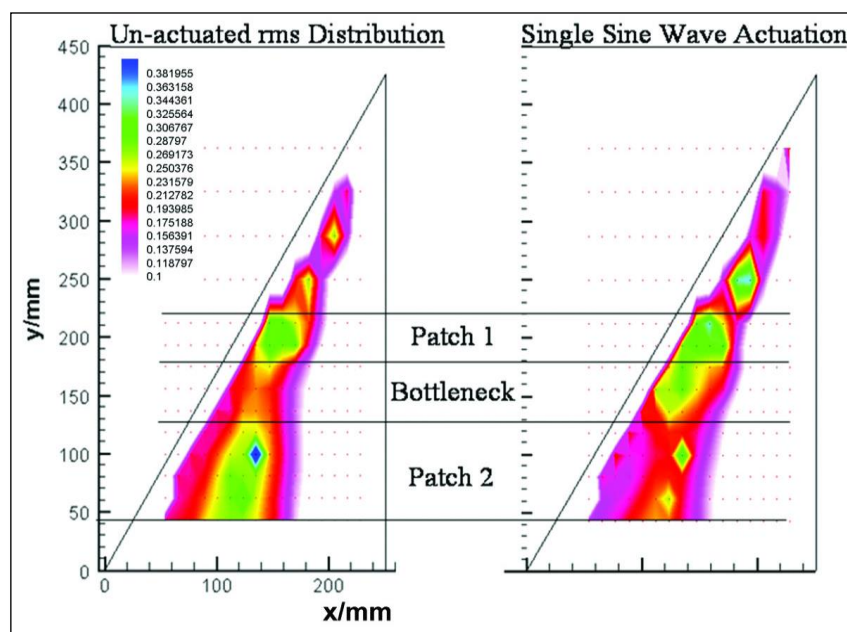
Figure 2.30: Effect of the synthetic jet actuation on the RMS value of the pressure fluctuations on the wing surface (Watson et al, 2007).

However, limited research has been carried out concerning to the flow separation control over a backward facing step. Yamada et al in 2009 used zero net mass flux at the edge of the step which create mixing and more momentum transmission in the shear layer thus affecting the separation length. They discovered that the separation distance could be lowered by 30% when the excitation frequency was double the shedding frequency in the flow. They were also able to show how control of the length of the reattachment region could be achieved using synthetic jet actuators. Similarly, the flow reattachment length is affected according to where the actuator is placed upstream from the backward facing step and this was observed by Sassoon, (2013) using time averaged particle image velocimetry measurements as shown

in **Figure 2.31**. The figure clearly shows that the placement of only one actuator upstream of the separation can change the stream-wise pressure gradient so that the length of separation is lowered. As can be seen in the figure below the reattachment length can be reduced by almost 55% using actuation of 1.07 h from the step whilst using actuation at 7.14 h from the step will still reduce the separation by 24%.
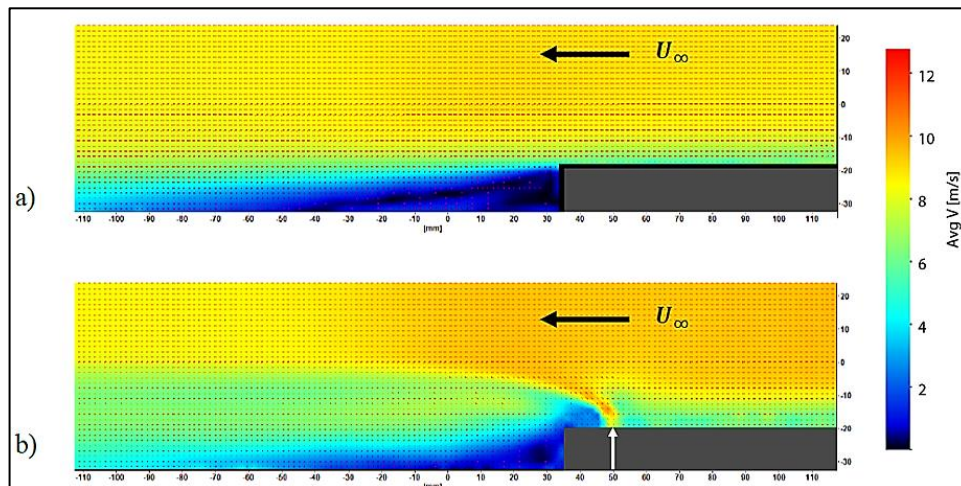
Figure 2.31: PIV velocity magnitude: a) un-actuated case; b) actuation case at distance = 1.07h (denoted by the white arrow) (Sassoon, 2013).

2.6. Conclusions

With environmental regulations now being pushed to the fore, the aircraft manufacturers tend to reduce costs and harm to the environment by using lighter and more compact flow control devices and technologies in aircraft designs. These devices would impact and reduce acoustic loads, total vehicle drag and emissions whilst at the same time improving the system transport capacities and safety. More research into innovative research topics such as the use of active flow control is essential for the sustainable future of the aviation industry even if some of it might be expensive and risky.

The preceding review of the existing literature concerning circular cylinder flow separation and synthetic jet actuators has highlighted that both of these fields have, individually, received a considerable attention. However, the amount of work involving both synthetic jet control techniques and convex hump models is very limited. The current research attempts to add to this limited body of research by implementing an array of synthetic jet actuators onto a convex hump model as the aims and objectives of the current research were explained in Chapter 1.

Chapter 3: Designing, Fabricating and Characterizing A Low Speed Open – Circuit Wind Tunnel

This chapter pertains to the development and construction of an open-circuit subsonic wind tunnel at the University of Leeds. It addresses each sequential stage of the wind tunnel design process. Primarily, the background, wind tunnel types, wind tunnel components and an overview of wind tunnel designs are presented. Then, the technical requirements of each component of the wind tunnel designed are outlined. Moreover, the pressure losses are calculated and then all the losses are added up, such that the loss of every constituent element is calculated to determine the overall pressure loss of the entire circuit, which helps to determine the power needed for the wind tunnel operation. This calculation technique is compatible with both open and closed-circuit wind tunnels, employing the standard elements combined in whichever order. Subsequently, Computational Fluid Dynamics (CFD) was used as the basis for comparison and analysis of the airflow properties through the wind tunnel test section with the help of the advanced computer software package FLUENT. The main advantage of this software is that it affords extensive mesh flexibility and facilitates flow problem resolution through unstructured meshes, which can be produced easily around complex configurations. Finally, experimental investigations were also conducted to evaluate the effectiveness of using CFD to substantiate airflow properties – these were additional tests carried out to validate the results and to verify the wind tunnel adequacy for further aerodynamic research.

The science of aerodynamics concentrates on studying the impact of airflow on solid objects. Wind tunnels designed to accommodate a variety of models are an essential part of aerodynamic research. The subjects of aerodynamic studies are effectively investigated through the use of wind tunnels, as wind tunnels are capable of simulating realistic airflow velocities, through the test section. However, despite the applicability of wind tunnels, there are constraints in terms of their cost, size and limited understanding of their design (Barlow et al, 1999).

The two major types of wind tunnel that generate airflow at specified speeds are closed-circuit and open-circuit. In the case of the latter, the test section can either be enclosed by the physical boundaries or open (so called "open-jet" wind tunnels). There are several reasons that justify the selection of the open-circuit type. First of all,

for the purposes of this research, an open-circuit wind tunnel is more cost-efficient than the closed-circuit type, providing an identical desired wind speed and flow area for aerodynamic studies. The second reason is, the ability to use this type of wind tunnel in the investigation of airflow around scaled models, for which a large test section is necessary to avoid the occurrence of blockages. This condition is fulfilled by the open-circuit wind tunnel, as it supplies more space in which the airflow can move around the model. Finally, the open-circuit wind tunnel is easier to use in a confined laboratory environment as it can be disconnected and moved around. Examples of early tunnel designs include Liverpool University's $4' \times 2'$ tunnel with an axial fan (1959) and the Clauser boundary layer tunnel (1954).

Due to the wide variety of wind tunnel designs and lack of understanding of flow through wind tunnel constituents such as the wide angle diffuser, mesh screens and the blower itself, it is difficult to formulate prescriptive rules for wind tunnel design a *priori*. The minimization of turbulence in wind tunnels has been a subject of major focus since the 1930s.

There are several components in any typical wind tunnel; the contraction, test section and diffuser are the key parts. The contraction component significantly increases airflow velocity prior to entering the test section; wind tunnels generally should have contraction ratios of 6-9 (Mehta, 1977). The test section houses the test object during the study and typically, the test object dictates the size of the test section.

As highlighted previously, the standard condition specifies that the flow of the test section should display stability, uniformity, and low turbulent intensity, which indicated the flow quality inside the wind tunnel. Efficient devices of the boundary layer controller in the settling chamber such as honeycomb and mesh screens or correct ratio of contraction are the typical factors causing the freestream velocity in the test section to be uniform with low turbulent intensity. Furthermore, significant attention needs to be taken to reduce flow separation in upstream elements like the diffuser which also makes the freestream velocity in the test section unstable with high turbulent intensity.

3.1. Overview of Wind Tunnel Designs

Fluid flow and heat transfer in configurations of great complexity can be modelled with the advanced computer software FLUENT. The main advantage of this software is that it affords extensive mesh flexibility and facilitates flow problem resolution, which can be produced easily around complex configurations. The software is compatible with a variety of mesh types, such as two-dimensional triangular and quadrilateral meshes, and three-dimensional tetrahedral, hexahedral, pyramidal, wedge, polyhedral, and hybrid meshes. Moreover, FLUENT allows the grid to be refined or broadened in accordance with flow solution.

Over the last decade, CFD modelling has seen widespread growth in aerodynamic and wind engineering research. There is a tendency for computational models to run in parallel with the experimental methodology for the validation purposes. However, the application of computational models, as CFD in respect to wind tunnels especially with open-circuit wind tunnels, is still an emerging area of interest with limited knowledge due to CFD usage concentrating on other areas of study. **Table 3.1** outlines an overview of previous studies conducted using CFD to assess an open-circuit and closed wind tunnels.

Table 3.1: Tabulated previous studies of subsonic wind tunnel facilities.

References	Location	Circuit type	Application	Test section (m2)	Speed (m/s)
FMRL Sathapornnanon et al (1999)	Bangkok, Thailand	Opened (Blower)	Fluid-dynamic research	0.6×0.18	30
Clauser (2012)	Gorgia, Atlantic	Opened (Blower)	Turbulent boundary layer studies	0.91×1.21	1.8 – 12.1
Westphal et al (1987)	Stanford, California	Opened (Blower)	Boundary-layer interaction	0.8×3	27
Schwarz and Bradshaw (1993)	Stanford, California	Opened (Blower)	Turbulent boundary layers	0.762×3.748	7
Calautit et al (2014)	University of Sheffield, UK	Closed	Fluid-dynamic research	0.5×0.5	10
Nader et al (2006)	Sao-Paulo, Brazil	Opened	Anemometer calibration	0.5×0.5	2-20
Azzawi et al (2016)	University of Leeds	Opened (Blower)	Fluid-dynamic research	0.5×0.5	3-25

3.1.1. Technical Requirements for the Wind Tunnel for the Current Study

The stages of the wind tunnel design and construction are outlined in the following sections. The initial stage is the identification of the major components, followed by the measurement and assessment of the properties of the airflow at the tunnel test section using CFD simulation. Then, fabrication and experimental tests of open-circuit tunnel components are the final stages of this chapter. In this regard, there are two major conditions that need to be taken into consideration with the initial design:

A. Freestream velocity should exhibit a variation of up to 25 m/s.
B. For a small-scale wind tunnel, the intensity of freestream turbulence should not exceed 1%.

The selection of tunnel type has been weighed carefully in keeping with considerations of functionality, time-efficiency, as well as the possibility of using the design guide from Mehta and Bradshaw, (1979) and Barlow et al, (1999). The components and dimensions of an open-circuit wind tunnel are summarized in the **Figure 3.1** sub-sections beginning with the centrifugal fan and a cross section flange outlet, followed by a wide angle diffuser, settling chamber, contraction and ends with the test section. In this regard, the design of each component is reviewed in subsections and the final fabricated design is shown in the following section.

3.1.2. The Choice of Centrifugal Fan

A centrifugal fan is capable of generating high airstream velocities, for which it has been chosen to drive the flow in the wind tunnel designed here. Compared to suction wind tunnels with an axial fan, open-circuit wind tunnels with centrifugal fan and backward-facing aerofoil type blades have been established to be better equipped to resist entry flow disruptions. Furthermore, unlike an axial fan, centrifugal fans can operate efficiently and stably under various flow conditions. Therefore, a Woodchook Ltd centrifugal fan with a single inlet and backward curved airfoil impeller was selected to derive the flow inside the wind tunnel. This fan is powered by a direct 3-phase, 1.5 HP electric motor. **Figure 3.2a** shows the load curve for the selected fan against the wind tunnel static pressure loss which clearly shows that the fan can deliver a flow rate of up to 6.25 m³/s against static pressure recovery up to 650 Pa. The fan can also be operated at several ranges of frequency using a variable frequency invertor;

from 5 Hz up to 50 Hz. **Figures 3.2b** shows the selected centrifugal fan layout and its dimensions.
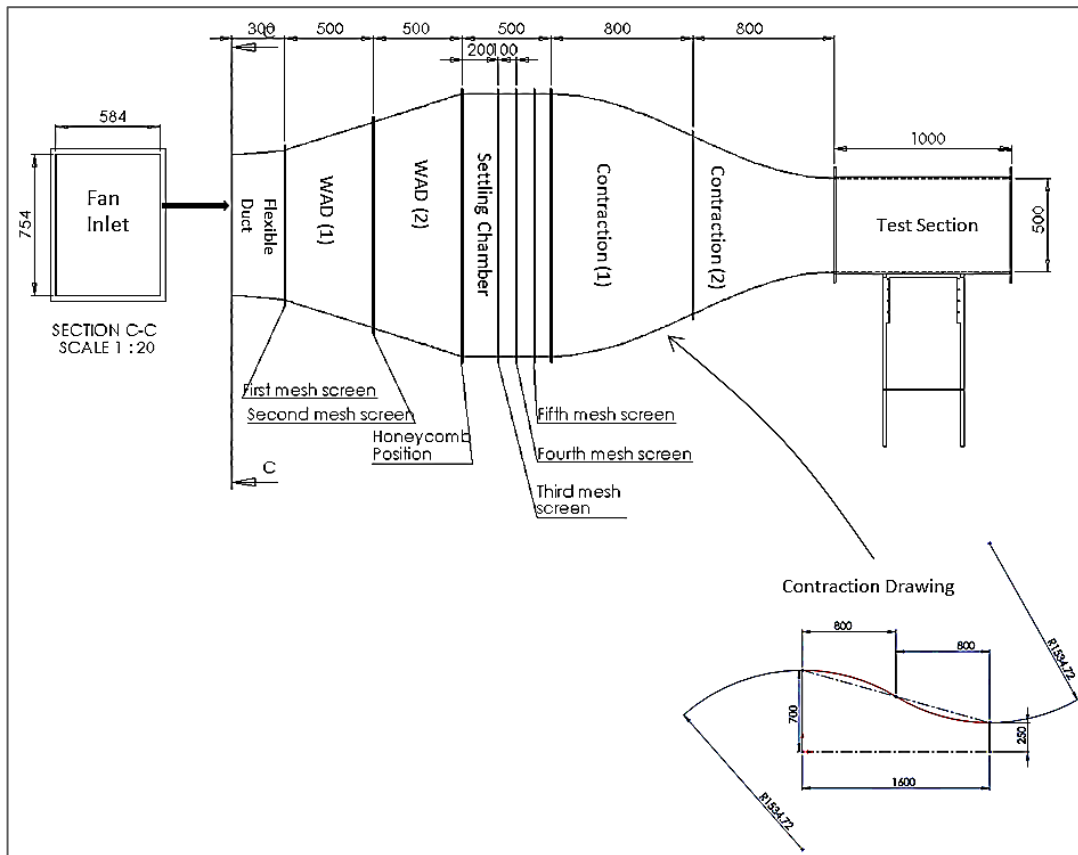
Figure 3.1: Detailed solid works model of the open-circuit wind tunnel.
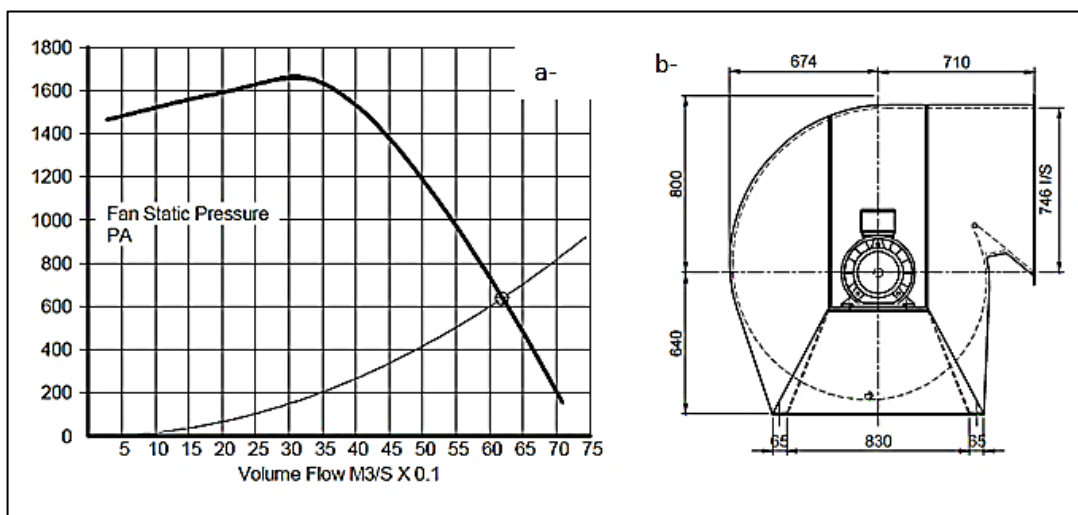
Figure 3.2: a) Fan load curve, b) The selected fan dimensions.

3.1.3. Wide Angle Diffuser

The outlet section of the fan is linked to the settling chamber by the wide angle diffuser and a flexible duct. Within this section, flow separation is reduced only when boundary layer control is conducted. To avoid flow separation or minimize the boundary layer controllers, the inlet and the outlet of the wide angle diffuser had an area ratio of 3:1 with a maximum diffuser angle of 33.4° (2θ) as shown in **Figure 3.3a**. Two mesh screens of a porosity of 67% are placed appropriately for this area ratio according to the design chart produced by Mehta et al, (1977), as shown in **Figure 3.3b**; one was fitted at the inlet point while the second screen was fitted at the middle of its length to prevent flow separation on its wall.
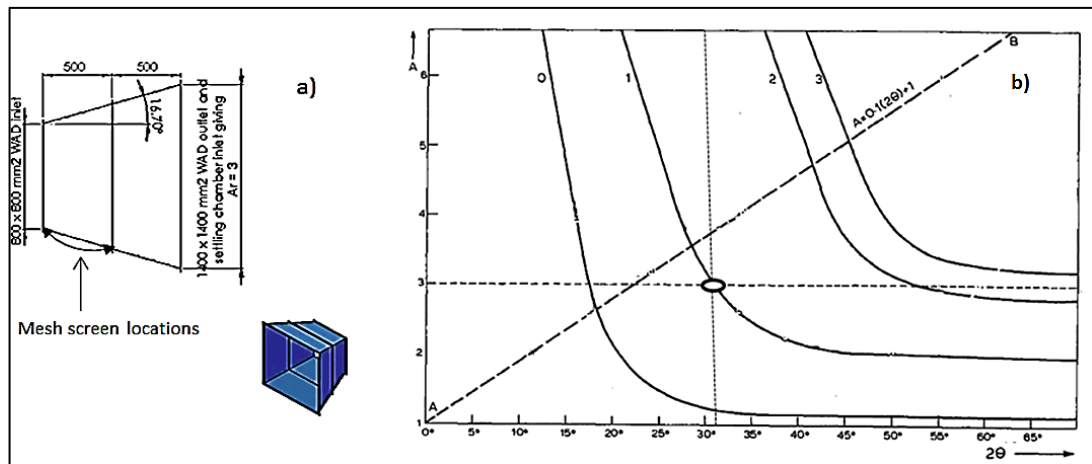
Figure 3.3: a) Wide angle diffuser b) Design boundaries for diffuser with screens.

3.1.4. Settling Chamber

The turbulence intensity and the fluctuation of the local average velocity at all points in connection with the average velocity across the entire measurement plane were the two quantities that may be negatively affected by the arrangements of the boundary layer controls inside the settling chamber. Therefore, the settling chamber was designed to maintain the steadiness, uniformity and smoothness of the flow by reducing the boundary layer growth and removing any lateral turbulence in the flow. One honeycomb and three mesh screens are the settling chamber's main constituents. The screens used here were made of stainless steel wire mesh 0.28 mm in diameter and with an opening of 1.27 mm and were introduced in positions A, B, and C as shown in **Figure 3.4a.** Sufficient space must exist between the screens to allow the flow pressure to restore itself from the perturbation caused by the movement of the

flow through one screen to the following one. Therefore, 100 mm spacing between each screen was selected and this was also the dimension of the space between the last screen and the contraction (Smith, 2003).

At first, an attempt was made to fix the mesh inside the settling chamber surfaces with the help of steel strips, but it proved challenging to keep the mesh flat and tense. Therefore, it was necessary to bolt them between flanges, which was accomplished successfully. Moreover, the honeycomb was positioned upstream of the mesh screens to reduce lateral velocity components and redirect the flow in the axis of the wind tunnel. An L/Dh honeycomb cell ratio should ideally be between 7 and 10 in order to minimize pressure drop. In consequence of this, an L/Dh ratio of 10 was selected for this tunnel design. A high quality aluminum honeycomb (ALUNID 3000-Expanded) was inserted inside the settling chamber. This honeycomb had a 9.5 mm cell size and was 1.4 m by 1.4 m with a100 mm thickness. **Figures 3.4a and 3.4b** show the locations and fixing points of the mesh screens and the honeycomb inside the settling chamber.
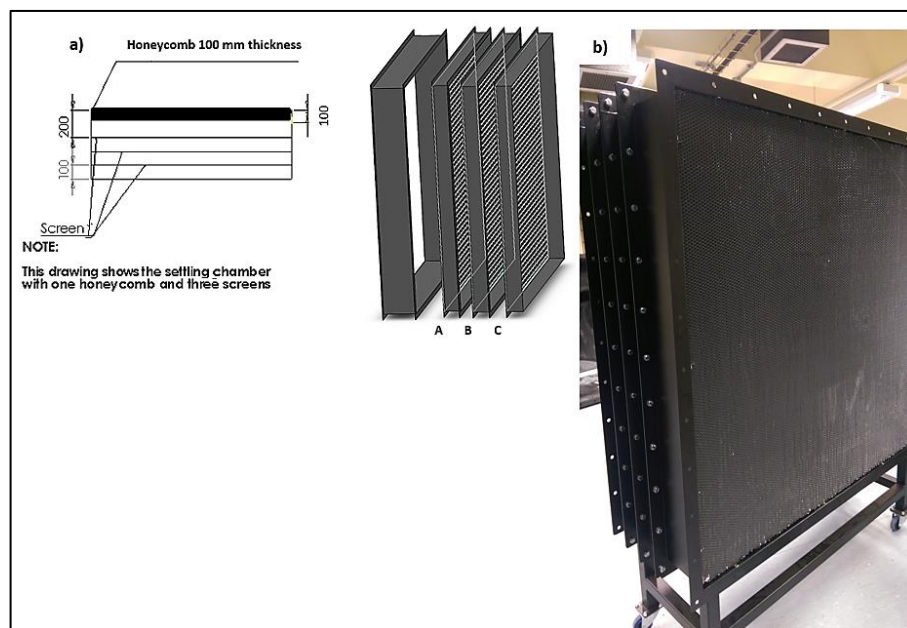
Figure 3.4: a) Settling chamber design layout showing the mesh screen locations; b) Constructed settling chamber showing the honeycomb.

3.1.5. Contraction

Contraction has a significant impact on the quality of the airflow in the test section, and therefore it is the wind tunnel constituent of the highest importance. The reduction in flow area leads to an acceleration of the flow through the contraction. Contraction

ratio (inlet area-outlet area ratio), wall shape, and contraction length are the primary factors of the contraction part which must be considered carefully. The length of the contraction used here was 1.6 m and was split into two equal parts for considerations of lab space and cost. A wall shape of an "eye design" has been used in this case (Mehta, 1977).

The proposed open-circuit wind tunnel has a contraction ratio of 7.8:1, which requires that the length (L) should be between 0.89 and 1.64 Hi, since Hi and length (L) are 1.4 m and 1.6 m, respectively as shown in **Figure 3.5a.** CNC machines produced guide beams compatible with the chosen profile that were assembled to create the contraction structure. Subsequently, the contraction length was made from two equal pieces connected to each other by bolted flanges at the match point in the middle. Considerable attention was made to fill the gap between the flanges using Soda filler which has been selected from three types of filler due to its firming and smoothing properties, as shown in **Figure 3.5b.**
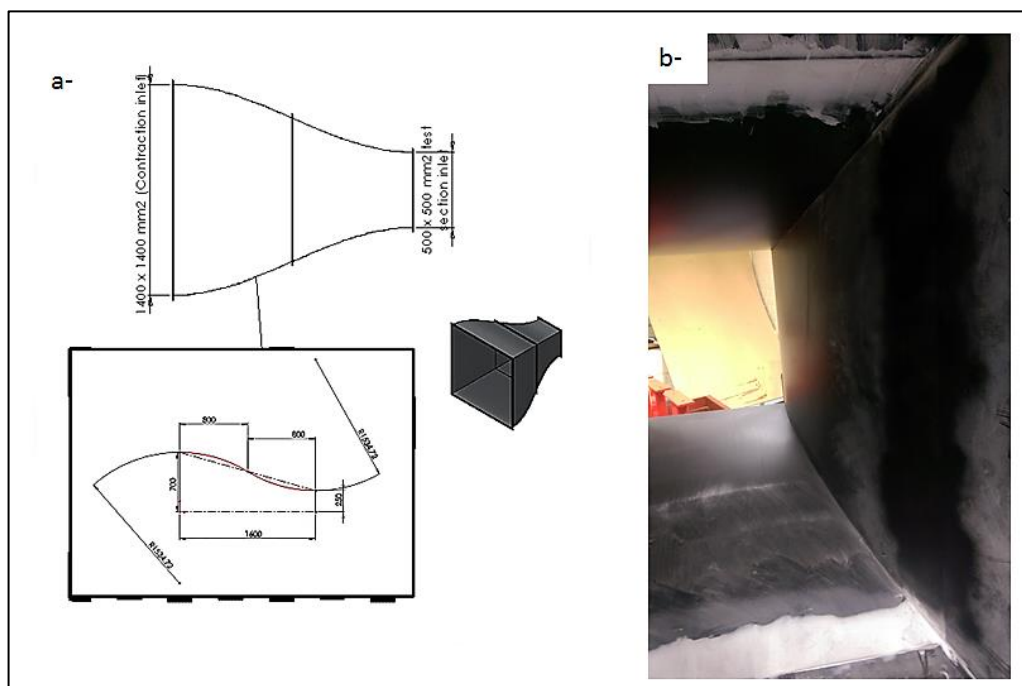
Figure 3.5: a) Contraction design layout; b) Constructed contraction set-up.

3.1.6. Test Section

The quantification of the effects of particular aspects of the wind tunnel on the quality of the flow in the test section is undertaken based on the technique proposed by Moonen et al (2006). They demonstrated that, in order to be able to effectively use

CFD to simulate wind speed and turbulence intensity in the test section, a detailed model of the whole wind tunnel has to be created. On the other hand, previous studies indicated that the fan-straightener section does not necessitate detailed modelling, it being enough to substitute with a fan boundary condition subjected to a pressure drop. The boundary layer straighter has an impact not only on the tunnel operating point, but also on the flow rate through it and the pressure losses within, and therefore has to be selected carefully. So, to maintain flow steadiness through the wind tunnel demands a power proportional to the total losses generated as the flow passes through the tunnel. Kinetic energy loss is reflected in a decrease in total pressure; this has to be compensated by using a fan to increase pressure. Wind tunnel test section design is totally dependent on the requirements of each individual experiment (Mehta, 1977). Wind tunnel test section should be neither too large to avoid the high cost of manufacturing nor too small to avoid the blockage ratio effects ($B.R = \frac{\text{maximum model cross} - \text{sectional area}}{\text{test section cross} - \text{sectional area}}$ which should be less than 10% (Choi and Kwon, 1998 and Liu, 1990). Therefore, if large aircraft models to be tested, larger size of wind tunnel test section need to be designed. For the current tunnel used here which are used for testing a hump model attached to the test section floor, the 0.5 by 0.5 m size and shape are usually dictated by the need to minimize tunnel blockage interference for a predetermined model size (B.R about 5%). Moreover, the Styrofoam models were successfully tested in a closed loop wind tunnel of the same dimension of 0.5 b 0.5 m (Calautit et al, 2014). Therefore, the current wind tunnel test section has dimensions of (L×W×H) of 1m × 0.5 m × 0.5 m respectively.

3.2. The Pressure Losses of Wind Tunnel Components

The centrifugal fan drives the wind tunnel by compensating the pressure losses that occur due to various parts of the wind tunnel. The centrifugal fan was rated by the drop of the static pressure that can overcome as well as the volume flow rate that it can provide. Consequently, this section presents approaches to the determination of the pressure loss of every wind tunnel element and discusses several fundamental concepts.

The method of dividing the wind tunnel into its constituent elements and calculating the losses of an individual element was conducted as a way of determining the total loss prior to the numerical simulation, which also helps in the choice of the

fan. The purpose of determining the pressure losses of all tunnel elements was to gain an understanding of how the circuit functioned. **Table 3.2** provides an overview of the total pressure loss coefficients with its formula provided by Barlow et al (1999) for both upstream and downstream tunnel components. It can be observed from the table that the wind tunnel had an overall total pressure loss of ~204 Pa including both honeycomb and mesh screens, and this is a useful calculation in applying the inlet boundary condition in the CFD analysis.

Table 3.2: Summary of the design description, pressure formula and loss coefficient of the wind tunnel sections.

Component	Description of the component	Pressure formula	Loss coefficient (K)	ΔP (Pa)
Wide-angle diffuser	Wide-angle diffuser area ratio of 3:1 and angle of 16.6º with L = (1 m)	$\Delta P = (K_f + K_{ex}) \times 0.5 \times \rho \times V_d^2$ $K_f = \left[1 - \dfrac{1}{Ar^2}\right]\left[\dfrac{f}{8 \times sin\theta}\right]$ $K_{ex} = K_{e(\theta)}(\dfrac{Ar - 1}{Ar})^2$	0.428	25.5
Settling chamber	Square cross sectional dimensions of 1.4 x 1.4 m2 and length of 0.5 m	$\Delta P = q \times K_{st}$, $K_{st} = \dfrac{f \times L}{2 \times (R_{st})}$	0.0214	1
Contraction	Contraction ratio of 7.84:1, 1.4 x 1.4 m2 (inlet) / 0.5 x 0.5 m2 (exit) length of 1.6 m	$\Delta P = q \times K_n$, $K_n = 0.32 \times (fav)[\dfrac{L_n}{D_{ts}}]$	0.01	~1
Test section	Square test cross section with dimensions of 0.5 x 0.5 m2 and length of 1 m.	$\Delta P = q \times K_{ts}$, $K_{ts} = \dfrac{f \times L_{ts}}{2 \times (R_{ts})}$	0.16	61.2
Screens + Honeycomb	Five screens with a porosity of 0.67 and wire diameter of 0.23 mm (dw). One honeycomb with 100 mm thickness and 9.5 mm cell size.	$\Delta P = q \times K_{screen}$, $K_{screen} = K_{screen} \times K_{Rn} \times \sigma_s$ $+ \dfrac{\sigma_s^2}{\beta_s^2}$ $K_{Rn} = [0.785\left(1 - \dfrac{R_{ew}}{354}\right) + 1.01]$	5.66	100
Flexible duct		The loss of this part is about 5-8% from the total losses (Pimpin et al, 1999)	----------	15
Total losses	Total losses include flexible duct			~204

3.3. Numerical Methodology and Governing Equations

The numerical design of the wind tunnel is based on the actual geometry of the wind tunnel. The commercially available ANSYS Fluent numerical code is used to study the numerical model corresponding to the real geometry. Therefore, good behaviour of the numerical model will agree with that of the current tunnel. The complete governing equations are available in Fluent (2006) and a brief overview of these equations is presented here. The time dependent Reynolds Averaged Navier-stokes (RANS) equation of the momentum for turbulent model is (Ilori et al, 2015):

$$\frac{\partial(\rho u_i)}{\partial t} + \frac{\partial}{\partial x_j}(\rho u_i u_j) = -\frac{\partial p}{\partial x_i} + F_i + \frac{\partial}{\partial x_j}[\tau_{uj}] + \frac{\partial}{\partial x_j}(-\rho \overline{u_i' u_j'}) + \frac{\partial}{\partial x_i}(-\rho u_i'^2) + S_m ..3.1$$

while the continuity equation can be written as follows:

$$\frac{\partial \rho}{\partial t} + \frac{\partial}{\partial x_j}(\rho u_i) = 0 \dots\dots\dots\dots\dots\dots\dots\dots\dots\dots\dots\dots\dots\dots\dots 3.2$$

The effective stress tensor and the Reynolds Stresses term used to model momentum equation for the turbulence affected flow are given by:

$$(\tau_{uj})_{eff} = \mu\left(\frac{\partial u_j}{\partial x_i} + \frac{\partial u_i}{\partial x_j}\right) - \frac{2}{3}\mu_{eff}\frac{\partial u_k}{\partial x_k}\delta_{ij} \dots\dots\dots\dots\dots\dots\dots 3.3$$

$$-\rho\overline{u_i' u_j'} = \mu_t\left(\frac{\partial u_j}{\partial x_i} + \frac{\partial u_i}{\partial x_j}\right) - \frac{2}{3}\left(\rho k + \mu_t\frac{\partial u_k}{\partial x_k}\right)\delta_{ij} \dots\dots\dots\dots\dots.3.4$$

The two equations of the turbulent flow ($k - \varepsilon$) model can be written in two separate equations, one for kinetic energy (k), and the second for the rate of dissipation:

$$\rho\left(\frac{\partial k}{\partial t} + u_j k_j\right) = \left(\frac{\mu_t}{\sigma_k}k_j\right)_j + \mu_t\emptyset - \rho\varepsilon \dots\dots\dots\dots\dots\dots\dots.3.3$$

$$\rho\left(\frac{\partial \varepsilon}{\partial t} + u_j \varepsilon_j\right) = \left(\frac{\mu_t}{\sigma_\varepsilon}\varepsilon_j\right)_j + c_1\frac{\varepsilon}{k}\mu_t\emptyset - \rho c_2\frac{\varepsilon^2}{k} \dots\dots\dots\dots\dots.3.4$$

where:

$$\emptyset = 2\varepsilon_{ij}\varepsilon_{ij} \dots\dots\dots\dots\dots\dots\dots\dots\dots\dots\dots\dots\dots\dots\dots..3.5$$

and:

$$\mu_t = c_\mu\rho\frac{k^2}{\varepsilon} \dots\dots\dots\dots\dots\dots\dots\dots\dots\dots\dots\dots\dots\dots 3.6$$

The values of the empirical constants $c_\mu, \sigma_k, \sigma_\varepsilon, c_1$ and c_2 in equations (3.3), (3.4) and (3.6) are the default values of 0.09, 1, 1.3, 1.44, and 1.92, respectively.

3.3.1. Solution Method and Boundary Conditions

Two distinct models of wind tunnel were assessed during the numerical design process. The initial model was taken as a basic configuration (Case 1) with an open test section without any artificial boundary condition. A second model (Case 2) was designed to assess the flow quality with an artificial outlet boundary condition. The second model was designed with an artificial boundary condition as an outlet pressure of $3 \times 2 \times 2$ m which represents the wind tunnel room itself. The two models are explained in **Figures 3.6 and 3.7**. A comparison was carried out between these two configurations (Case 1 and Case 2) and the experimental results. The impact that the present artificial boundary condition had on the quality of the flow in the test section was analyzed in terms of velocity profiles of the flow field and turbulence intensity.

For both numerical cases, the commercial CFD code was applied to calculate the three-dimensional Reynolds-Averaged Navier-Stokes (RANS) equations as well as the continuity equation. This code utilizes the control-volume method alongside the Semi-Implicit Method for Pressure-Linked Equations (SIMPLEC), a velocity-pressure coupling algorithm with second order up-wind discretization. Furthermore, the numerical simulation was performed mainly on the basis of the standard k-epsilon model (Gartmann et al 2011; Calautit et al 2014). **Table 3.3** provides an overview of the CFD model boundary conditions**.** Furthermore, the modelling of the walls, floor, ceiling and test section took the form of solid walls with a set roughness height and constant. The roughness height associated with the floor, side walls, ceiling, and guide vanes was established as 15×10^{-6}, while that for the test section was 15×10^{-7}. The roughness constant was the same for all surfaces − 0.5 (Moonen et al., 2006; The Engineering Toolbox, 2012). However, the flow straightener section, including, fan blades and flow straighteners is not modelled in detail. It is altered by a so called ''fan intake boundary condition''.
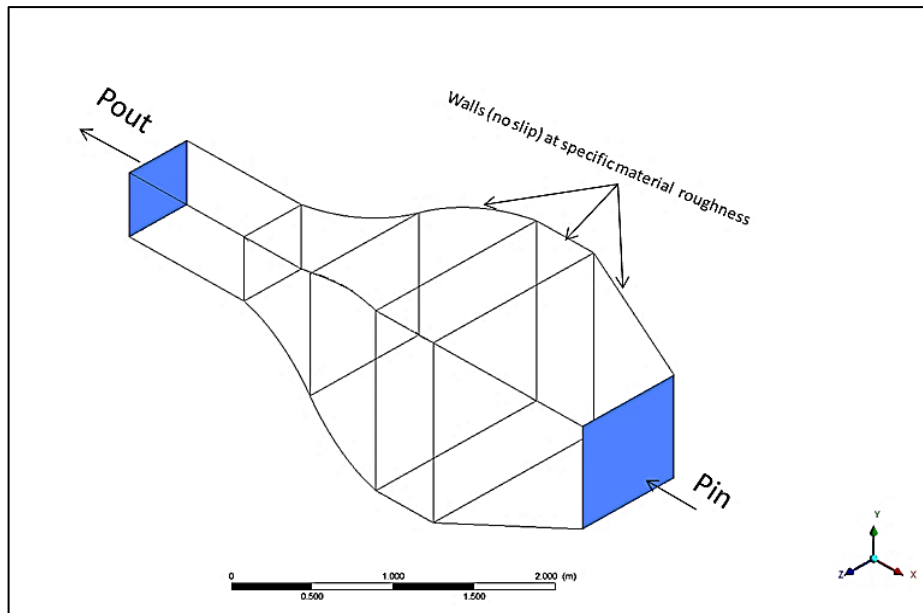
Figure 3.6: Wind tunnel geometry in CFD (Case 1)
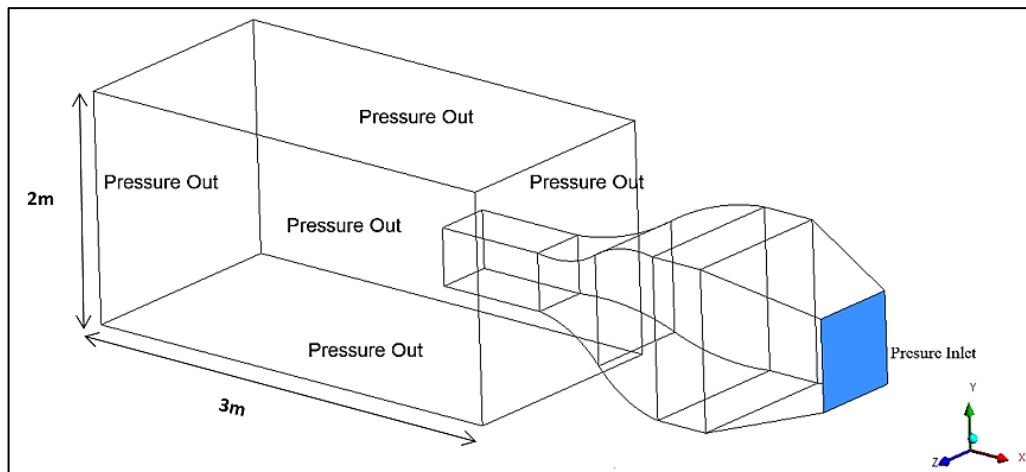
Figure 3.7: Wind tunnel model with artificial boundary condition (Case 2)

Table 3.3: Summary of the numerical simulation boundary conditions

Parameters	Set value
Discretisation scheme	Second-order upwind
Algorithm	SIMPLEC
Time	Steady state
Intake fan (pressure loss)	Wind tunnel components losses (Pa)
Pressure outlet (Case 1 + Case 2)	Atmospheric pressure (Pa)
Gravity	-9.81

3.3.2. Mesh Structures

To save computational costs, this research integrated the benefits of both structured and unstructured grids. Structured prismatic mesh was applied to the wind tunnel sections with uncomplicated structure and one-dimensional flow. On the other hand, tetrahedral/hybrid cells were employed in sections such as the diffuser, and contraction, with complex structure and three-dimensional flow as shown in **Figure 3.8**. The type of mesh that has been employed is specified in **Table 3.4**, alongside the total number of elements that the various wind tunnel sections contained.
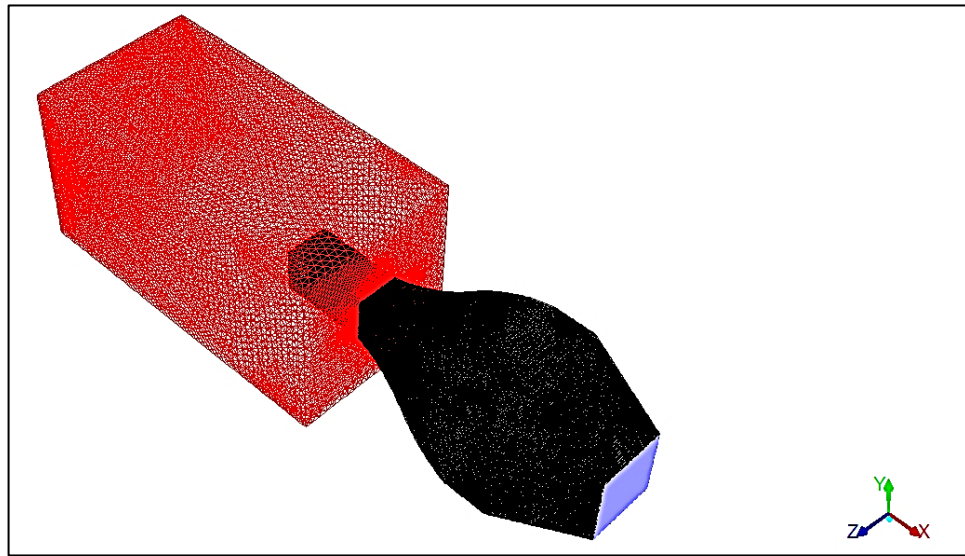
Figure 3.8: Meshing imported to fluent software.

Table 3.4: Mesh type and distribution in open-circuit wind tunnel

Wind tunnel parts	Type of mesh	Elements number
Wide angle diffuser	Tetra	421875
Settling chamber	Hexa	225000
Contraction	Tetra	450000
Test section	Hexa	421875
Total		1518750

3.3.3. Mesh convergence investigation

Despite being used in different contexts, the mesh convergence test and grid independent test have the same design. They are both geared towards the identification of the grid size which is most suitable for a specific problem simulation and allowed grid size to be increased without affecting the solution. A number of different meshes were created with the purpose of analysing mesh independence. The verification of the computational model's programming and the operation was undertaken through grid sensitivity analysis. A single solution was issued by the previously described approach results for the selected mesh. However, despite having "converged" on the basis of RMS error values, monitor points and imbalances, the solution must also be unaffected by mesh resolution, otherwise the CFD results will be incorrect. It is advised that this procedure be applied at least once for different problem types to enable the use of a similar size of mesh when a similar problem occurs. This increases the result reliability. Both mesh convergence and grid independent tests have the same meaning although some research says the grid independent test and some mesh convergence study and this is a way to find an optimum grid size for a particular simulated problem after this size the solution will not be affected irrespective of increasing grid size.

A simulation of the wind tunnel was modeled using 1518750 mesh elements for Case 1 with turbulent intensity and average velocity being recorded; values are presented in **Table 3.5**, along with the number of cells. It can be seen that the final number of mesh was 1518750 cells based on the mesh dependency study. The convergence of the two parameters with 3 - 11% imbalances was achieved in the case of 506250 cells. Moreover, a rise in the interest value resulted from the increase in the number of cells to 759375 cells. When the mesh size was increased even more, the simulation of the 1518750 cells produced a value situated in a satisfactory range, of 0.1 - 0.3%. What this implied was that the mesh resolution had no impact on the value of interest. Therefore, to obtain results within the user-defined range, 1518750 cells were employed in additional analysis. Additionally, the same process has been carried out for Case 2 and it was found that increasing the number of mesh had no large effect on the monitored values.

Table 3.5: Average velocity and turbulent intensity as a function of the number of cells

Number of elements	Turbulent intensity (%)	Average velocity
506250	1.8	18.94
759375	1.76	19.16
1518750	1.60	19.51
2025000	1.61	19.42

3.4. Overall Layout of the Built Wind Tunnel

A Woodchook Ltd. centrifugal fan (with backward-facing aerofoil-type blades) with a 5.5 kW and 1.5 hp electric motor was used to drive the open-circuit wind tunnel. This fan can deliver a flow rate of 6.25 m^3/s against a static pressure of 650 Pa. The fan can be operated at several ranges of frequencies using a variable frequency invertor, from 5 Hz up to 50 Hz. This blower supplies air into a wide angle diffuser through a rectangular to a square transition duct. The diffuser is simply designed of two parts connected in the middle through a bolted flange. The first diffuser part expands from 80×80 cm^2 to 110×110 cm^2 across 50 cm length, resulting in maximum area ratio of 1.89. The second diffuser expands from 110×110 cm^2 to 140×140 cm^2 over a length of 50 cm, giving a maximum angle of 33.4^o and an area ratio of 1.61. Two screens with a porosity of 0.67 are placed in the middle between the two diffusers. A settling chamber is used to merge the airflow of two branches before it passes through the contraction segment of the wind tunnel.

The honeycomb and screens are its two main constituents. The honeycomb with a thickness of 100 mm is placed at the inlet of the settling chamber, while three mesh screens with a sufficient space of 100 mm are placed in the settling chamber. This should also be the dimension of the space between the last screen and the contraction. The merged flow passes through the contraction section. The contraction has a square cross section of 140×140 cm^2 at the inlet, 50×50 cm^2 at the exit, and a contraction ratio (CR) of 7.8:1 that is agreed to the recommended contraction ratio (6:9); over a length (L) of 160 cm. The final-constructed wind tunnel is shown in **Figure 3.9**.

Figure 3.9: The final constructed layout of the built open-circuit wind tunnel.

3.5. Wind Tunnel Calibration and Assessments

3.5.1. Wind Tunnel Calibration

The purpose of the initial set of experiments conducted with an empty test section was to measure the velocity inside the test section using a pitot static tube and calibrate the open-circuit wind tunnel test section velocity against motor frequency. The test section velocity is controlled by varying the fan rotation frequency (rpm). The wind tunnel is designed to operate in an adjustable speed range from 3 m/s to greater than 20 m/s with a motor frequency range from 5 Hz up to 50 Hz. The variable frequency driver (VFD) responds to control signals from the remote keypad. The velocity control results measurements were determined using a Pitot static tube, U-tube manometer and hot-wire anemometer. The experimental set-up and the measurement techniques were described in the relevant chapter. The velocity has a linear fitted line against frequency as shown in **Figure 3.10,** which clearly showed that the motor frequency increased linearly with the velocity of the wind tunnel. This test will help in any aerodynamic test in future such that any velocity can be selected with the corresponding motor frequency.
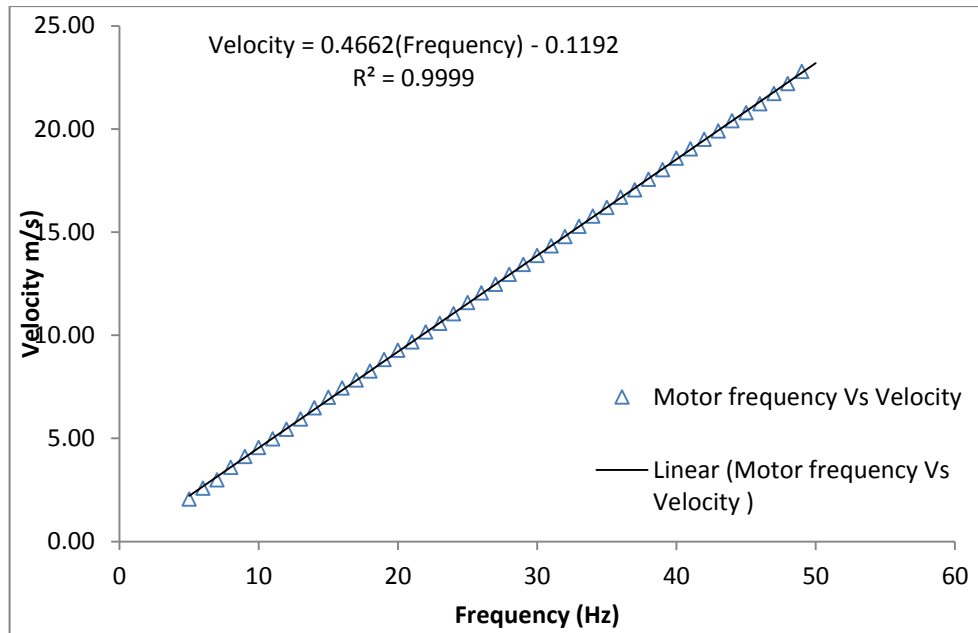
Figure 3.10: Wind tunnel velocity calibration line.

3.5.2. Validation of Sampling Parameters Using the Circular Cylinder Model

Prior to the wind tunnel performance measurements, a study to determine the acceptable sampling parameters such as sampling frequencies, sampling periods and software check for data acquisition was conducted using the circular cylinder model. The set-up and measurement techniques are also described in the relevant chapter and not repeated here.

The hot-wire probe was mounted behind the circular cylinder in the wake flow at a distance of one-cylinder diameter. It was traversed in the x, y direction to measure the velocity fluctuation signal level (RMS) at different sampling frequencies and sampling period. The wind tunnel speed was set to 12 m/s, which gave a Reynolds number of $Re = \frac{U_\infty \times D}{v} = 1.6$ x 10^4 (~ critical flow). The results clearly showed that the cylinder was shedding vortices with a 'right' dominated frequency compared to the empty test section. The comparison of power spectral density (PSD) with and without the wake flow behind the cylinder is summarized in **Figure 3.11**. The frequency spike on the power spectrum plot indicates the existence of the vortex shedding in the wake flow due to the flow separation as shown in **Figure 3.11**. The non-dimensional Strouhal number (St = $\frac{f \times D}{U_\infty}$) estimated from the figure was 0.185 ($f \approx 89$ Hz) for the

range of sampling frequency which varied from 1000 to 10000 Hz. Therefore; it can be concluded that the wind tunnel performance can be tested at sampling frequencies from 1000 up to 10000 Hz with an optimal processing resolution at 8192 points to determine the frequency spike, with the help of the Fast Fourier Transform (FFT).
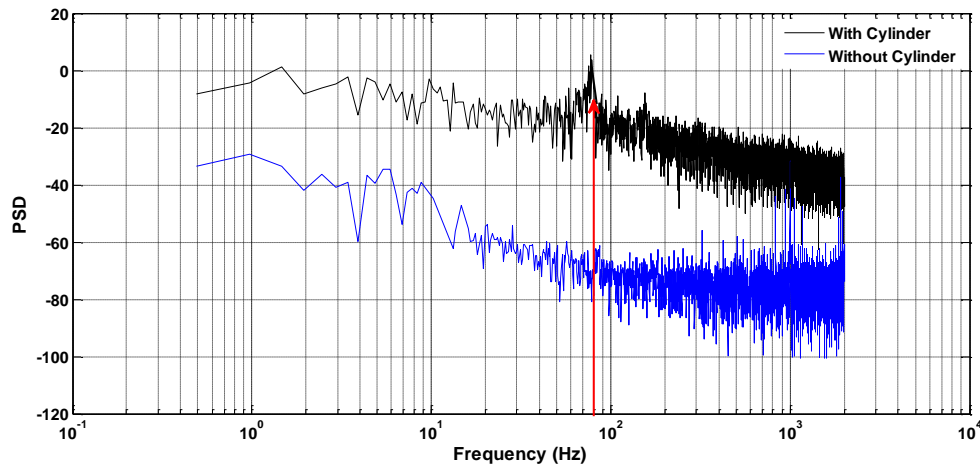
Figure 3.11: Power spectral density with and without circular cylinder at sampling frequency = 4000 Hz.

3.5.3. Wind Tunnel Assessment Results and Discussion

In order to examine if the velocity distribution at the contraction exit and test section was homogeneous and had the desired turbulence intensity, the wind tunnel performance was tested using a single hot-wire anemometer. The experimental set-up is explained in Chapter 4 in more detail and will not be repeated here. Since the experimental results can be negatively affected by wind tunnel flow quality, accurate and steady flow quality measurements are vital, alongside the understanding of the reasons and characteristic of flow turbulence in the wind tunnel. **Table 3.6** summarizes the instruments used in the measurements of wind tunnel flow quality, together with the relevant mathematical expression. The parameters measured included detailed pressure, velocity and turbulence values that are essential in the assessment of test section flow quality. Turbulence intensity was measured using a constant temperature anemometer positioned at different locations inside the test section. The velocity signal and turbulence intensities are illustrated in **Figure 3.12**, which shows a typical signal sample acquired by the hot-wire with the help of the FFT, such that turbulence intensity is equivalent to the ratio of the standard deviation of mean velocity to the mean velocity (in percentage).
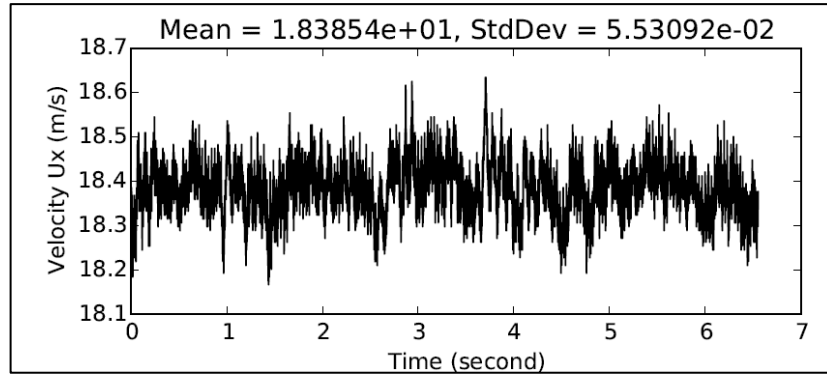
Figure 3.12: Typical signal sample acquired at 18 m/s mean velocity using a hot-wire anemometer.

Table 3.6: Airflow quality examined and measurement devices.

Measurement Relation	Method	Tools	Relevant
Velocity (m/s)	Empty test section at ten points	Pitot static tube and hot-wire anemometer, (IFA-300), Calautit et al (2014)	$U_\infty = \sqrt{\dfrac{2 \times \Delta P}{\rho}}$
Turbulent Intensity (%)	Empty test section	Hot-wire anemometer, (IF-300), Chong et al (2008)	$T.I = \dfrac{\sigma_v}{\overline{u}}$
Flow Symmetry	The velocity profile was measured with tunnel heights	Hot-wire anemometer, (IFA-300), Moonen et al (2006)	$Symmetry = \dfrac{U_i}{u_{max}}$

Figure 3.13 shows the experimental and comparison of both CFD case results of the centerline turbulence intensity with stream-wise distance in the wind tunnel at a maximum velocity of 19 m/s. The figure illustrates the positive effect that the conditioning devices had on flow turbulent intensity levels and uniformity. The figure clearly shows that the maximum velocity change recorded between the beginning and the end of the test section was 5.3% for Case 2 followed by 4.2% for Case 1 as compared to the experimental tests of 1.7%. Moreover, the maximum reduction in the turbulent intensity was seen in the experimental test results followed by Case 1 and Case 2 respectively. The most likely reason for this is due to the conditioning devices (honeycomb, mesh screen and settling chamber) that were carefully designed and inserted inside the constructed wind tunnel, which have not been considered in CFD models such that the flow separation on the wind tunnel corners have a great impact on the flow quality inside the test section. The mesh screens were placed at five different points which break up large turbulent eddies into small-scale, hence reducing

the turbulent intensity levels of the incoming flow. These series of screens help in reducing non-uniformity and turbulence by removing nearly all of the longitudinal mean velocity fluctuations.

Moreover, the honeycomb is able to remove the swirl and minimize the lateral turbulence in the flow by forcing small sections of the flow to straighten through small hex-tube cells hence increasing the flow uniformity inside the test section. The honeycomb used here had a significant impact on the flow due to its length of 6 - 8 times the size of the cell and positioning at 100 mm upstream of the next three screens which had been strongly recommended by Mehta and Bradshaw (1979).
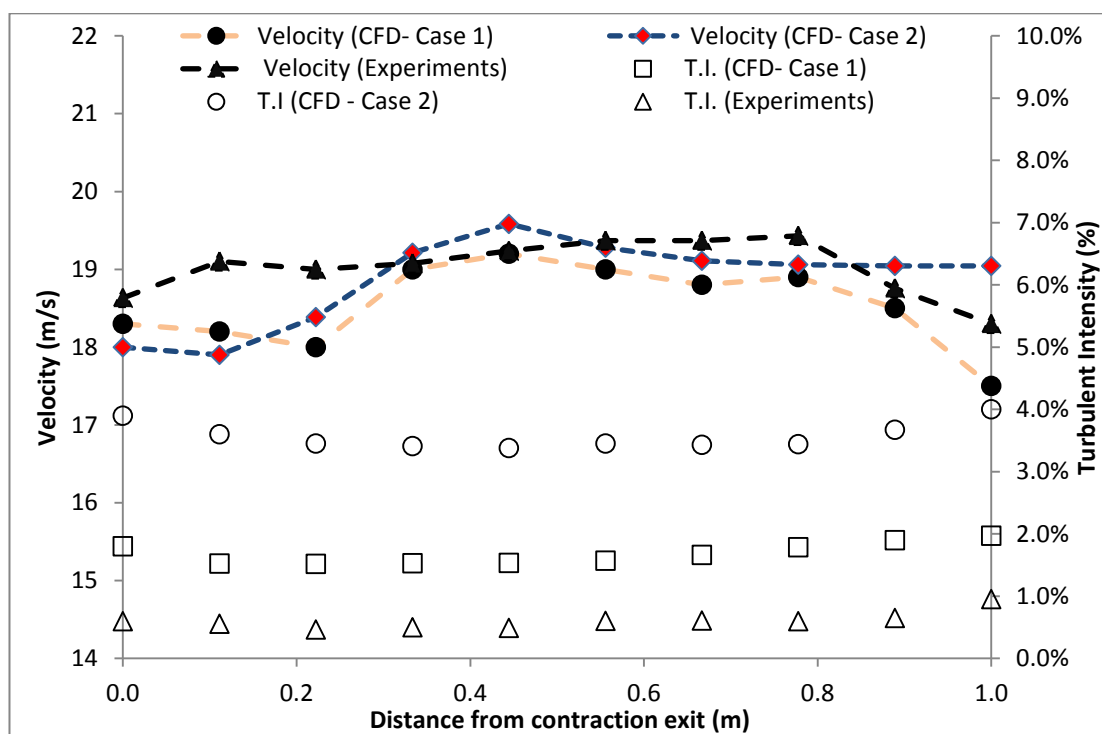
Figure 3.13: Comparison of centreline velocity and turbulence intensity of CFD cases (Case 1 and 2) and experimental results.

Figures 3.14 and 3.15 show the characteristic of the air velocity contour over the whole wind tunnel for both Case 1 and Case 2 of CFD models with an inlet pressure loss calculated previously. The combined boundary layer controllers (mesh screens and honeycomb) inside the constructed wind tunnel significantly decreased the flow separation on the corners and enhanced the flow quality inside the test section with an improvement on the flow quality of ~ 40% and 32% compared to Case 1 and Case 2 respectively of CFD results. However, the test section velocity was not as homogenous

as expected in the CFD, the top and bottom area of the tunnel diffuser revealing a higher fluctuating velocity as shown in the figures below. Despite these limitations, the tunnel was not modified further in CFD, as ample efforts and time had already been dedicated in reaching this stage. As expected with the constructed wind tunnel, more uniform and symmetric flow was seen throughout the whole test section length and good general airflow distribution in the wind tunnel circuit.
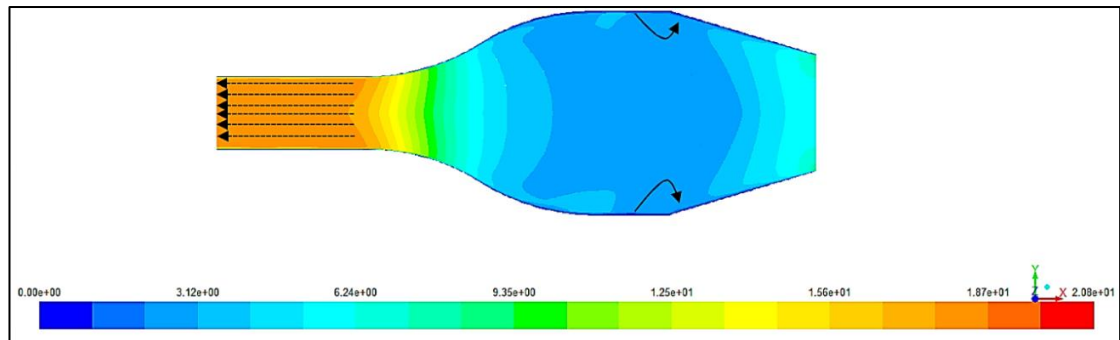
Figure 3.14: Contours of velocity magnitude for basic configuration (Case 1).
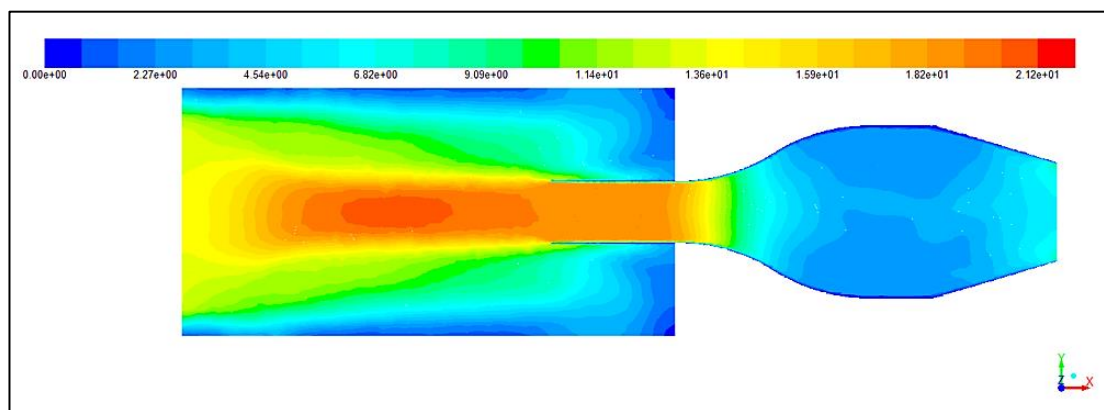
Figure 3.15: Contours of velocity magnitude for basic configuration (Case 2).

The experimental and CFD results (both Case 1 and Case 2) of the turbulent intensity are explained in **Figures 3.16 of planes 1 to 5**. The figures clearly show the turbulent intensity of an empty wind tunnel at five planes and 15 lines in total as a function of the test section height. The planes co-ordinates and its set-up is described in Chapter 4 and not repeated here. As expected, the turbulence intensity is significantly improved compared to both CFD case results (Case 1 and 2). The turbulent intensity shows a value of 1.8 % at a velocity of 19 m/s for Case 1 (basic configuration with open test section), 3.4% for Case 2 (with artificial boundary conditions with the closed test section) and then reduced to ~ 0.6% when the boundary

layer controllers were inserted. The most likely reason for this is due to the conditioning devices (honeycomb, mesh screen and settling chamber) that were carefully designed and inserted inside the wind tunnel, which have not been considered in the CFD models. This rise in turbulent intensity in both CFD model results is due to the flow separation on the wind tunnel corners that have a large impact on the flow quality inside the test section.
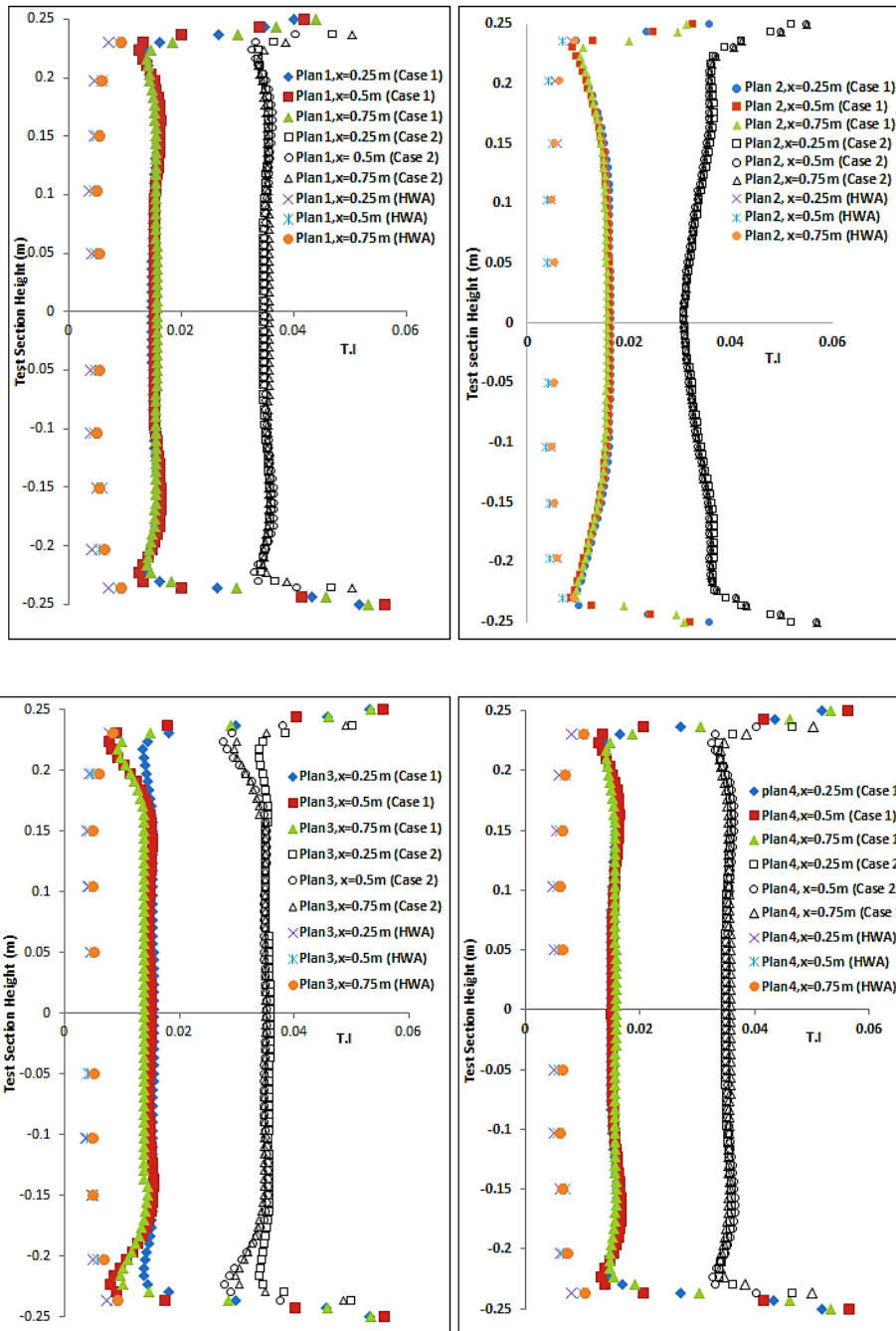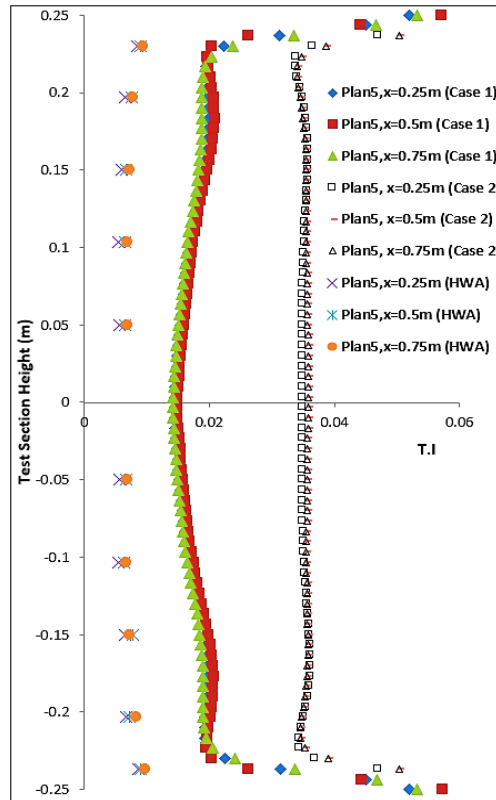
Figure 3.16: Experimental and numerical turbulence intensity results of the flow located at planes 1-5 for the free stream velocity of 19 m/s.

Moreover, a symmetric flow profile was seen in the wind tunnel test section as shown in **Figure 3.17a and b** at locations of 0.25 m and 0.75m from the inlet of the test section. This helps in giving a new lease of life to the layer by removing the direct impact of the layer growth and early separation. Consequently, it can be concluded that the flow quality was approximately homogenous through the whole length of the test section.
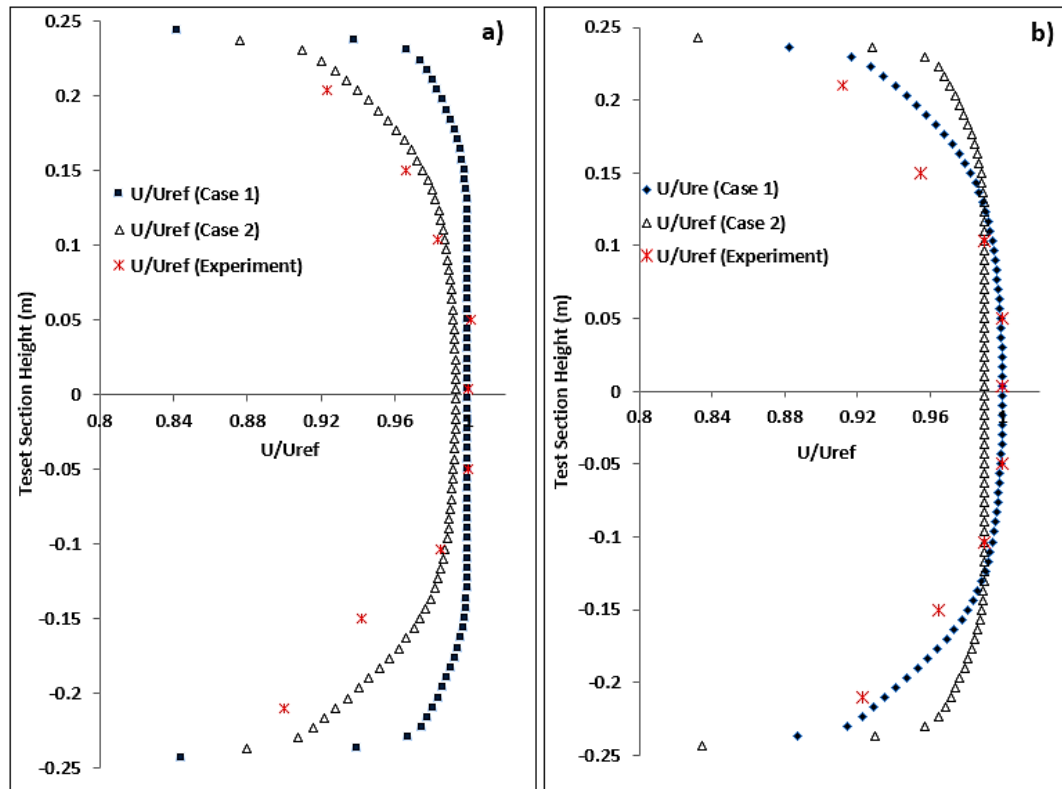
Figure 3.17: Comparison between CFD and experimental data of the dimensionless velocity profile (a) at X = 0.75 and b) at X = 0.25m).

3.6. Conclusions

A new low-speed open-circuit wind tunnel has been designed and constructed at the University of Leeds with test section dimensions of 1m × 0.5 m × 0.5 m (Length × Width × Height). A series of Computational Fluid Dynamic (CFD) models and experimental evaluations were conducted to determine the flow quality and to verify the wind tunnel adequacy for aerodynamic studies. Analysis of the flow quality results in an empty test section showed that adding flow conditioning devices (five mesh screens and one honeycomb) to the constructed wind tunnel reduced the turbulent intensity by more than 50 % compared to both CFD case results at 19 m/s. An improvement in flow quality is achieved by adding flow conditioning devices. Throughout the test section, the turbulence intensity is diminished to approximately 0.6% compared to CFD results, which approached the desired value. This represents a significant endorsement of flow conditioning devices, illustrating that design focus should concentrate on the settling chamber boundary layer controller – especially where it aligns with the test section. Some useful guidelines can be derived from this chapter for the requirement of wind tunnel design. Therefore, to validate the suitability

of the current wind tunnel for aerodynamic research, additional experimental tests in active flow control using synthetic jet actuators were carried out.

Chapter 4: Experimental Models and Wind Tunnel Mounting System

In this chapter, a description of the models used and the experimental set-up is provided. Therefore, the construction of convex hump models, synthetic jet actuator and wind tunnel mounting system in which most of the experiments in the thesis were undertaken is described.

4.1. The Convex Hump Models and Wind Tunnel Mounting System

4.1.1. The Convex Hump Models Design and Fabrication

Three convex "hump" models (section of cylinder) were used for all experiments carried out in this thesis depending on the experiments being performed. Initial investigations into the un-actuated flow-field were carried out over two Styrofoam convex hump models fabricated in the University of Leeds workshop, as shown in **Figure 4.1b**. A Styrofoam product was used for variety of reasons. The first reason was that it is very cheap and easy to manufacture, while the second reason was that it would only be used to examine the flow behaviour and investigate whether the flow separation can be detected. This enabled the selection of a final single model to be used to study the effect of an array of synthetic jet actuators as active flow control. Therefore, in order to establish a single model that would be used in all flow separation control, a number of different flow visualisation techniques have been applied to these two hump models without any SJAs being inserted on the surface. These flow visualisation techniques, in addition to the CFD analysis allowed the development and changes in the separation location to be tracked. The results of these un-actuated measurements will be introduced in Chapter 7 in more detail. The final selected model was then constructed from aluminium to accommodate the array of synthetic jet actuators and give the cylinder a smooth exterior surface. The geometrical dimensions of the two hump models used here are shown in **Table 4.1.**

The model geometry details of the convex hump are shown in **Figure 4.1a.** These models were constructed maintaining a constant apex height (H) of 30 mm, s is the span length of 500 mm and R represents the radius of curvature of each hump of 181.2 mm and 389.9 mm, respectively. This apex height H was non-dimensionalised by the streamlined cylinder maximum width which would help in analysing the results against the aspect ratio of each model (H/L).

Table 4.1: Dimensions of the convex hump models

Apex, h(mm)	L (mm)	R (mm)	Aspect ratio H/L
30	200	181.6	0.15
30	300	389.96	0.1
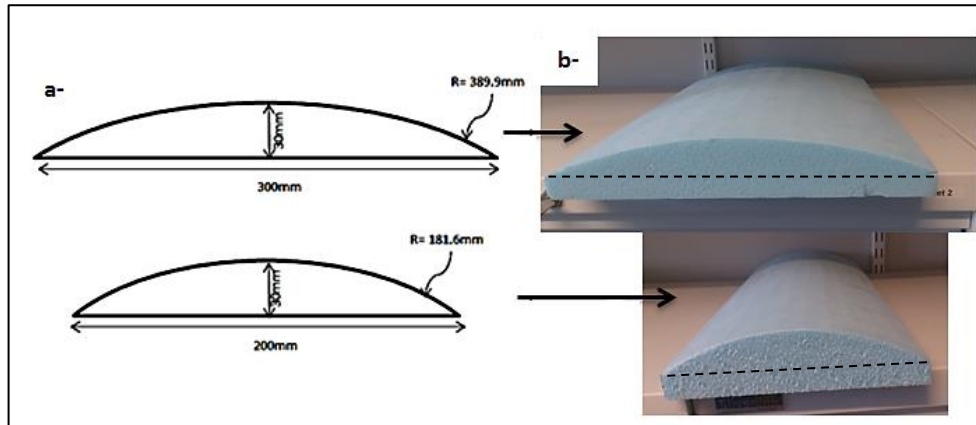
Figure 4.1: a) Convex hump models and their dimensions; b) Styrofoam hump models.

The final convex hump model selected (based on the CFD and flow visualization results explained in Chapter 7) had the same height as the Styrofoam model of H = 30 mm, which represents the part facing the wind tunnel free stream air, span length (s) of 500 mm and hump radius curvature (R) of 181.7 mm. **Figure 4.2a** clearly shows the main convex hump model and its removable parts. The figure also clearly shows that the main hump model had two removable parts in order to facilitate the synthetic jet actuators and rotating hump procedures creating a "mushroom-like" shape, as shown in **Figure 4.2b**. These parts are described briefly here and addressed in more detail in the following sections. The first removable plate was used to accommodate 12 SJAs to investigate the impact of the synthetic jets on the flow separation and wake flow behind the convex hump model. The second removable part had a semi-triangular shape, a base length of 70 mm, a maximum height of 100 mm and a thickness of 25mm. This plate is called a "stalk" removable plate that formed part of the rotating hump model. It was positioned 108 mm below the main convex hump model. It is the main part of the rotating joint where the pivot bar (the trunnion) is inserted. This part was itself laid flush directly onto the main hump model via a set of four 8 mm holding brackets on both sides, which allowed the main hump to be

rotated around its centre line up to ±32 degrees (see **Figure 4.2b**). The pivot bar was positioned in a hole of 25 mm diameter that represented the central rotation of the main hump model. The angles of rotation were monitored by a digital inclinometer protractor meter upright magnet 360° sloped angle which gave more accurate readings than normal graded protractors.
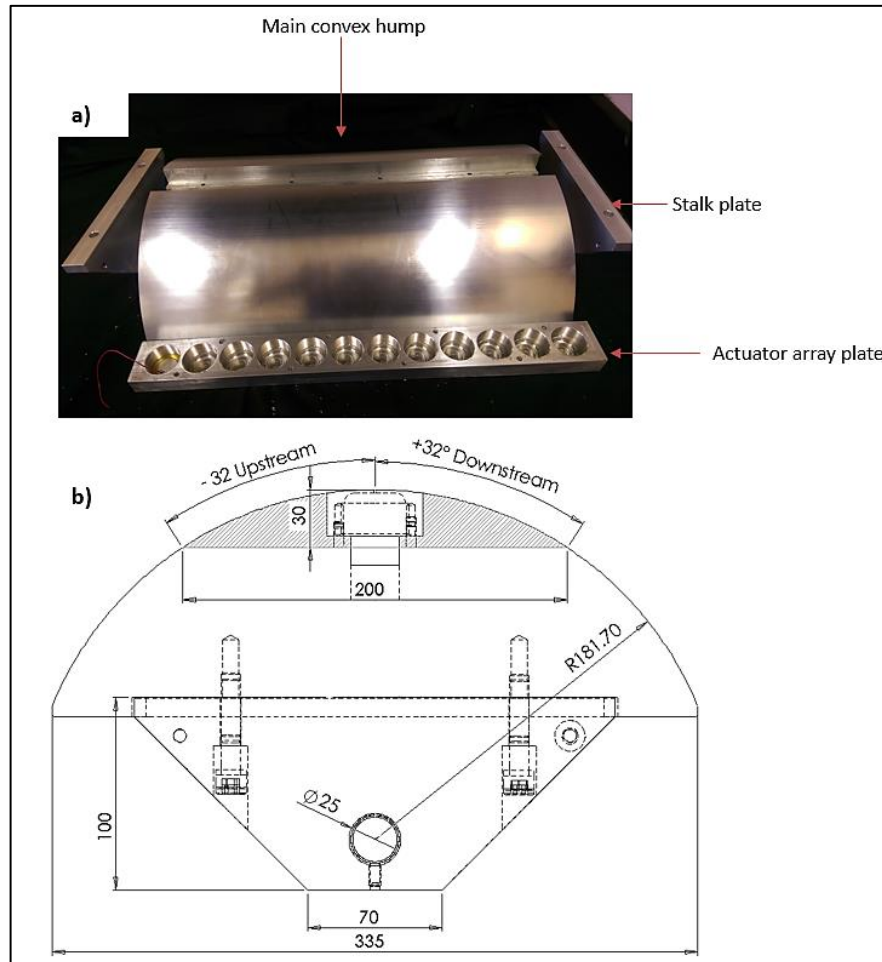
Figure 4.2: a) The main convex hump model and its parts; b) Convex hump dimensions.

4.1.2. The Removable Actuator Array Plate and the Driving Circuitry

The first removable plate was constructed and laid flush along the span centre of the convex hump model surface. This section could be entirely removed along the whole length of the hump surface by loosening eight separate M6 holding brackets. The purpose of this arrangement was to enable the 500 mm long plate to be removed and modified in such a way as to accommodate an array of piezo-ceramic diaphragms and to be altered as required. The actuators were positioned to energize the boundary layer

through span-wise radially drilled orifices. 36 orifices (three orifices per cavity) were drilled, with each orifice spaced every 10 mm such that the synthetic jet actuators ejected air perpendicular or at specific angle (β) against the wind tunnel free stream velocity. The SJA removable part is shown in relation to the entire convex hump model in **Figure 4.3a**. This removable plate had a series of 12 embedded synthetic jet actuators, whilst maintaining the hump's circular profile. The curved face of the section contained 12 cavities, three orifices per cavity of 1.2 mm diameter along the hump centerline. The reason for using more than one orifice per cavity, the specified orifice diameter and the orifice space was to increase the strength and circulation of the vortex rings, which have been described in Chapter 6 in more detail.

The front walls of the cavity of the synthetic jet actuators used in this model were formed from the rounded body of the convex hump itself. The resulting cavity had a maximum depth of 5.5mm which was chosen from among three different cavities with a maximum diameter of 32mm, as also described in Chapter 6. In order to oscillate the diaphragm, a clamping piece of threaded brass 10 mm deep, and 35 mm wide was used to hold the piezo-ceramic diaphragm in place at the back of the cavity. Each clamp could be loosened or tightened as required to alter the clamping on any particular disk, which allowed the properties of the actuator to be varied if required. A 1.2 mm diameter orifice was drilled out at the centreline of the convex hump model. Each orifice was 1.5 mm deep, since the extension of the whole cavity into the hump body with a depth of 24 mm was 22.5 mm. A close up view of a section of the removable part is presented in **Figure 4.3b**, with four actuators and clamping being clearly seen.
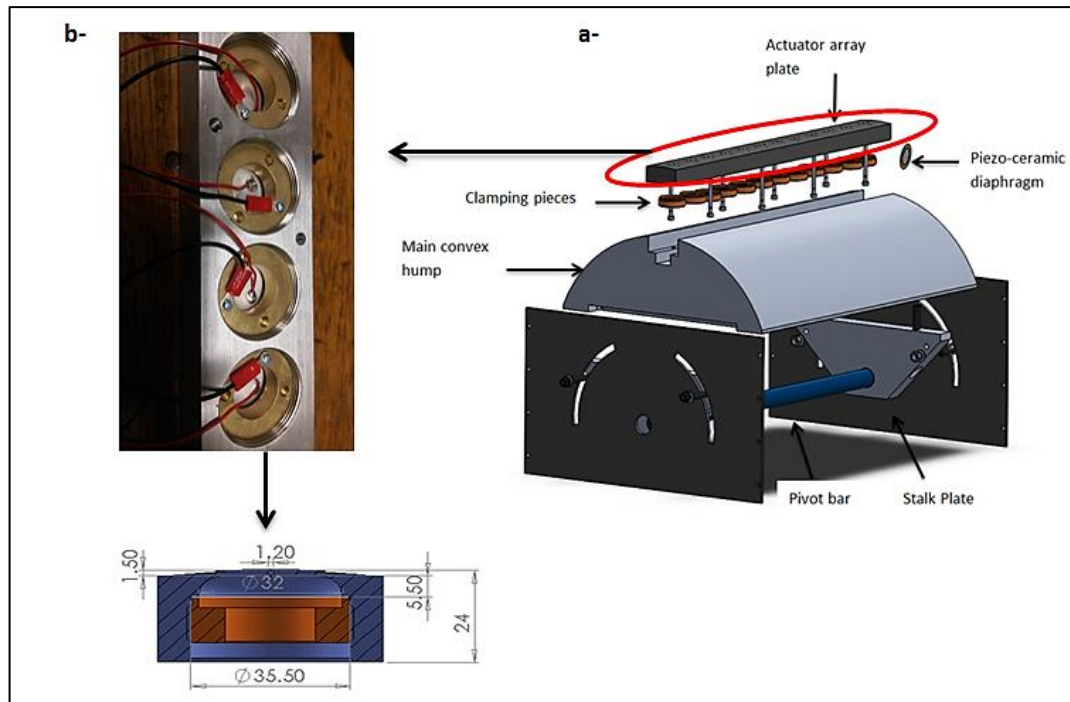
Figure 4.3: a) SJA removable plate in relation to the main convex hump model; b) Close up view of four individual actuators showing wire connections, cross section of a single SJA's dimensions, clamping piece

Two different sets of experiments were used throughout this research depending on the experiments being performed. Initial investigations into the un-actuated flow-field were carried out with covered SJA orifices using very thin Sellotape. This arrangement was simply used to avoid any flow disturbance due to the presence of the orifices on the hump surface. The second set of experiments was used to investigate the effect of synthetic jet actuation on the wake flow-field behind the hump through the orifices.

The synthetic jet actuators used here were fabricated at the University of Leeds. A FT-35T-2.6A1 piezo-ceramic diaphragm was used as a disk element. This formed the oscillatory surface essential to produce zero net mass-flow from each actuator. Each disc consisted of a brass disk of 35mm diameter, D_o, and 0.47 ± 0.05 mm thicknesses, t_o. A 25 mm diameter, D, of ceramic material has been bonded to one side of this disc, with a thickness, t, of 0.25mm. The advantages of this type of piezo-ceramic are that it is cost-effective and has a peak deflection in the disc centre when its edge is clamped and a current is applied, which has been explained in the displacement measurement results in Chapter 5. The application of an oscillatory excitation waveform (sine wave, for example) will result in an oscillatory deflection

of the diaphragm and, when applied within an actuator cavity, can provide a train of vortex rings which have a zero net mass-flow.

The driving circuitry that supplies the signal to the piezo-ceramic diaphragms used in this thesis consists of two components. The function generator (TG1010A) is the first component, which allowed modulated and un-modulated excitation waveforms, excitation frequency and voltage amplitude to be altered as required. One function generator was used to generate single excitation waveform (un-modulated case), whilst a second function generator was used when the amplitude modulation was applied.

The output from the function generator was then subjected to six high performance piezo-driver amplifiers (PDm-200). Each amplifier is able to provide a 20-times gain voltage amplitude. This amplifier is a complete high-performance power supply and linear amplifier module for driving capacitive loads such as the piezo-ceramic actuators. The output voltage range can be switched between bipolar or unipolar modes with a range of 100 V, 150 V, or 200 V in the bridged configuration. In the unipolar mode, the negative output range is fixed at 30 V for use with stack actuators and the jumper should always in the 'E' position. However, bipolar mode was used in this project to get the ± 100 V and the jumpers should always be in the 'B, F' positions. **Figure 4.4 b** clearly shows that each amplifier has an internal RMS output current-limit of 100 mA at ±100 V output. This limit was encountered when driving only two diaphragms of synthetic jet actuators with a sine wave at a near maximum voltage of +/- 5 volts input. Each amplifier can only drive two diaphragms that need a maximum of 73 mA current to be oscillated as shown in **Figure 4.4b**. Therefore, six amplifiers were needed to oscillate the 12 piezo-ceramic diaphragms in parallel. The driving circuitry of the parallel connection method of the 12 synthetic jet actuators to the six amplifiers is shown in **Figure 4.4a**.
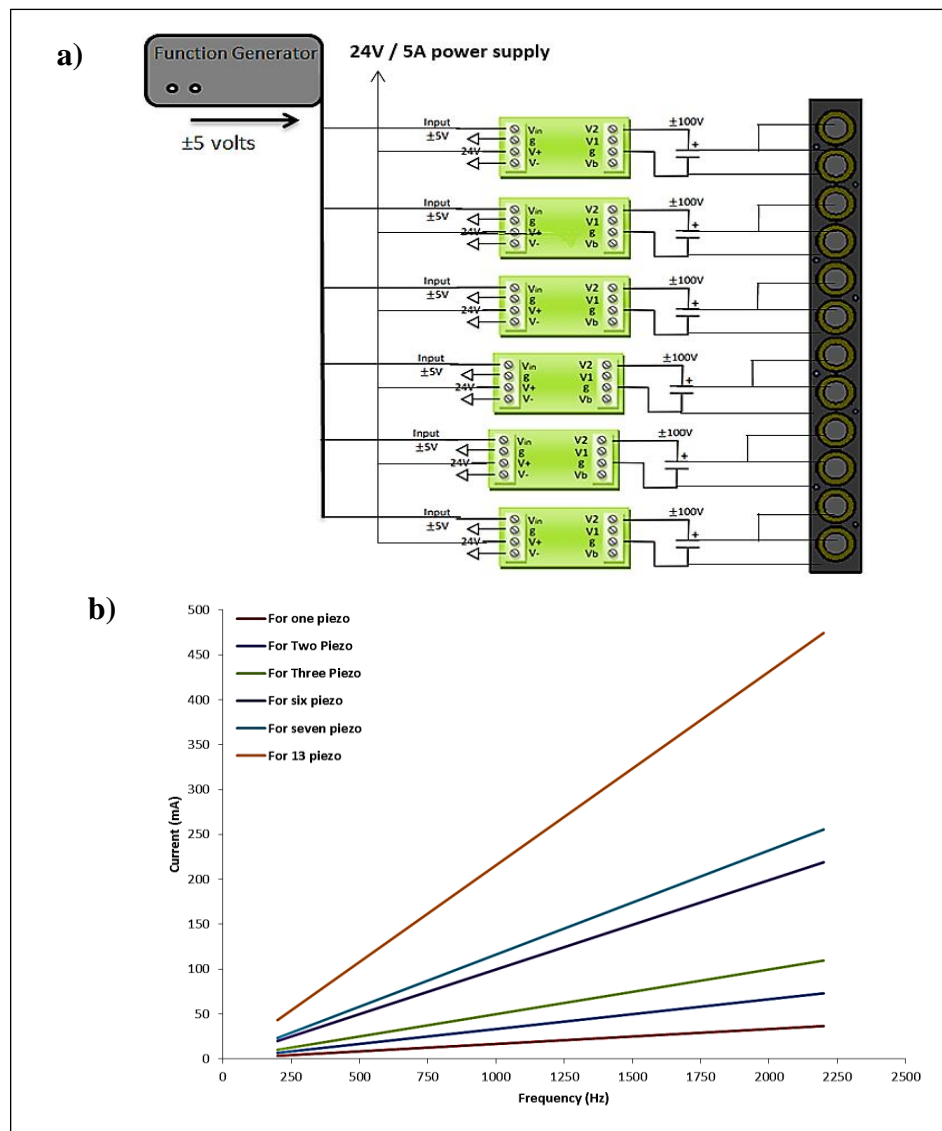
Figure 4.4: a): Driving circuitry connection diagram; b) Amplifier calculations in terms of current limits.

The whole connections of the driving circuitry box are shown in **Figure 4.5a.** The figure clearly shows that the driving circuitry box consists of three main parts; the first part was the six amplifiers mounted on the base of an electrical box via 12, M8 brackets. The second part was a 24 Vdc, 3.1 W axial cooling fan to reduce the heat transfer during operation of the amplifiers. However, the PDm200 is protected against over-current and thermal overload. If the temperature exceeds 70℃ the amplifier will be disabled until the temperature reduces. The final part was the amplifiers main desktop power supply which has 120 W and 24Vdc output at 100 - 240 input voltage. From this driving circuitry box, the signal then passed into the wires that travelled to

each of the 12 actuators and oscillated the piezo-ceramic diaphragms as shown in **Figure 4.5b.**
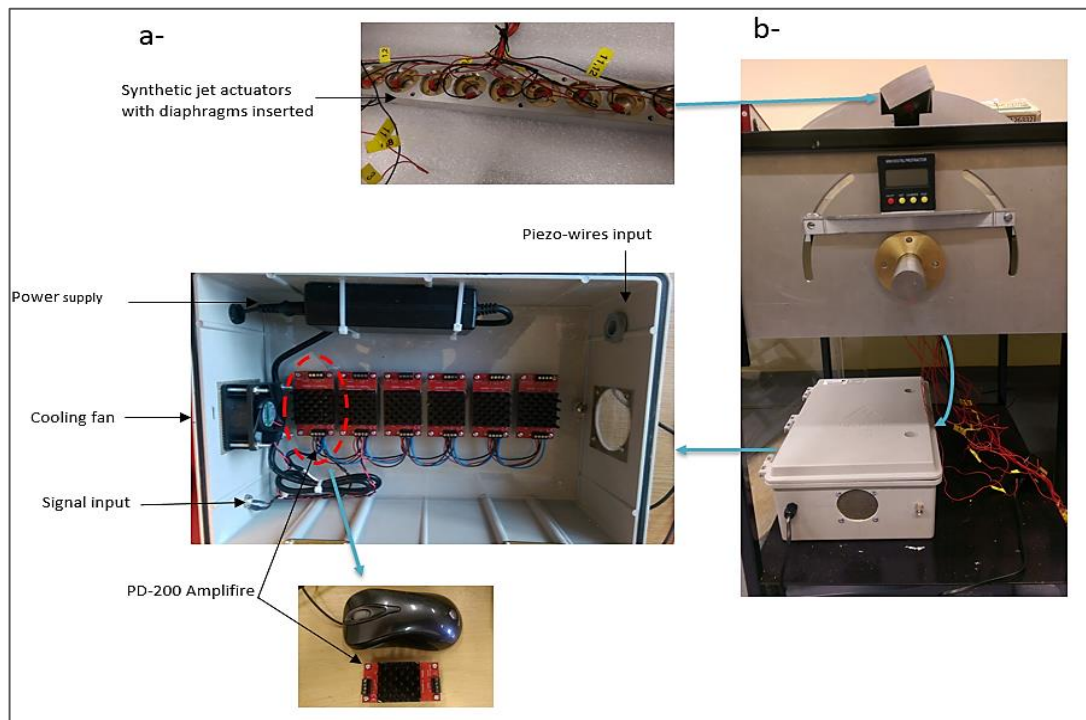
Figure 4.5: a) Driving circuitry parts; b) Piezo-ceramic wires connection.

4.1.3. The Stalk Removable Plates and Rotation Procedure

A second removable plate was designed and fabricated to produce the whole rotating system of the convex hump model. This plate had a semi-triangular shape known as the "stalk" of the "mushroom" shape. It has a base length of 250 mm, a maximum height of 100 mm and a thickness of 25 mm. It was positioned 25mm below the main convex hump model as shown in **Figure 4.6b**. Alongside the sidewall of the main convex hump, the plate lays flush and was fixed to a sunken shelf via four cap-screw bolts of 10 mm diameter to support it. Two holes of 25 mm diameter were positioned at 40 mm away from the plate base.

A stainless steel shaft of 25mm diameter went through these holes and created the central rotation of the hump as shown in **Figure 4.6a**. This central rotation was advantageous because it enabled the variation of the angular position of actuation (β) to be set as required. This angle (β) is varied by rotating the whole hump into a radial slot (which has the same centre) via loosening and tightening two M8 brackets fixed

on two side wall plates. These two side wall plates of 230 mm × 300 mm were positioned on a separate frame outside the wind tunnel which allowed the removable plates to be attached to the wind tunnel. These plates were fabricated out of Aluminum and have radial slots parallel to the hump curvature which helps to rotate the hump within these slots. Subsequently, the central mounting shaft ran through a 25 mm wide hole on the first side wall plate and came out from the second sidewall plate at a distance of 700 mm from the mid-plane spanning the full width of the test section. **Figure 4.6a** clearly shows the convex hump model fixed to the side wall plates, hence the whole system was attached to a black metal frame. This figure also illustrates how the angular position of actuation can be varied using the digital protractor. From here, the whole rig is now ready to mount into the wind tunnel test section which is explained in the wind tunnel mounting system section in more detail.
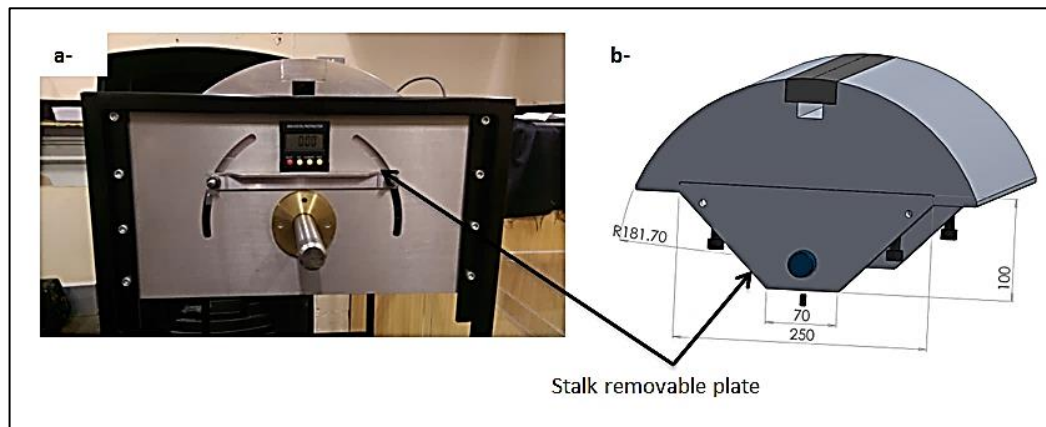
Figure 4.6: a) The complete set of the rotating convex hump model; b) The hump model showing the stalk removable plate.

4.2. The Wind Tunnel and Model Mounting System

The convex hump model was mounted in a 0.5 m × 0.5 m, the wind tunnel, at the Chemistry Laboratory of the University of Leeds. This wind tunnel had a square test section 0.5 m high, 0.5 m wide and 1 m long with a pre-test section contraction ratio of 7.8:1 as shown previously in **Figure 3.9**. The tunnel had a top speed of 23 m/s, and turbulence intensity at 19 m/s of 0.6%. The process of design, construction and testing was described previously in detail in Chapter 3 and not repeated here.

Two different wind tunnel configurations were introduced in this thesis as shown in **Figures 4.7and 4.8**. The first configuration was the benchmark configuration in which no convex hump model was presented (wind tunnel test section only). The

test section middle slot was covered with an appropriately designed Perspex plate to ensure no leak could occur during the operation as shown in **Figures 4.7a and 4.8a**. This configuration was utilised to evaluate the flow quality on the test section in terms of turbulent intensity and flow uniformity, which was described previously in more detail in Chapter 3. The second configuration involved the attachment of the convex hump model span to the wind tunnel test section through a rectangular slot in the wind tunnel bottom plate as shown in **Figure 4.7b and 4.8b**. This rectangular slot had a 60° cutting angle to avoid any contact between the hump edge and the test section that may damage the Perspex material (**see Figure 4.8b**). The presence of two 25 mm wide holes positioned 40mm away from the stalk plate base. These holes are penetrated by a stainless steel shaft of 25 mm which created a central pivot. The attachment of the pivot shaft to the wind tunnel was enabled by 230 mm $\times$ 300 mm side wall plates situated on a 20 mm $\times$ 20 mm metal frame, outside the wind tunnel. Subsequently, the central mounting shaft ran through a 25 mm wide hole on the first sidewall plate and came out from the second side wall plate at a distance of 700 mm in the same direction as the span of the primary convex hump model.

The altering of the angular position of the actuation, (β), was achieved by simply rotating the entire convex hump model (mushroom shape) by $\beta = \pm 32$ degrees using a digital inclinometer protractor to characterize the effect of synthetic jets actuation angular position with regard to the flow separation and the wake flow. At zero-degree actuation, the actuation angular position is perpendicular to the tunnel freestream and parallel to the top and bottom walls of the wind tunnel. The rotation was achieved by loosening the four locking screws in the side plate sections attached to the front and rear of the metal frame. Either dropping or raising these locking screws resulted in alteration of the actuation angle and, implicitly, of the convex hump, as required. This type of mounting system is required for different measurement techniques. The convex hump orientation used depended on the particular measurement technique being utilized.
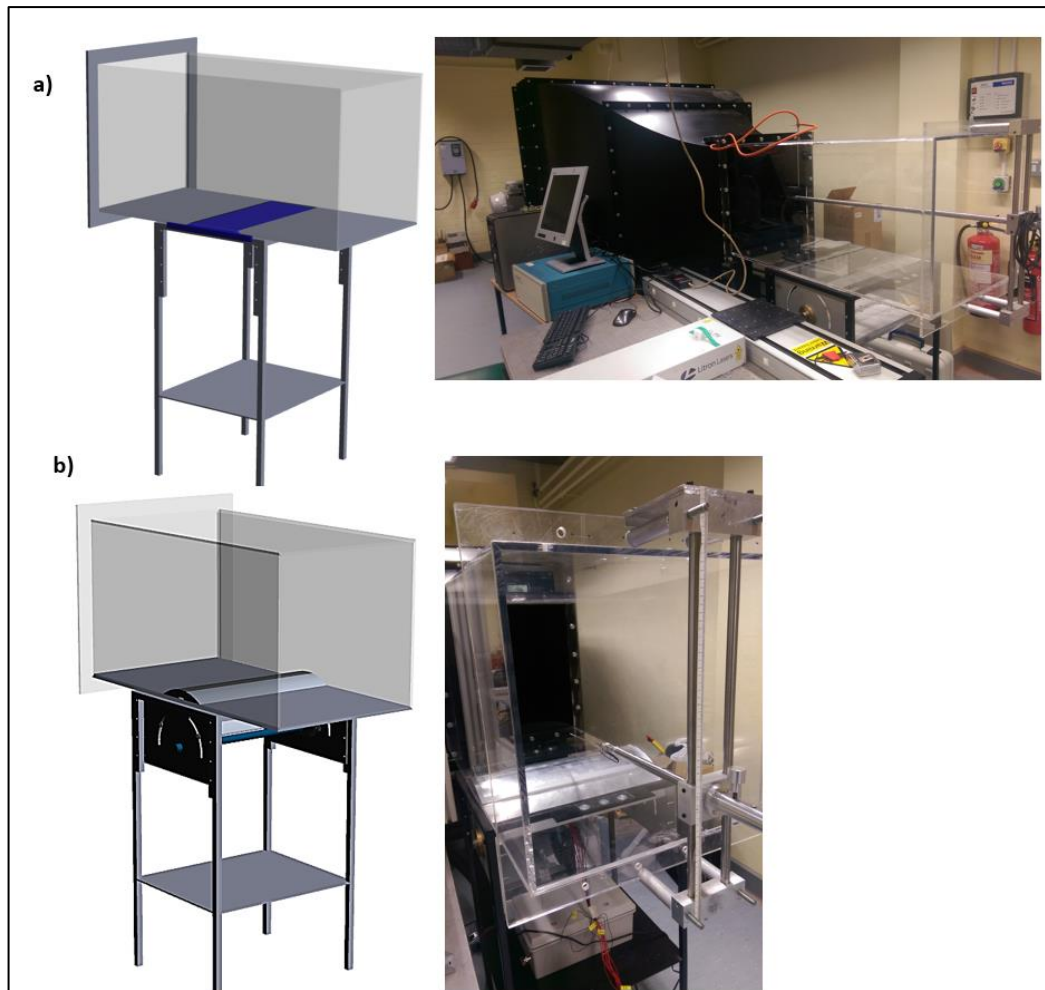
Figure 4.7: a) benchmark wind tunnel configurations (Solid Works and real set-up); b) convex hump attached to the wind tunnel test section (Solid Works and real set-up).
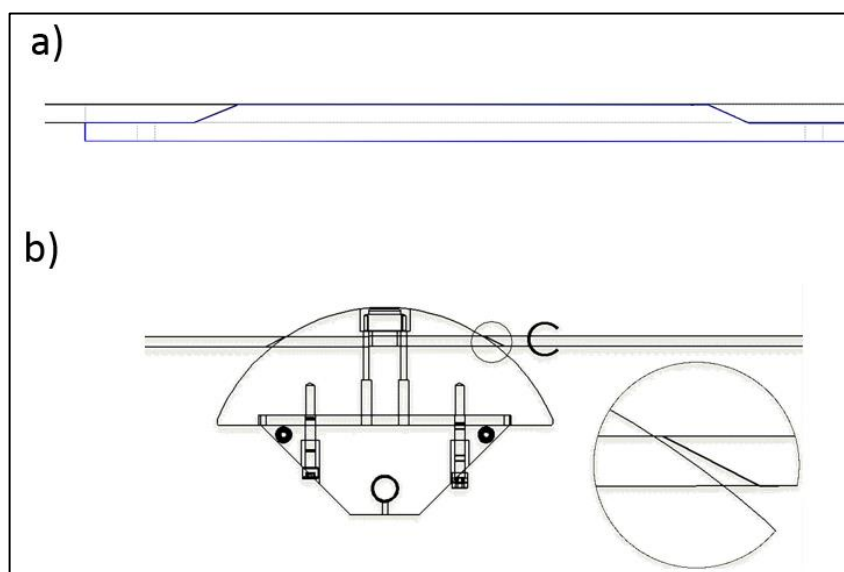
Figure 4.8: Wind tunnel configurations showing: a) The plate attached to the middle slot; b) 60° cutting angle.

4.3. Synthetic Jet Actuator Analysis in Quiescent Flow

The synthetic jet actuators used in the present experiments were selected based on two types of measurements in quiescent flow conditions. Firstly, the actuators were clamped in three different ways, between two O-rings, neoprene rubber and metal-to-metal clamping to investigate the effect of the clamping method on diaphragm displacement using Polytec Scan Vibrometer (PSV), which will be described in Chapter 5 in more detail. Secondly, in order to enhance the efficiency of the synthetic jets, the geometrical and operational parameters' effect on the peak jet velocity was also investigated using the hot-wire anemometer technique. This investigation enabled the final selection of the optimum jet parameters (geometrical and operational parameters) to be utilized over the convex hump to achieve the desired flow control. Chapter 6 contains the results and discussion of this investigation in more detail.

4.3.1. Synthetic Jet Actuator Design and Fabrication

The housings and clamping for the actuators used here were machined out of aluminum in the University of Leeds mechanical workshop. The geometrical parameters of the baseline actuator model are indicated in **Table 4.2**. These baseline actuator model dimensions were altered such that the cavity and orifice diameter can be changed as required. In this experiment, synthetic jet actuators of three different scales were examined. Therefore, in order to easily alter the cavity volume and orifice diameter, a number of aluminum plates were used above the existing baseline model.

Table 4.2: Geometry properties of the baseline synthetic jet actuator.

Actuator Parameters	Value (mm)
Orifice diameter (D_o)	1.2
Orifice Length (L_o)	1.5
Cavity Height (H)	3
Cavity Diameter (D_c)	32

The cavity was replaced with aluminum top plates of different thickness and orifice diameters providing a simple way to study the effect of geometrical parameters on jet formation and jet velocity. Circular orifices of 1.2 mm, 2.5 mm and 5 mm in diameter and cavity height exhibited variation between 3, 5.5 and 8 mm were used. **Figure 4.9** illustrates the synthetic jet actuator baseline model and its components. The figure clearly illustrates the piezo-ceramic diaphragm attached to the base plate together with the sample plates employed to alter cavity volume as well as orifice diameter.
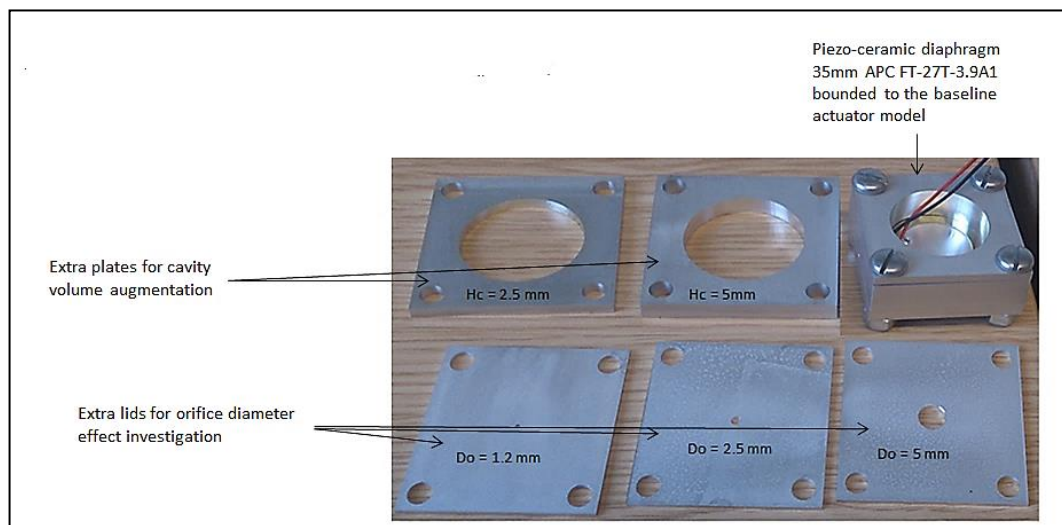
Figure 4.9: Baseline actuator model and its components.

4.3.2. Diaphragm Clamping Effect Test

To characterize the effect of the clamping method on the displacement of the diaphragm used in this research, three clamping types were used, as shown in **Figure 4.10,** to investigate which clamping method could provide a strong seal and prevent any leaks which could have a detrimental effect on the actuator performance. The clamping inside the cavity of each actuator was maintained as constant as possible and the dimensions of the actuator were kept the same. For a piezo-ceramic diaphragm, a groove was machined on the cavity which was reinforced with three types of clamping, neoprene rubber, O-rings and metal-to-metal clamping. This investigation has helped to identify which of these clamping methods could provide both a cushion and seal to give maximum displacement, hence promoting peak jet velocity output at constant dimensions. This experiment was done using the Polytec Scan Vibrometer technique

and the results of the effect with the three types of clamping are presented in Chapter 5.
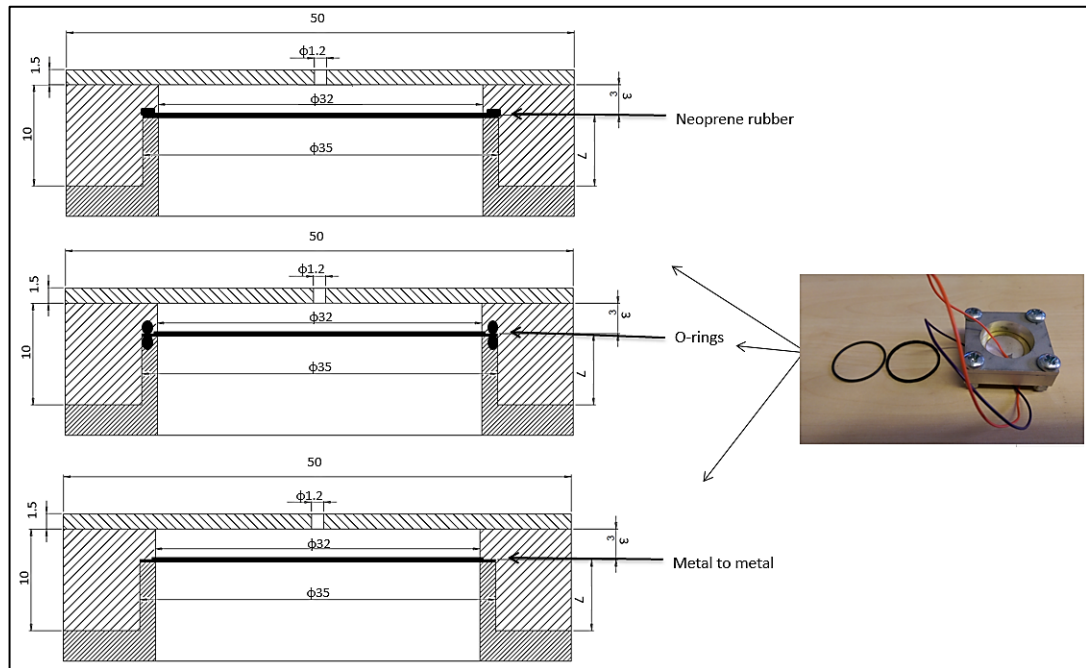
Figure 4.10: Different ways of clamping: a) Between two O-rings; b) using neoprene rubber; c) metal to metal clamping.

4.3.3. Identifying Frequency of Interest

The scanning vibrometer tests are not only able to provide information about the clamping method effect, but also was useful tests to measure the maximum displacement and resonance frequency of the piezo-ceramic diaphragm at different operating frequencies. Therefore, this investigation is helped to identify what the maximum frequency of the diaphragm can be safely operated without affect its longevity. This test is carried out without any cavity being considered and hence only one resonance frequency can be seen.

Chapter 5: Measurement Techniques and Tools

This chapter mainly describes the different measurement devices that were used in the current thesis. However, the results and discussion are presented in the relevant chapter of the thesis.

5.1. Polytec Scan Vibrometer Measurement Technique

Prior to the SJA tests, it was necessary to characterize the effect of the clamping method on the displacement of the diaphragm used in this research, three clamping types were used to investigate which clamping method could provide a strong seal and prevent any leaks which could have a detrimental effect on the actuator performance. The clamping inside the cavity of each actuator was maintained as constant as possible and the dimensions of the actuator were kept the same. For the piezo-ceramic diaphragm used here, a groove was machined on the cavity which was reinforced with three types of clamping, neoprene rubber, O-rings and metal-to-metal clamping. This investigation could identify which of these clamping methods could provide both a cushion and seal to give maximum displacement, hence promoting peak jet velocity output at constant dimensions.

5.1.1. Theory of Operation

The Polytec Scan Vibrometer, PSV-400 from Polytec consists of a controller (OFV-5000), a junction box and a PC system equipped with a 4 channel 5 MHz sampling card from National Instruments. The laser beam can be scanned in an angle region of ±20º in the horizontal and vertical directions. Thereby, the angle resolution is < 0.002º. The controller includes several parts, two velocity encoders with analogue and digital outputs, an analogue displacement output and a digital decoder for the output of a down-converted signal. The velocity decoder, referred to as VD-07, for frequency ranges up to 350 kHz, can measure velocities up to 500 mm/s and a second decoder, referred to as VD-09, for frequencies in the range from 10 Hz – 2.5 MHz, can measure velocities up to 10 m/s.

The PSV is manually controlled and provides displacement and velocity measurement at only one point. To obtain better results and have results at multiple points a scanning laser vibrometer was used. The scanning laser vibrometer is PC controlled. The software controls the focus, scans a set of points marked by the

operator and finally provides a map of wave propagation or displacements at those points. The working principle of the scanning laser vibrometer is available at **www.polytec.com** if more detailed information is required.

5.1.2. Experimental Set-up, Results and Discussion

It has been proven that the boundary conditions in a piezo-ceramic actuator are going to be subjected to an application having a significant impact on the final performance of the device. Different boundary conditions and applied voltages could affect the shape and displacement of the piezo-ceramic composite disc (Liew et al, 2002). Jue (2007) also showed that clamping the actuator diaphragm between two O-rings would damp its displacement out. Therefore, characterizing the effect of the clamping method on the displacement of the diaphragm used in this research has not yet been investigated. Three clamping types were used to investigate which one could provide a strong seal and prevent any leaks which could have a detrimental effect on the actuator performance. **Figure 5.1** shows how the diaphragm disc was set inside the cavity and clamped at three different clamping conditions, without any plates being inserted. The clamping inside the cavity of each actuator is maintained as constant as possible. The figure clearly shows the experimental set-up for the PSV to study the displacement and motion of the diaphragm at different excitation parameters.
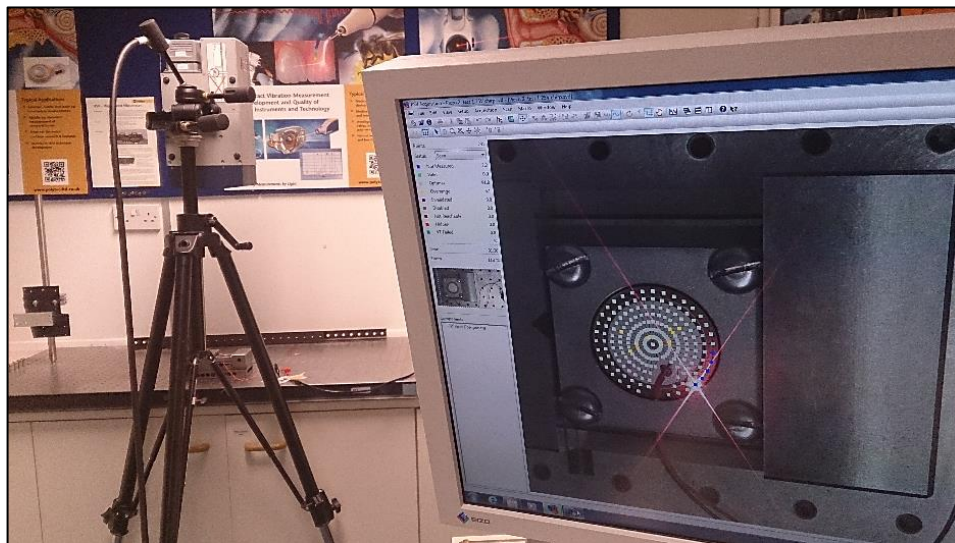
Figure 5.1: Polytec scan vibrometer experimental set-up.

Analysis of the isolated diaphragm (without any cavity attached), with the three types of clamping forming the boundary condition was conducted using the Polytec Scanning Vibrometer (PSV). The diaphragm of each clamping was excited with a sine sweep over a frequency range of 10 Hz to 3 kHz (in 2 Hz increments) while measuring the spatial and temporal distribution of the actuator vibration. The boundary condition applied to the piezo-ceramic diaphragm disc reduced the maximum allowable excitation voltage from 60 V at free boundary condition to 50 V (35 Vrms). At each excitation of frequency, diaphragm vibration visualization was obtained with PSV which was accompanied by the displacement data. Animated diaphragm motion also showed that the diaphragm had different modes at different clamping conditions which allowed a quick and easy verification of the uniformity of the boundary condition all around the actuator circumference as shown in **Figure 5.2a and b**. **Figure 5.2b** shows that metal to metal clamping produced the best uniformity of boundary condition and smooth motion with higher displacement compared to the other two clamping methods. However, clamping the diaphragm between two O-rings could damp its displacement which was responsible for non-uniform motion and hence low displacement. It was also a useful test for both the final operation of the actuator as well as for the guarantee of the symmetry of the bonding. Once being assured that a uniform boundary condition was established, the fundamental resonant frequency of the diaphragm at these conditions was measured to be ≈ 2200 Hz as explained in **Figure 5.3.** This figure shows the displacement of the diaphragm when it was excited at 35 Vrms with a maximum displacement of 0.027 mm. Maximum membrane displacement for the metal to metal clamping case was measured to be 27 μm. The most likely reason was that metal to metal clamping was able to overcome the damping force and provided an air tight seal to hold the diaphragm in place without restricting the desired displacement hence jet velocity when excited. Moreover, the figure clearly shows only one resonant frequency without the Helmholtz frequency of the cavity as the cavity plate was not yet inserted.
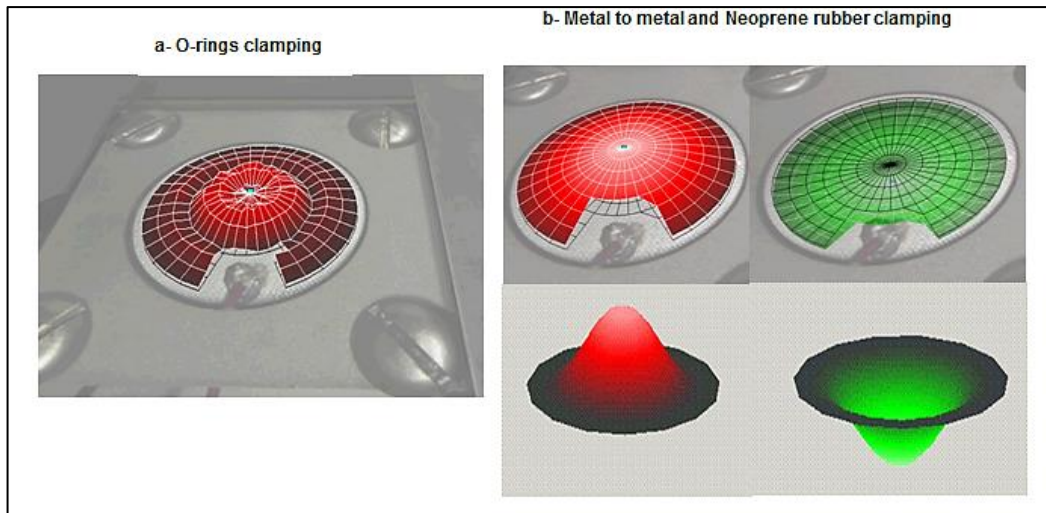
Figure 5.2: The clamping effect on the uniformity of boundary conditions around the actuator circumference at different clamping methods.
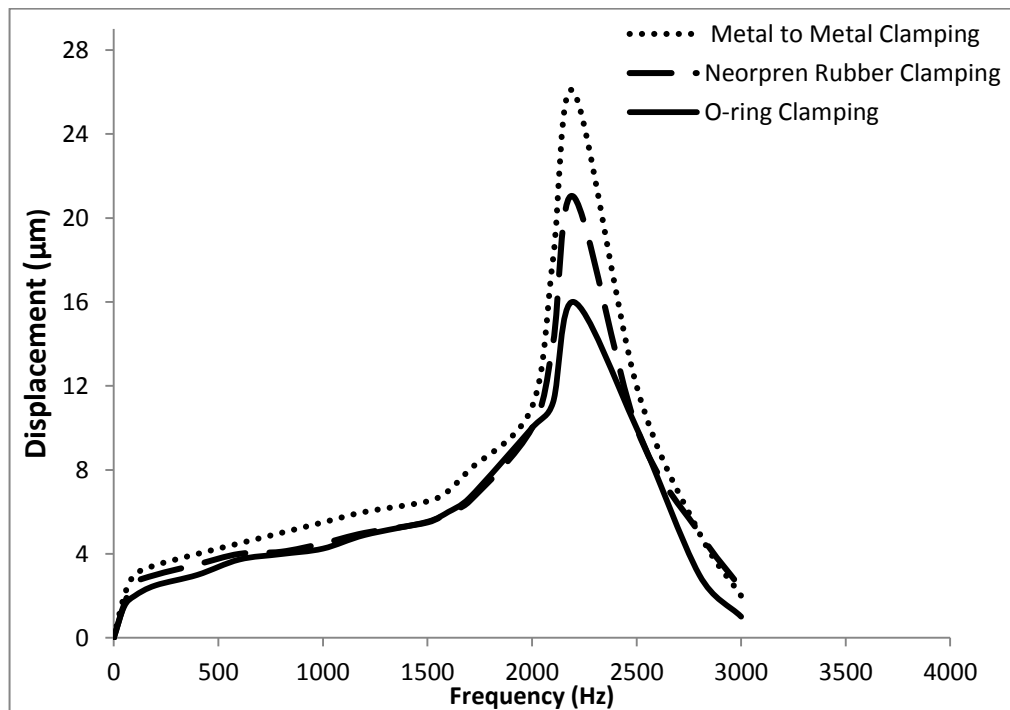
Figure 5.3: The diaphragm displacement at different excitation frequencies and fixed Vrms = 35 V.

5.2. Time-averaged Velocity Measurement Techniques

The experimental approach of the next sections includes how the hot-wire velocity measurements are used in both cross-flow conditions (wind tunnel) and quiescent flow conditions. The initial measurements were made to examine if the velocity distribution at the wind tunnel test section was homogeneous and had the desired turbulence

intensity, which already presented in Chapter 3. The second test was to investigate how the temporal response and peak exit velocity from each actuator varied when different geometrical and operational parameters were applied. A bench top hot-wire test was employed in quiescent flow to achieve such an investigation. Constant Temperature Anemometer electronic circuitry was used to keep the resistance in the sensor high and constant. The sensor is electrically heated to maintain a constant temperature that is higher than the ambient temperature. When the sensor is placed in a test fluid, the changes in the velocity of the fluid are reflected through the heat transfer or heat loss from the heated sensor to the surroundings. The heat is convected away by the fluid is determined by measuring the current required to maintain a constant wire temperature. Heat loss can then be converted into a fluid velocity in accordance with calibration theory.

The hot-wire anemometry system used throughout this thesis consisted of a TSI triple channel IFA-300 Constant Temperature Anemometer (CTA) with a single probe, 5 μm (Dantec dynamic 55P11). This wire was mounted in the stainless steel tube of 4 mm outer diameter. The CTA used here was a constant temperature anemometer with a flat DC to 300 kHz frequency response (TSI Inc.). A Power DAQ PD2-MFS 12 bit, 8 channel data acquisition card was used to digitize, transfer, and store the data generated by the bridge unit on a computer in the form of spreadsheets. This acquisition card also presented an input voltage range at ± 5Volts. The acquisition of hot-wire data occurred at the same time as the acquisition of the actuator excitation signal which, to preserve the ± 5Volt input range, took place prior to amplification. A BNC cable with a length of 5m and a 50Ω probe cable facilitated the attachment of the bridge unit to the probe. The signal was then collected, saved and analyzed using Thermalpro software at a sampling frequency of 200000 Hz and 8 kilo points per channel (one kilo point has 1024 samples). Thus, the length of time that the system gathered data at every point in the flow field prior to proceeding to the next point was 0.04096 seconds.

5.2.1. Hot-wire Velocity Measurement in Quiescent Flow Conditions

Measurements that illustrate changes in stream-wise and cross-stream jet peak mean velocity above the orifice as a function of the actuator design parameters are presented here. However, the data that highlight the importance of the influence of actuator

design parameters, on jet formation and circulation are presented and discussed in Chapter 6 in more details.

Measurements of time varying exit velocities from each of the three cavity heights of synthetic jet actuators were conducted using six different categories of equipment. These categories are explained in a block diagram as shown in **Figure 5.4**. The experimental set-up of each category was explained in the relevant section. The driving circuitry that supplies the excitation signal to the piezo-ceramic diaphragm used consists of two components. The function generator is the first component, which allowed the waveform types, excitation frequency and amplitude to be altered as required. The output from the function generator was subjected to a PDm-200 power amplifier which is able to provide a 20-times gain voltage amplitude. From this driving circuitry box, the signal then passed into the wires that travelled to the actuator and oscillated the piezo-ceramic diaphragm.

The velocity was measured using the IFA 300 CTA, hot-wire anemometry system. The hot-wire sensor was positioned to measure the jet velocity above each actuator using a two axis, manual controlled traversing mechanism with a 250×250 mm travel length as presented in **Figure 5.5a**. A not-to-scale illustration of the range of movements in relation to the synthetic jet actuator is provided in **Figure 5.5b**. The movement of the traverse towards the orifice was carried out in an increment of one orifice diameter. The figure clearly shows that time-average velocity was measured in both the stream-wise (Y/D) and cross-stream directions (X/D). The hot-wire sensor was moved manually along a pre-defined grid. The grid selected was a 0-10 mm region in one diameter increments in the jet cross-stream direction and a 0-50 mm range in the vertical or jet stream-wise direction. The origin of the grids was centered 1 mm above the centre of the orifice.
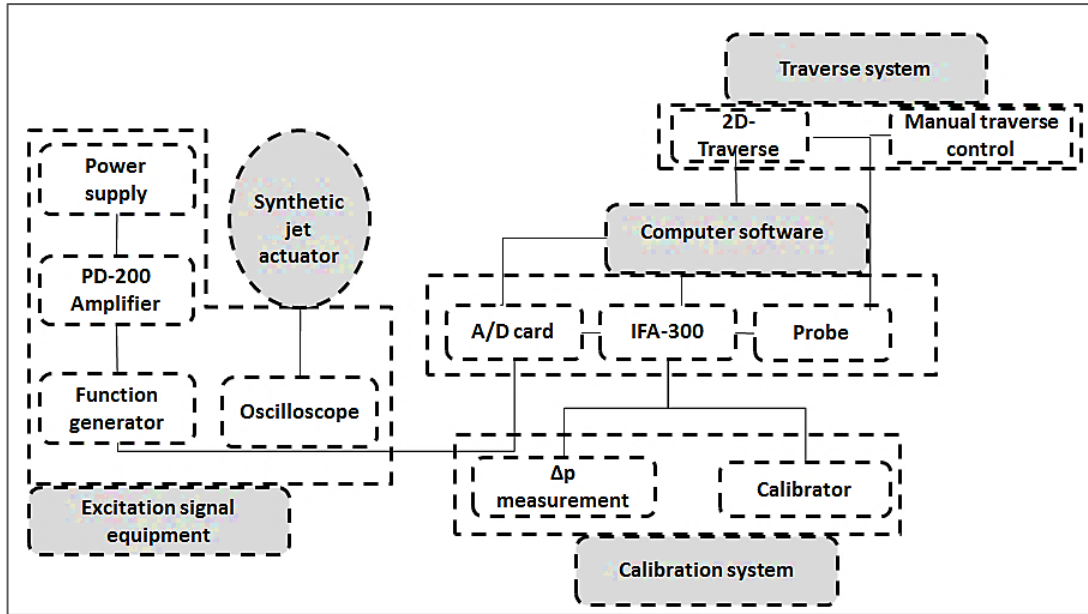
Figure 5.4: Flow chart of the experimental set-up.
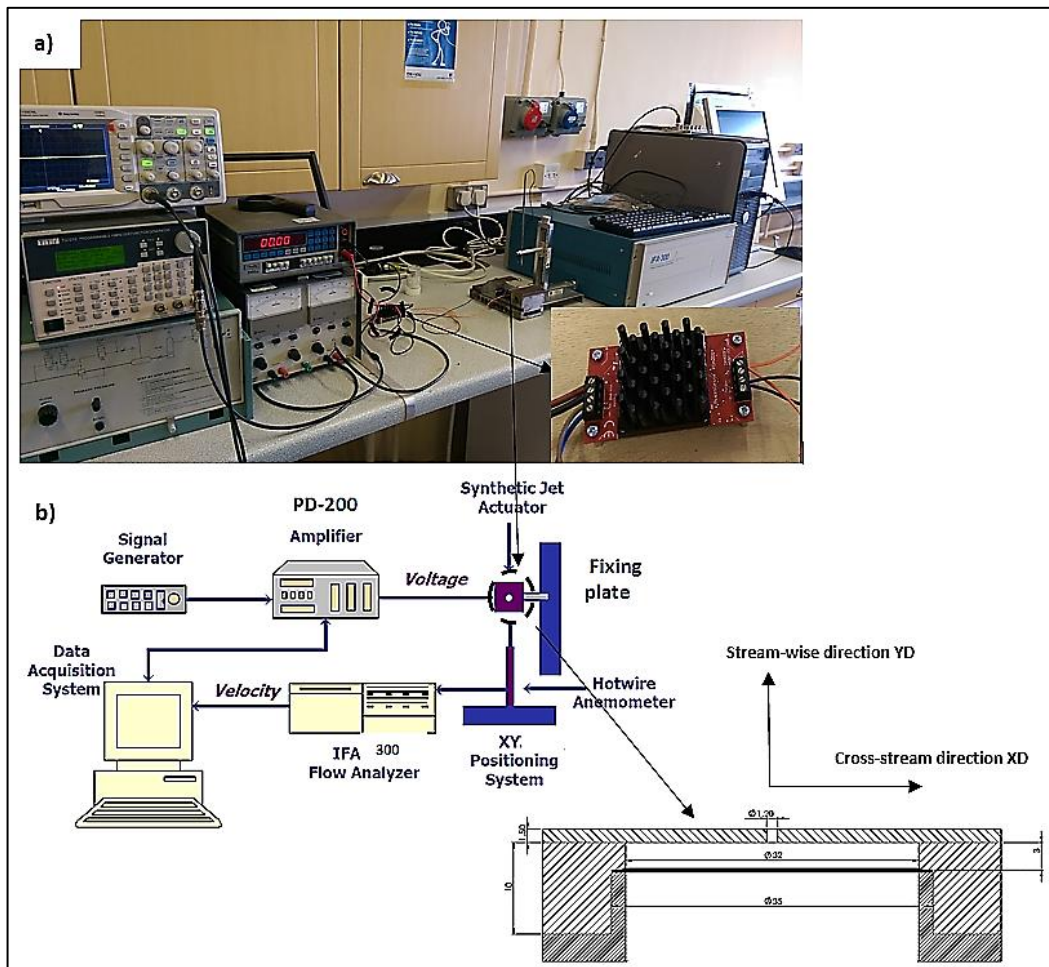
Figure 5.5: a) Time average velocity measurement set-up; b) Instruments layout and measurement regions.

Prior to the experiments, the anemometer was calibrated over the range of expected jet velocities using the 55D90 (DISA) calibration equipment. This device consists of two distinct parts: a 55D45 nozzle unit and 55D44 pressure control unit. Four nozzle areas are available with this facility which allows a maximum velocity of 15 m/s to be obtained without demanding excessive air flows. The exit areas of the nozzle are 6, 12, 24, and 60 mm^2. The 60 mm^2 area nozzle was used in this study. In all the tests, the probe was placed approximately one diameter away from the exit of the 60 mm^2 nozzle in the middle of the jet. The calibration set-up is shown in **Figure 5.6**. The jet velocity was evaluated from the pressure difference across the nozzle using a manometer. The pressure difference was then adjusted to the next value and the data acquisition procedure repeated, until all calibration points had been obtained. In this manner, the calibration data in the form (ΔP, *E)* was achieved.
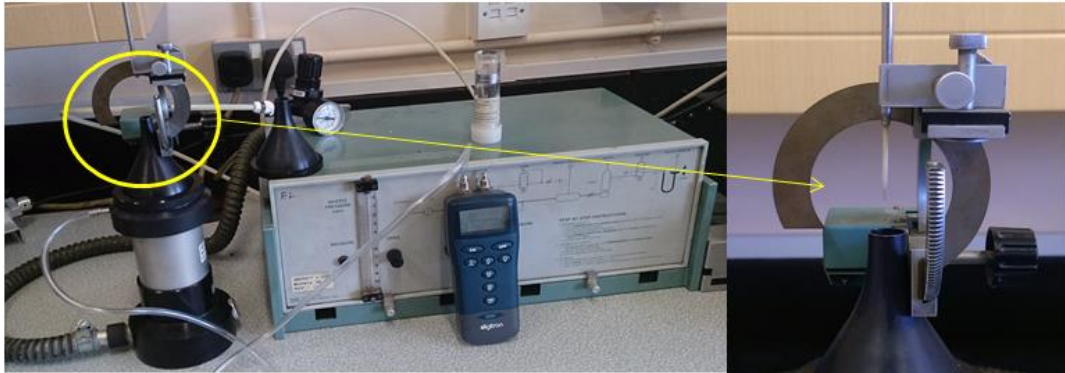
Figure 5.6: Hot-wire anemometer calibration set-up.

The jet centre line velocity at the probe position was evaluated from the pressure difference across the nozzle $\Delta P = Pnozzle, - Patm$. The ambient temperature and jet velocity were recorded along with the anemometer output voltage. The range of air velocities in the calibration dataset spanned from 0 to 15 m/s. A signal conditioner was required to scale and bias the raw voltage output signal to yield maximum resolution over the +/-5V range of the data acquisition hardware. A fourth order polynomial curve was used to translate the conditioned output voltage from the CTA to air velocity. The calibration curve can be seen in **Figure 5.7**, which includes the polynomial equation and coefficient of multiple determination. This approach was selected because it yielded better agreement with the data as well as the repeatability with an error of approximately 1.5%.

$$E = -6E\text{-}06U^4 + 0.0003U^3 - 0.0052U^2 + 0.0615U + 0.92$$
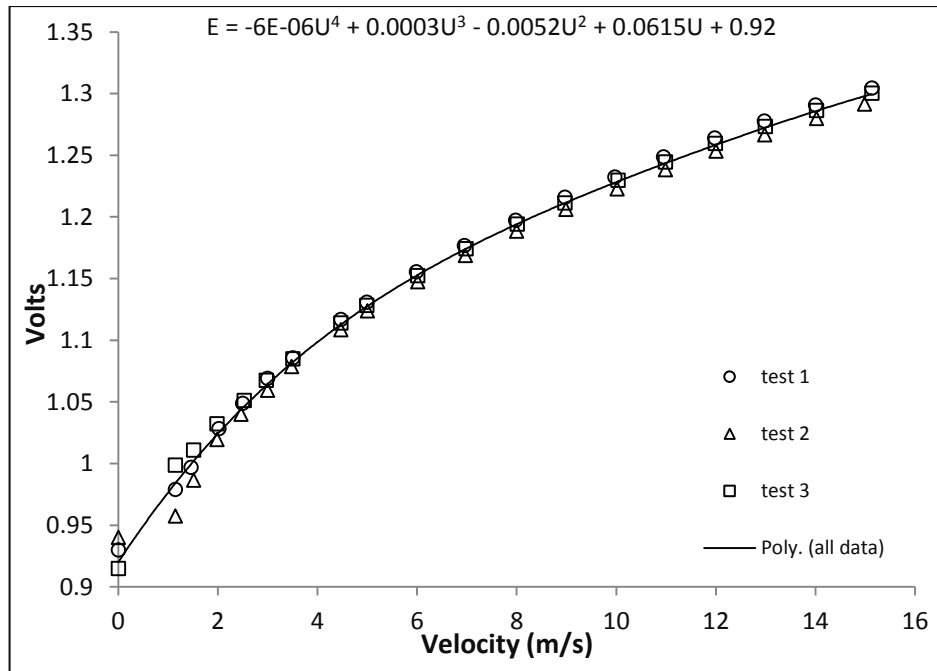
Figure 5.7: A typical hot-wire calibration curve and its repeatability.

It is important to bear in mind that, due to the fact that the HW probe is incapable of differentiating whether the velocity passing over it is positive or negative, such that a single-wire produces a non-directional signal. However, this issue can be easily corrected for a synthetic jet actuator because the position of the probe is in the exit plane of the actuator orifice. For instance, during the first half of the cycle of the jet (blowing phase), the fluid comes out of the actuator via an orifice that is quite narrow and, as a fluid jet, it is characterized by relatively high velocity. In contrast, during the second half of the cycle (suction phase); fluid is drawn into the cavity from the external area of the actuator. The outcome of this is that the cycle halves differ markedly, the velocity produced by the flow as it entered the cavity during the suction cycle being much lower than the peak mean velocity produced when the flow exited the cavity (Smith and Glazer, 1998). The poignancy of the effect intensifies when the probe is moved from the orifice, the suction velocity dropping to zero but the jet-like exit velocity being maintained at a considerable distance downstream of the orifice. Based on this aspect of the flow-field around a synthetic jet actuator, it was easy to identify the parts of an adjusted velocity signal associated with the blowing and suction cycle, respectively. This approach made it possible to overcome the space and accessibility limitations related to this actuator array which hindered the use of a

displacement transducer, allowing the identification of the diaphragm displacement and its alignment not with the driving signal but with the velocity measurements.

5.2.2. Hot-wire Velocity Measurement in Cross-Flow (Wind Tunnel)

5.2.2.1. Validation of Sampling Parameters Using Circular Cylinder Model

In order to examine if the velocity distribution at the contraction exit and test section of the wind tunnel was homogeneous and had the desired turbulence intensity, the wind tunnel performance was tested using a single hot-wire anemometer and pitot static tube. The hot-wire anemometer measurements were conducted by the same means of IFA 300 with a single probe (Dentec Dynamic type 55M11) fixed in the stainless steel probe support of a 4 mm outer diameter (**Figure 5.8 a and b**). The probe was introduced into the flow by the manual three-axis traverse fixed on the test section. This traverse was designed to be mounted on a key clamp frame on the test section outlet flange as indicated in **Figure 5.8b** such that the whole traverse could be moved horizontally, vertically and Z co-ordinates over a stream-wise distance of approximately 1, 0.5, 0.5 m respectively. Therefore, fine movements of 3 mm in the x and y directions could be accomplished by using the manual traverse whereas another 5 mm movement could be made by moving the whole traverse on the flange.
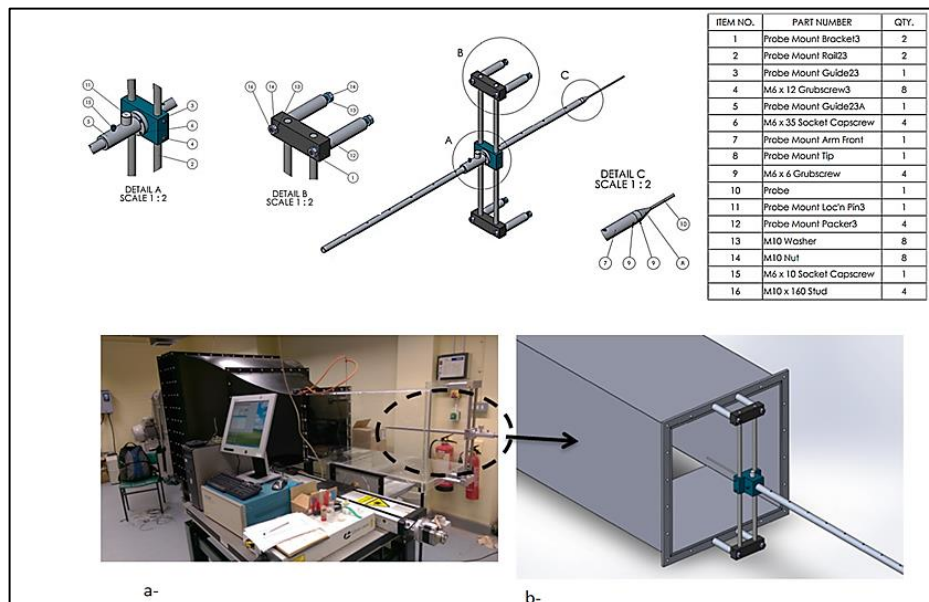
Figure 5.8: a) Wind tunnel with empty test section; b) Hot-wire anemometer probe traversing design.

Prior to the wind tunnel performance measurements, a study of determining the acceptable sampling parameters such as sampling frequencies, sampling periods and software check for data acquisition was conducted using the circular cylinder model. The test on the circular cylinder is shown in **Figure 5.9a and b**. The cylinder was 25 mm in diameter. One end of the shaft had a fixed pad fastened to it using an M6 cap-screw, while the opposite end had an adjustable pad that screwed on using a M10 stud (fixed within the central shaft). This provided a linear adjustment for locating the circular cylinder inside the test section which helps to place it horizontally in the middle between the wind tunnel side walls. The outside faces of the fixed and adjustable pads were a nitrile pad to prevent damage to the test section walls. The resulting data was highlighted in Chapter 3 and therefore not repeated here.
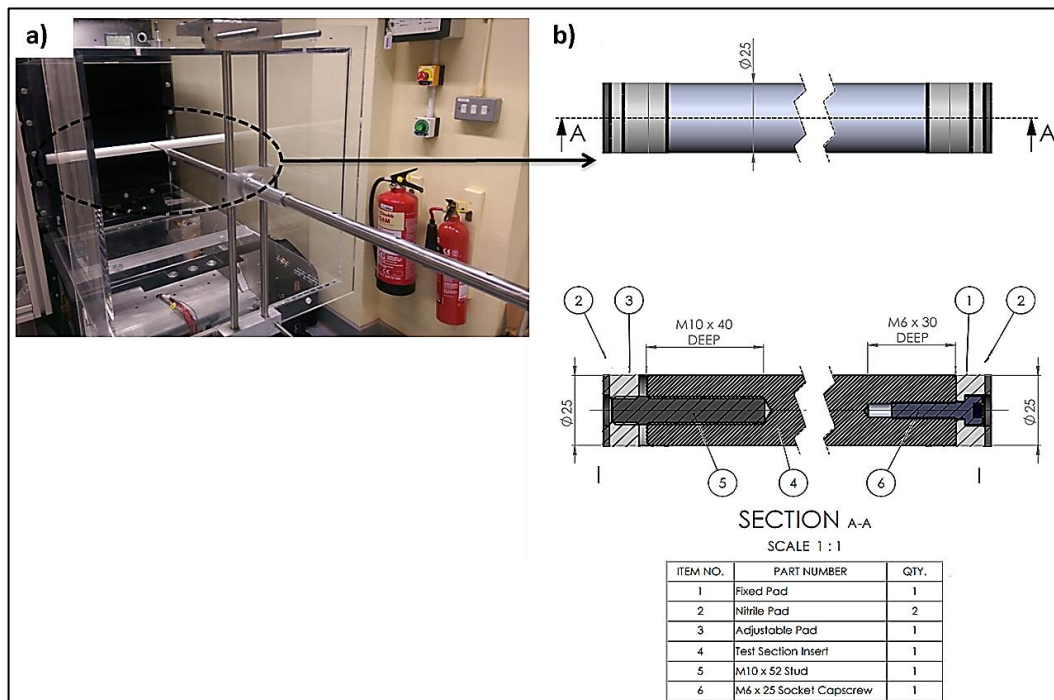
Figure 5.9: a) Hot-wire with circular cylinder installed; b) Schematic view of circular cylinder design.

5.2.2.2. Wind Tunnel Test Section Assessment (without convex hump)

The hot-wire anemometer was used to measure the air velocity fluctuations and turbulence intensity inside an empty test-section. Wind speed measurements were achieved along 15 perpendicular lines located on five planes in the test section (L1–L15), at intervals of 0.25 m (horizontal) and 0.83 m (perpendicular) with one

horizontal plane as shown in **Figure 5.10**. **Table 5.1** summarizes the co-ordinates of the measurements points. These points were then compared with the CFD results to evaluate the flow quality inside the tunnel test section and validate its suitability for aerodynamic research. The experimental and numerical results were analyzed and discussed in Chapter 3 and not repeated here.

Table 5.1: Summary of the measurement point co-ordinates

Plane/Lines	X (mm)	Y (mm)	Z (mm)
Plane 1 / L1	0	0 - ± 250	166
L2	250	0 - ± 250	166
L3	-250	0 - ± 250	166
Plane 2 / L1	0	0 - ± 250	83
L2	250	0 - ± 250	83
L3	-250	0 - ± 250	83
Plane 3 / L1	0	0 - ± 250	0
L2	0	0 - ± 250	0
L3	0	0 - ± 250	0
Plane 4 / L1	0	0 - ± 250	- 83
L2	250	0 - ± 250	- 83
L3	-250	0 - ± 250	- 83
Plane 5 / L1	0	0 - ± 250	- 166
L2	250	0 - ± 250	- 166
L3	-250	0 - ± 250	- 166
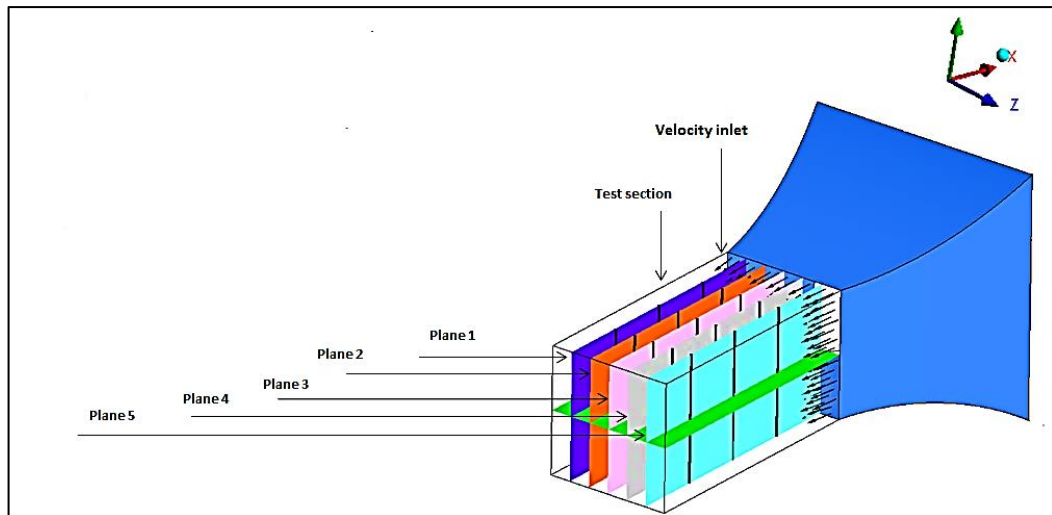
Figure 5.10: Measurement lines co-ordinates and planes.

5.2.2.3. The Power Spectral Density measurement (with convex hump)

The purpose of this section was to obtain the power spectral density (PSD) from the velocity measurements signal. This provides quantitative measurements of the vortex shedding behind the convex hump which is a method of representing the frequency content of velocity signals into the hump wake region.

A similar hot-wire anemometer system was used to measure the velocity profile and the fluctuated velocity in the wake area. The time average velocity fluctuation signals in the wake area were captured using the data acquisition system at a range of downstream locations which varied from *X/L = 1 to Y/h = 0 to Y/h > 3* respectively (see **Figure 5.11**), at different free stream velocity varying from $U_\infty = 7$ m/s to $U_\infty = 10$ m/s. A considerable attention is taken to move the hot-wire probe within 3-5 mm downstream of the convex hump using the three dimensional manual traverse system which has a resolution of 2 mm in x, y and z. After the signal was captured, a Fast Fourier transform (FFT) was performed to convert the data from time domain into spectral data using the MATLAB program in order to obtain the PSD of the velocity in the wake region using 8198 points of FFT. This program is listed at the end of thesis in **Appendix B**. The specific measurements taken are explained fully in the relevant section.
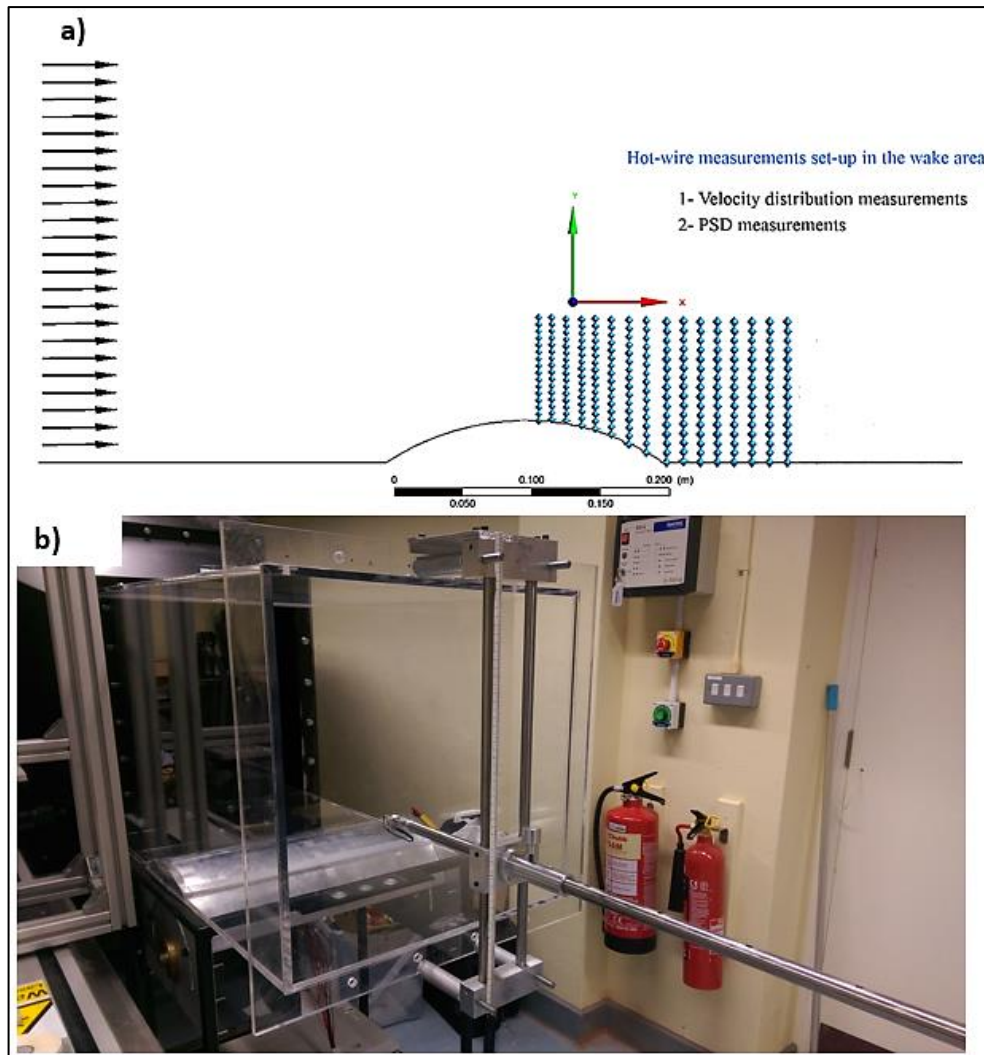
Figure 5.11: a) co-ordinate system in the measurement area; b) Experimental set-up in the wind tunnel (aluminum convex hump shown).

5.3. Flow Visualisation Techniques

The experimental method of flow visualization is designed to facilitate the investigation of flow patterns around and across the surfaces of two Styrofoam hump models. In the present experimental study, two types of flow visualization namely tuft flow visualization and surface flow visualization have been qualitatively conducted over the two convex hump models. These models were described in Chapter 4 (section 4.1) in more detail and so not repeated here.

The first flow visualization has been achieved with the help of what are known as cotton tufts, which are small tufts of yarn affixed to the body. Therefore, the flow field was interpreted based on the orientation and movement of these cotton tufts. For both models, the hump surface was covered with a 0.18 mm black sheet to reduce the

surface roughness and increase the colour contrast and hence improved the image quality. The flow over the hump was captured with a Nikon camera, and the best results were obtained in the 100 mm upstream of the hump models, where the wake and velocity deficit area occur. For the present experiment, the hump surface was attached with thread tufts number 60. Every thread was 35 mm long, of which 25 mm constituted the active length, while 10 mm represented the length used for hump surface attachment. Moreover, small rectangular segments of adhesive tape (10 x 14 mm) were used to secure the threads. Moreover, to make the tufts even more visible and thicker, the threads were soaked in UV dye.

However, to get more validated results for what has been done, important information can be collected from applying surface flow visualization methods. As far as the convex hump models selected, these methods offer valuable information about the location of the separation and recirculation zone. The technique used here utilizes different mixtures of liquids (i.e. kerosene, silicone oil, etc.) and powders (i.e. illumines, titanium dioxide and temper powders) that are painted onto the hump surface in a thin layer for many trial and error attempts. Exposure of the hump to the flow causes the evaporation of either the kerosene or oil, the only particles remaining on the surface being a dried layer of powder, which is made up of streak lines that highlight the average surface flow patterns. The relevant results and discussion of these measurements are presented in Chapter 7 in more detail.

5.4.   Particle Image Velocimetry

The cross section of the flow field across a convex hump in un-actuated as well as actuated cases employing an array of SJAs across the convex hump model is investigated in the present study with the help of Particle Image Velocimetry (PIV). Upon the occurrence of synthetic jet excitation, all changes in the wake region behind the hump can be tracked.

5.4.1. General Overview

A quantitative tool of analysis that can generate flow field-defining velocity vectors is named the PIV measurement technique which enables flow field cross sections to be captured. The procedure consists of two steps, namely, insertion of seeding in the flow field intended for measurement and lighting of a field plane with two laser pulses divided by extremely small time intervals. Upon laser pulsing, a flow field image is

captured by a video camera (CCD) directed at the measurement plane and synchronized with the laser. The two images are captured when the two laser pulses are emitted and are not entirely identical due to the movement of the seeding particles in the intervening interval. The change in position of the seeding particles between the first and second image can be determined by the software based on cross-correlation of the pixels in the images according to the interval between the two images. Provided that the seeding particles present are neutrally buoyancy and in appropriate amounts, such an approach can ascertain the direction in which the flow moves by establishing the direction of seeding particle movement. Furthermore, an average velocity vector plot indicative of the flow field upon capture of the initial image is created by the software in keeping with the velocity of movement of every particle determined on the basis of the interval between frames and the distance of travel. In addition to these instantaneous images, the technique can be used to acquire a series of vector plots for a given flow and then produce an average vector plot for the flow-field. **Figure 5.12** illustrates the formation of these components in a standard PIV set-up which is relatively similar to the set-up used in this research.
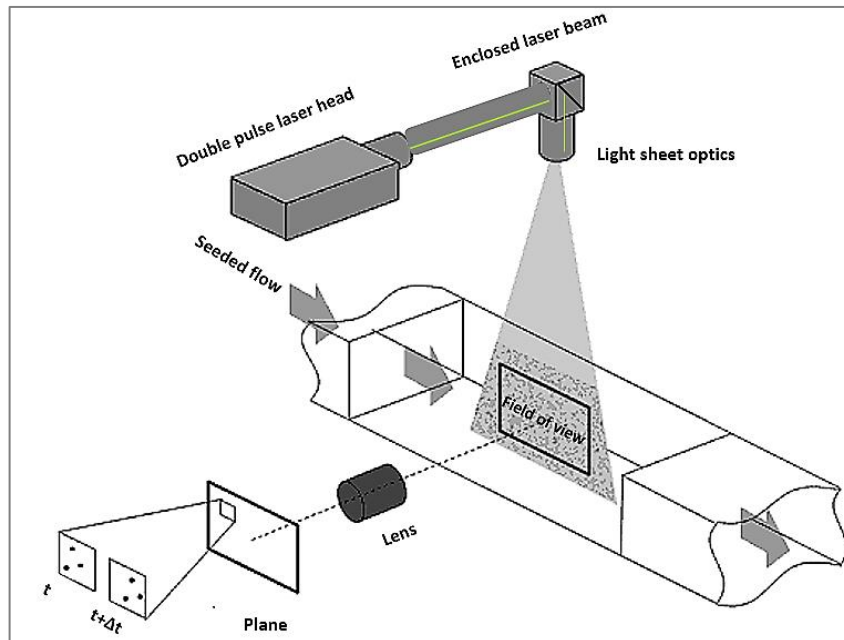

Figure 5.12: Basic PIV set-up showing a PIV component system.

Flow illumination does not occur when image capture starts because the laser is not operating yet. A crystal oscillator with a frequency of 10 Hz regulates and triggers the whole mechanism and, as a result, the capture of an image pair can be

114

achieved every 0.1 seconds (t = 1/f). To ensure that the pulse and the end of the first frame concur, the first pulse is emitted by the laser following a delay established by the unit of pulse separation control. The seeded flow field is lit by this pulse in the area necessary, therefore, a flow image is incorporated in the first frame. The second frame is captured by the camera when it opens its closed shutter after a minor delay. The second pulse is emitted by the laser following an interval known as the pulse separation which, despite exhibiting variation, is usually established by the pulse separation unit. The purpose of this interval is to make sure that the flow illumination occurs once again immediately following the opening of the camera's shutter to capture the second frame. The camera sends the data associated with the second frame to the computer after its shutter has closed. Thus, the two flow field images transferred to the computer are captured at intervals divided by the pulse separation time.

As has already been mentioned, the scheduling of the laser pulses is done in accordance with the so-called method of frame straddle acquisition, which ensures that the pulses concur with the end of the first frame and the start of the second frame, respectively. In addition, to make sure that the flow in each image is lit in a manner that makes the seeding particles visible, the levels of energy of the two pulses should be the same.

5.4.2. Experimental Set-up and Seeding Techniques

The tools and simplified representation of the experimental set-up employed in this study for PIV measurement are illustrated in **Figure 5.13a and b**. The commercially available PIV system (LAVision) was used, which consisted of one Nd:YAG pulse laser head and a LAVision Image (*pro* X 4M) CCD camera with a resolution of 2048 × 2048 pixels which is equipped with a Sigma high standard micro AF 105 mm focal length lens. The maximum power, repetition rate and pulse width of the lasers are 135 mJ and 10 Hz, respectively. The intensity dynamic range and frame rate of the camera are 14-bits and up to 14 fps, respectively.
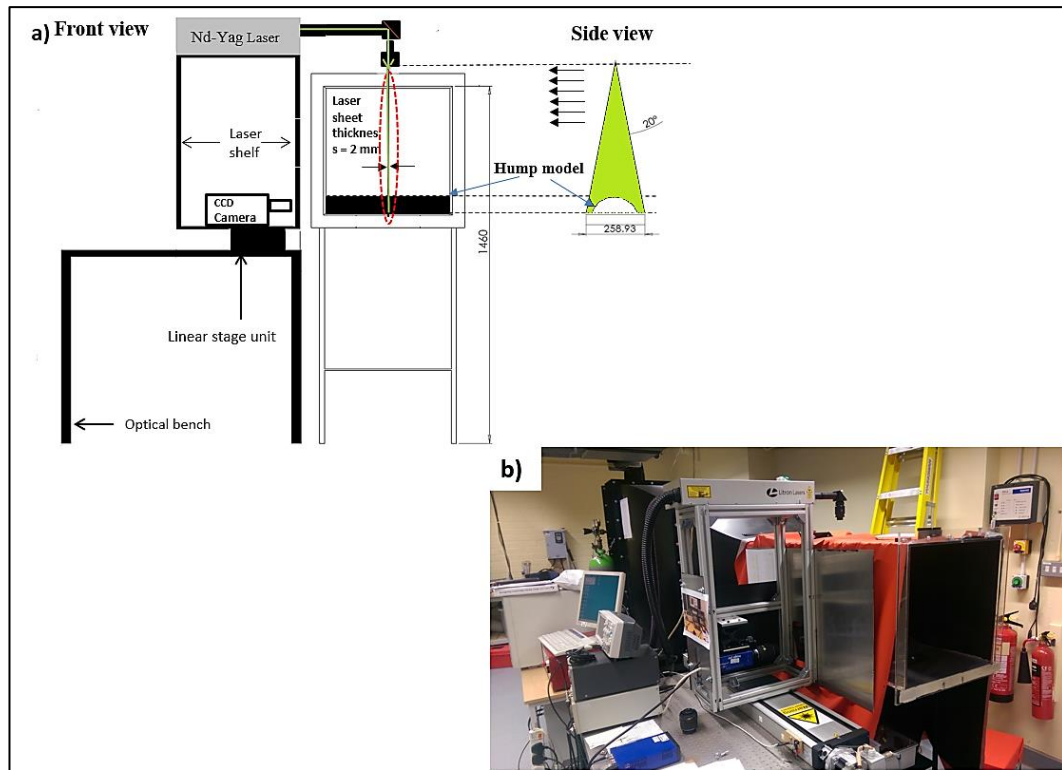
Figure 5.13: PIV experimental set-up showing a) Schematic of PIV set-up; b) Experimental set-up.

Prior to the PIV tests, the convex hump surface is painted matt black to avoid any unnecessary laser light reflection. After establishing the measurement locations and positioning the camera and the laser, the PIV measurements were conducted with the equipment and procedures outlined previously. Di-Ethyl-Hexyl-Sebacat (DEHS) oil is used to produce nearly 1 μm of seeding particle size from a LaVision seeder (Sv-23113) with the help of compressed air. In this research the seeding technique is applied to several configurations, including the seeding of the flow field through elbow, straight, perforated, and slotted pipes as well as close to the wind tunnel fan inlet. These pipes were inserted at the inlet of the wind tunnel contraction part via a ½ inch hole to feed the flow as shown in **Figure 5.14.**

The reason for using several seeding techniques was to accomplish the difficult task of ensuring that the seeding particles were compatible with the flow boundary layer, it was justified to use more than one seeding method, in keeping with the debugging test findings. Furthermore, the seeding had to display neutral buoyancy in the flow medium (i.e. neither too heavy nor too light) and its direction had to be closely similar to that of the flow. Therefore, from these debugging tests, it has been found

116

that the best way to seed the flow is that the wind tunnel test section should be seeded from its own room by seeding the whole room which is explained in Chapter 7 in more detail.
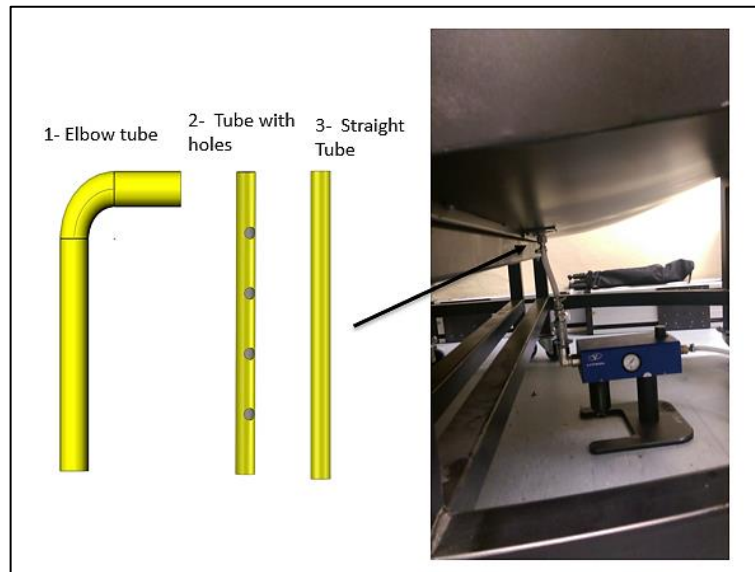

Figure 5.14: Seeding techniques installation.

A laser light sheet was focused at right angles to the hump creating the measurement plane which was necessary to conduct measurements along the stream-wise plane (x-y) normal to the surface of the hump. Such a laser sheet is produced by expanding a vertical laser beam as it passes through the laser sheet optics (cylindrical lens) and is focused at the required area on the convex hump using a laser mirror with a thickness of 6 mm (1-inch diameter, 532 and 1064 nm) placed at the end of the tube on a suitable support (**see Figure 5.13).** The positioning of the camera should be moved with the laser beam in such a way that its optical axis is at right angles to both the wind tunnel side wall and the laser sheet. Moreover, the laser path between the laser head and the sheet optics is enclosed by black tubes screwed to the end of the laser head, in order to prevent the escape of any reflected or scattered light. Additionally, a sticky black fabric sheet was also used to cover any area of the test section irrelevant to the present investigation, to avoid the possible reflected light from the inner wall of the test section.

To ensure the functioning of every element of a controlled time order, both laser and camera were linked to a synchroniser. The laser system element used here was configured with the Flow Master software (*DaVis 7.2*). The time separation between the two laser pulses was chosen in such a way so as to permit adjustment with

up to 1µs precision. The Flow Master software was used for display, storage and processing of the images.

Prior to the test, a 2D velocity calibration was carried out using a known size target as a requirement of the PIV method. The calibration procedure was extended in the following way for this study. The first step involves calculation of the pixel to distance ratio on the basis of the specified view field (in this case, 60 mm $\times$ 60 mm) and the camera resolution (2048 $\times$ 2048 pixels). The next step is the fixation of a grid of known size at right angles to the camera, situated in the plane close to the SJA orifice along its centreline and vicinity to the laser sheet. To attain the determined ratio of pixel to distance (pixel/mm), the position of the camera was reset, focusing it on the grid.

The interrogation region size dictates the time separation dt. Upon capture of the second image, the majority of the particles in the first image should already be included in the interrogation to ensure the reliability of the velocity vectors. According to the general consensus, the maximum displacement of particles possible among the two pulses must not exceed one-fourth of the interrogation region, due to the statistical nature of the process of cross-correlation. Conversion of velocities into pixels per second on the CCD chip to metres per second in the measurement plane is done. It is necessary to have the ratio, among the distance in pixels on the CCD and the physical distance determined in the desired region. The calibration process provides this ratio. The collection of data is straightforward after the organisation of the system, as indicated above. The number of images stored on the computer was restricted by specifying in the acquisition software that only one hundred image pairs have to be collected. The series of one hundred pairs are processed by the software in a batch, generating one vector plot for every pair (i.e. one hundred vector plots in total).

Chapter 6: Development of Synthetic Jet Actuators for the Purpose of Flow Separation Control

Prior to performing any tests with the convex hump model in the wind tunnel, an experimental investigation of the time-averaged velocity and jet strength of the SJA in quiescent flow conditions at different parameter settings was conducted. The deliverables of this chapter were to examine the influence of both geometrical and operational parameters on the flow topology of synthetic jets in fully quiescent flow conditions. As **Crook and Wood (2001)** stated that, *"…one should pay close attention to the geometry of the synthetic jet….failure to do so could lead to incoherent structure being ejected into the surrounding flow or possibly nothing at all,"*.

The objective of the SJA developed here was not only to study the basic fluid mechanics of synthetic jet systems, but rather to evaluate the efficiency of synthetic jets when they needed to be subjected to flow control applications. Therefore, the purpose of this chapter is to provide two distinct types of results; the initial results enabled the selection of optimal and efficient SJA geometrical parameters such as cavity height, orifice diameter and number of orifices to achieve the required strong jet flow. This was achieved by measuring the velocity distribution in both the stream-wise and cross-stream directions above the orifice as a function of the geometrical dimensions with constant excitation parameters. Given that perspective, the preference was to generate maximum jet velocity whilst reducing the form-factor that is feasible for integration into the convex hump model later. Then, results that highlight the importance of the influence of operational parameters, such as the Helmholtz frequency, mechanical frequency and amplitude modulation, on jet peak mean velocity are presented and discussed to estimate what level of blowing could be anticipated. Based on these results, the final geometrical and excitation parameters used for flow control applications such as waveform types, frequencies, and amplitudes were chosen. The details of the experimental set-up and measurement techniques are described previously in the related sections so will not repeated here.

6.1. Synthetic Jet Actuator Test Validation

Based on the clamping effect results given in Chapter 5 (see Figure 4.10), the metal to metal clamping method was selected from the three clamping methods available to be used in all the following experiments. It is important to ensure that both mechanical and electrical failure of the diaphragms are averted and this is achieved by ensuring that the voltage amplitude and frequency of the applied signal are maintained below the diaphragm acceptable maximums. A sine waveform driving signal was used in all experiments. In the case of amplitude modulation, the second sine wave signal is also used. The synthetic jet actuator baseline dimensions were described in **Table 4.2** and therefore will not be repeated here.

Continuous and pulsed jet systems have a different momentum distribution during an excitation cycle compared to a synthetic jet system and it was possible to verify that the zero-net mass flux over a cycle is equal to zero for the appropriate formation of a synthetic jet. This was achieved by experimental investigation to record the velocity time traces close to the orifice exit at various axial points. The jet peak mean velocity, as a function of the radial distance (Y/D), is shown in **Figure 6.1**, which was conducted in the stream-wise position varied from Y/D = 0.5 to Y/D = 6 above the exit of the orifice at an excitation voltage of 35 Vrms. Flow reversal or the suction phase is observed as a second peak which clearly confirms that the hot-wire measurements are not sensitive to the direction of flow. This second peak is caused by the variation in the effective cross sectional area of the synthetic jet actuator during the two halves of the cycle and this is what causes this second peak to have a lower jet velocity compared to the blowing phase. When the hot-wire probe was shifted away in the stream-wise direction to Y/D = 4 and 6 respectively this second peak beside the orifice disappeared completely. This caused a clearly observable difference between the blowing and suction halves of the cycle such that the velocity observed as the flow enters the cavity is significantly smaller than the peak exit velocity during the blowing phase (Smith and Glezer (1998); Watson (2004)). This phenomenon is increased when the probe is moved even further from the orifice with the suction velocity decreasing quickly, however, further downstream of the orifice the only jet-like exit velocity is maintained. This results in the observation that the second peak ceases to exist with increasing axial distance from the centre of the orifice, and ultimately, only a single small peak is observed for each unique oscillation cycle. With this feature of the flow-

field surrounding a synthetic jet actuator, it was relatively easy to determine the corresponding relationship between the parts of the velocity signal which related to the blowing cycle or the suction cycle.
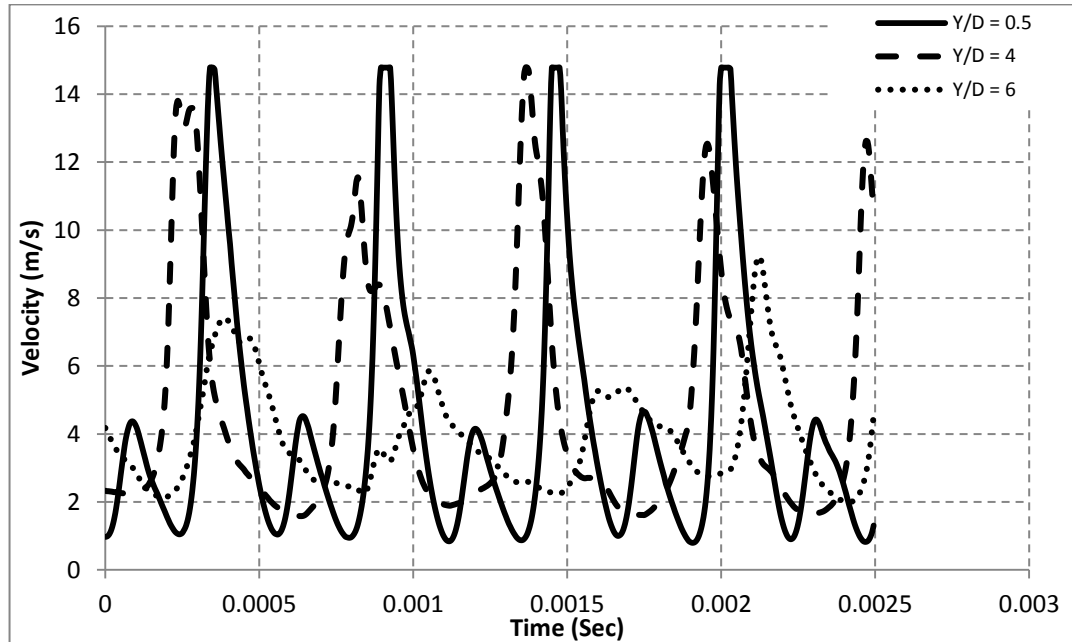

Figure 6.1: Time history of the mean velocity of the jet measured at 0.5, 4, 6D$_o$ above the orifice (Vrms = 35 volt and frequency = 1800 Hz).

Figure 6.2 validates a normal velocity curve configured with two cycles of the sine wave and as expected, there are two jets evident, one large which followed the leading edge of the input signal and the second being smaller which followed the trailing edge. These jets are created during the two cycles, with the larger jet being associated with the blowing cycle and the smaller jet with the ingestion cycle. This feature suggested that the flow re-enters the cavity from the boundaries of the orifice. Consequently, some of the velocity vectors more likely to enter the actuator cavity during the suction phase perpendicular, relative to the hot-wire probe, which possibly caused the second jet. However, only one jet was created during the low excitation frequency cycle which implies that the flow during the ingestion cycle at low frequencies cannot be observed as it is almost parallel with the hot-wire anemometer.
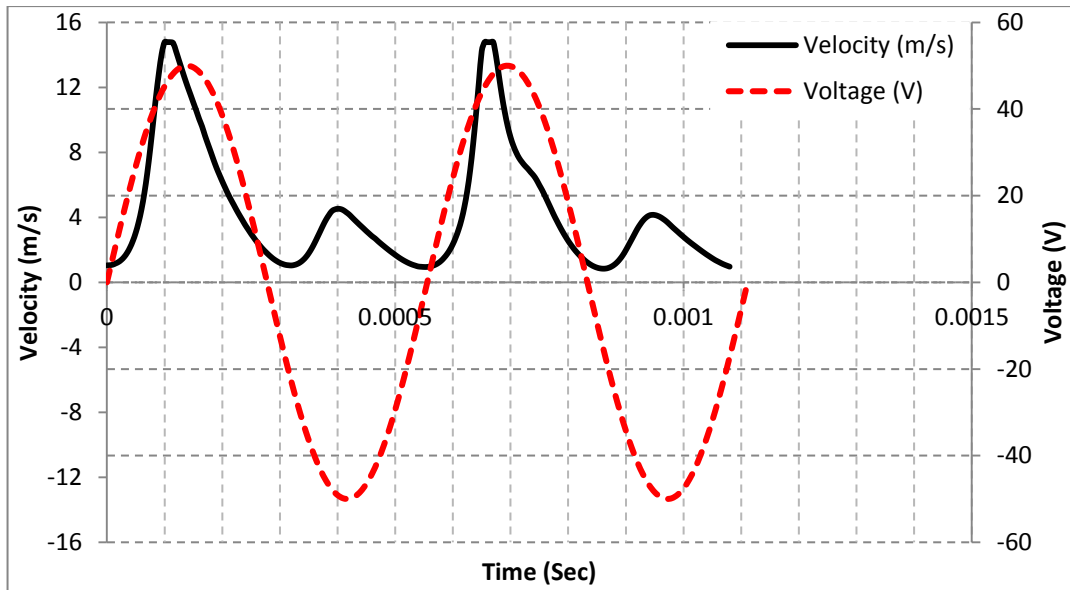
Figure 6.2: Time history of the jet velocity measured at 0.5 D above the orifice (Vrms = 35 volt, Frequency = 1800 Hz).

To examine if the vortex rings and coherent structures are produced at the actuation frequency, the power spectral density (PSD) into two axial directions of Y/D = 0.5 and Y/D = 15 above the orifice are highlighted in **Figure 6.3.** The figure clearly shows that the vortex ring at Y/D = 0.5 had a highly coherent structure compared to Y/D =15 which the later showed a flat PSD with lower energy, suggesting that either the vortex ring lost its coherence when the hot-wire probe moved further in the axial direction or the synthetic jets not reached this point. Moreover, it can be seen from the figure that the first vortex ring generated appeared as distinct peak at the excitation frequency of 1000 Hz, then followed by peaks that are multiples of the excitation frequency "harmonics". However, the oscillating diaphragm had no effect on the flow when the probe moved to Y/D =15 which was responsible for the peaks dissipation.
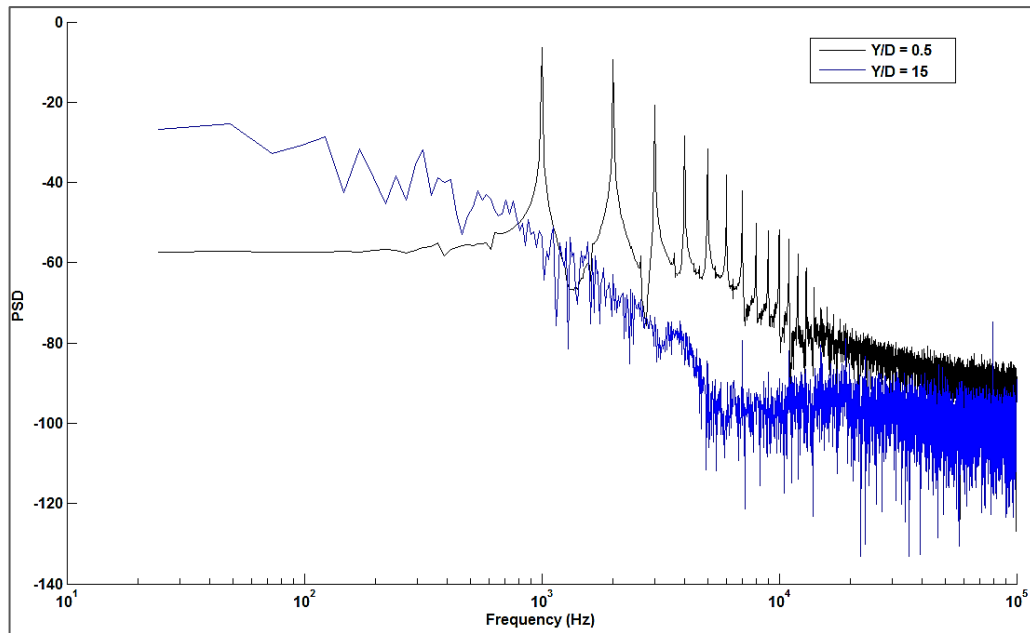
Figure 6.3: Power spectral density at Y/D = 0.5 and Y/D = 15 (f = 1000 Hz, Vrms = 35V).

6.2. Effect of Geometrical Parameters on the Synthetic Jet Actuator

Figure 6.4 shows the peak jet velocity against the excitation voltage. From the figure, it can be seen that at fixed excitation voltage of 35 Vrms as the cavity height was increased from H/D_c = 0.09 to 0.17 to 0.25, the peak jet velocity was decreased from 15 m/s to 13.5 m/s to 9.6 m/s. Moreover, the difference between the first two cavity heights was low and did not significantly affect the jet velocity. However, when the cavity height was increased further by almost 2.7 times (H/D_c = 0.25), the jet velocity was significantly reduced which suggests that at this cavity volume, the diaphragm was unable to push all of the air above it and hence the air sucked back inside the cavity during the suction cycle as a result low momentum can be generated through this cavity.
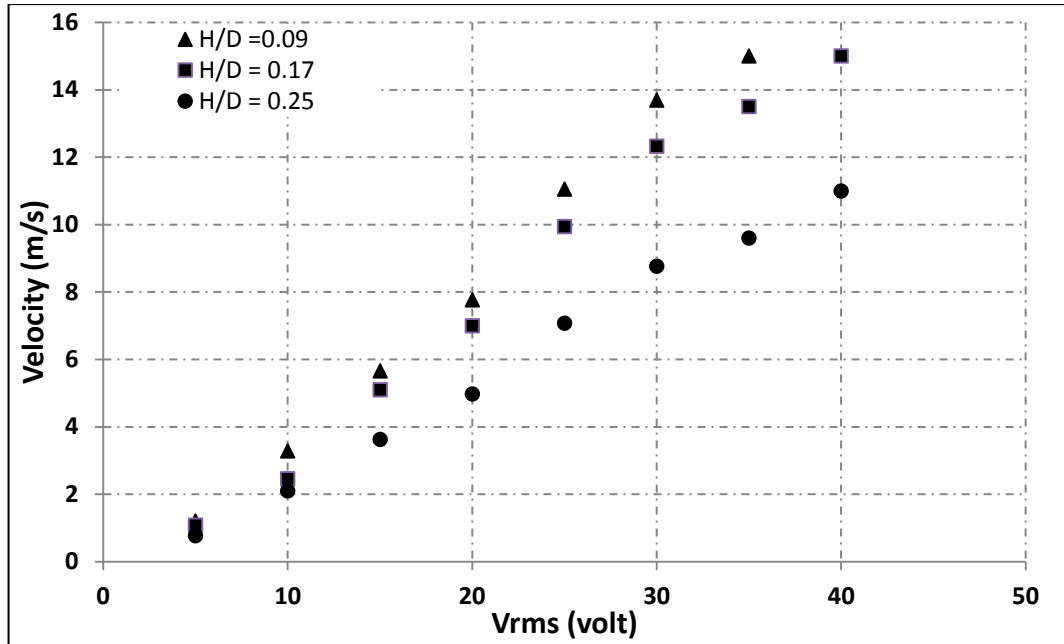
Figure 6.4: Peak mean jet velocity at different excitation voltages; (f_e = 1800 Hz).

Piezo-ceramic diaphragms can be operated at their mechanical frequency; however, such frequency may not be ideal from the point of view SJA performance. It is well known that in a cavity arrangement, an acoustic resonance may play a significant role and therefore, both mechanical and Helmholtz frequencies need to be investigated. The current piezo-ceramic diaphragm has a mechanical frequency of 2200 Hz, which is identified from the PSV test, while the Helmholtz frequency is calculated based on the following relation (Van et al, 2015):

$$f_H = \frac{c}{2\pi}\sqrt{\frac{A}{LV}} \dots \dots \dots \dots \dots \dots \dots \dots \dots \dots \dots \dots \dots \dots \dots \dots \dots \dots .. \dots \dots \dots \dots \dots .. \dots \dots \dots .6.1$$

$$f\ resonance = (Speed\ of\ sound)\ \frac{(Area\ of\ opening\ port)}{[volume\ of\ cavity][length\ of\ opening\ port]}$$

Consequently, the next tests could determine if the Helmholtz frequency was equivalent to or comparatively less than, the mechanical frequency of the diaphragm. For all cases the orifice length and the cavity diameter were maintained at a constant of 1.5 mm and 32 mm respectively. The distance between the diaphragm motion and the jet expulsion represents the cavity height and, in this thesis, the baseline cavity height has risen progressively from H/D_c = 0.09 to 0.17 to 0.25, whilst the orifice diameters were changed from 1.2, 2.5 and 5 mm (L/D_o = 1.25 to 0.6 to 0.3). **Figure**

124

6.5 presents the relationship between the Helmholtz frequency and cavity height (H) for a given orifice diameter.

It can be deduced from the figure that for a particular orifice diameter of SJA as the height of the cavity was increased from $H/D_c = 0.09$ to 0.17 to 0.25 the resonant frequency of the cavity decreased from ~ 965 Hz to ~712 Hz to ~ 610 Hz respectively. At these frequencies, a resonance occurs within the cavity of the SJA due to a simple mass/spring system. However, further increase in the cavity height pushed the Helmholtz acoustic mode far from the piezo-ceramic actuator resonant mode. Furthermore, the figure clearly shows that when the orifice diameter increased, the Helmholtz frequency was also increased. These results suggesting that both cavity height and orifice diameter had an effect on the synthetic jets, which is agreed with **Mane (2005)**. A derived relation has been introduced to characterize the jet velocity related to the cavity height and orifice diameter as follows: $U_j \propto \frac{H}{D_o^2}$. The relation clearly shows that the jet velocity is largely affected by the orifice diameter rather than the cavity height; therefore, the orifice diameter effect has to be considered in any study on cavity volume.
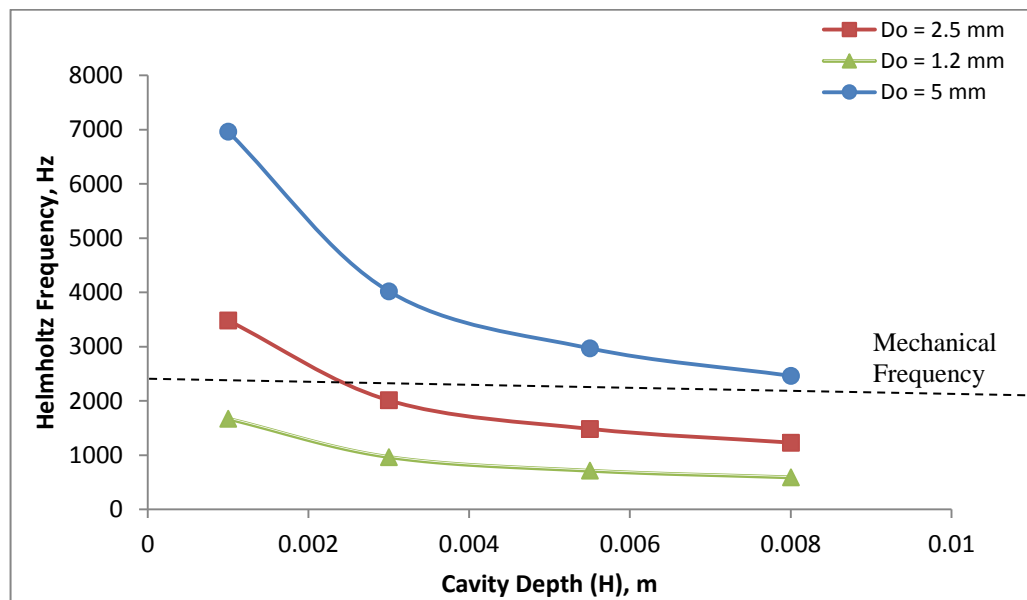

Figure 6.5: Calculated Helmholtz frequency against cavity height for three orifices diameters.

The velocity profiles derived from the three cavities were also compared so that the effects of cavity height variations with similar orifice diameters were presented. **Figure 6.6** shows two interesting data; the first is the velocity profile as a function of the cavity height and secondly the Helmholtz frequency, f_H effects. Velocity profiles for cavity $H/D_c = 0.09$ and 0.17 in the case of a sine wave driving signal were reduced from 14 m/s to 10.3 m/s with the smaller height/volume cavity producing the higher velocity. Similarly, a cavity of $H/D_c = 0.17$ and $H/D_c = 0.25$ was also compared; the velocity was significantly reduced from 10.3 m/s to 2 m/s. Moreover, the figure clearly shows the effect of the Helmholtz frequency, f_H on the jet velocity at specified H/D_c. For example, the jet velocity at $H/D_c = 0.17$ increased when the excitation frequency was reduced from 965 Hz to 712 Hz which was expected to be decreased, but because the latter represented the Helmholtz frequency of this cavity and similarly, at a cavity height ratio of 0.25, the jet velocity was increased when the f_H reduced from 965 to 610 Hz. However, if the cavity height increased further, the Helmholtz frequency would be suppressed due to the viscous effect.
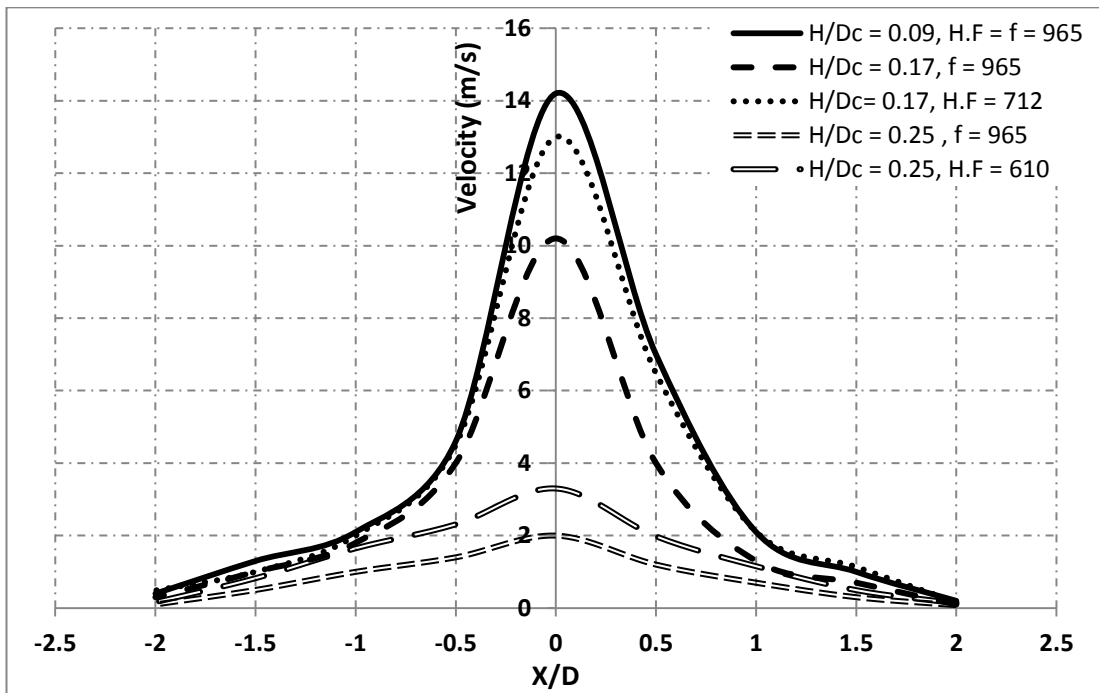

Figure 6.6: Cross-stream jet velocity profile 1 mm above the jet exit plane for synthetic jet actuators with $D_o = 1.2$ mm but different cavity height (Vrms = 35 volt).

For the SJA, the simple relationship between the orifice diameter and jet velocity based on continuity equation does not really hold. This was not the situation for the synthetic jet actuator; it was noticed previously from **Figure 6.4** when the orifice diameter increased the Helmholtz frequency also increased. Moreover, at L/D_o = 0.3 (D_o = 5 mm), the Helmholtz frequency shifted beyond the resonant frequency of the diaphragm of f_H = 5000 Hz; therefore, this diameter was not considered here to avoid damaging the diaphragm at a high excitation frequency. **Figure 6.7** explains in more detail how the increase of the orifice diameter from 1.2 mm (L/D_o = 1.25) to 2.5 mm (L/D_o = 0.6) increased the peak jet velocity. Such behaviour can be explained by considering that the Helmholtz frequency of the cavity is approaching the resonant frequency of the piezo-ceramic diaphragm. This suggested that at lower diameter of orifice, the jet velocity was suppressed by the viscous effect and boundary layer growth.
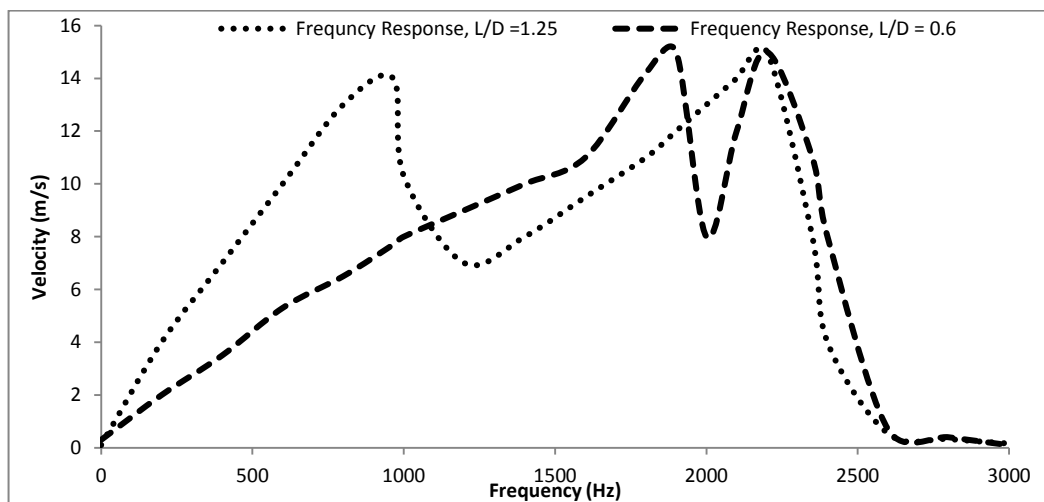

Figure 6.7: Experimental results of frequency response of SJA at (D_o = 1.2 and 5 mm, Vrms = 35 V).

However, Razi (2011) was able to demonstrate numerically that at fixed input energy the synthetic jet strength could be improved by as much as 300% by reducing the orifice diameter whilst at the same time increasing the number of orifices. In the case of synthetic jet applications whereby high circulation is required, with little input energy, this behaviour is quite advantageous. The vortex ring circulation is a significant parameter which measures the vortex ring strength, thus identifying how much momentum can be added to flow as such an increase in the circulation of the vortex ring leads to an increase in the required momentum to achieve such an

application. Therefore, the use of multiple-orifice actuators could facilitate the possibility of using this type of actuator geometry for applications that require a significant introduction of systematic circulation into the flow, such as shear layer control. Furthermore, Watson et al. (2003) has concluded in their qualitative investigation that in the situation where there are two circular orifice actuators, then the complete circulation within a given quantity of fluid exiting a cavity depends on the whole internal area of the orifices that the fluid passes through. The conclusion to be drawn from this is that two modestly sized, orifices next to each other with a given total exit area can provide more circulation for a particular mass of fluid leaving through them than would be generated by a larger orifice of similar exit area. The question now is whether increasing the number of orifices of a particular actuator can improve the actuator efficiency or not?

In this regard, an experimental study of hot-wire tests was performed on single, double and multiple orifice synthetic jet actuators in order to investigate the advantages of multiple orifice actuators over one orifice actuator to achieve higher circulation. It is vital that the vortex rings be formed and developed individually without interacting with each other to avoid any circulation cancellation. Therefore, two dominant parameters featured in the present study, namely the orifice diameter and the spacing between the orifices to explore their effect on the vortex rings produced in one, two and three orifice actuators. The optimum orifice space was experimentally investigated, as shown in **Figure 6.8** to compare between two orifices spaced, at 5 mm and 10 mm respectively.
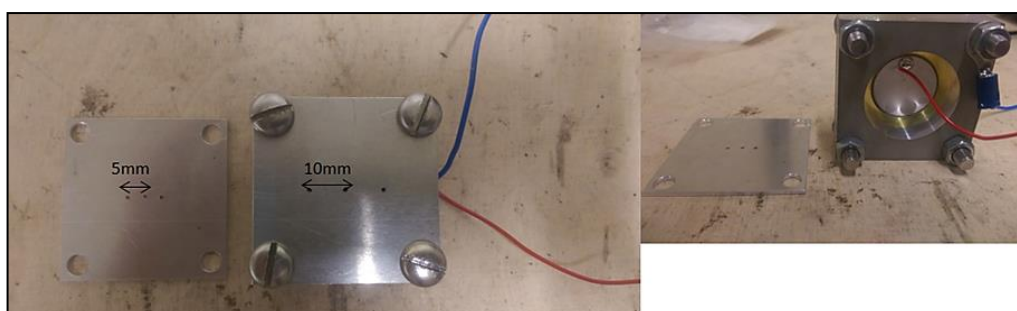

Figure 6.8: Experimental set-up of the most efficient orifice spacing study.

Figure 6.9a and b reflect an investigation into orifice spacing and show that the minimum spacing between the two orifices has to be no less than 10 mm which

enables the process for the vortex rings in jet1 and jet2 to form individually and to move away on a straight line without interacting. This suggested that the orifice is sufficiently spaced such that each vortex ring is formed and developed in a separate coherent manner downstream. As a result of this space the complete circulation generated will be kept constant without any loss reduction or cancelation. Moreover, in the 5 mm spaced orifice (see **Figure 6.9b)**, a lower velocity profile was seen in the two jets compared to the jets produced in 10 mm orifice spacing, suggesting that high mixing and interaction between the two jets was generated by the 5 mm spaced orifice and hence a reduction in the velocity peak can be seen. This reduction in the peak mean velocity can be caused by the interaction between the edges of the vortex rings nearest to each other, which led to forcing the flow to dissipate the energy and reduce the flow preparation. Therefore, for the purpose of this study, 10 mm was used as the minimum spacing so as to reduce the loss or cancellation of the vortex rings.
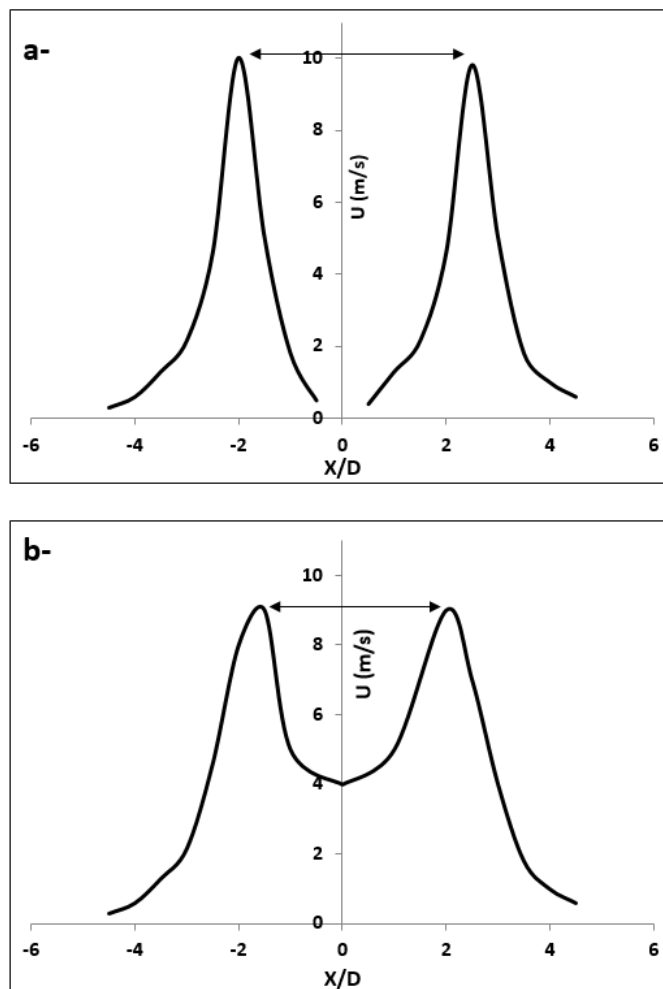

Figure 6.9: Radial velocity profile in the cross-stream direction (X/D) at location of Y/D = 3 for orifice spaced a) 10 mm and b) 5 mm (f = 1000 Hz, V = 35 Vrms).

Additionally, the effect of the number of orifices on the vortex rings circulation was studied experimentally with the appropriate spacing between orifices of 10 mm, all within the same operational parameters. The governing equation for each vortex ring as a function of the jet average velocity during the blowing phase was used based on the following relation (Jabbal et al, 2006):

$$\Omega = \frac{\pi^2}{128} f \Delta^2 \left(\frac{D_c}{D_o}\right)^4 \dots\dots\dots\dots\dots\dots\dots\dots\dots\dots\dots\dots\dots\dots\dots\dots\dots\dots.6.2$$

The equation above was used to calculate the amount of synthetic jet circulation from each orifice, therefore, in order to determine the total amount of vortex ring circulation, the number of orifices need to be multiplied as follows:

$\Omega_{Total} = n \times \Omega_{each\ orifice}$; where n is the number of orifices.

It can be seen in **Figure 6.10** that the total circulation increases by increasing the number of orifices from one to three. This raises the total circulation by 200 % or from 0.043 m²/s to 0.131 m²/s, which is a noteworthy outcome for multiple orifice actuators. The figure clearly shows the advantages of using a larger number of orifices per actuator such that increasing the number of orifices can result in an improvement in the overall circulation generation. The conclusion drawn from this test is that having three orifices with same total area of larger single orifice increases the total vortex ring circulation and as a result a larger amount of fluid and momentum can be transferred to the cross flow. This result is encouraging and raises the question whether an additional circulation enhancement can be achieved by increasing the number of orifices further.
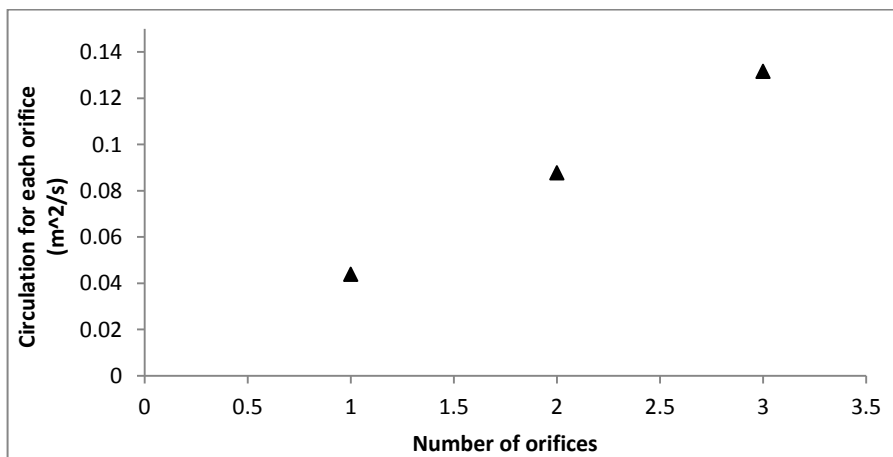

Figure 6.10: Total circulation variation with the number of orifices.

Once the number of orifices and the space between them was confirmed, the question now whether the Helmholtz frequency was altered due to an increase in the number of orifices too. A frequency response of one, two and three orifices was also presented in **Figure 6.11**. It can be noticed from the figure that as the number of orifices per cavity increased, the f_H moved towards the mechanical frequency of the diaphragm. It is worth noting that although increasing the number of orifices slightly reduces the jet velocity at each orifice, this is still within the required jet velocity for flow control application. The highest resonance peak corresponds to the exciting frequency about 2.2 kHz (output velocity 15 m/s) and the second resonance maximum about 0.7 kHz (output velocity 13 m/s). The highest peak corresponds to the resonance frequency of the piezo-ceramic diaphragm and the second to the resonance frequency of the cavity. As the number of orifices was increased further from two to three, the f_H was pushed further towards the mechanical frequency of the diaphragm and increased from 0.83 to 1 kHz respectively. This is because increasing the number of orifices not only increased the total circulation but also pushed the Helmholtz resonant frequency towards the mechanical frequency of the diaphragm.
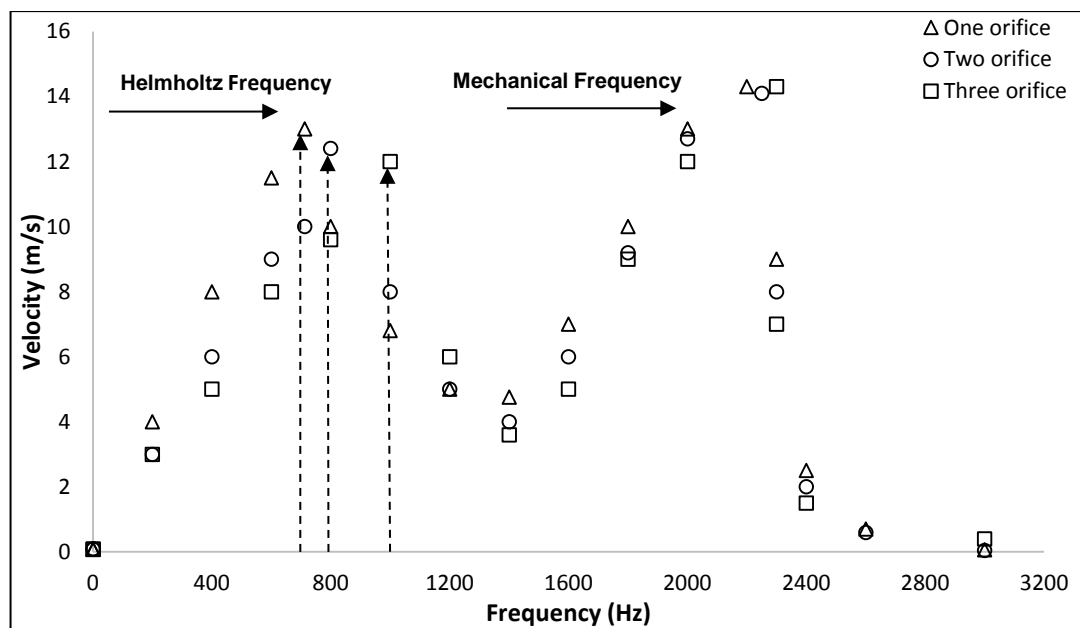

Figure 6.11: Experimental data of the frequency response of the synthetic jet actuator at different numbers of orifices (Vrms = 35 volt).

6.3. The Choice of SJA Geometrical Parameters

As part of this particular investigation it was required to choose which SJA geometry should be utilized for flow separation control over a convex hump model. The overall conclusion that can be drawn from the results presented is that the optimal and efficient synthetic jets can be designed to achieve the required circulation and momentum for a specific application using multiple orifice actuators with a minimum input energy. Therefore, the above results have significant implications and suggest that for higher circulation purposes, using a three-orifice actuator with a smaller diameter increased the circulation produced by 200 % over a single orifice actuator with a larger orifice diameter. As such, three orifices of 1.2 mm orifice diameter (total area = 3.4 mm^2) were used instead of a 2 mm single orifice diameter having the same area of 3.4 mm^2. The length of the orifice and the cavity diameter were set to 1.5 mm and 32 mm respectively. Moreover, it was noticed that the cavity height, in terms of the diameter of the cavity of (H/D$_c$ = 0.17), is needed to ensure the required jet velocity was achieved. These dimensions were also chosen due to their ability to be constructed without damaging the mounting surface and they are still able to produce the required jet velocity at different excitation parameters. The overall SJA geometrical dimension is shown in **Figure 6.12.**
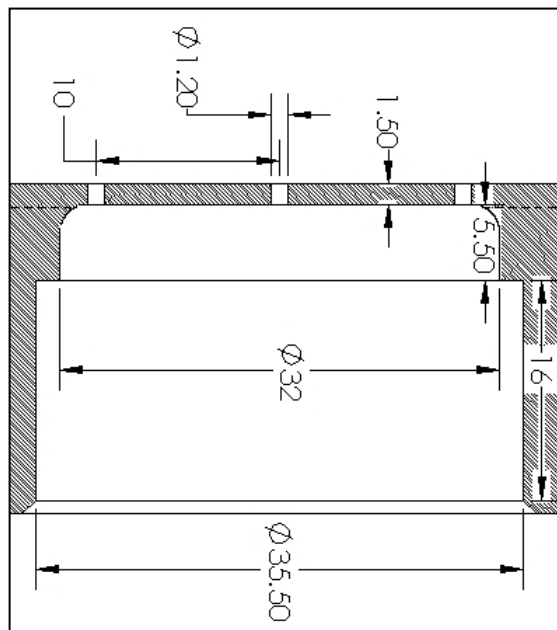

Figure 6.12: Final geometrical layout of the single SJA.

6.4. The Choice of Excitation Parameters

Once the geometrical dimensions were chosen, it was necessary to enhance the possibility of synthetic jet structures interacting with particular unsteady features in the wake flow. It was noticed that the synthetic jet structures possessed an exit velocity which related to the actuation frequency and the voltages of the actuation waveform. As explained previously, the maximum displacement is generated when the piezo-ceramic diaphragm was driven at the resonant frequency of the cavity and/or the mechanical frequency of the diaphragm. These resonant frequencies were 1000 Hz to 2200 Hz respectively for the SJA designed. Higher exit velocities can be produced using 1000 Hz which allows the actuators to run continuously for several hours during data acquisition as bench top tests had demonstrated that the fatigue life of the bonded ceramic on the disks was significantly impaired for frequencies nearer the mechanical resonance frequency. In the situation where the related flow frequency is used to select the frequencies at which the disks were to be oscillated, then the diaphragm movement is so small (Watson, 2004), which resulted in an imperceptible peak exit velocity from the actuator orifice. As such, using Helmholtz actuation frequencies f_H, of 1000 Hz allowed the production of a large jet velocity whilst simultaneously emitting structures into the main flow that would interact with shear flow features and for the single sine wave this was found to be the most useful case. This frequency is also used to avoid damaging the piezo-ceramic diaphragm if it excites at its mechanical frequency.

The excitation frequency of diaphragm is related to acoustic resonance or Helmholtz frequency but not to any frequency presented in the flow, therefore, a question arises if the flow related frequency could be superimposed on the carrier Helmholtz frequency in order to affect the flow to a greater extent. Hence, the idea of signal modulation is considered in this work. In order to operate the synthetic jet actuator using amplitude modulation excitation, a second actuation frequency needed to be implemented other than just the resonant frequency of the cavity. The resonant frequency of the cavity represents the natural carrier frequency of the amplitude modulation excitation ($f_H = f_c$) for the synthetic jet actuators, whereas the low modulated frequency f_m, represents the natural frequency of the flow vortex shedding f_s, in the wake flow. Studies and literature reviews on the effect of the amplitude modulation methodology on the synthetic jet formation and velocity profile were limited, compared to un-modulated operation research. Therefore, the use of hot-wire

to represent the jet velocity profile was investigated as this would give an indication of the effects of amplitude modulation excitation on a synthetic jet actuator in quiescent flow.

As will be shown later the flow related frequency for 7 m/s is 76.6 Hz and twice of this frequency was chosen to try higher frequency effect. Therefore, a sine wave with relevant frequencies f_m, 75 Hz and 150 Hz, were used to develop the modulated waveform with the carrier waveform being maintained at the resonant frequency of the cavity, $f_H = f_c = 1000$ Hz, and the latter was used to generate the necessary exit velocity. **Figure 6.13** shows an example of the time domain schematic of both singles as well as the modulated waveform.
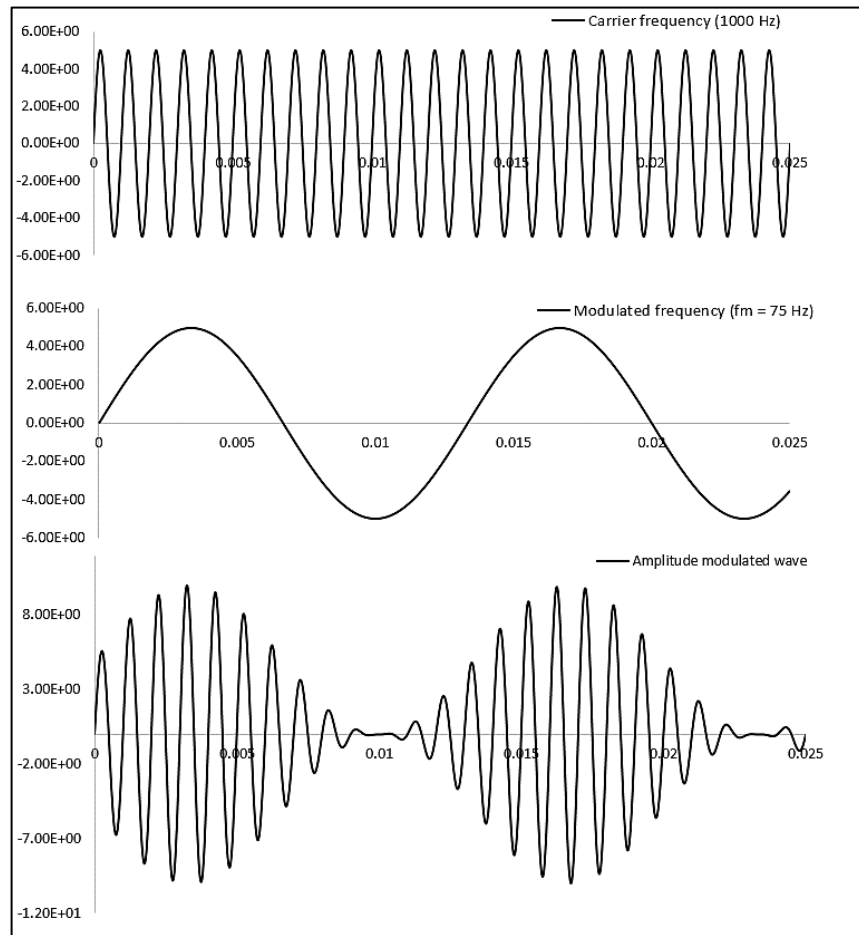

Figure 6.13: The creation of a modulated signal by adding a carrier with a modulated wave.

With the excitation voltage set at 35 Vrms, two modulated frequencies, 75 Hz and 150 Hz have been investigated, as shown in **Figure 6.14**. The figure illustrates a comparison of the power spectral density for both modulated and un-modulated

waveforms. For un-modulated case, first distinct peak of the vortex ring is highlighted at the Helmholtz frequency excitation (f_H = 1000 Hz) (see **Figure 6.14a**). This peak is followed by smaller peaks repeated as "harmonics". When the carrier signal at the Helmholtz frequency is modulated, two additional peaks appear at the modulated frequencies (75 Hz and 150 Hz) as shown in **Figures 6.14b and c**. In contrast to the un-modulated case, sidebands containing additional information are clearly seen in the power spectra of the modulated synthetic jets that occur at frequencies that are a sum and difference of the Helmholtz and modulated frequencies ($f_H - f_m$ and $f_H + f_m$).
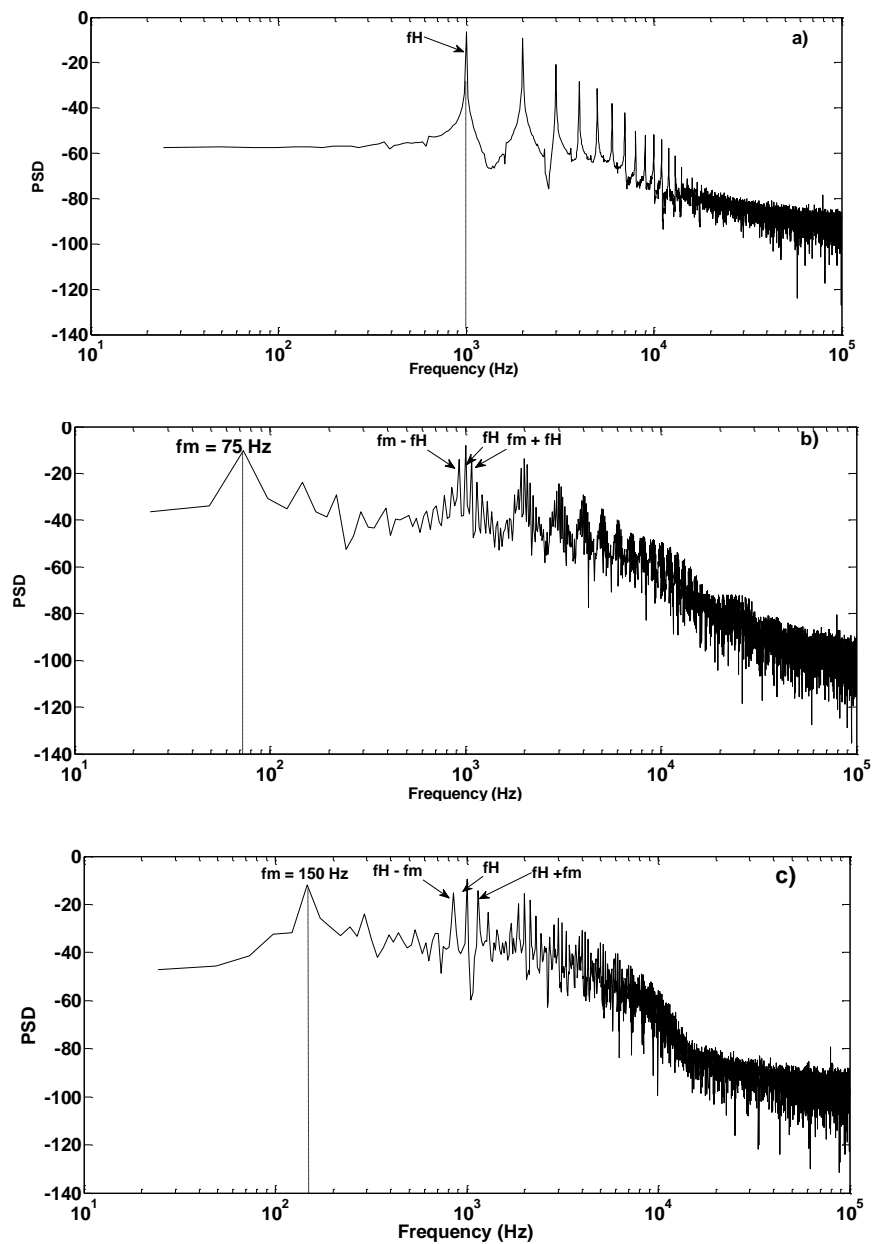

Figure 6.14: Power spectral density at Y/D = 0.5, a) Un-modulated jets ($f_c = f_H = 1000$ Hz), b) Modulated jets ($f_c = f_H = 1000$ Hz, $f_m = 75$ Hz), c) Modulated jets ($f_c = f_H = 1000$ Hz, $f_m = 150$ Hz).

135

The velocity profiles in the stream-wise direction at Vrms = 35 Volts is shown in **Figures 6.15a to c**. For un-modulated case, the maximum peak mean velocity of 12 m/s is clearly seen in **Figure 6.15a** and this peak mean velocity magnitude remained constant over the whole period of signal. In contrast to the amplitude-modulated cases, the peak jet velocity is altered from maximum value to zero in each cycle (see **Figure 6.15b and c**). Moreover, when the amplitude modulation excitation used to drive the SJA, a significant increase in the jet velocity was achieved at both modulated frequencies. This jet velocity increase is more likely to be caused by the amplitude of Helmholtz frequency (carrier signal) which becomes altered by the instantaneous amplitude of the modulated signal (e.g. f_m = 75Hz). This means that with constant excitation voltage and at 100% modulation, the amplitude of the modulated signal adds to the amplitude of the carrier signal to generate the "envelop" of amplitude modulation signal which may responsible for the peak jet velocity increase. Furthermore, at the minimum modulated frequency of 75 Hz, as shown in **Figure 6.15b**, the maximum peak mean velocity for the amplitude modulated jet can be seen as 15 m/s. This peak mean velocity magnitude somewhat reduced to 14.2 m/s as the modulation frequency increases to 150 Hz, suggesting that in case of high frequency modulation, the blowing period is of shorter duration compared to low frequency modulation, and consequently the jet velocity is pulled into the orifice at some point in the suction cycle.
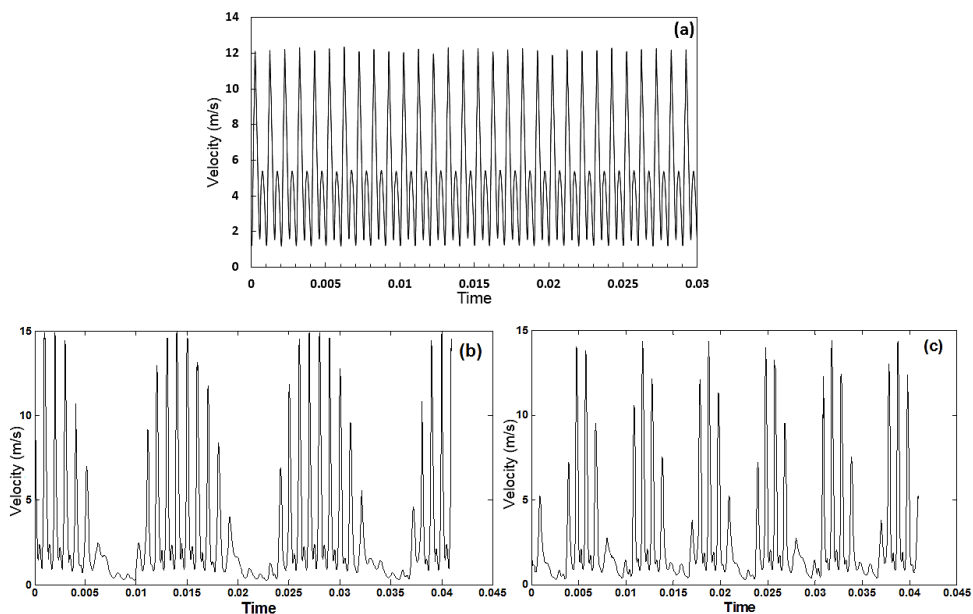

Figure 6.15: Synthetic jet velocity at Vrms = 35 volts for a) Un-modulated synthetic jets, b) Modulated wave (fc = 1000Hz, f_m = 75 Hz), c) Modulated (fc = 1000 Hz, fm = 150 Hz).

Figure 6.16 presents the peak jet velocity for both modulated and un-modulated signals excitation voltage ranged between 4 to 30 Vrms. Generally, the figure clearly shows that when the excitation voltage was increased, both modulated and un-modulated jet velocity also increased. However, the figure supports the results shown in **Figure 6.15** and shows that at the same excitation voltage, e.g. 30 Vrms, the jet velocity was significantly increased from 10.5 m/s for un-modulated jet to a maximum velocity of 13.5 m/s for modulated jet at f_m = 75 Hz, while for modulated jet at f_m = 150 Hz the jet velocity is 12.5 m/s. This test would help to identify the jet to free stream velocity ratio for the purpose of studying the effect of this ratio on the flow control application. For example, at 7 m/s free stream velocity, a maximum ratio of 1.5 can be achieved from both modulated and un-modulated excitation waveforms.
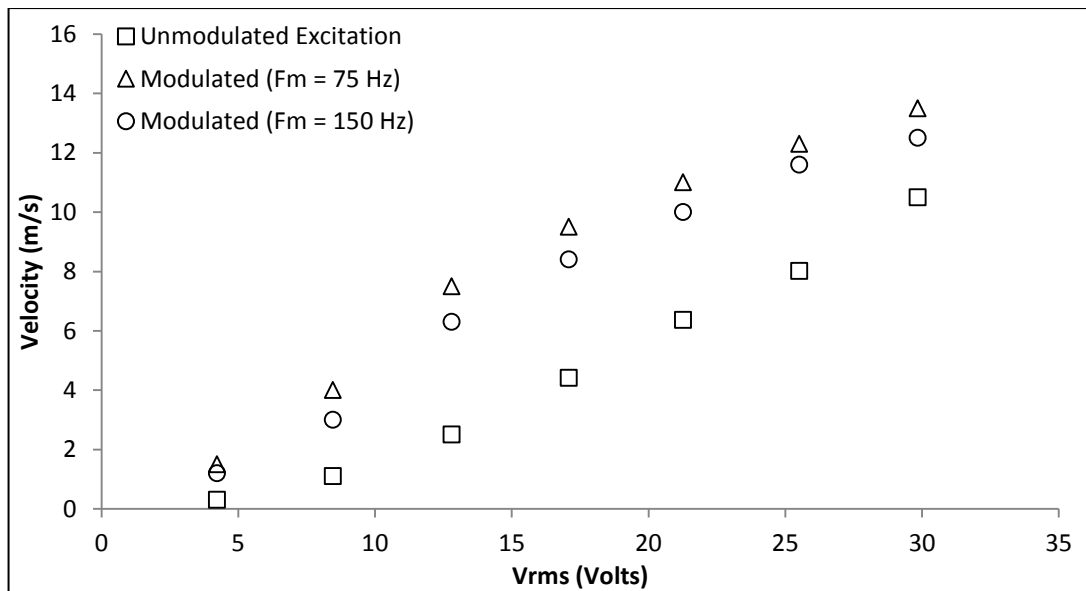

Figure 6.16: Peak jet velocity for both modulated and un-modulated wave at (Y/D = 0.5, f_c = f_H =1000 Hz).

6.5. Conclusions

The geometrical and operational parameter effects on three scales of synthetic jet actuators are presented. Some useful guidelines on the influence of both geometrical and operating parameters on SJA design can be derived from this study. The results showed that the cavity height, orifice diameter, number of orifices and the space between the orifices all have an effect on the jet strength and jet velocity. Moreover, it can be deduced from the results that the circulation can be increased by 200 % when

the number of orifices is increased from one to three. Additionally, the results showed that it is desirable to operate the SJA using Helmholtz frequency of the cavity instead of the diaphragm resonant frequency to avoid damaging the diaphragm material. It has been seen that by utilizing the Helmholtz resonance of the cavity and amplitude modulation excitation waveforms, the actuator can exhibit significant blowing velocity with a diminished power input, thus demonstrating that these excitation parameters have a useful function in practical engineering.

The effect of both excitation and geometrical parameters on the jet velocity was considered fully in quiescent flow conditions such that the final overall SJA geometrical dimensions and operating parameters were chosen for the purpose of flow control application. Finally, the effects of the SJA which has been designed through this chapter as well as the waveform type, jet-velocity ratio (*Vr*), and the angular position of the actuation (β) on the flow structure has been conducted in a later chapter. This investigation has evaluated the effectiveness of using an array of synthetic jet actuators (SJAs) developed here in changing the recirculation bubble size and power spectral density (PSD) in the wake flow behind a convex hump model using both HWA and PIV techniques. This is a necessary test to calculate whether this SJA could produce the correct level of control authority, which could have a significant effect on such boundary layer flows.

Chapter 7: The Un-actuated Convex Hump Models

In order to establish a single model that would be used in all flow control tests, numerical and experimental investigations were carried out over two convex hump models. The main objective of this chapter is to examine the flow behind these convex hump models using different qualitative and quantitative measurements, discuss the results obtained and comparison of the experimental results to the CFD simulation was also conducted.

Initially, CFD simulation was used to simulate the air flow over two models (as explained in Chapter 3 and repeated in **Figure 7.1a**) to examine the onset location of separation and re-circulation. Then, these results were compared to different flow visualization images over two Styrofoam models (**see Figure 7.1b**). This allowed the development and changes in the separation location to be tracked and hence, the final aluminium model that would be used in the flow control study was selected. Moreover, the power spectral density of the final selected model was examined at different freestream velocity using a hot-wire anemometer (HWA). These PSD plots were not only used to establish the baseline case, but also to provide significant information which could be used in detecting the separation incipient and identifying the characteristics of the excitation parameters of synthetic jet actuators. Finally, the recirculation area and reattachment point behind the convex hump model was examined using the PIV technique. The geometrical dimensions of the two hump models are shown again in **Figure 7.1a and Table 7.1.** Finally, based on the results obtained here, the aerodynamic performance under the influence of an array of synthetic jet actuators can be studied.
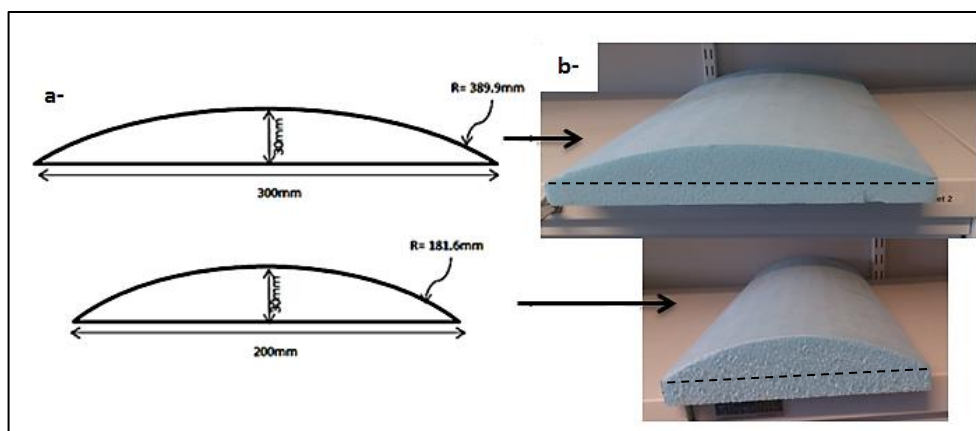

Figure 7.1: a- Convex hump models and their dimensions, b- Styrofoam hump models.

Table 7.1: Dimensions of hump models

Apex, t(mm)	L (mm)	R (mm)	Aspect ratio H/L
30	200	181.6	0.15
30	300	389.96	0.1

7.1. Numerical Simulation Investigation and Governing Equations

The Fluent-ANSYS software is often used in the design and analysis method. The ANSYS finite elements analysis software enables a computer model or transferring CAD/Soil works models of the structures, products, components, or systems. In the present work, a methodology for developing separation location and reattachment flow over convex hump models was examined. The methods for calculating the velocity contour were also defined. For the purpose of validation, experimental tests of different flow visualisation and PIV measurements were conducted to validate the CFD results. The details of the viscous model flow are calculated by using averaging of the Navier-Stokes equations. The numerical model is two-dimensional, and the flow is assumed to be laminar air flow based on Reynolds number ($Re_H = \frac{\rho\, U_\infty\, H}{\mu}$) of 1400, where H is the convex hump height (H = 30 mm) and U_∞ is the free stream velocity ($U_\infty = 7$ m/s).

Based on such assumptions, the governing equations for conservation of mass, momentum equations in X and Y dimensions, the momentum and the mass conservation governing equations are:

$$\frac{\partial u}{\partial x} + \frac{\partial v}{\partial y} = 0 \quad \ldots\ldots\ldots\ldots\ldots\ldots\ldots\ldots\ldots\ldots\ldots\ldots\ldots\ldots. (7.1)$$

$$X - momentum: U\frac{\partial U}{\partial X} + V\frac{\partial U}{\partial Y} = -\frac{\partial P}{\partial X} + \frac{1}{Re}\left(\frac{\partial^2 U}{\partial X^2} + \frac{\partial^2 V}{\partial Y^2}\right) \ldots\ldots\ldots (7.2)$$

$$Y - momentum: U\frac{\partial U}{\partial X} + V\frac{\partial U}{\partial Y} = -\frac{\partial P}{\partial Y} + \frac{1}{Re}\left(\frac{\partial^2 V}{\partial X^2} + \frac{\partial^2 V}{\partial Y^2}\right) \ldots\ldots\ldots (7.3)$$

7.1.1. Boundary Conditions and Numerical Scheme

Boundary conditions are specified in FLUENT to capture the real conditions of the flow. The initial boundary condition at the inlet is chosen to be the inlet velocity and

the values of velocity and pressure are chosen to be zero and adiabatic everywhere in the computational domain as shown in **Figure 7.2**. The far boundary was selected such that the effect of the boundary is absent in the area of flow near to the convex hump models. There is no-slip boundary condition at the wall of the two convex hump models. A pressure second order solution method in Fluent was selected for all computations using a uniform grid. For steady state, the pressure-velocity coupling was considered using the PISO scheme which can maintain a stable calculation with a larger time step. A second order *upwind spatial discretization* for pressure is assumed which can better simulate the direction of propagation of information in a flow field along the characteristic hump curve. Second order spatial discretization was chosen for marching in time. The freestream velocity applied as the inlet boundary condition is $U_\infty = 7$ m/s.
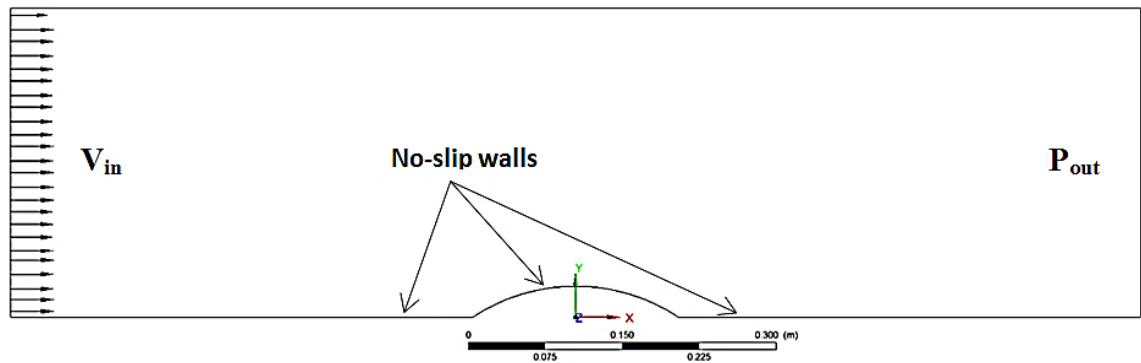

Figure 7.2: Example of boundary conditions set in Fluent (200 mm hump model).

7.1.2. Mesh Structures and Mesh Sensitivity

Steady incompressible flow simulations were performed using a commercial solver, FLUENT 14. The computational geometries used in the simulation is shown in **Figures 7.3a and b** and to ensure adequate spatial resolution of the flow structures, the grids were densified in the area near the hump surface and the region close to the ground floor. A mesh independent solution has been undertaken in which the effects of three meshes (10500, 15750, and 22050 mesh cells) were examined in terms of the variation of shear stress at freestream velocity of 7 m/s. It was found there is only about 1% difference between the medium mesh used in the present study and the fine mesh and all the three meshes are nearly similar in the maximum shear stress. Therefore,

22050 mesh numbers are selected in the present study as a compromise of computational accuracy and time.
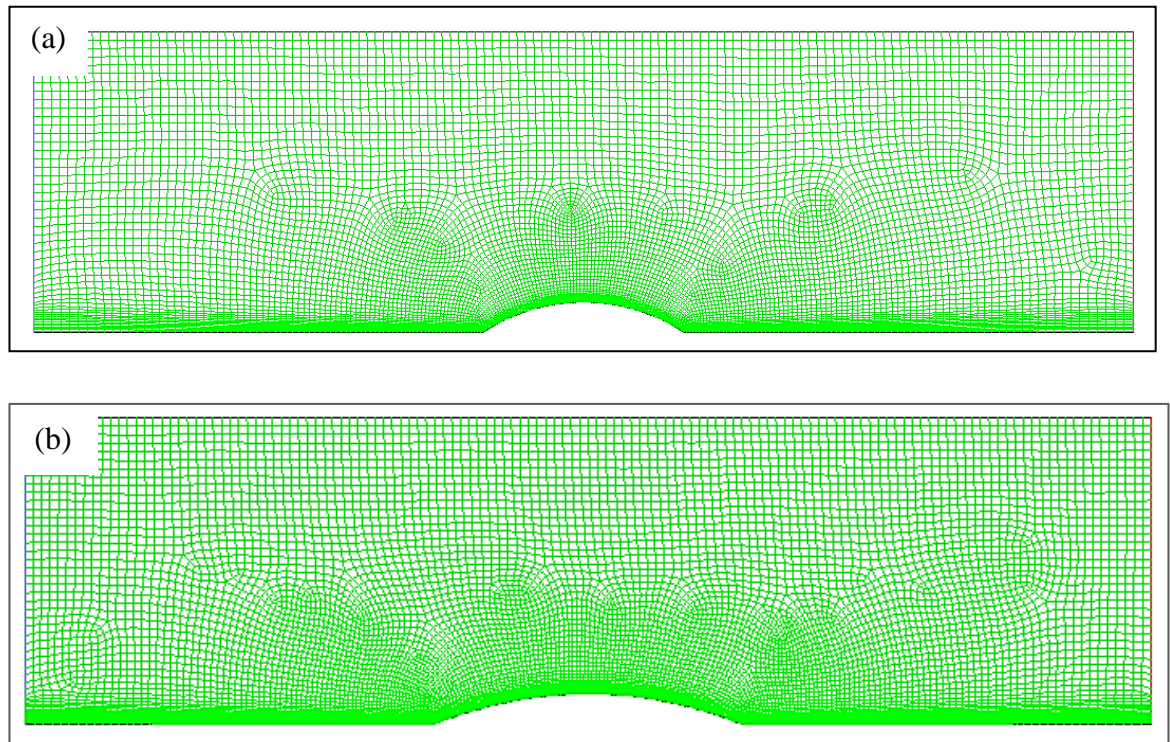

Figure 7.3: Meshing imported to Fluent software; a) L = 200 mm, b) L = 300 mm.

Figures 7.4a and b illustrate the results obtained from the numerical simulation over the 200 mm and 300 mm convex hump models at $U_\infty = 7$ m/s while A.R (*H/L*) was 0.15 and 0.1 respectively. In both cases, the results revealed that the flow had been accelerated on the front surface of the models and had separated into two parts. One part when the flow is unable to overcome the adverse pressure gradient and hence it moved up and achieved separation just behind the hump midpoint, while the other flow part when the flow moved downwards to reattached again in the wake area to generate a recirculation zone. However, despite these similarities, a delay in the separation position had been noticed on the surface of the 300 mm model which had a lower aspect ratio and the same Reynolds number.
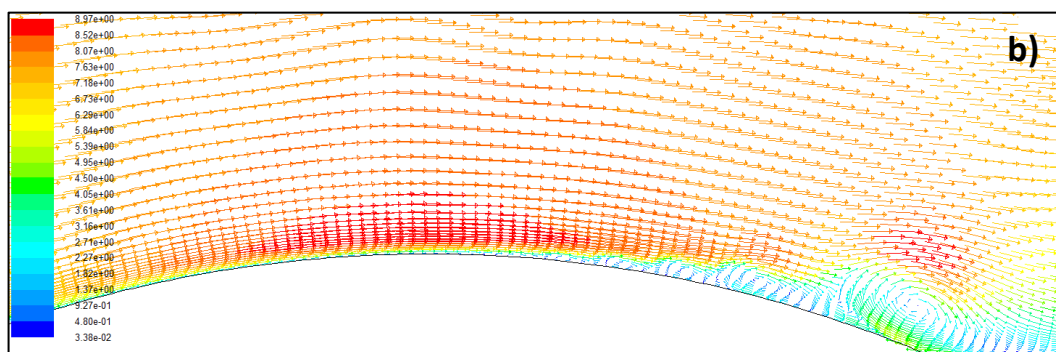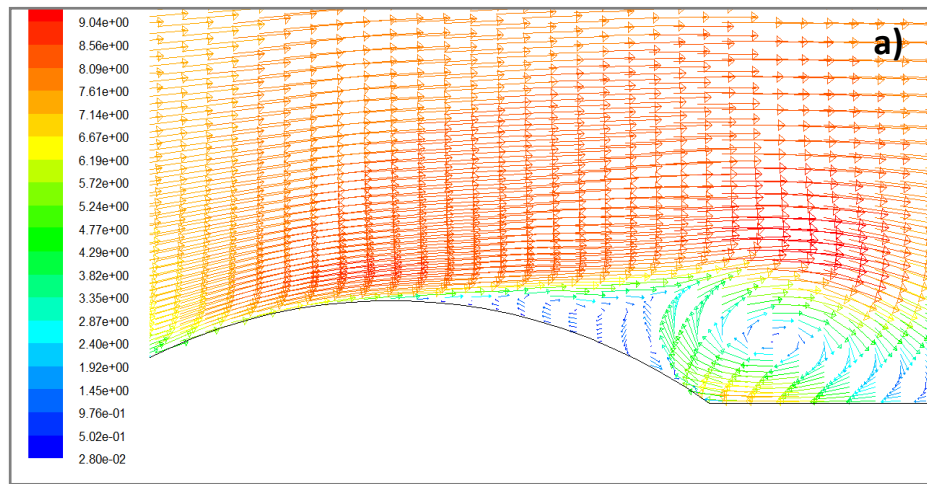
Figure 7.4: Velocity vectors; a) 200 mm hump, b) 300 mm (at $U_\infty = 7$ m/s).

Figures 7.5a and b show the velocity streamline of the two models, the figures clearly show that the 300 mm model is exhibited a smaller recirculation area compared to the 200 mm model. This delay in the initiation of separation location can be caused by the decrease in the aspect ratio (*H/L*), suggesting that any further increase in the aspect ratio could delay or push the onset of separation location further downstream. Therefore, the numerical results showed that the flow field over the two convex hump models would take the form of the hump aspect ratio and the freestream velocity value for which the flow appeared to separate in the wake area behind the hump model. For the 200 mm model, the onset of the separation location occurred just behind the centre of the hump model while, for the 300 mm model, the separation has been significantly delayed toward the hump edge in the wake area at the same Reynolds number. If the separation phenomena occurred in this area over the hump model then the effect of synthetic jet actuation can be examined in pre- and post-flow separation by rotating the hump by ±32°. In order to extract more validated results in terms of the separation

143

occurring and re-attachment flow, a comparison between the numerical simulation results and experimental study using flow visualization and PIV techniques over the convex hump has been carried out.
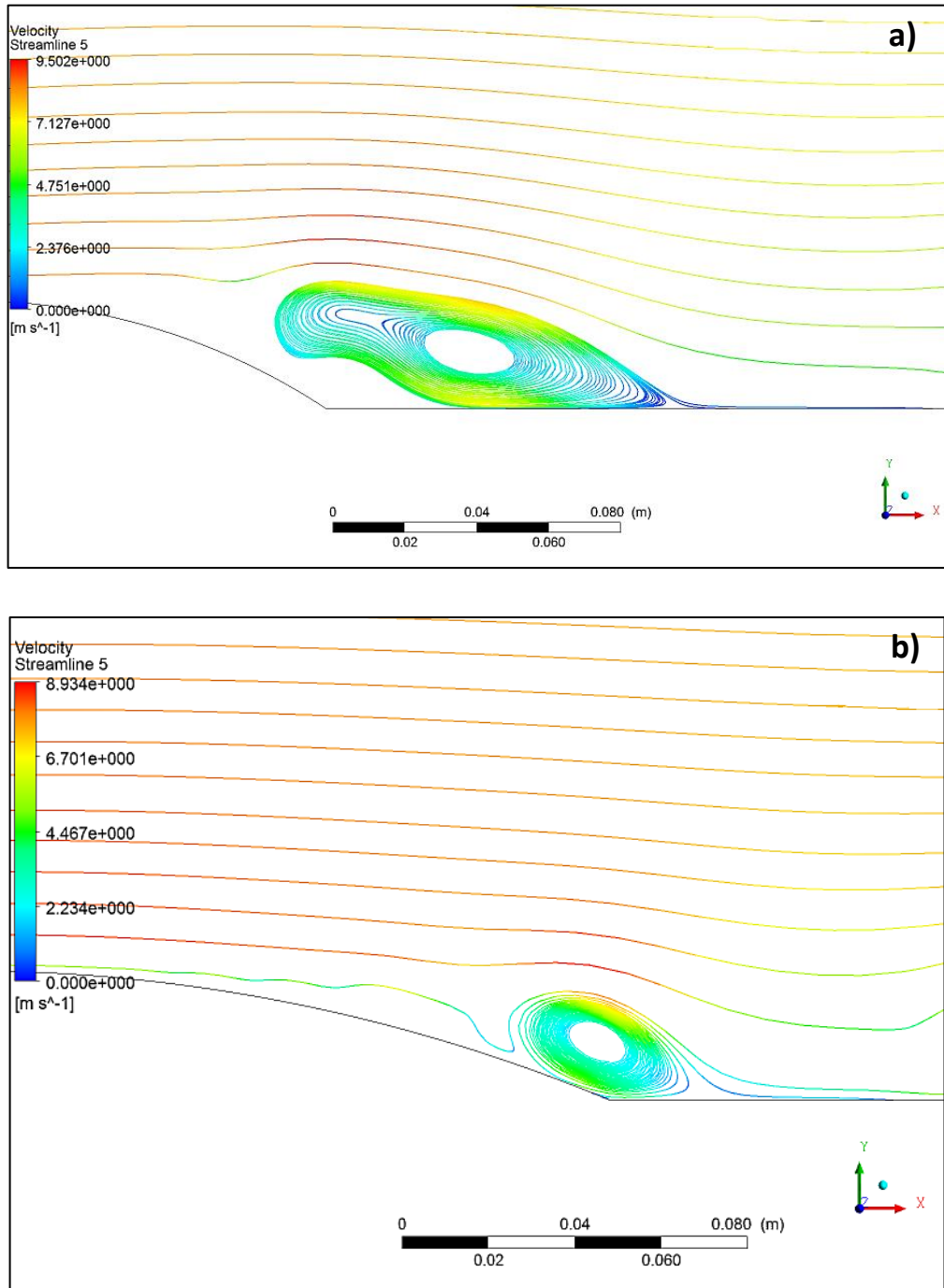

Figure 7.5: Velocity streamline at U∞ =7 m/s; a) 200 mm, b) 300 mm.

7.2. Flow Visualisation Techniques

The numerical simulation is followed by an experimental study of two different types of flow visualization techniques namely, tuft flow visualization and surface flow visualization. The first flow visualization technique is called tuft flow visualization which is achieved with the aid of cotton tufts. These cotton tufts are made up of small yarns fixed to the surface of each hump model. The flow field can be interpreted based on the orientation and movement of these cotton tufts at the same operating conditions as the numerical simulations e.g. $U_\infty = 7$ m/s. For the present experiment, the hump surface had 60 thread tufts attached. Each thread was 35 mm long, of which 25 mm constituted the active length and 10 mm represented the length used for hump surface attachment. Small rectangular segments of adhesive tape (10×14 mm) were used to attach the tufts to each surface of the models. To make the tufts even more visible and thicker, the threads were soaked in UV dye. With this technique it was possible to obtain a substantial amount of information regarding the condition of the boundary layer on the surface of the model, which allowed the identification and tracking of flow separation and the re-attachment zone. **Figure 7.6** shows three distinct parts in the flow across the two models, namely, strong cross-flow, flow separation and recirculation flow. The orientation of the tufts as shown in **Figure 7.6a and b,** helped to give initial suggestion to the location of the primary separation line and reattachment point of about 30-35 mm downstream of the 200 mm hump edge and about 10-15 mm downstream of the 300mm hump edge. Similarly, the results agreed with the CFD and showed that the reduction in *H/L* from 0.15 to 0.1 delayed the primary separation line towards the model trailing edge as shown in **Figure 7.6a**.
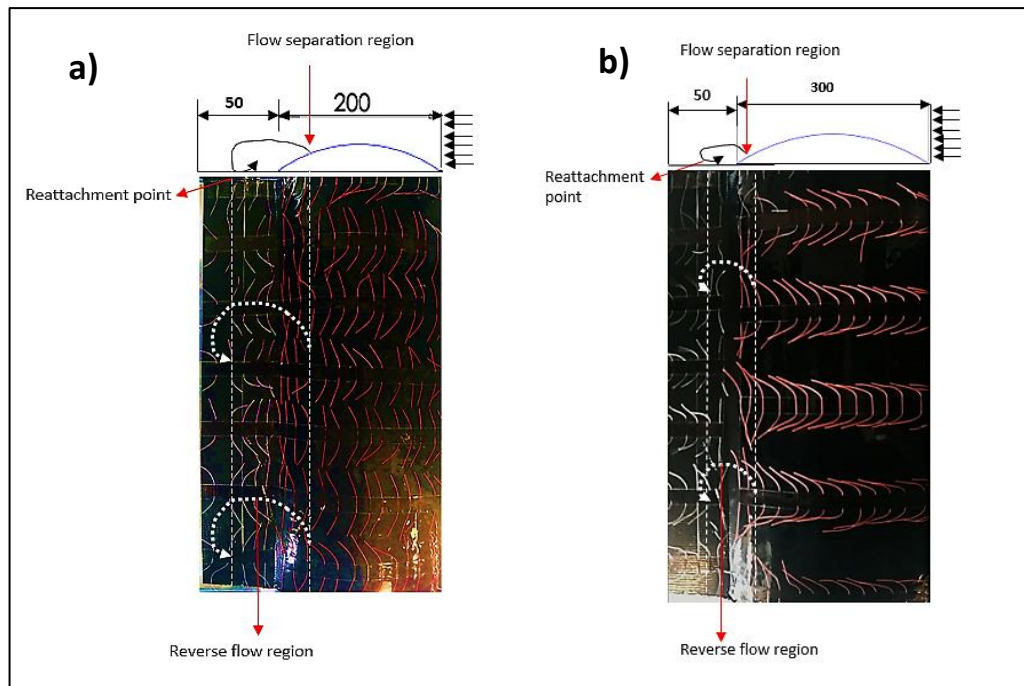
Figure 7.6: Tufts flow visualisation over a) 200 mm, and b) 300 mm hump models.

To obtain more experimental validation information, a second flow visualization technique called surface flow visualization was used. This technique was used over the 200 mm convex hump model only because it is showed better results regarding the onset of separation location and re-circulation flow compared to the 300mm model. For observation of flow characteristics close to the surface of the model, the hump was coated with a thin layer of either kerosene or silicone oil combined with luminous powder on the surface of the hump. Exposure of the hump to the flow causes the evaporation of the kerosene, the only particles remaining on the surface being a dried layer of powder, which is made up of streak lines that highlight the average surface flow patterns.

The surface flow visualisation method was applied a number of times over the aluminum model in order to confirm the features of the flow that were displayed across the Styrofoam hump. Only a tiny amount of tempera powder was added to the kerosene-powder mixture to maintain the ratio of one part powder to four parts of kerosene with a small amount of linseed oil added to maximize the viscosity of the mixture, since a mixture with a high level of viscosity would give rise to its own flow field across the surface, thereby affecting the validity of the results. After the mixture was obtained, the synthetic jet orifices on the hump surface were rotated by -30° to

146

avoid any disturbance which might occur and then, the wind tunnel was run at the optimal speed until the evaporation of the kerosene was completed.

Similarly, two distinct parts of the flow were observed where the flow accelerated and the separation occurred, then the re-attachment occurred. The first part revealed that the estimated separation location began downstream of the hump mid-point. The separating flow was highlighted by the dark region across the surface of the hump, clearly indicating the high streak flow zone. This streak line appeared as dark areas within the luminous powder. The second part moved downwards towards the wake zone, close to the trailing edge of the model leading the flow mixture to recirculate and reattach about 30-35 mm behind the hump edge such that the flow tended to climb the hump in the opposite direction of the freestream to form a wake flow area as shown in **Figure 7.7**.
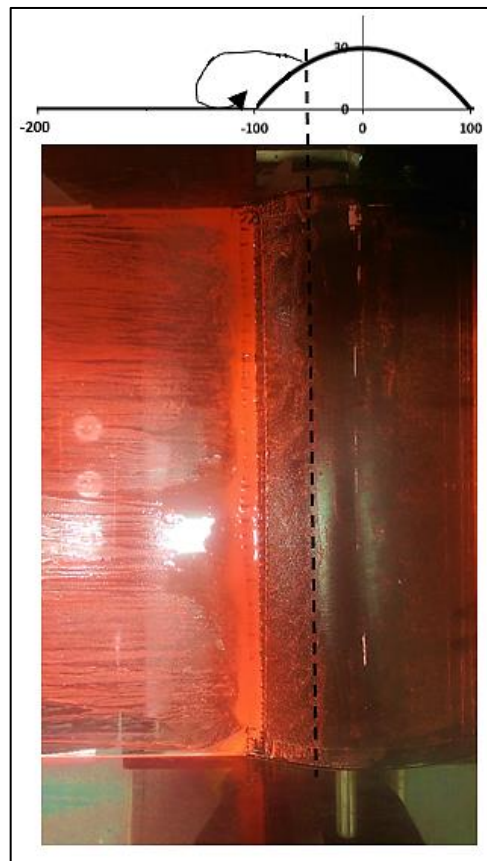
Figure 7.7: Surface paint flow visualisation over the 200 mm convex hump using an oil-illuminating powder mixture.

Finally, the flows behind the two circular convex hump models were investigated experimentally and numerically using FLUENT software. Overall, the flow visualization techniques over both models have accurately introduced the beginning of the separation and re-circulation zone. Moreover, in spite of some degree of difference in the onset of separation location and reattachment point between the experimental and numerical investigation, they agreed in that an increase in the H/L increased the size of the wake area, suggesting that H/L had an impact at a particular location on flow separation and pressure gradient independently of the Reynolds number. However, there was greater clarity of the separated flow in the case of the 200 mm model, which is therefore; this model has been established as a single baseline model that would be used in all future tests for active flow control using the synthetic jet actuator technique.

7.3. Power Spectral Density Investigation

The velocity signal behind the convex hump was measured and then processed to obtain the power spectral density (PSD) into the wake area. This would help to provide a quantitative measurement for further recognition of the separation and vortex shedding which is a way of representing the frequency content of velocity signals into the wake region. The PSD plots were not only used to establish the baseline case, but would provide significant information which will be used in detecting the separation incipient and identifying the characteristics of the excitation parameters of synthetic jet actuators because it allows the unsteadiness downstream of the convex hump to be examined in more detail. The experimental set-up and measurement techniques were introduced in Chapter 5 (section 5.2.2.3) and will not be repeated here.

The time average velocity fluctuation signals in the wake area were captured using HWA system at downstream locations which varied from $X/L = 1$ and $Y/h = 0$ to $Y/h = 3$ respectively, at four free stream velocities which varied from $U_\infty = 6$ m/s to $U_\infty = 10$ m/s as shown in **Figure 7.8**. Considerable attention has been taken to move the hot-wire probe within 3-5 mm downstream of the convex hump using the three dimensions manual traverse system. After the signal was captured, a Fast Fourier transform (FFT) was performed on the data using the Matlab program in order to obtain the power spectra in the wake region using an 8192 point of FFT.
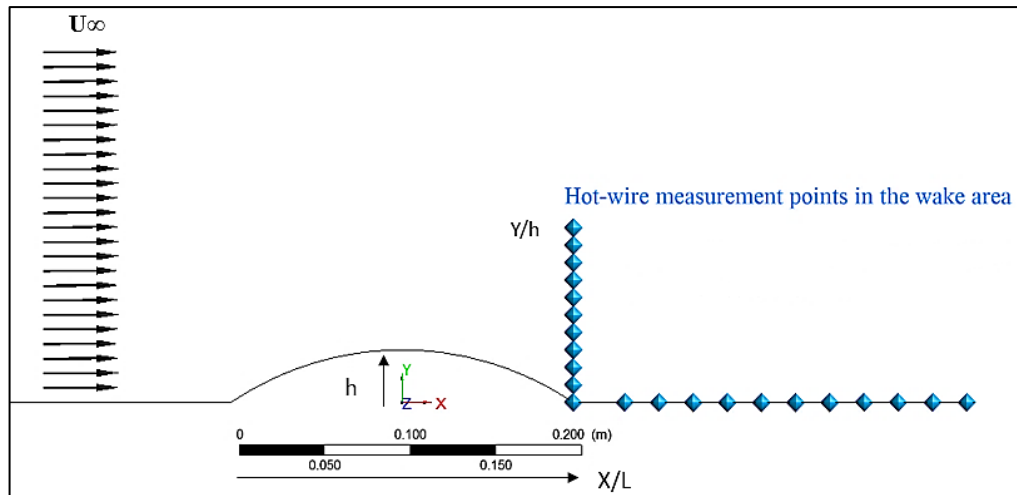
Figure 7.8: Coordinate system in the measurement area behind the hump model.

The PSD results of the time-averaged velocity signals versus *Y/h* and *X/L* downstream of the convex hump are shown in **Figures 7.9a and b** at the same freestream velocity of $U_\infty = 7$ m/s. **Figure 7.9a and b** introduce a comparison of both mean velocity and PSD at *X/L* = 1 and *Y/h* = 0 (inside the wake area) and the mid-test section at the same freestream velocity. The figures have shown the major contribution to the unsteady flow which creates a high fluctuation in velocity over the mean velocity at any given point close to the hump edge inside the wake region compared to mid test section (**see Figure 7.9a**) due to the separation incipient over the convex hump surface. The figure clearly shows that the velocity fluctuation inside the wake area ranged between zero and positive values due to the hot-wire probe not being sensitive to the flow direction and thus reversing any negative signals.

However, considerable differences can be observed in **Figure 7.9b**. The highest energy of the flow has been found for *Y/h* = 0 which indicates that the flow became a mixing of coherent structures with turbulence as a result of the flow separation incipient. This energy of the flow became lower as the hot-wire probe moved towards the wind tunnel mid-test section until the turbulence became less than 1%, suggesting that the probe was out-side of the wake area behind the convex hump. Therefore, it can be concluded that at the lowest *Y/h* location, the fully unsteady flow with high energy expected was displayed compared to the highest *Y/h*.
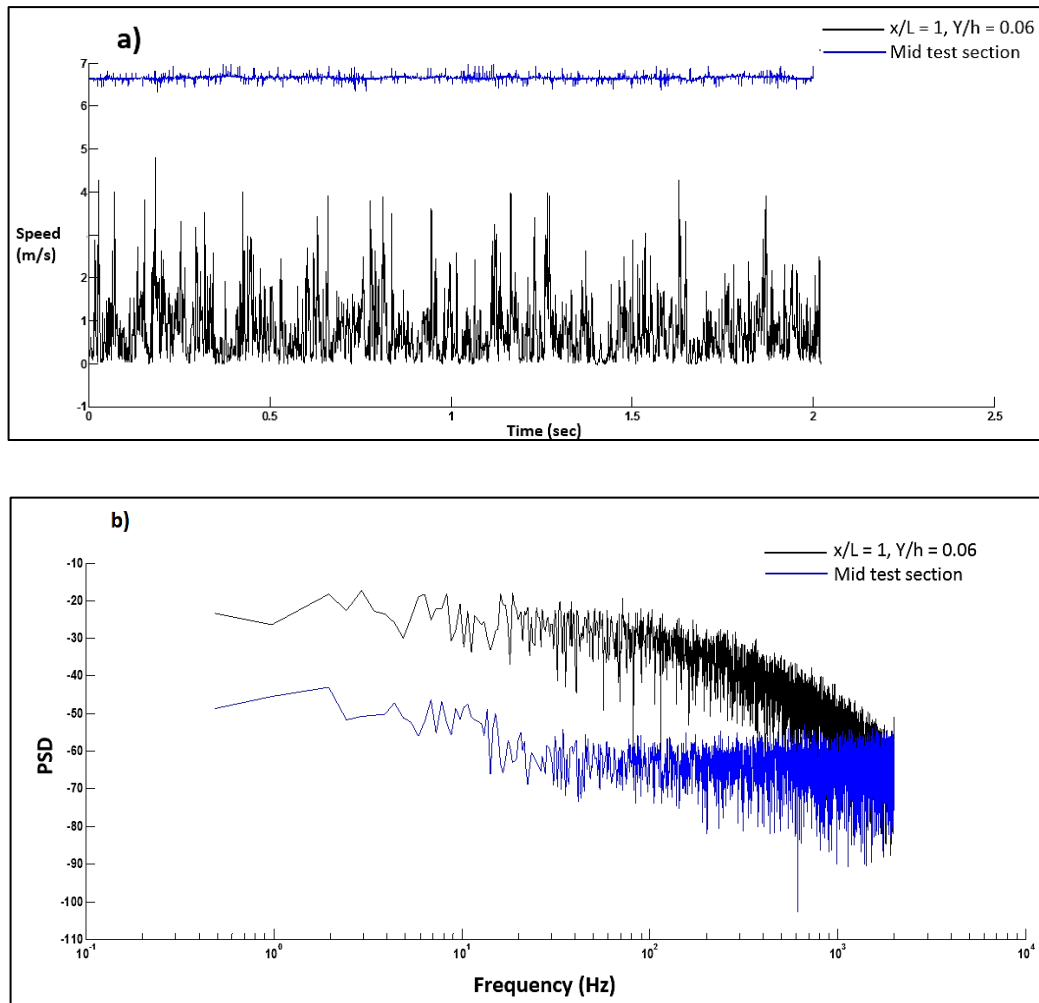
Figure 7.9: a) Velocity deficit and b) PSD in the wake area and mid-tunnel section.

Figures 7.10a to d show that the PSD distributions of the fluctuated velocity signal for the hot-wire probe moved from $Y/h = 0$ to 3 having the same location of $X/L = 1$ in the wake region of the convex hump at the four freestream velocities. At $Y/h = 0.5$, the energy of the flow became lower and the spikes of the spectral peaks were clearly seen in this region suggesting that the probe was inside the vortex shedding area behind the convex hump. However, a dominant spectral peak is located at $Y/h = 0.5$ in the wake region that exists about $f_s = 66.4$ Hz at 6 m/s freestream velocity, which is more likely to indicate that a vortex shedding (f_s) is generated downstream of the convex hump. Similarly, the experiments were repeated at the same locations for the other three freestream velocities of $U_\infty = 7$, 8 and 10 m/s, which is illustrated in **Figure 7.10b to d**. Again the figures clearly show that at the given Y/h location, the expected spikes of the vortex shedding are clearly seen.
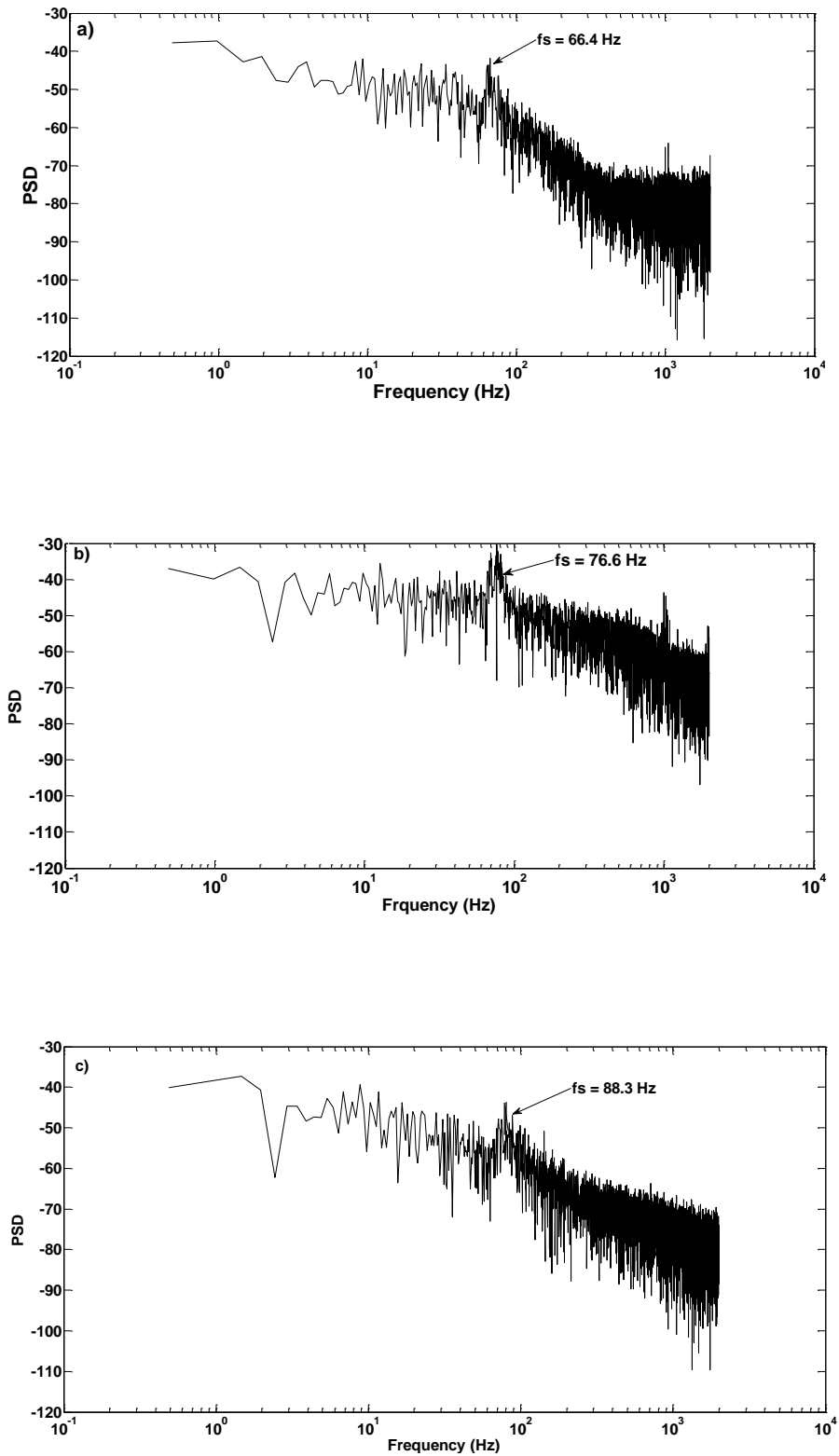
Figure 7.10: Power spectral density at a) $U_\infty = 6$ m/s; b) $U_\infty = 7$ m/s; c) $U_\infty = 8$ m/s; (Y/h = 0.5)
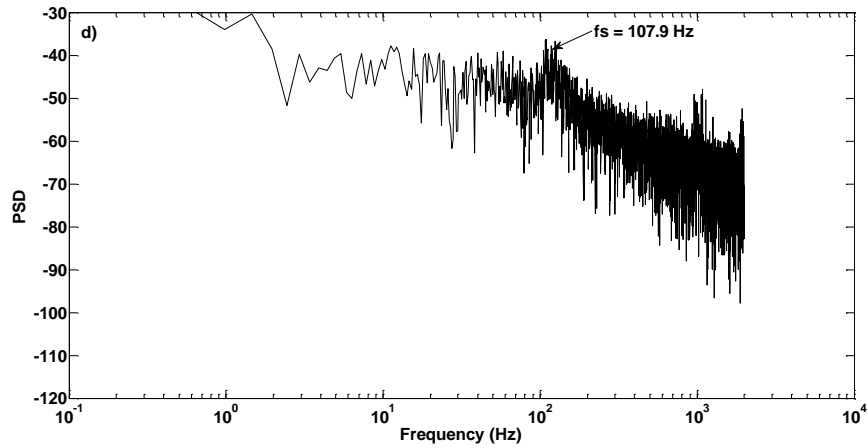
Figure 7.10: Power spectral density (continued) d) $U_\infty = 10$ m/s; (Y/h = 0.5).

As shown in the previous figures, with the increasing of the freestream velocities from 6 to 10 m/s, the vortex shedding frequency also increased. This increase agreed with results obtained by other researchers (Sarioglu and Yavuz (2000); Butt and Egbers (2013)). Therefore, a linear relationship between the freestream velocity and vortex shedding frequency can be seen in **Figure 7.11**. The figure clearly shows that the dominant peaks of $f_s = 76.6$, 88.3 and 107.9 respectively occurred about the same value of $Y/h = 0.5$.
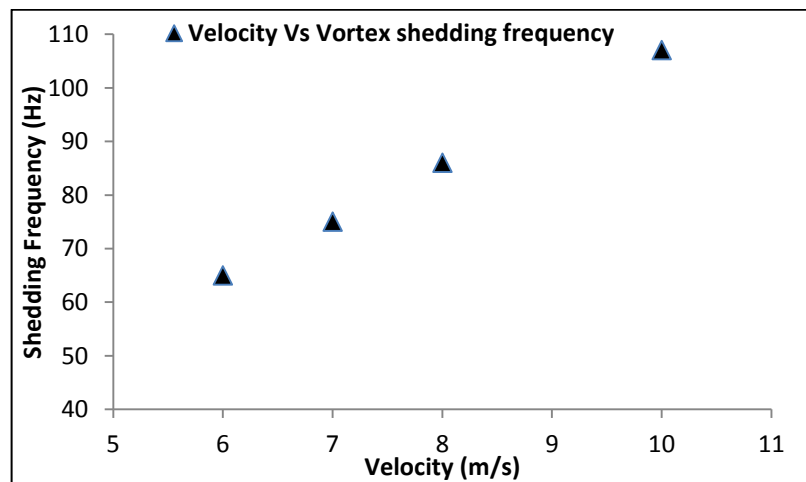

Figure 7.11: Vortex shedding frequency vs freestream velocity.

Additionally, the oscillating flow can be described by a common non-dimensional number to identify the characteristic associated with the vortex shedding frequencies which is named the Strouhal number which is defined as:

$$St = \frac{f_s \times D}{U_\infty} \dots\dots\dots\dots\dots\dots\dots\dots\dots\dots\dots\dots\dots\dots\dots\dots\dots\dots\dots\dots\dots.7.4$$

where f_s is the vortex shedding frequency of the given freestream velocity, D is the diameter (represented by height in the present hump) and U_∞ is the freestream velocity. The convex hump height is 30 mm and the vortex shedding frequencies based on the four freestream velocities are 66.4, 76.6, 88.3 and 107.9 Hz resulting in a Strouhal number of about 0.31.

From the experimental outcomes and different plots shown above, the overall results from hot-wire anemometer measurements were capable of providing vital information regarding the existence of flow separation over the convex hump model which was responsible for the vortex shedding seen in the power spectral density results. However, to determine the wake flow field behind the convex hump, the characteristics of this flow were detected using PIV techniques. The PIV system used in this study is the same as that described in section 5.4. The CCD camera was mounted in front of the wind tunnel pointing towards the side wall of the test section to capture images of the flow in the X-Y plane. The laser was located above the camera and the laser was fired from the top to the bottom of the wind tunnel test section.

7.4.   The Baseline Case Identification Using PIV

The collection of data is not straightforward after the organisation of the system as indicated in Chapter 5. The system was set up so that during the experiments, measurements of the flow were taken at three equally spaced field of view of 60 by 60 mm. Image-1 captured the flow at the hump inlet to check the flow quality at the beginning of the hump while images 2, 3, and 4 are captured the second half of the convex hump with a 10 mm overlapping as shown in **Figure 7.12**. This set-up helped to capture a large area of interest, especially in the near wake close to the separation location and the reattachment area which is clearly indicated in the figure. One hundred image pairs were captured for every image configuration and measurement position,

so as to make sure that enough data was gathered and that the average data files were reliable. The number of images stored on the computer was restricted by specifying in the acquisition software that only one hundred image pairs should be collected. The series of one hundred pairs are processed by the software in a batch, generating one vector plot for every pair (i.e. one hundred vector plots in total).
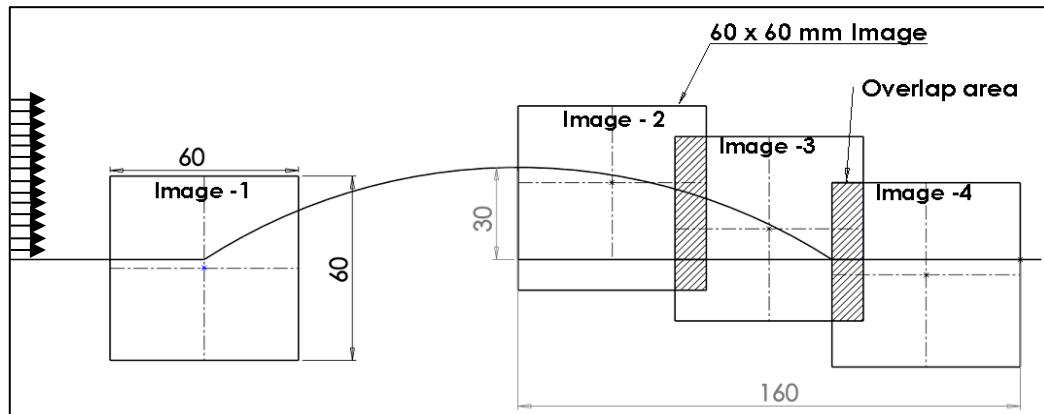

Figure 7.12: PIV experimental set-up showing the images captured.

Prior to capturing the PIV images, the seeding technique was applied into several configurations, including the seeding of the flow field through elbow, straight, perforated, and slotted pipes, as well as close to the wind tunnel fan inlet as explained previously in the experimental set-up and measurements techniques section. However, after so many trial and errors, there are some final procedures of capturing good quality images which need to be followed. Initially, prior to capturing the PIV images, the laser beam reflection needs to be reduced by offsetting the image centreline below the object and switching off the ambient light source. Moreover, the wind tunnel test section should be seeded as closed loop using its own room by filling the whole room with seeding. The advantage of this seeding device is that it mixes well with the wind tunnel flow. Additionally, the images need to be refocused each time to avoid any out of focus particles.

For the set-up used here the camera was located downstream of the hump edge, always 0.6 m of any given light sheet location. For different light sheet locations this gap between the camera and the light sheet was maintained by mounting the camera directly below the laser head on the same traverse such that they moved

together on the same aluminium frame. This set-up is explained in Chapter 5 (section 5.4.2).

All the PIV tests were performed at a fixed freestream velocity of $U_\infty = 7$ m/s. For the un-actuated case, the PIV images (Image 1 to 4) were acquired as shown in the image explained in **Figures 7.13a, b, c and d**. The two-component PIV velocity fields were acquired at three different locations (with an overlap of 10 mm) with respect to the flow separation and reattachment area in order to provide sufficient flow information. Conditional sampling was used to acquire 100 image pairs at each location in order to form a conditionally averaged flow field from which movies of the dynamic behaviour of the near-wake were created. The figure clearly showed the stream-wise velocity vectors in the un-actuated case obtained using PIV. The recirculation area and reattachment point are clearly indicated in **Figures 7.13c and d** which is associated with the boundary layer separation. This area is responsible for the high level of velocity deficit that is described in the HW results. However, compared to CFD results, the flow does not separate at the same location, but rather there is a little difference in the onset location of the separation point which separates at some distance further downstream.

The exact locations of the separation and reattachment are somewhat close to what is seen in the flow visualization results. Nevertheless, for the purpose of evaluating the effectiveness of synthetic jet actuators operated at different conditions in modifying the wake area behind the hump, this is not an issue because the PIV results obtained at the same measurement plane will be compared. The width of the recirculation area and the location of the reattachment point from the hump rear edge are found to be $Y = 13$ mm (*Y/h = 0.43*) and $X = 30$ mm (*X/L = 0.15*) respectively.
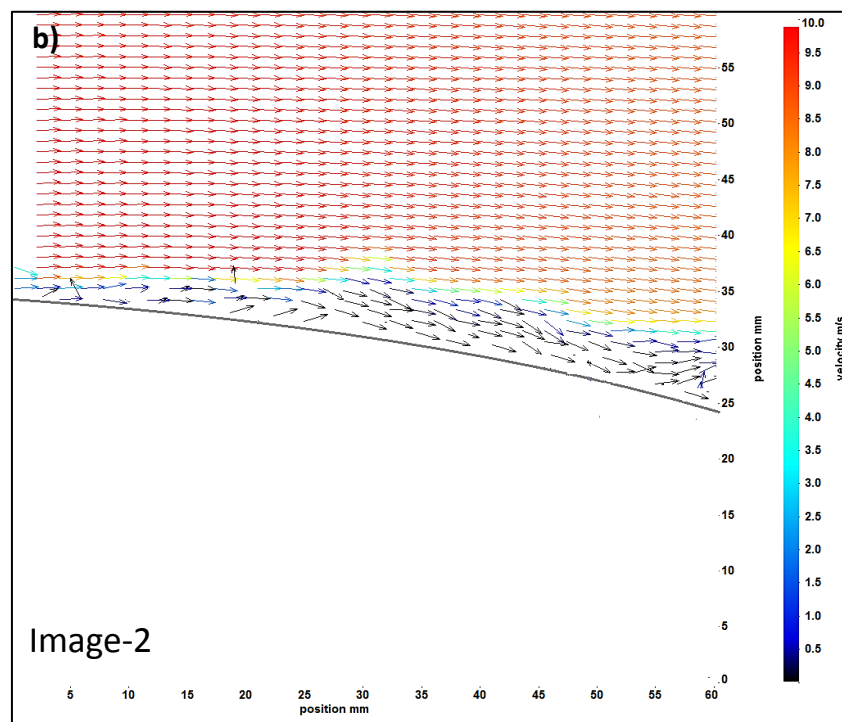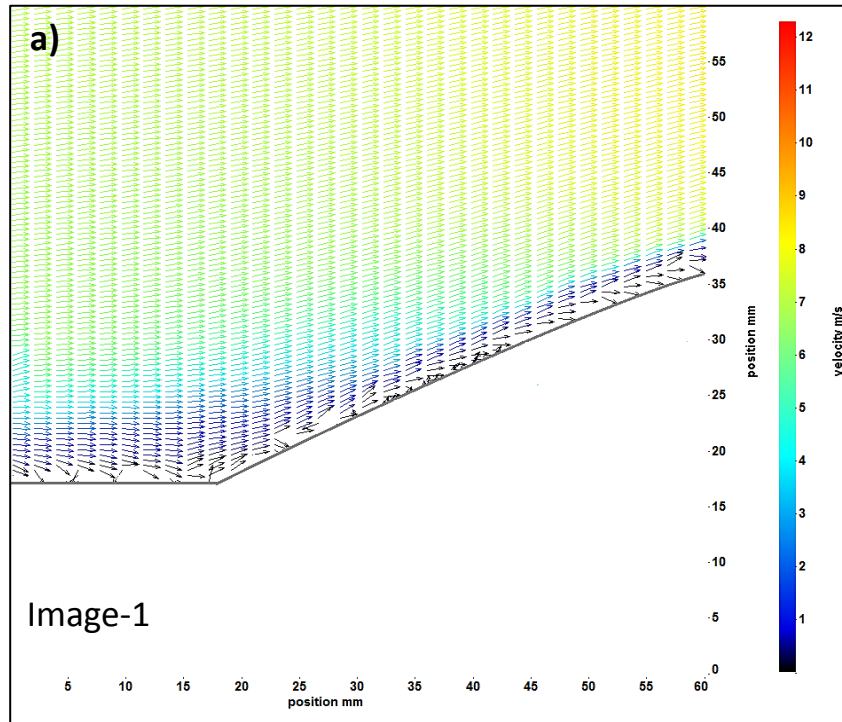
Figure 7.13: PIV images a) Image-1 and b) Image-2 of velocity vectors for the un-actuated case at $U_\infty = 7$ m/s.
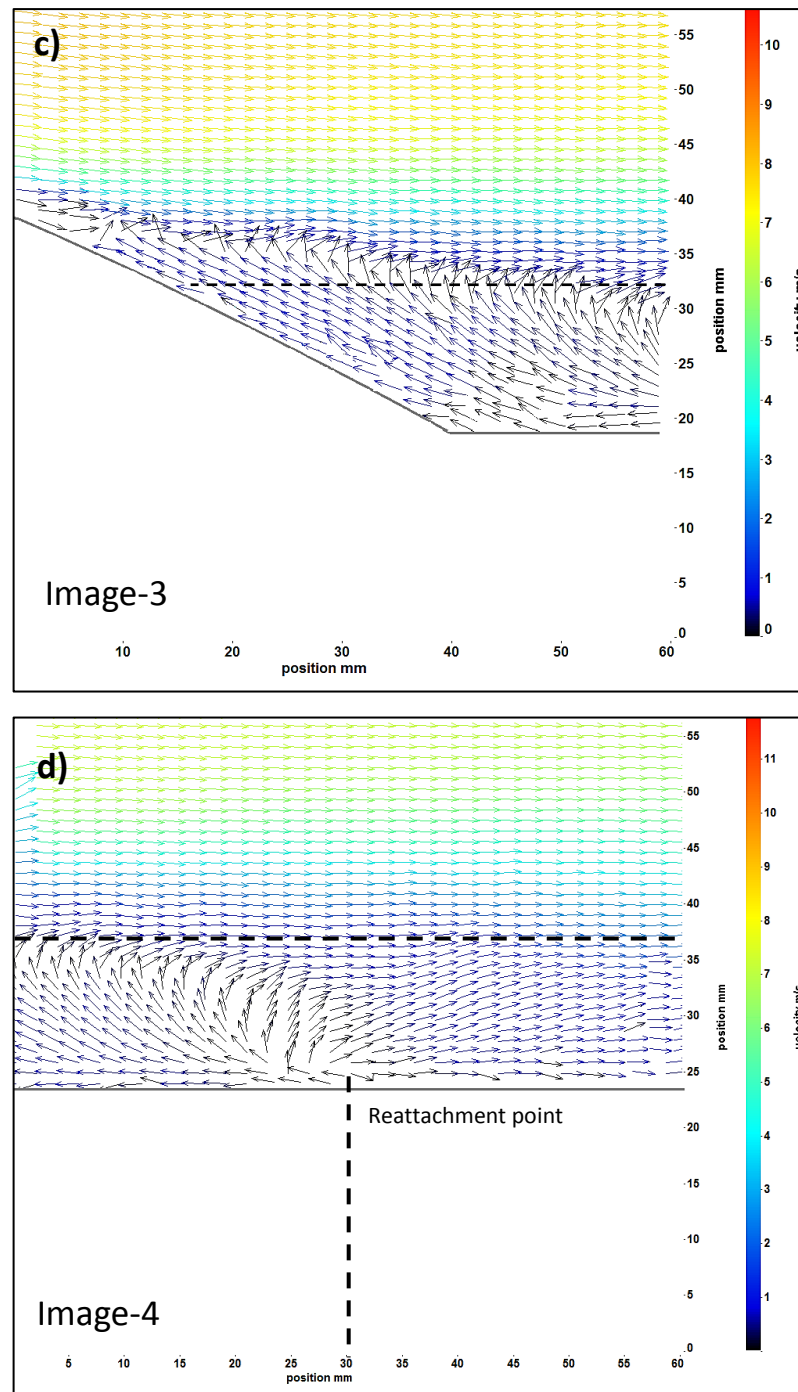
Figure 7.13: PIV images (continued) of velocity vectors for the un-actuated case showing c) the recirculation width and d) reattachment point at $U_\infty = 7$ m/s.

A typical boundary layer of velocity profile obtained from a PIV measurement is compared with the associated lines shown in image number three (**Figure 7.14a**) to validate the pre-and-post separation area. The results of these profiles are shown in **Figures 7.14b and c**; the results indicated that, both boundary layer profiles compare well with the location of the onset of separation location.

157
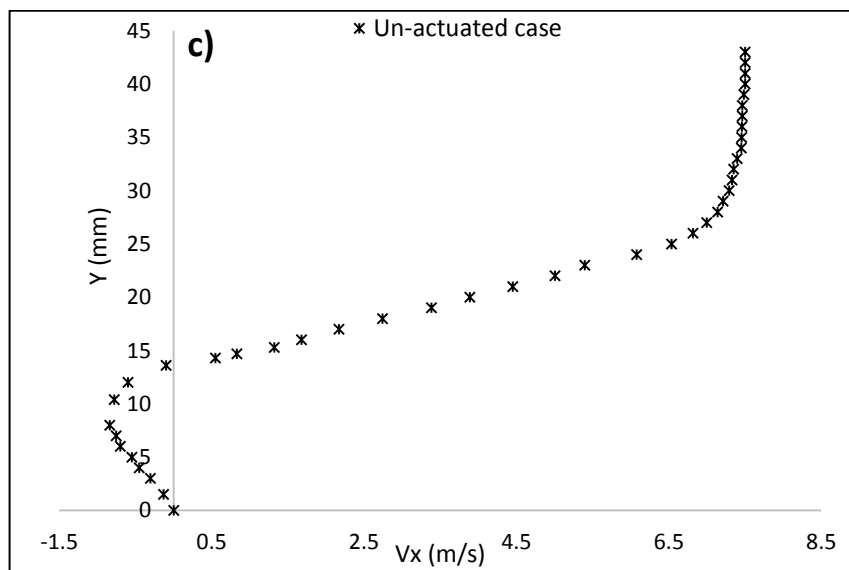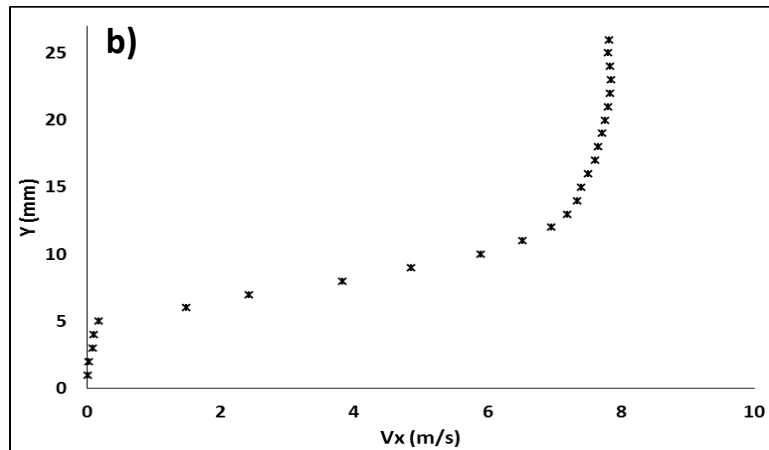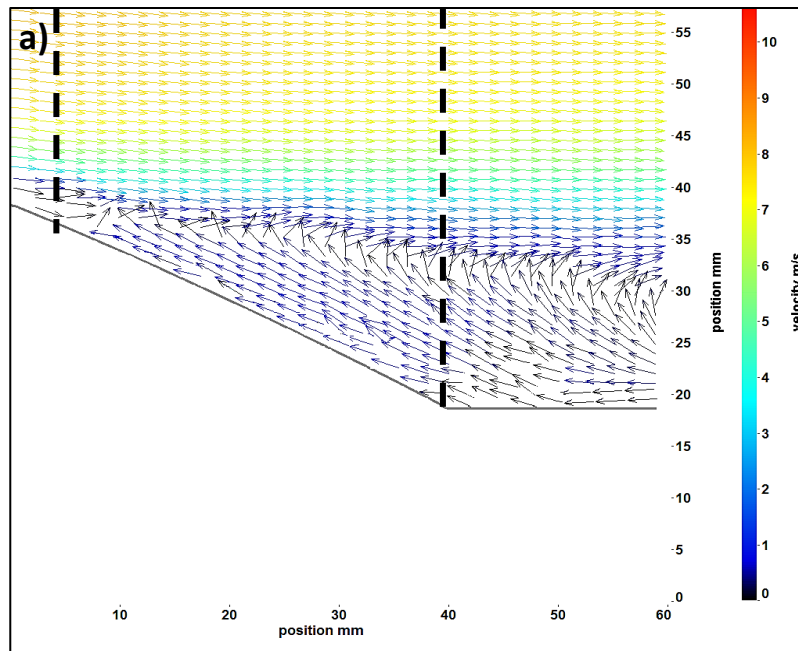
Figure 7.14: a) Image number three (recirculation zone) showing pre-and-post separation lines; b) boundary layer of velocity profile at pre-separation area and c) post-separation location.

7.5. Conclusions

The present work involves experimental and numerical investigations of flow past two circular convex hump models (section of cylinders) at a fixed height of H = 30 mm and two different lengths (L) 200 mm and 300 mm. The comparison of experimental and numerical results was conducted at a fixed freestream velocity of $U_\infty = 7$ m/s. Two different flow visualization techniques have been used to investigate the flow separation and reattachment region named tufts flow visualization and surface flow visualization.

The experimental and numerical results showed that the incipient of flow separation and recirculation zone over the 200 mm model is strongest in the region near the trailing edge compared to the 300 mm model. Both flow visualization and numerical investigation showed that an increase in the H/L ratio increased the size of the separation bubble, suggesting that H/L had an impact at a particular location on flow separation and pressure gradient independently of the freestream velocity. However, the flow visualisation and PIV results clearly showed the flow does not separate at the same location as CFD, but rather the latter showed a little difference in the separation location which separates some distance further downstream. Therefore, flow visualization techniques, HWA and PIV results are accurately showing the beginning of the separation and recirculating zone in the case of the 200 mm model compared to the 300 mm model, which is therefore, the most reasonable model and would be employed in active flow control tests.

Chapter 8: Investigations into the Actuation Effects on a Convex Hump with Synthetic Jet Actuators

In order to demonstrate, experimentally, the flow control over a convex hump using the array of SJAs, consideration is given to the application of a synthetic jet actuator to control the power spectral density (PSD), recirculation area and separation length in the wake area using both HWA and PIV techniques. In this chapter, the flow control over the convex hump using an array of SJAs is presented in both un-actuated and actuated cases. The free stream velocity was fixed to 7 m/s for the current series of experiments. This freestream velocity was selected in order to achieve the required velocity ratio ($Vr = U_j/U_\infty = 0.5$, 1 and 1.5) and then the study is extended to a higher free stream velocity of 10 m/s. The hump model was mounted in the open-circuit wind tunnel using the mounting system as demonstrated in section 3.1.4 and the flow field around the hump was modified by exciting the synthetic jet actuator array using un-modulated and modulated signals.

8.1. Summary of the Actuation Parameters

The effect of SJA on the convex hump flow field can induce a downstream and upstream actuations by simply rotating the hump by $\pm$ 32 degrees. For example, by rotating the hump as shown in **Figure 8.1b**, a downstream actuation is established. An upstream actuation can be achieved by rotating the hump as shown in **Figure 8.1a**. Considerable cares are made to identify the most effective angular position of the synthetic jet actuation angle (β) in the wake area and velocity deficit behind the hump. Moreover, both un-modulated and modulated signals used to excite the wake area behind the convex hump are chosen based on related flow frequency and Helmholtz frequency. The un-modulated signal which is equal to 1000 Hz (Helmholtz frequency) and this frequency is set as the carrier frequency for the amplitude modulation signal ($f_c = f_H$) while the second frequency (Modulated signal) is set to 75 Hz which represents related flow frequency at 7 m/s. However, this second frequency is selected based on the separated shear layer frequencies in the wake area ($f_s \approx f_m$).
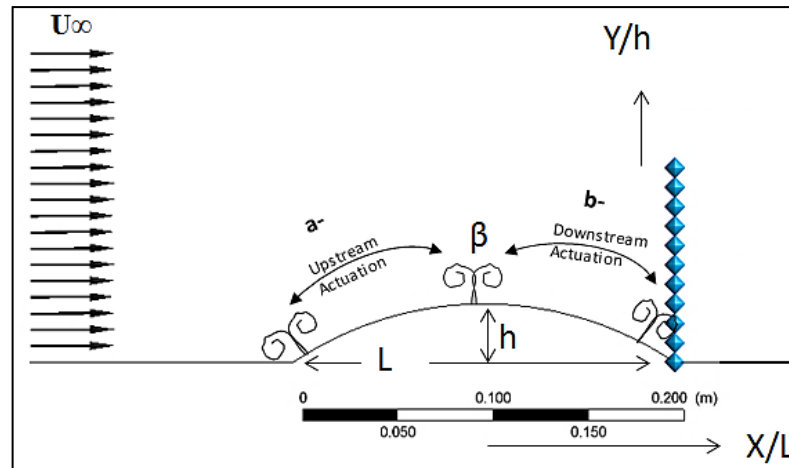
Figure 8.1: Configuration of the Synthetic jets actuation.

The results from different available actuated and un-actuated cases are introduced as a flowchart in **Figure 8.2**. The figure clearly shows that the results are presented in two separate sections based on the excitation waveform type used to actuate the flow. In this study single sine wave (un-modulated) and modulated sine wave excitation techniques were used. Within each section, the results are further split into sub-sections. Initially, for each actuation configuration, power spectral density (the set-up is described in section 3.4) was used to evaluate the flow energy and vortex shedding distributions in the wake area behind the hump. This allows the effect of each actuation configuration on the flow to be compared with the spectral content of the un-actuated flow field case, and any changes due to actuation can be identified. Moreover, the effect of SJAs on the separation length, recirculation size area and reattachment point in the hump wake area was analyzed. All of these measurements were presented in both un-actuated and actuated flow field behind the hump.

8.2. Summary of the Un-actuated Hump Flow Field

In order to facilitate comparisons between the actuated and un-actuated cases, the PSD results for the un-actuated hump case are repeated in **Figure 8.3**. Discussions of PSD plots have already been presented in Chapter 7 (section 7.3) and will not be repeated here. The synthetic jet orifices were covered with Sellotape during these tests to avoid any flow disturbance which might occur.
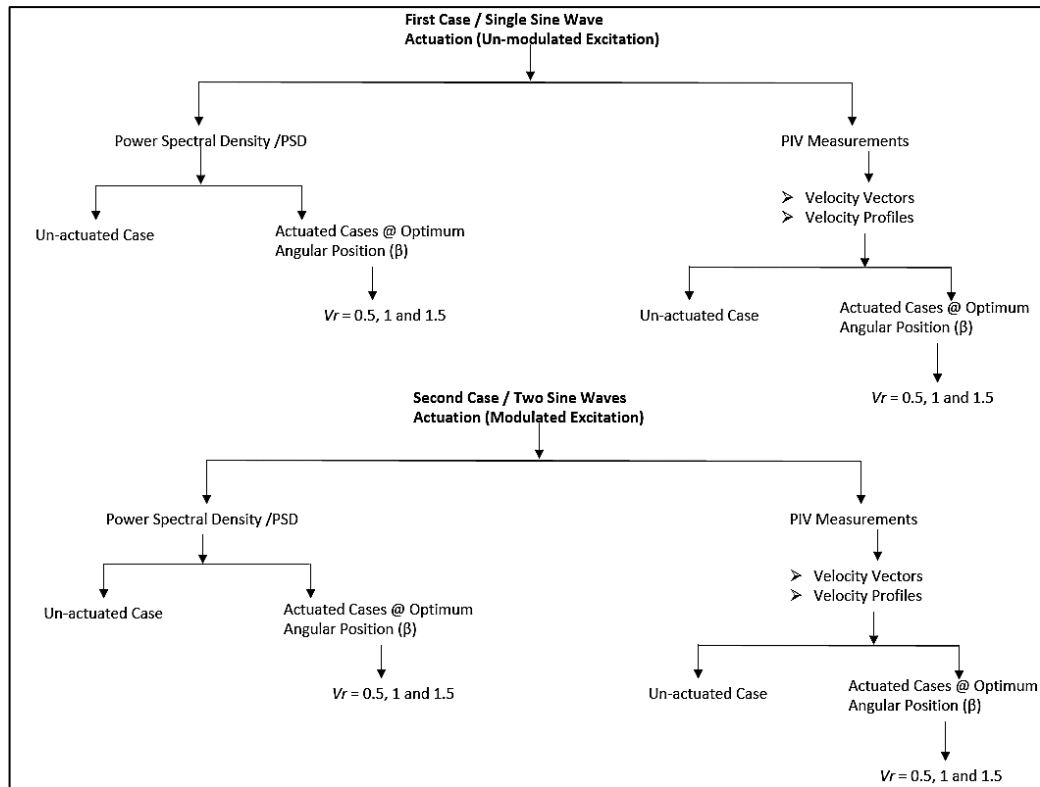
**Figure 8.2:** Flowchart of the excitation parameters examined in the current flow control study.
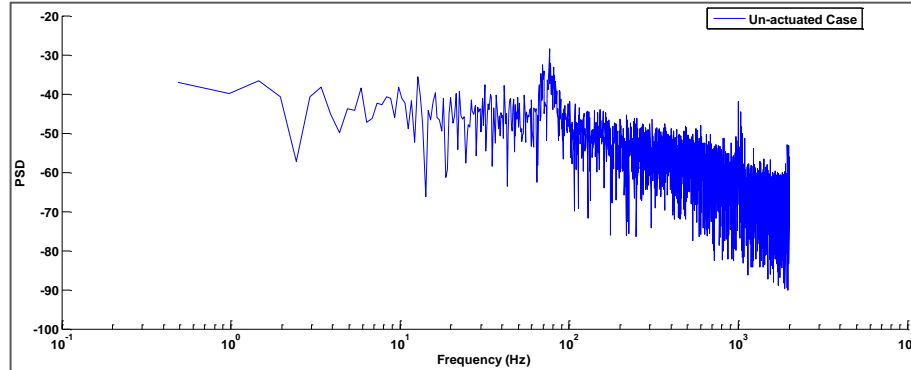
Figure 8.3: Power spectral density of the baseline case at $U_\infty = 7$ m/s, (Un-actuated case, Y/h = 0.5, X/L = 1).

Additionally, both images, number three and four of the velocity vectors which represents the recirculation area and separation length are also re-presented in **Figures 8.4a and b** respectively. These images are already explained in the un-actuated results in Chapter 7 (shown in Figure 7.13) and used here to investigate whether the SJAs are able to alter the separation length, recirculation width and hence reattachment point in the hump wake area. In each section of this chapter, the general effect of the actuation

will be compared to these un-actuated results and the trends seen as the actuation parameters vary will be discussed. **Figure 8.4a** clearly shows that the width of recirculation area of about 13 mm which is about 43.5% of the total hum height. Moreover, the reattachment point is located 30 mm (*X/L* = 0.15) measured from the rear of the hump as shown in **Figure 8.4b.**
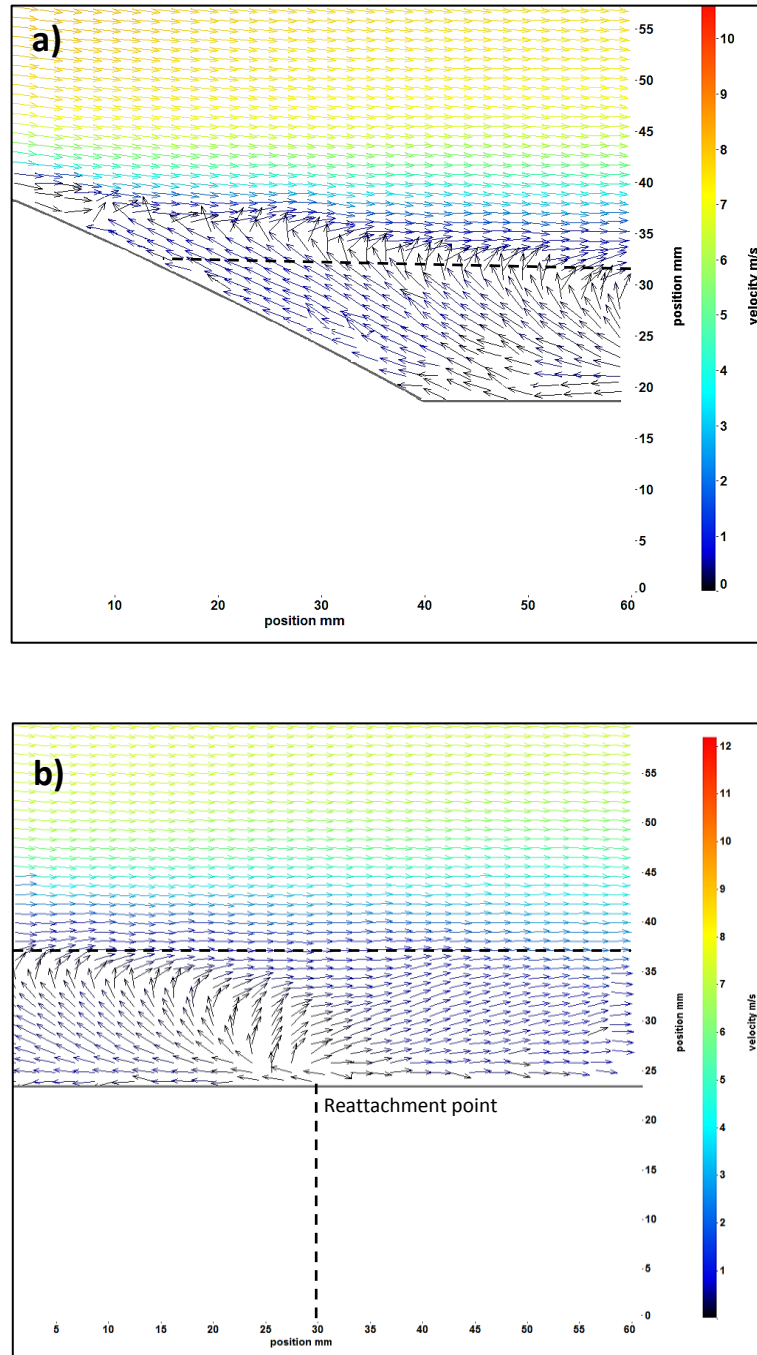

Figure 8.4: Velocity vectors of the un-actuated case; a) Recirculation width; b) Reattachment point at $U_\infty = 7$ m/s.

8.3. Results: Single Sine Wave Actuation (Un-modulated Excitation)

In this section, a series of experimental investigations were conducted with a single sine wave excitation as described in Flowchart 8.2. The angular position of the synthetic jet actuation angle relating to the cross-flow (β) was set at the optimum value of 10°. The angular position of the synthetic jet actuation angle relating to the cross-flow (β) was set at the optimum value of 10°. This angle was extracted from power spectral density measurements at different actuation angles as indicated in **Appendix C**. The piezo-ceramic diaphragms were excited by a single sine wave (Un-modulated signal) using function generator with a combination of six amplifiers. The excitation frequency, f_e for the present tests was set to 1000 Hz (based on the Helmholtz frequency of the cavity). In order to achieve the required velocity ratios Vr, the jet peak mean velocity at the exit of the orifice was measured and presented in Chapter 6. The influence of the synthetic jet actuation and velocity ratio Vr on the hump wake region was performed at the optimum angular position of actuation of β = 10° behind the hump model.

Figures 8.5a, b and c present the PSD under the un-actuated and actuated hump wake area at Vr = 0.5, 1 and 1.5 and β = 10° over X/L = 1 and Y/h = 0.5. The results clearly showed that at Vr = 0.5, the dominant peak frequency was not affected by the synthetic jet actuation compared to the baseline case. This suggested that the synthetic jets are quickly deflected and lose their structure to the dominant influence of the freestream flow above it and hence the perturbation introduced by the synthetic jets is completely dissipated inside the boundary layer. For the control case of Vr = 1, the synthetic jets are more likely to affect the boundary layer, and the vortex shedding frequency was slightly reduced due to the interaction of the synthetic jets with free shear layers. The comparison of the control case at Vr = 1 and Vr = 1.5 suggested that at Vr = 1.5, the jet is stronger and more likely to affect the boundary layer above it. **Figure 8.5c** suggested that the forming of vortex rings appeared to enhance the external flow above it, causing a reduction in the flow energy by around 20 % compared to the un-actuated layer frequency. This reduction in the PSD peak frequency is likely to be caused by the interaction between the synthetic jets and boundary layer above it. In summary, it can be seen in **Figures 8.5a to c** that, apart from a prominent spectral peak at a Strouhal number (St) value of 0.3 which is related to shear layer shedding from the separated flow area, a broadband character is

displayed by the power spectral density attained during an inactive synthetic actuation and this vortex shedding is significantly reduced during the operation of the twelve SJAs. Therefore, the synthetic jet actuation was able to diminish both the discrete peak at $St = 0.3$ and the spectral levels in the wake region.
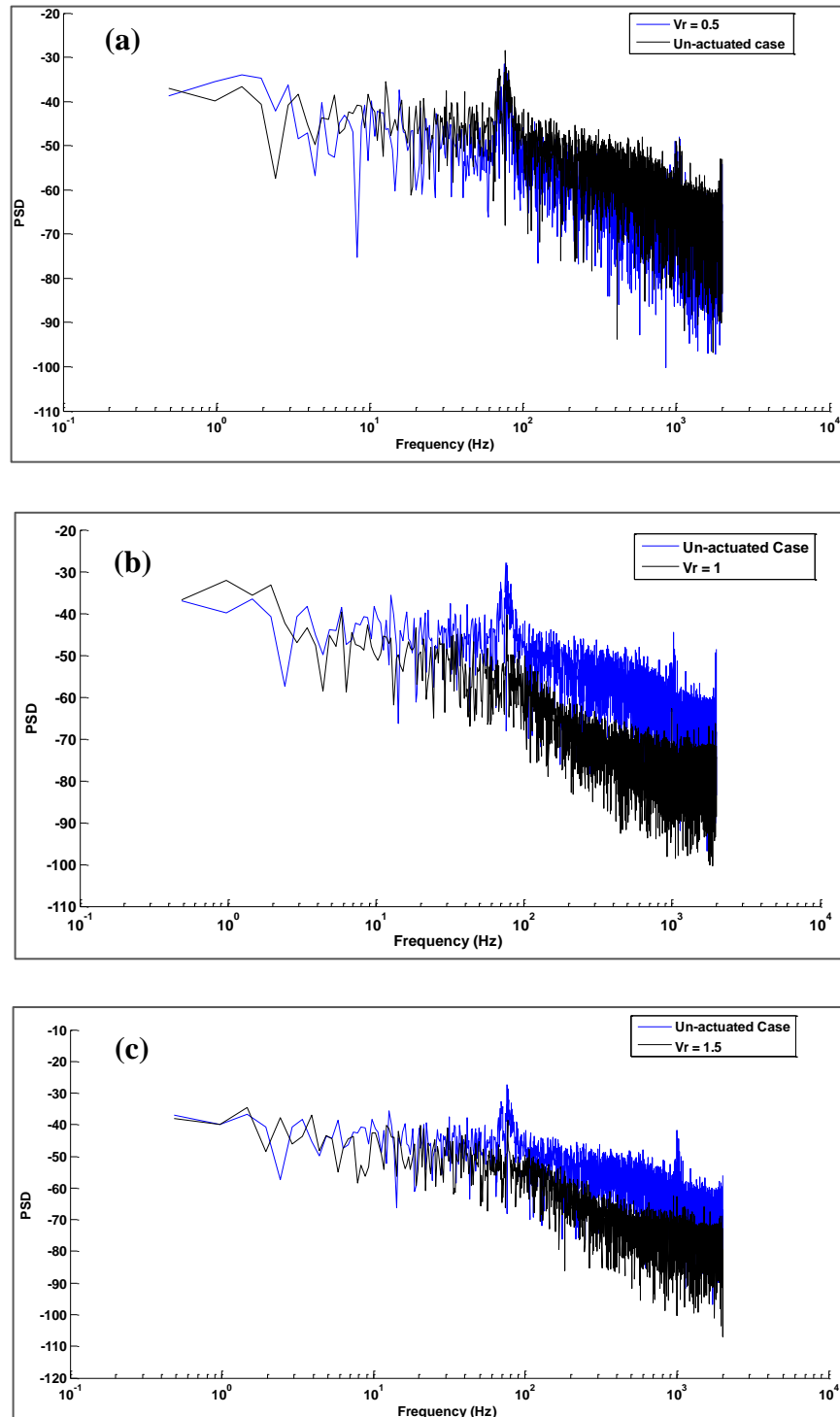

Figure 8.5: The power spectral density with and without actuation cases at different velocity ratios ($U_\infty = 7$ m/s, Y/h = 0.5, X/L = 1, $f_e = f_H = 1000$ Hz, $\beta = 10^o$).

Additional analysis based on the PIV technique is required to improve understanding of how the hump wake region is affected by the SJA. Thus, the following parts offer examinations of the manner in which the separation length, recirculation zone width and reattachment point are influenced by the actuation process. For the purposes of characterisation of the hump wake flow in both actuated and un-actuated cases, the examination is conducted at the un-modulated excitation signal in the range of $Vr = 0.5$ to 1.5 and β of 10°. Furthermore, a comparison is carried out between the findings obtained in the actuated cases and those from un-actuated cases indicated in **Figures 8.4a and b**.

The impact of SJAs on reverse flow width and reattachment location in the wake region attained at various Vr and constant β locations is shown in **Figures 8.6-8.8.** At $Vr = 0.5$, the recirculation width and reattachment point in the wake region are unaffected by the SJA **(see Figure 8.6)**, which is similar to what is seen in the PSD results. At $Vr = 1$ (**see Figure 8.7**), the recirculation width is slightly reduced, suggesting that a minor stream-wise velocity being triggered in the on-coming flow above and somewhat downstream from the synthetic jet orifices, due to the ejecting of the synthetic jets along with the cross-flow. The recirculation width zone in the wake region becomes even smaller in width at $Vr = 1.5$, ultimately becoming 24% more diminished by comparison with the un-actuated case (**see Figure 8.8**). What can be implied from this is that an increase in the jet-to-stream velocity ratio (*Vr*) to 1.5 afforded sufficient momentum to the synthetic jet that it could affect the near-wake flow field behind the hump, leading to a decrease in the width of the recirculation area through vectoring some of the negative velocity in the reverse flow region. It is believed that the generated vortex rings became stronger at high velocity ratio and more likely within the near-wall region and hence enhance the wake flow area.

Another phenomenon that can be observed from the figures is that comparison with the un-actuated case, there is movement in the reattachment point towards the hump edge. This movement reaches as much as 8 mm as the velocity ratio is raised to 1.5 suggesting that the flow separation is delayed. On the other hand, at velocity ratios lower than one, the cross-flow is greater than the flow within the synthetic jet orifices, while the ejected vortex rings lack their momentum inside the boundary layer to facilitate their departure from the near walls. As a consequence, the jet is almost instantly deflected while the main flow field is disrupted to a more minor extent.

Hence, the findings suggest that, at a higher velocity ratio, the recirculation width and reattachment point become diminished more significantly for a specific flow condition and actuator operating conditions (e.g. un-modulated excitation signal in this case); this means that the velocity ratio has a notable impact on the extent to which the wake region is affected by the SJA.
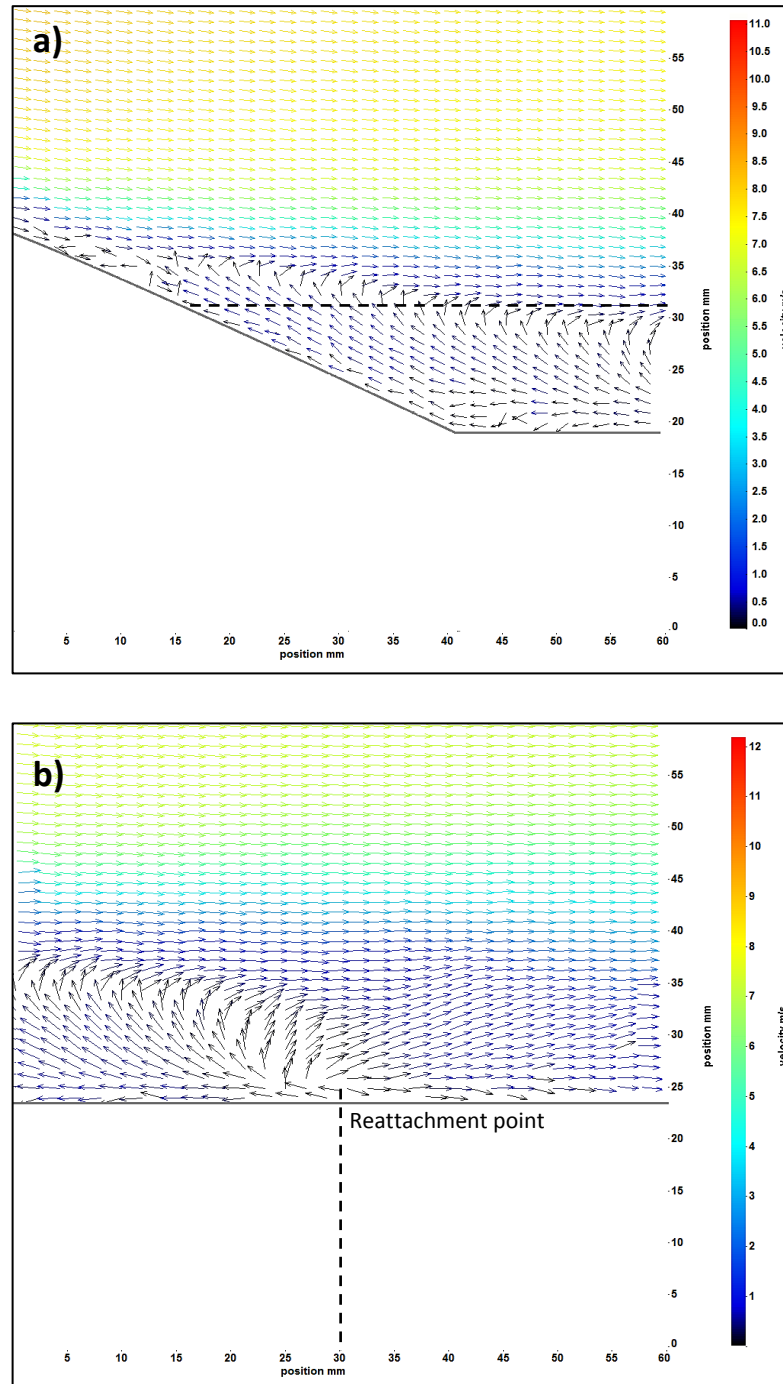

Figure 8.6: Velocity vectors of the wake area; a) Recirculation width wake (dead zone); b) Reattachment point (Un-modulated excitation, $\beta = 10^\circ$, $f_e = 1000$ Hz, $Vr = 0.5$, $U_\infty = 7$ m/s).
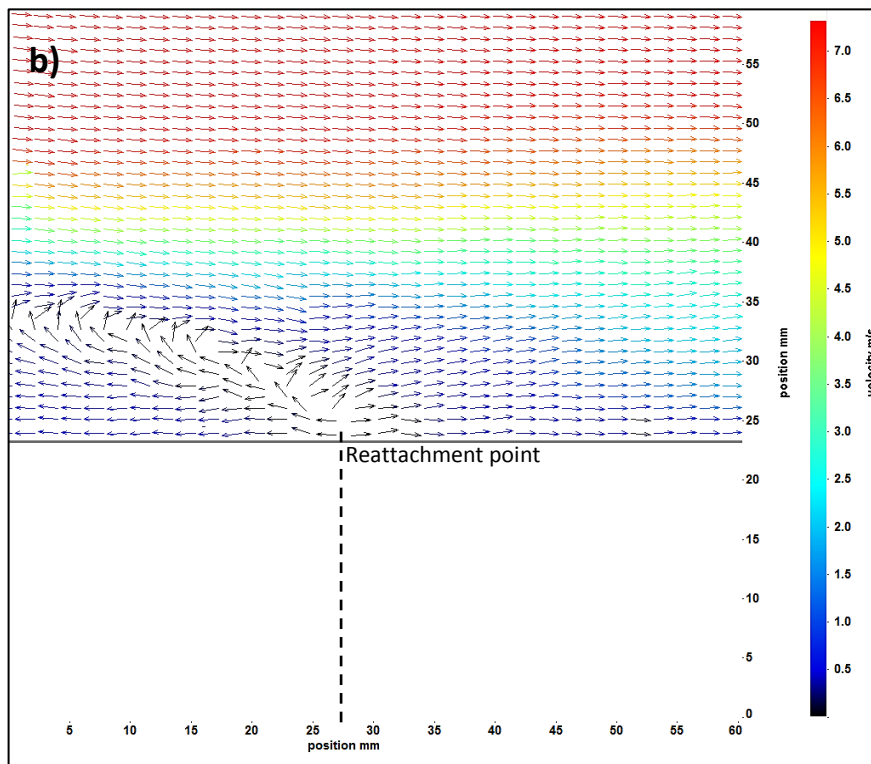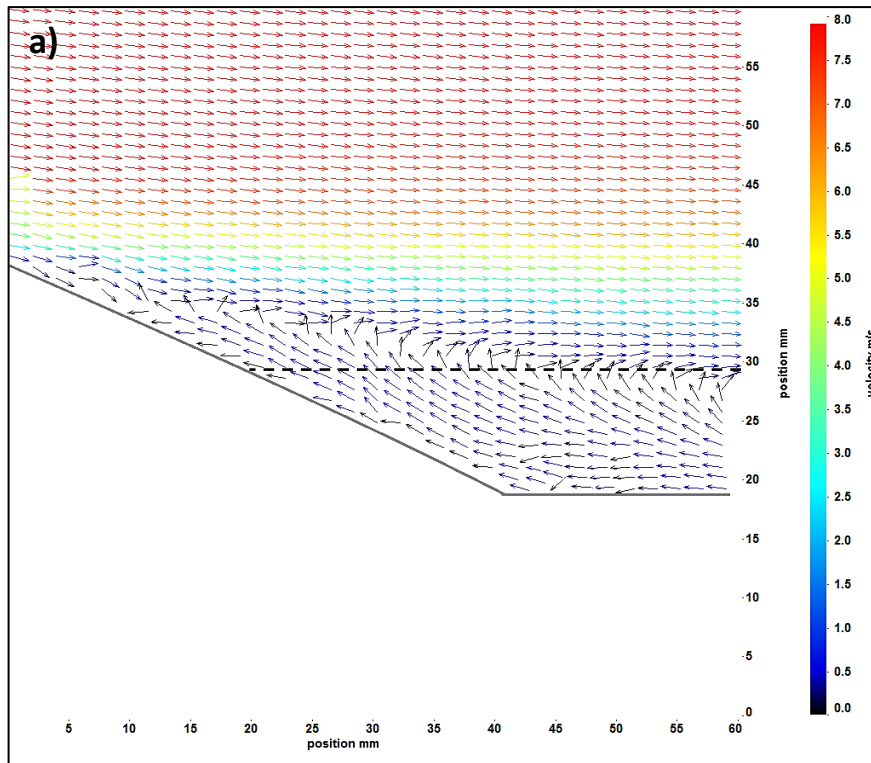
Figure 8.7: Velocity vectors of the wake area; a) Recirculation width wake (dead zone); b) Reattachment point (Un-modulated excitation, $\beta = 10^{\circ}$, $f_e = 1000$ Hz, $Vr = 1$, $U_{\infty} = 7$ m/s).
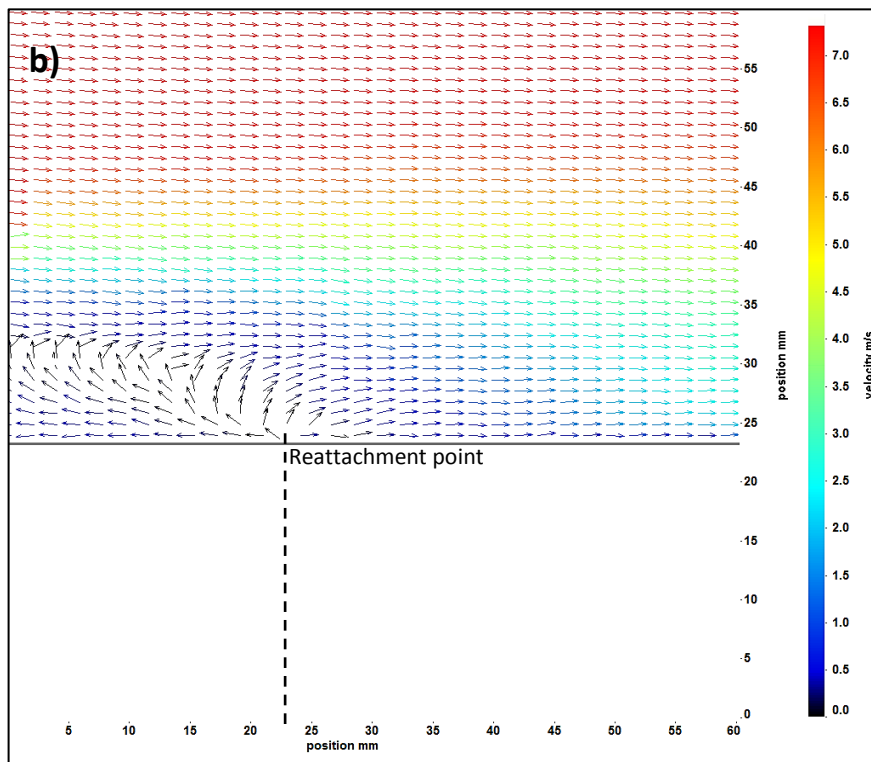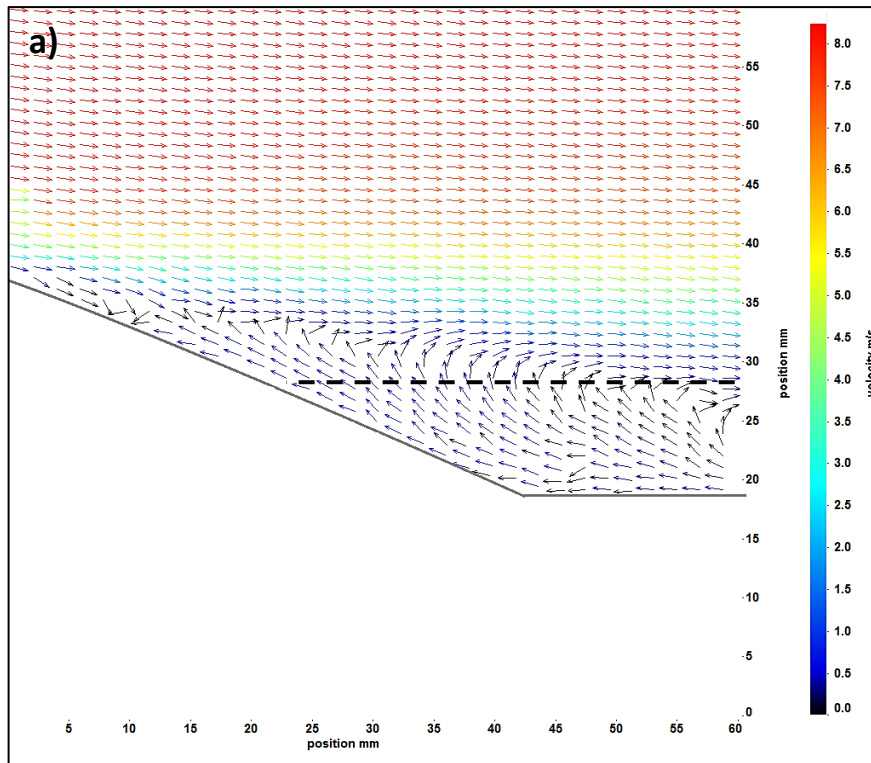
Figure 8.8: Velocity vectors of the wake area; a) Recirculation width wake (dead zone); b) Reattachment point (Un-modulated excitation, $\beta = 10°$, $f_e = 1000$ Hz, $Vr = 1.5$, $U_\infty = 7$ m/s).

To enhance understanding, **Figures 8.9 to 8.11** present the actuated and un-actuated streamline and vorticity in the wake area under ideal variables of excitation ($Vr = 1.5$, $f_e = 1000$ Hz, $\beta = 10°$). It can be seen that shear layer shedding and peak fluctuation take place in the wake region at the rear of the convex hump model, which is a defining feature of the recirculation area. **Figures 8.9a and b** support the results indicated above and it can be observed that the flow separation produces the un-actuated downstream recirculation zone which causes the velocity defect in the near wake. By contrast, in the actuated case, **Figures 8.10a and b** clearly showed that the wake area behind the hump model is narrowed by 24% compared to the un-actuated case as well as the reattachment point is shifted towards the hump edge by the effect of using un-modulated excitation signal to drive the actuators. This suggests that the actuation enhances the velocity and consequently, by comparison with the un-actuated case, the total separation bubble dimensions are reduced.

Furthermore, the main characteristic of vorticity in the un-actuated wake region at the rear of the hump is illustrated in **Figure 8.11a**. Again, the same ideal parameters of excitation ($Vr = 1.5$, $f_e = 1000$ Hz, $\beta = 10°$) are applied in conjunction with the vorticity structure in the un-actuated case (**see Figure 8.11a**) and the actuated case (**see Figure 8.11b**). The figure clearly shows that the actuated vorticity is slightly shifted towards the hump and the ground area due to the presence of SJA. The interaction between the synthetic jets and separated boundary layer could be responsible for bringing the vorticity shedding towards the hump surface at high velocity ratio, which could enhance the flow mixing in the wake region. An essential methodology for lowering both the separation length and recirculation width is to improve the mixing through bringing in more coherent structures into the boundary layer and this would allow high velocity fluid to be entrained from the outer area of the boundary layer to the near wake area behind the convex hump. Consequently, the SJAs could work as "vortex generators" that able to inject some coherent structure in the recirculation bubble and hence delaying the flow separation.
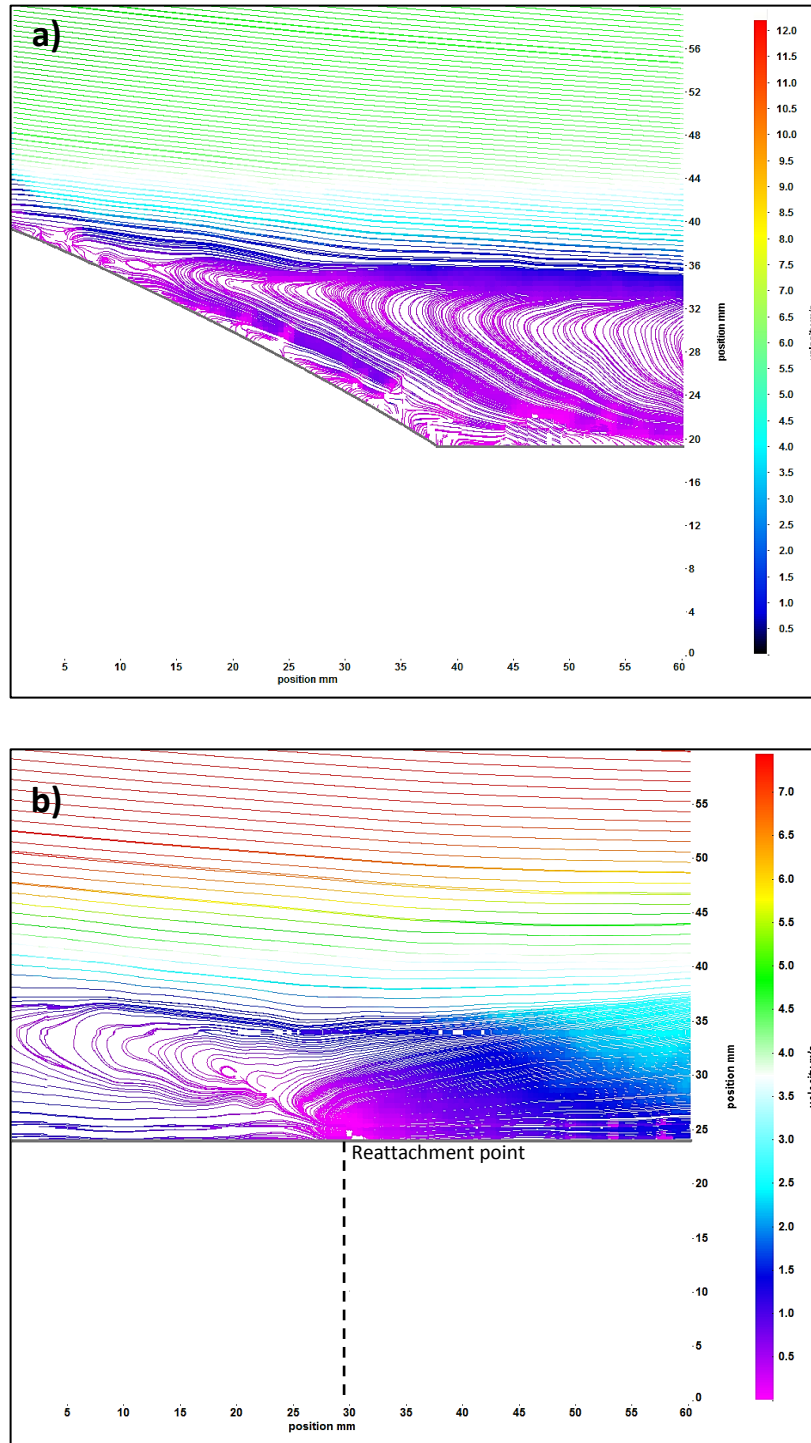
Figure 8.9: The velocity streamline of the un-actuated case showing: a) Recirculation zone; b) Reattachment point at $U_\infty = 7$ m/s.
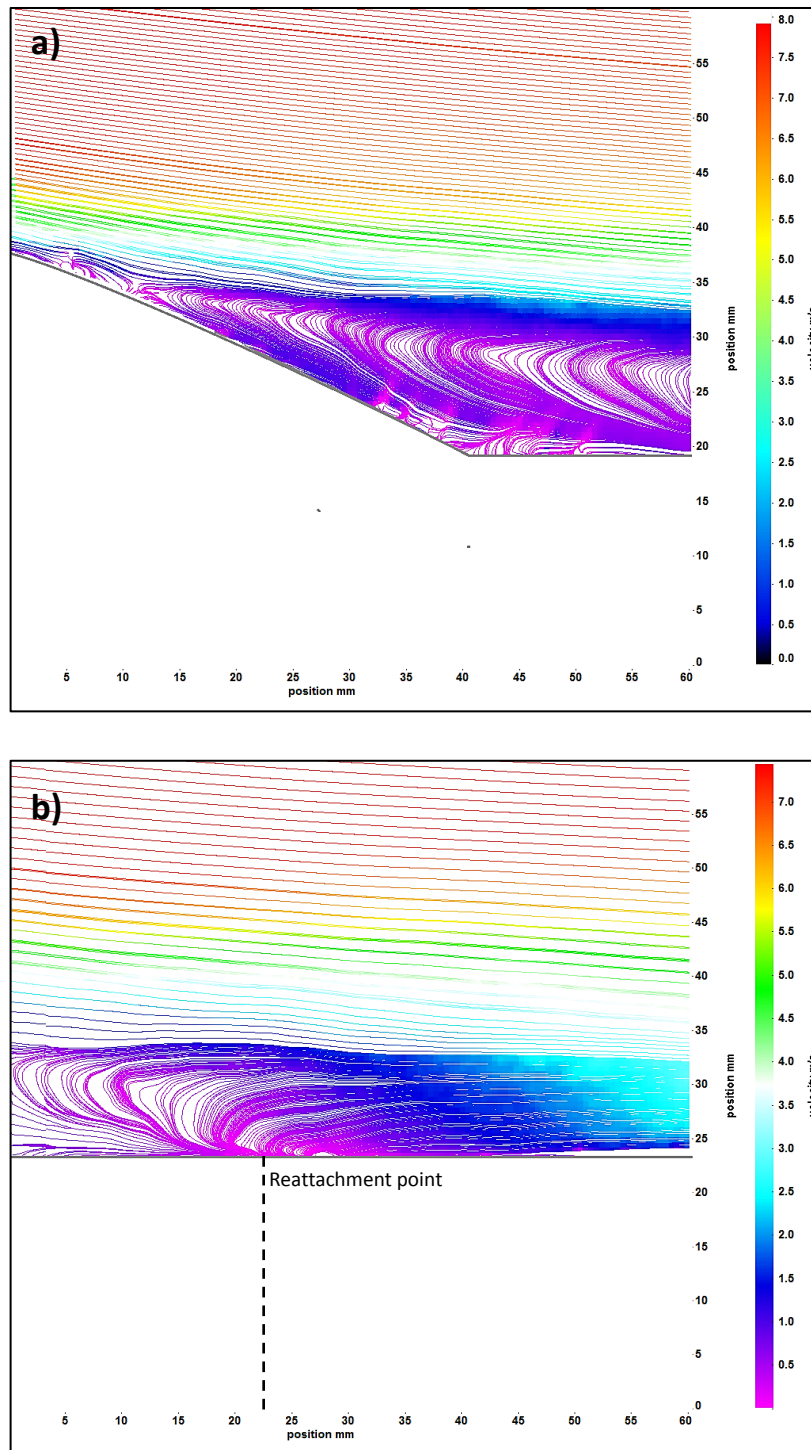
Figure 8.10: The velocity streamline of the un-modulated excitation case showing: a) Recirculation zone; b) Reattachment point at (U_∞ = 7 m/s, Vr = 1.5, f_e = 1000 Hz, β = 10°).
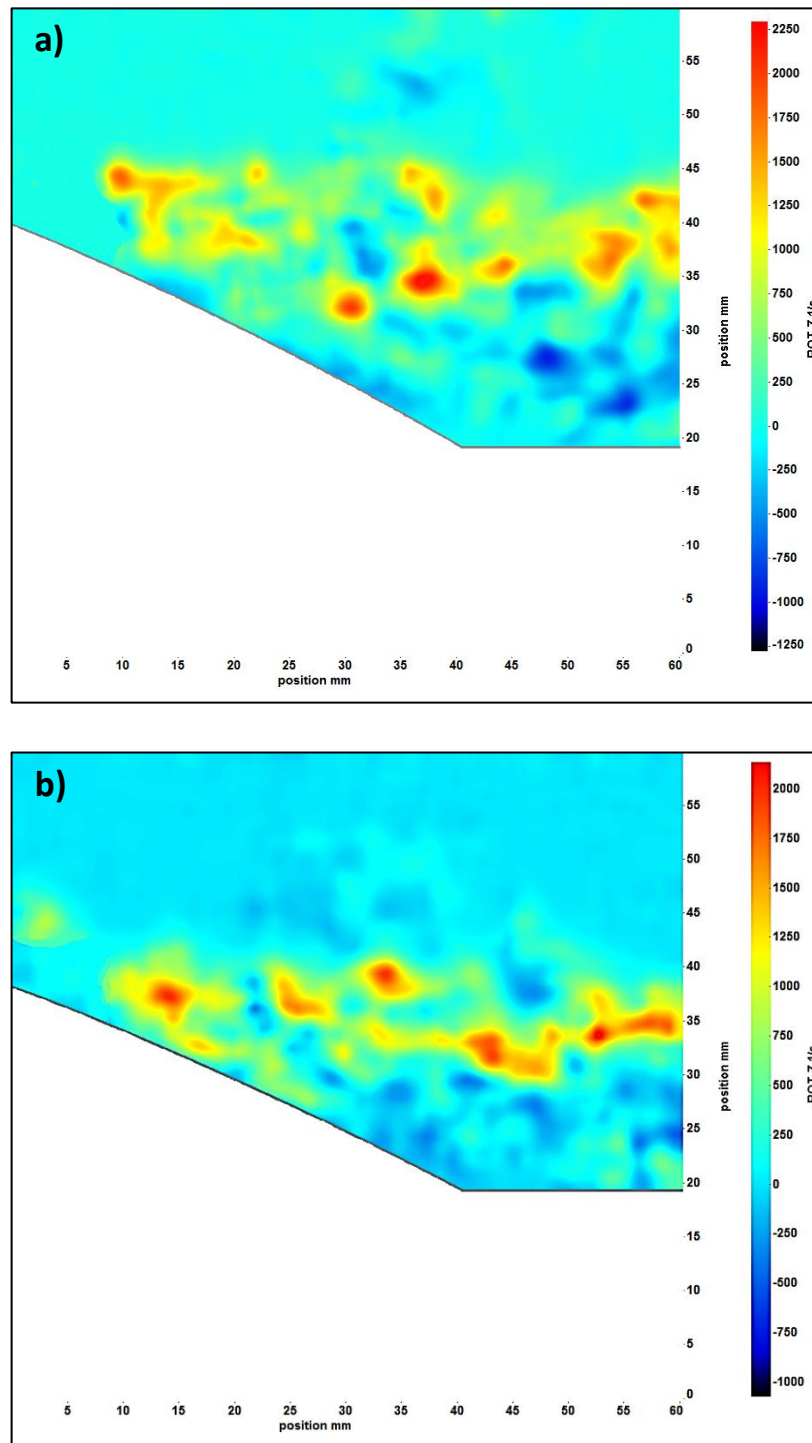
Figure 8.11: The vorticity images of: a) Un-actuated case; b) Actuated case at ($Vr =$ 1.5, U$_\infty$ = 7 m/s, f_e = 1000 Hz, β = 10°).

The velocity profile depicted in **Figure 8.12** supports the result mentioned above. By comparison to the un-actuated profile, the stream-wise velocity (Vx) profile is shown in this figure at X/L = 1 (at the edge of the hump). According to the findings,

an area of high velocity gradient is clearly seen by the un-actuated case in the shear flow with a reverse flow area in the range of about 0-14 mm. The velocity profile is identical to that in the un-actuated case when the synthetic jet activated at $Vr = 0.5$. On the other hand, at $Vr = 1$, a single sine wave is added and modifying the mean velocity in the wake region such that the recirculation width diminishes by up to 24%. Likewise, a rise in velocity ratio accentuates the decrease in recirculation width in the wake region. By contrast to the un-actuated case, a maximum decrease in reverse flow width occurred at $Vr = 1.5$, suggesting that the occurrence of synthetic jets considerably enhances the velocity in the boundary layer. In another words, the velocity deficit more likely to be augmented with high velocity ratio, resulting in effective flow control.
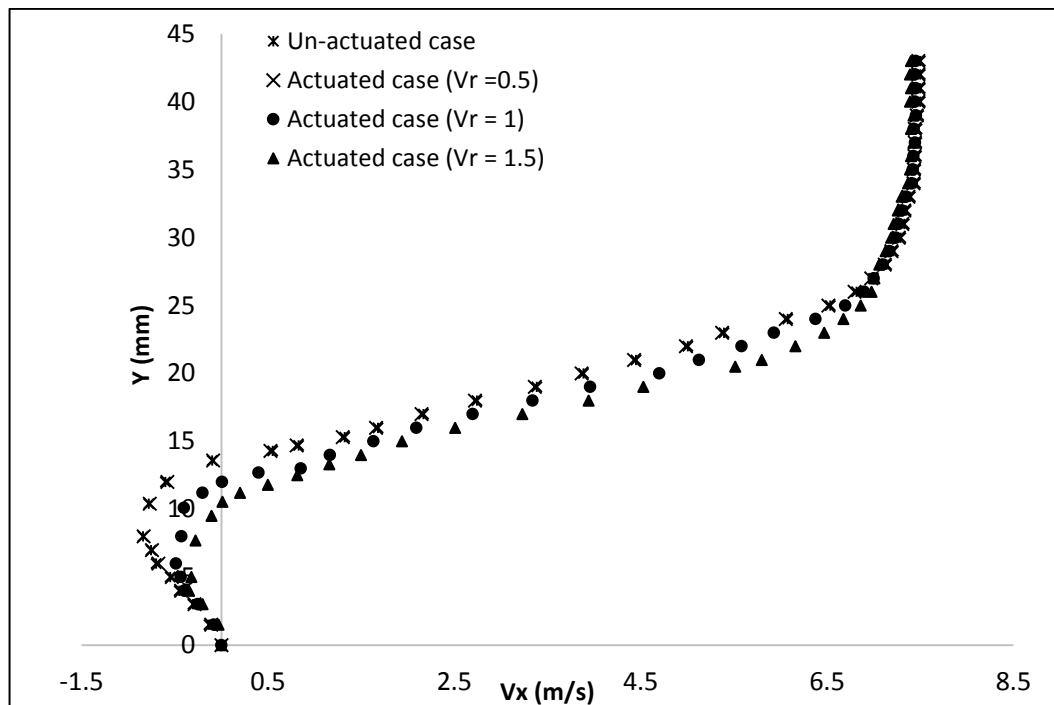

Figure 8.12: Stream-wise velocity profiles (Vx) at (un-modulated case, X/L = 1, β = 10°, U∞ = 7 m/s).

Therefore, the author infers that the control mechanism of the wake area behind the hump using synthetic jets located upstream of the recirculation area are similar to the explained shown in **Figure 8.13**, the figure clearly shows how the near-wall boundary layer is enhanced upstream of the separation location. The influence of this synthetic jets concept includes reduction in both the width of the reverse flow and the actual separation length. This reduction in the whole recirculation bubble is caused by the continuous vortex generated from the orifices which may entrained high velocity fluid from the outer area of the boundary layer to the near wake area behind the convex

174

hump which are then injected inside the recirculation bubble and hence promoting flow mixing. However, synthetic jet interaction was not able to achieve a completely separated bubble breakdown.
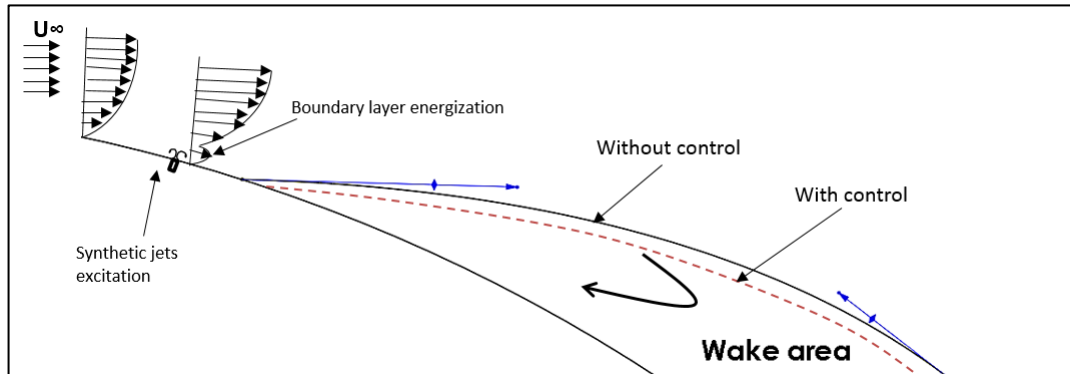

Figure 8.13: Synthetic jet actuator control mechanism in the wake area.

8.4. Results: Amplitude Modulation Excitation

This section demonstrates again how the PSD, reverse flow, separation length and the reattachment point in the wake area behind the hump model are altered under the influence of the amplitude modulation actuation (Case two in **Figure 8.2**). The effect of amplitude modulation excitation on the wake region behind the convex hump model is again excited at the same velocity ratio range, and at the same angular position for the actuation angle (β). The carrier frequency of the modulated signal is set to the Helmholtz frequency of the cavity ($f_c = f_H = f_e = 1000$ Hz) while the modulated frequency was set similar to the shedding frequency (at 7 m/s the $f_s \approx f_m$ 75 Hz) and hence $f_e/f_s = 1$. Similarly, the angular position of the actuation angle (β) was set to 10°, while the velocity ratio (*Vr*) ranged between 0.5, 1, and 1.5 respectively.

In much the same way as was seen for the single sine wave actuation (Un-modulated case), the results indicate that the amplitude modulation actuation can also change the spectral distribution in the wake area when compared to the un-actuated case. This change in the power spectral content takes place when the jet is activated and this is illustrated in **Figures 8.14a to c**. From the figure it is obvious that in the un-actuated case, the small 76 Hz peak is completely decreased at velocity ratio *Vr* = 1.5 and β = 10°, and there is a clear visible reduction in the broadband energy level between 0 and 500 Hz. However, the ability to affect the spectral peak was decreased as the velocity ratio of the actuation decreases, until *Vr* reaches 0.5 which showed no

effect can be seen on the spectral peak and hence the entire level of energy, this is similar to some extent to that seen in un-modulated excitation. Again, this suggested that a minimum velocity ratio (*Vr*) of one was needed for the synthetic jets to be able to affect the PSD and the flow above it, particularly in the wake region behind the hump model.
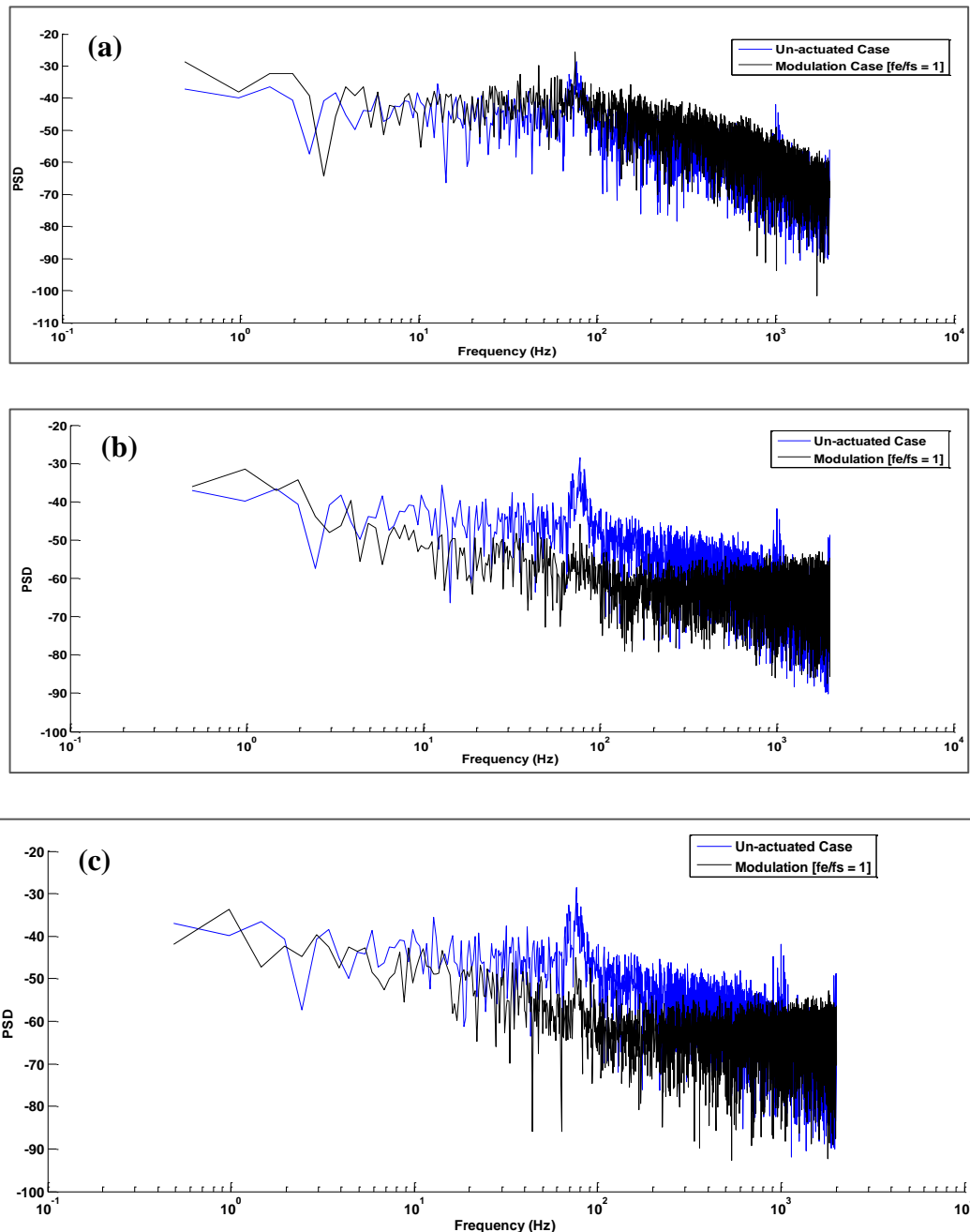

Figure 8.14: The power spectral density with and without modulation actuation at different velocity ratios a) *Vr* = 0.5, b) *Vr* = 1, c) *Vr* = 1.5 (U$_\infty$ = 7 m/s, β = 10$^\text{o}$).

However, it can be clearly observed that with amplitude modulation excitation, the output from the PSD still shows a small peak at 76 Hz. If the modulated frequency is changed from 76 Hz ($f_e/f_s \approx 1$) to 150 Hz ($f_e/f_s \approx 2$) then it is possible to ascertain whether this small high point in the dominant frequency is associated with the shedding frequency of the separated shear layer (f_s) or if it is linked to the synthetic jets vortex rings (f_e). The results of this analysis are illustrated in **Figure 8.15** and whilst the effect of the synthetic jet actuation is visible, it is still at 76 Hz and this is an indication that this peak is linked to the shedding frequency. From this it can be inferred that the velocity ratio is seen to be efficient in determining the degree to which both PSD are reduced. In general, it can be deduced from the results that the increase in the excitation frequency, f_e, ($f_e/f_s \approx 2$) has no influence on the PSD. Additionally, in general, the un-modulated excitation has a slightly higher effect compared to the modulated one in reducing the energy level in the wake area. This feature has been examined further in the following sections using PIV technique.
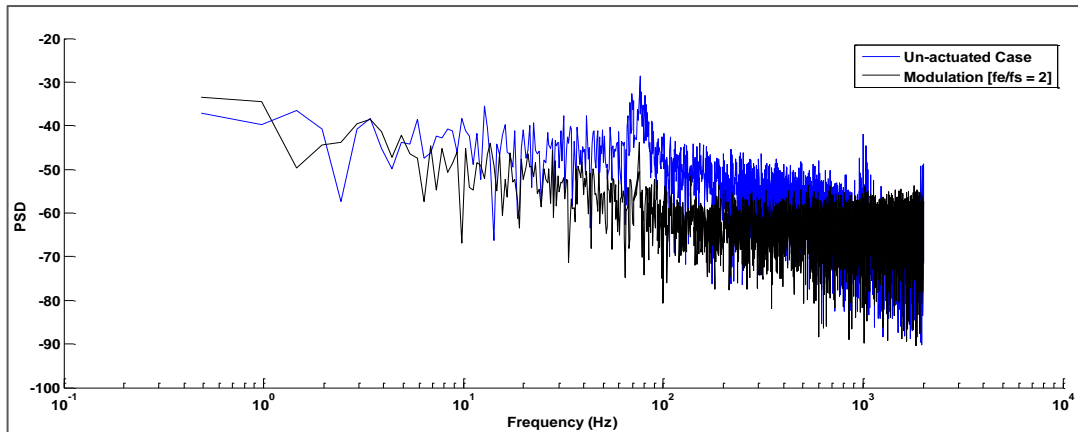

Figure 8.15: The power spectral density under the modulation frequency of 150 Hz at $Vr = 1.5$ ($U_\infty = 7$ m/s, $\beta = 10^o$, $f_e/f_s = 2$).

Figures 8.16 to 8.18 below show how the recirculation width and reattachment point in the wake area changes under the influence of using an amplitude modulated excitation signal to drive the actuators using the PIV technique. As was the case for using the un-modulated excitation signal at $Vr = 0.5$, the recirculation area and reattachment point are almost the same as in the un-actuated case which implies that there is no obvious control effect at this velocity ratio and this can be seen in **Figures 8.16a and b**. Looking at **Figures 8.17 and 8.18**, using amplitude modulation

excitation has the ability to reduce the recirculation width and move the reattachment point towards the hump edge at both $Vr = 1$ and 1.5 as compared with the un-actuated cases. As the velocity ratio increased to the maximum value of 1.5, then by looking at the un-actuated cases shown previously, it can be seen that the width of the recirculation region is reduced and the reattachment point is moved by 6.5 mm towards the hump edge. Moreover, at $Vr = 1.5$, the control effect is improved significantly and the recirculation width became even thinner, and this was decreased by about 21% compared to the un-actuated case as shown in **Figure 8.16a.**

Again, similar to what has been seen in the un-modulated excitation, it was noted that a non-dimensional velocity ratio (Vr) of more than one was required for the synthetic jets to have an impact on the recirculation region and the reattachment point in the wake region. This suggested that at this velocity ratio ($Vr \geq 1$), the synthetic jets were able to affect the boundary layer and the flow above it. Furthermore, with a larger velocity ratio of 1.5, the synthetic jets more likely to vector the wake flow and as a result the flow separation is delayed which resulted in a reduction of the whole recirculation bubble. Therefore, it is evident from the results that for velocity ratios greater than one the vortex generated by synthetic jet actuators could have enough momentum to emerge through the boundary layer and significantly affect the flow above it
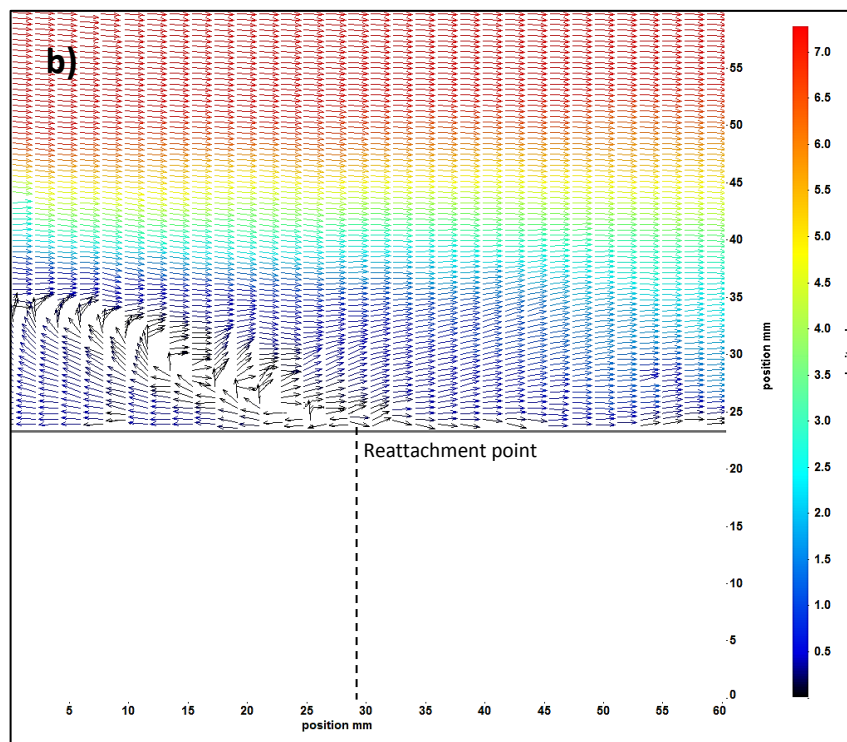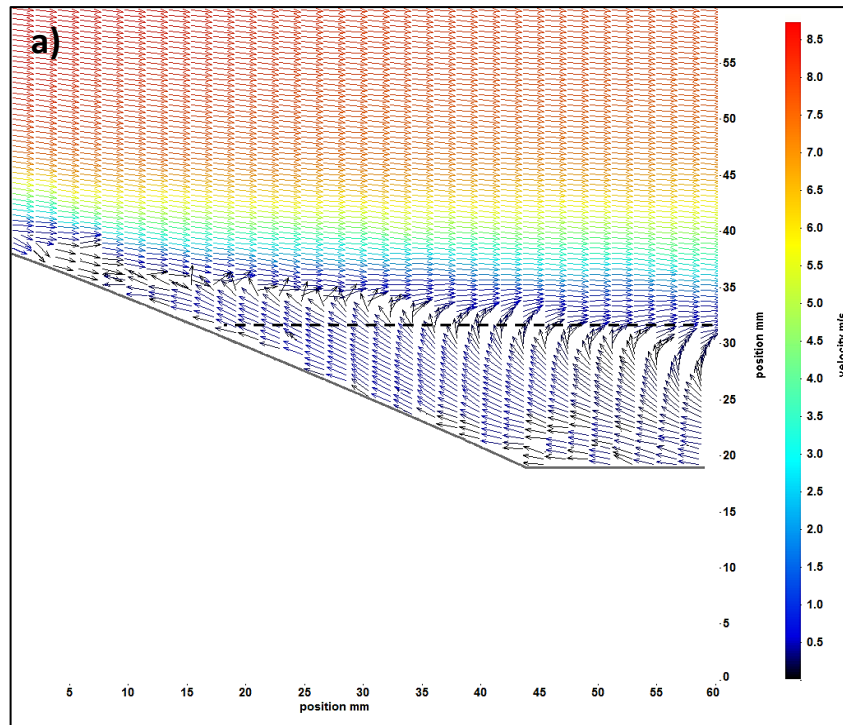
Figure 8.16: Velocity vectors of the wake area; a) Recirculation width wake (dead zone); b) Reattachment point (Modulated excitation, $\beta = 10^{\circ}$, $fc = 1000$, $f_{m} = 75$ Hz, $Vr = 0.5$, $U_{\infty} = 7$ m/s).
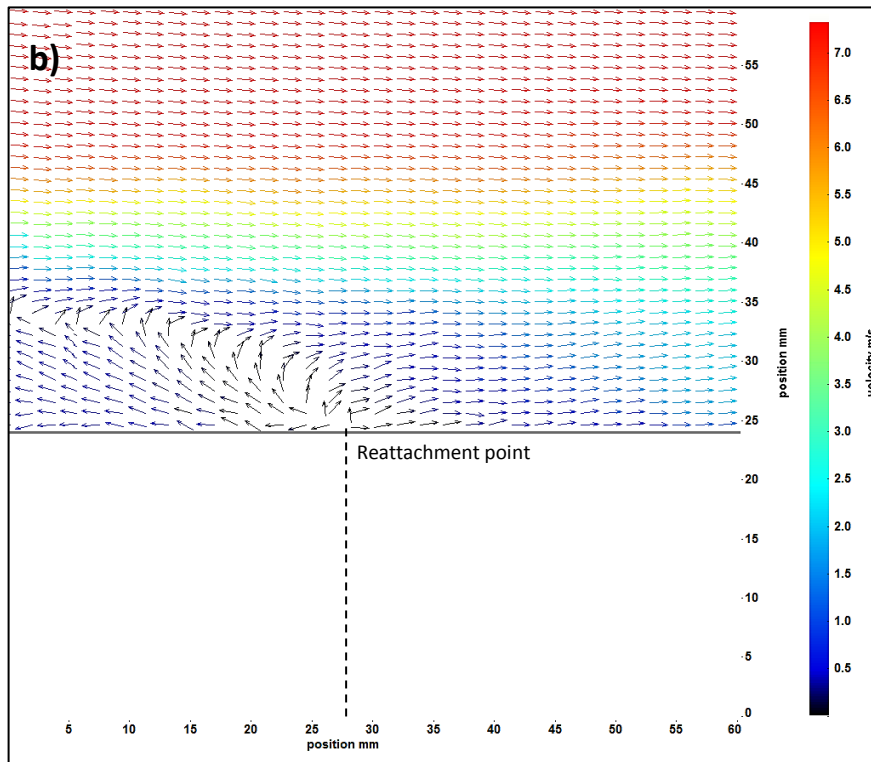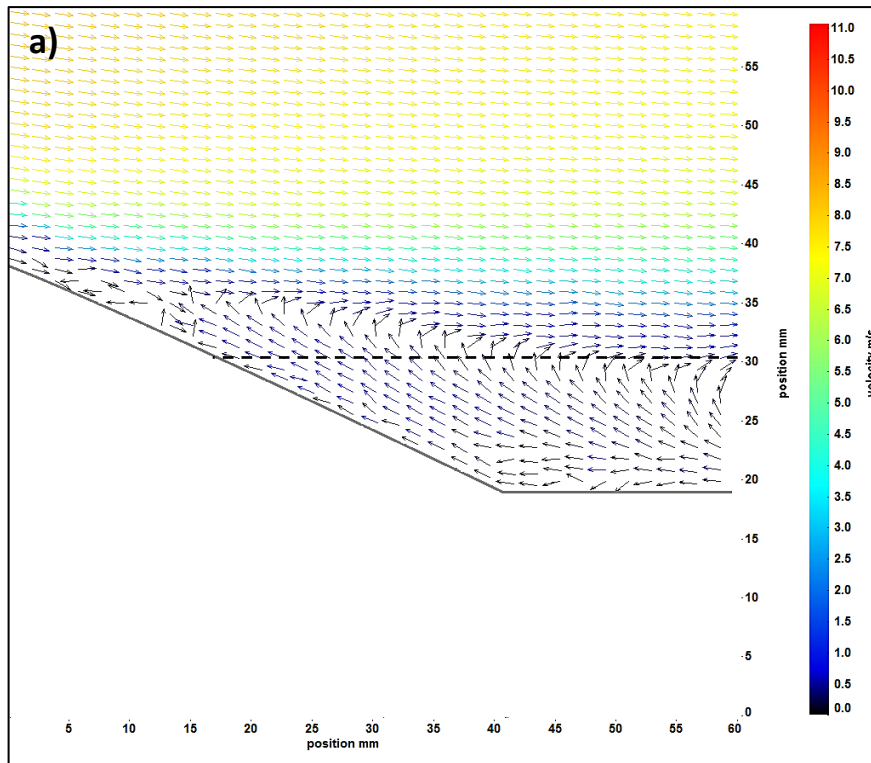
Figure 8.17: Velocity vectors of the wake area; a) Recirculation width wake (dead zone); b) Reattachment point (Modulated excitation, $\beta = 10^o$, $fc = 1000$, $f_m = 75$ Hz, $Vr = 1$, $U_\infty = 7$ m/s).
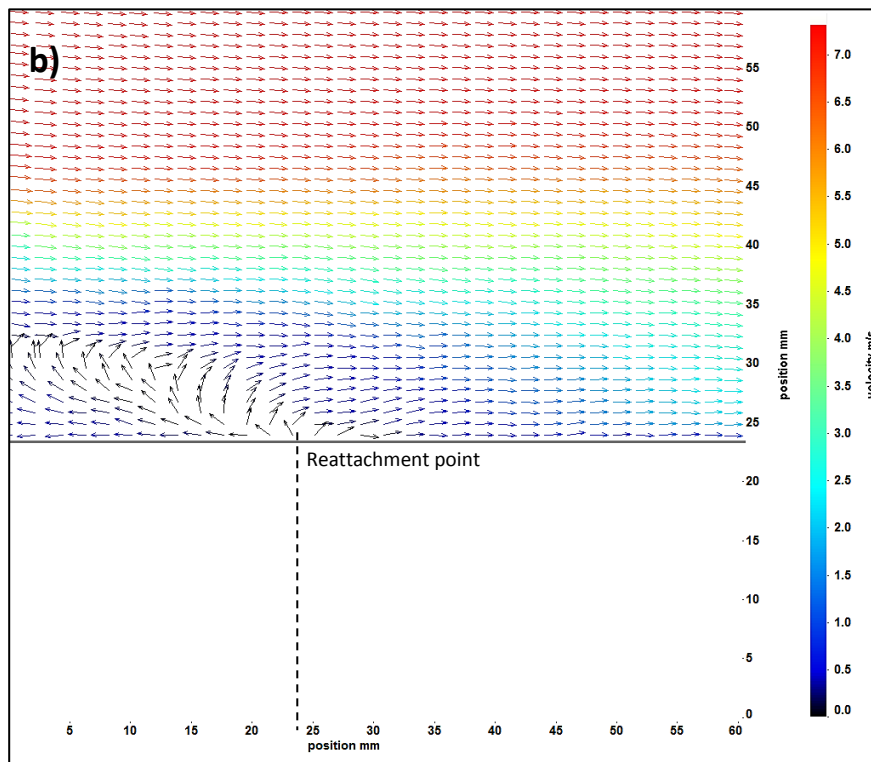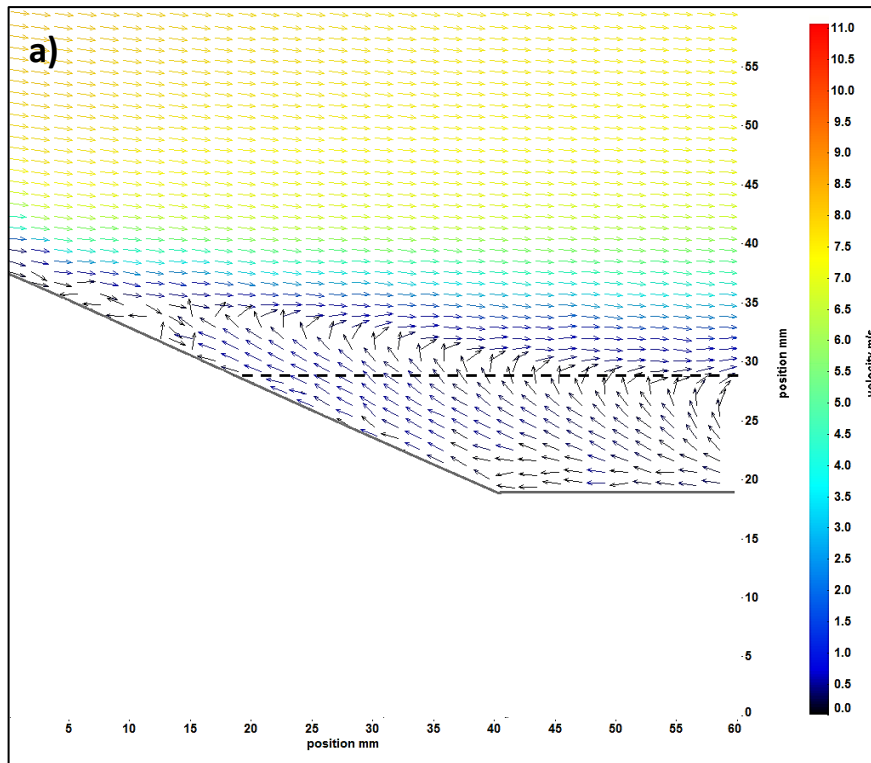
Figure 8.18: Velocity vectors of the wake area; a) Recirculation width wake (dead zone); b) Reattachment point (Modulated excitation, $\beta = 10^\circ$, fc $= 1000$, $f_m = 75$ Hz Hz, $Vr = 1.5$, $U_\infty = 7$ m/s).

Similarly, the velocity profile of both un-actuated and actuated flow fields at different velocity ratios with amplitude modulation excitation at X/L = 1 is illustrated in **Figure 8.19**. The figure clearly shows that the velocity profile supports the results shown above and a small pocket of recirculation flow can be seen along the vertical direction at the edge of the hump. Again, by contrast to the un-actuated case, a maximum reduction of up to 21% in recirculation width appeared at Vr = 1.5, suggesting that the interaction between the synthetic jets and the boundary layer in the wake region considerably enhances the velocity in the wake region at a high velocity ratio, resulting in effective flow control.
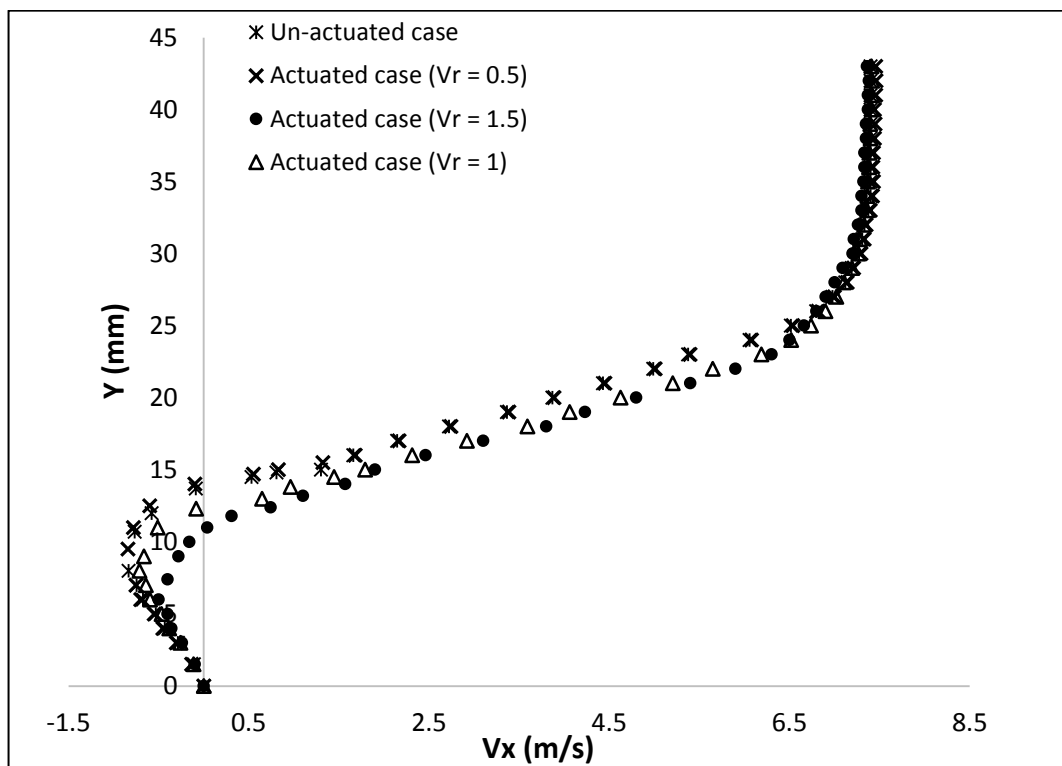
Figure 8.19: Stream-wise velocity profiles (Vx) using amplitude modulation excitation at (X/L = 1, β = 10°, U_∞ = 7 m/s).

Again, both un-actuated and actuated cases with the amplitude modulation excitation signal used to drive the actuator are presented as streamline and vorticity of flow pattern in the wake region behind the convex hump which are illustrated in **Figures 8.20 to 8.22**. Similarly, the optimum velocity ratio and angular position of the actuation angle of Vr =1.5 and β = 10° respectively were used in flow control. It can be seen that the control effect is clearly noticeable such that the recirculation width

was decreased to a larger value at $Vr = 1.5$ compared to the un-actuated case which is linked to the synthetic jet actuation as illustrated in **Figure 8.21a**. Moreover, the reattachment point also moved by 6.5 mm towards the hump edge when the SJAs activated which again resulted in total separation bubble decrease as shown in **Figure 8.21b**. Furthermore, the effect of actuation on the vorticity patterns is indicated in **Figure 8.22b.** The figure clearly shows that for a maximum velocity ratio, $Vr = 1.5$, shear layer vorticity is pushed towards the hump surface because of the interaction between the synthetic jets and the detached shear layer. This interaction could generate a complex vortical structure at a high velocity ratio which could be responsible for bringing the vorticity shedding towards the hump surface. Therefore, the output from PIV measurements confirmed that the effect of using amplitude modulated excitation to drive the actuator in the recirculation area, reattachment point and hence the actual length of the separation bubble is caused by the vortex generated by the synthetic jet actuators which could deliver the best flow control at high velocity ratio. These vortices might remain within the boundary layer and continue further downstream and thus provide more efficient mixing and vorticity strength. Moreover, the author infers that an essential methodology for reducing both the separation length and recirculation width and hence delaying flow separation is to improve the mixing through bringing more consistent structures into the boundary layer.
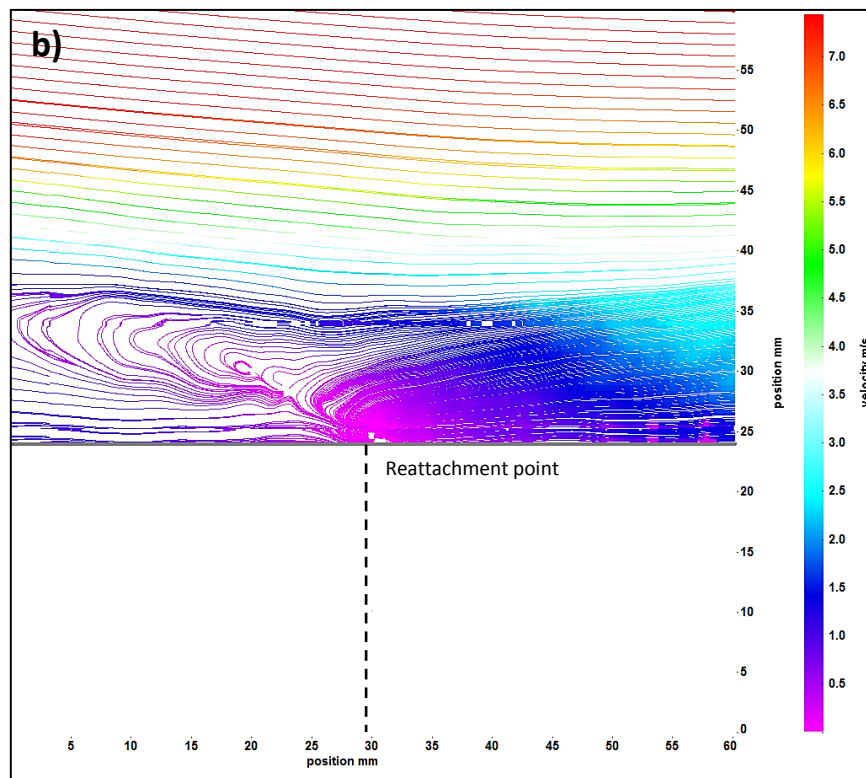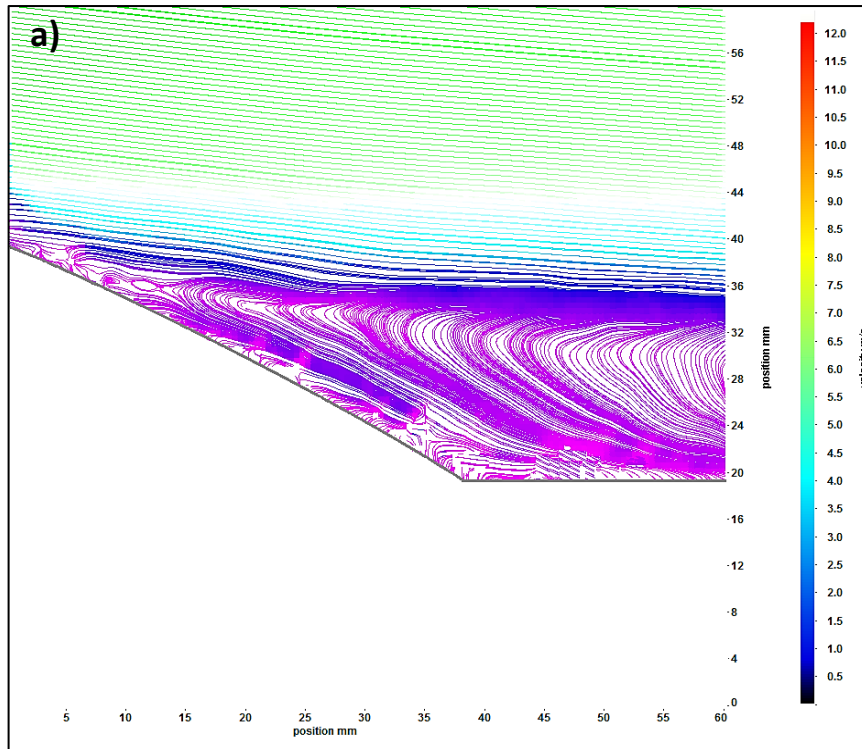
Figure 8.20: The velocity streamline of the un-actuated case showing: a) Recirculation zone; b) Reattachment point at $U_\infty = 7$ m/s.
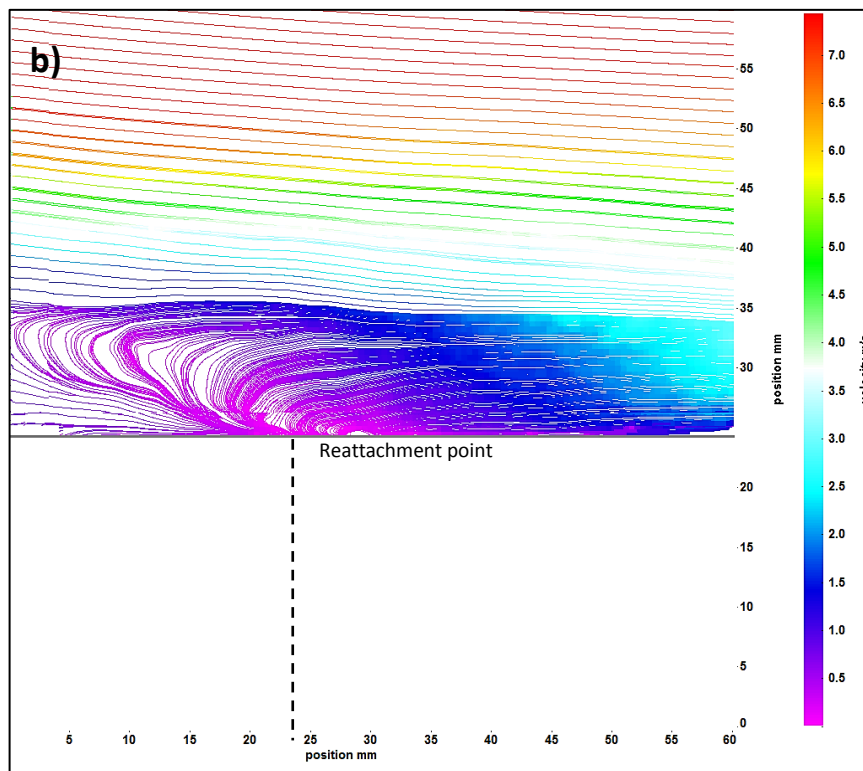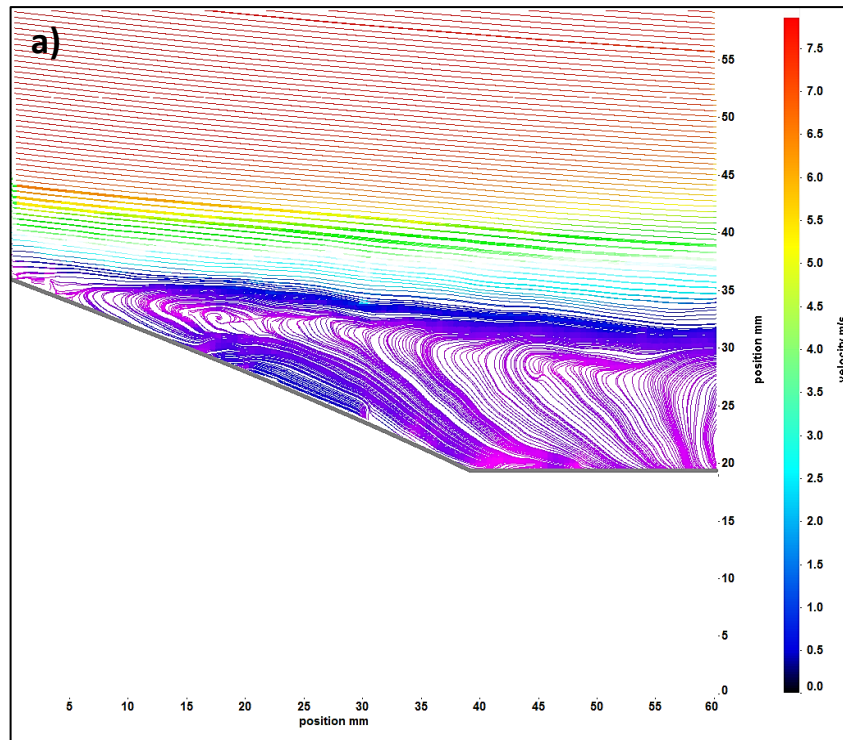
**Figure 8.21:** The velocity streamline of the modulated excitation case showing: a) Recirculation zone; b) Reattachment point at (Amplitude modulation, fc = 1000 Hz, f_m = 75 Hz, Vr = 1.5, U_∞ = 7 m/s, β = 10°).
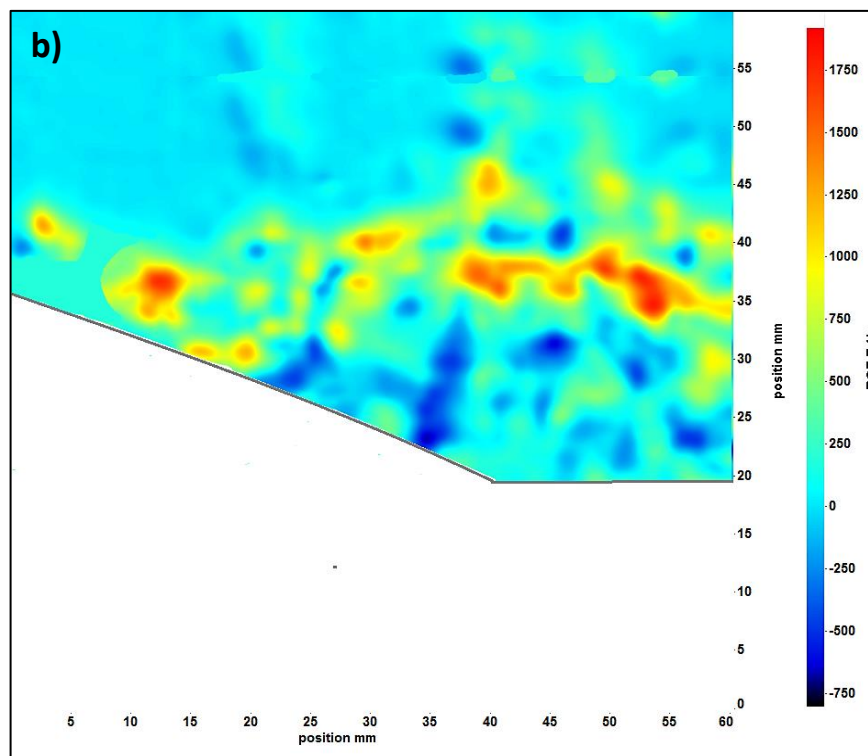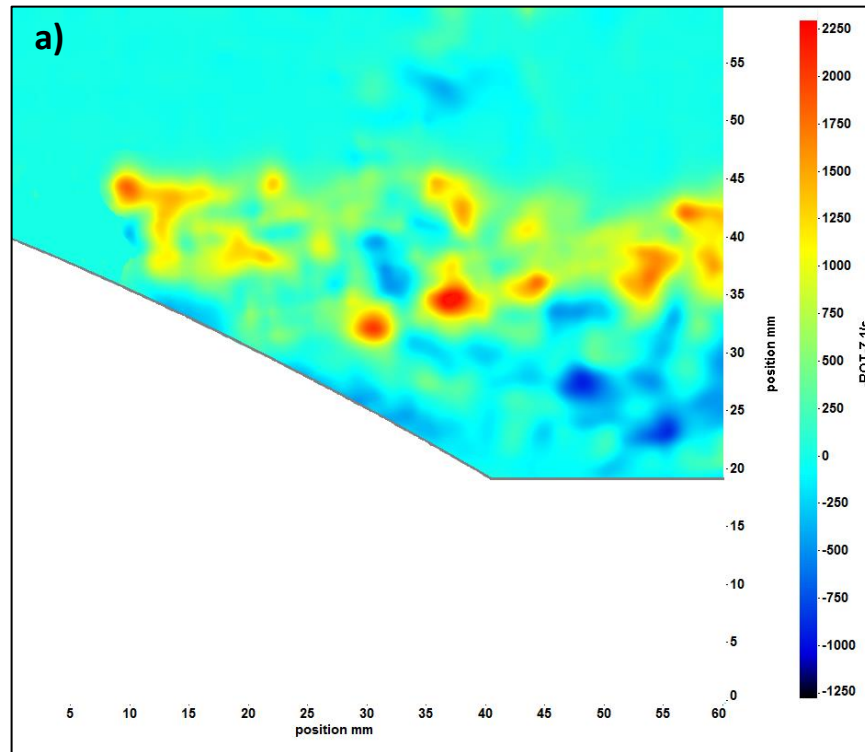
Figure 8.22: The vorticity images of; a) Un-actuated case; b) Actuated case at (Amplitude modulation, fc = 1000 Hz, f_m = 75 Hz, Vr = 1.5, U$_\infty$ = 7 m/s, β = 10º).

In general, the findings given earlier demonstrated that the reduction of both recirculation width and reattachment point is again seen when the synthetic jet actuators are operated at either modulated or un-modulated excitation signals, but the effect is slightly weaker for the modulated excitation than the un-modulated one. However, for the two excitations, the width region of reverse flow, reattachment point and hence the actual separation bubble dimensions behind the hump model are decreased when the actuators are activated and this reduction became larger as the velocity ratio was increased. In addition, at $Vr = 1.5$, the results showed that the highest reduction in recirculation width was seen to be 24% when the un-modulated excitation signal was used, while this reduction in the recirculation width reduced to 21 % when the amplitude modulation excitation was used compared to the un-actuated cases. However, this reduction in the recirculation width when the amplitude modulation signal used was seen to be lower than the maximum reduction seen for the single sine actuation case (Un-modulated case). Moreover, when the un-modulated excitation signal was used, the reattachment point was moved towards the hump rear edge and this movement was somewhat higher compared to the modulated excitation signal.

As observed earlier the PIV and hot-wire measurements (HW) showed that using the un-modulated excitation signal, $Vr > 1$ and $\beta = 10^o$ had profound influence on the separation bubble dimensions in the wake area. Therefore, it is worth to extend the experiments to a higher freestream velocity of 10 m/s, and to implement this, the optimum excitation parameters were used in this test, for example, the velocity ratio was set to a maximum value of 1.1 (as the maximum velocity of the synthetic jet actuator is limited to 11m/s at 32 Vrms), a single sine wave excitation is selected to drive the actuator which showed better control effect compared to the modulated wave. Near-wake flow measurements behind the hump were conducted using the PIV system with both actuated and un-actuated flow fields and all of these measurements were performed both with and without synthetic jet actuation. The un-actuated flow fields over the convex hump at a freestream velocity of 10 m/s are shown in **Figures 8.23a and b**. The flow again can be divided into two regions. The first region is the recirculation area while the second zone consists of the reattachment point.
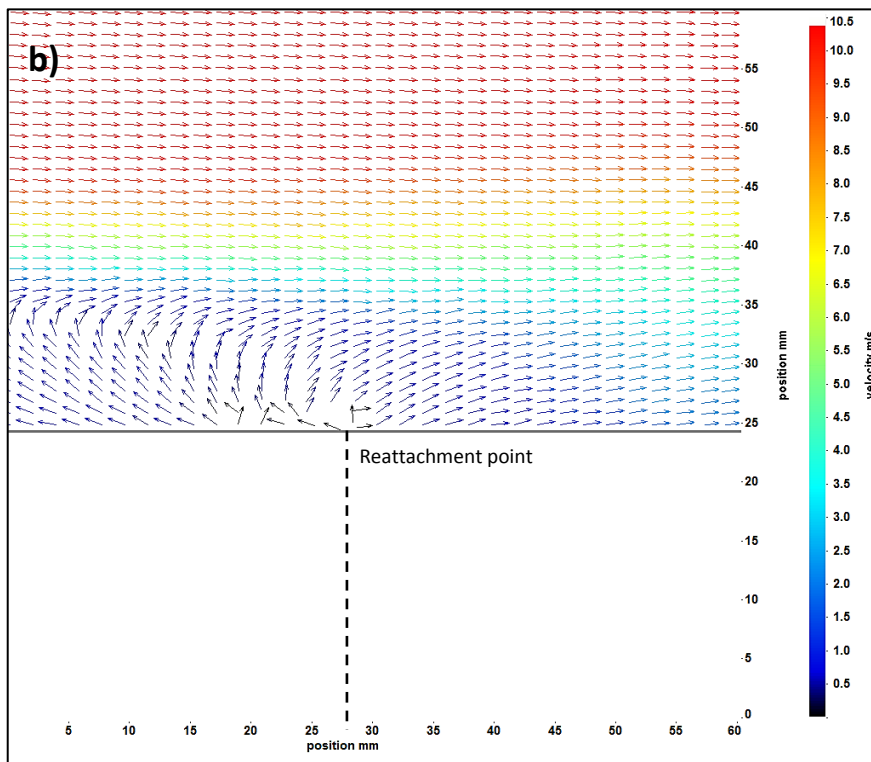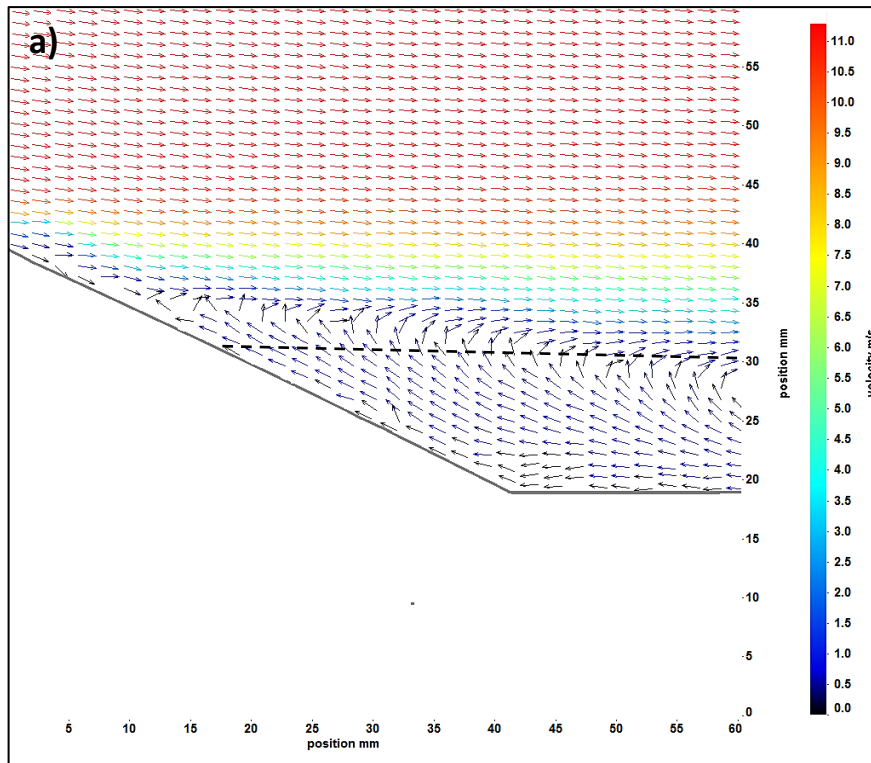
Figure 8.23: Velocity vectors of un-actuated case a) Recirculation width; b) Reattachment point ($U_\infty = 10$ m/s).

The viscous effect reduces when the freestream velocity is increased from 7 m/s to 10 m/s and at higher velocity, the onset of separation location is delayed compared to 7 m/s velocity. This delay in the onset of the separation location as the freestream velocity rises is caused by the fact that at larger velocities the momentum of the cross-flow increases. As well as the total length of separation, the width of the recirculation area is also affected by these factors. Anyway, the width of the recirculation area and reattachment point are found to be $Y = 11$ mm ($Y/h = 0.36$) and $X = 28$ mm ($X/L = 0.14$, measured from the rear of the hump) respectively.

In order to achieve a clearer picture of what the synthetic jets consequences are on the reverse flow and reattachment point at a higher free stream velocity, the alterations to the un-actuated case indicated above are illustrated in **Figures 8.24a and b**. **Figure 8.24a** clearly shows that the reverse flow width is reduced by 14% and moved downwards compared to the un-actuated case. Moreover, the reattachment point is also moved towards the rear of the hump by about 3 mm compared to the un-actuated case such that it is reduced from 28 mm to 25 mm when the SJA operated as shown in **Figure 8.24b**. This reduction in the recirculation area and separation length is again due to the interaction between the synthetic jets and the separated shear layer in the wake area and as a result the region of negative velocity is slightly reduced. However, this effect is seen to be significantly lower compared to 7 m/s velocity, suggesting that the momentum of the cross-flow at higher freestream velocity, is higher than momentum added by the synthetic jets and hence these jets are more likely to be contained inside the boundary layer and are not able to move further downstream in the wake area and hence it is not capable of bringing the momentum to the boundary layer and produces a better control effect.
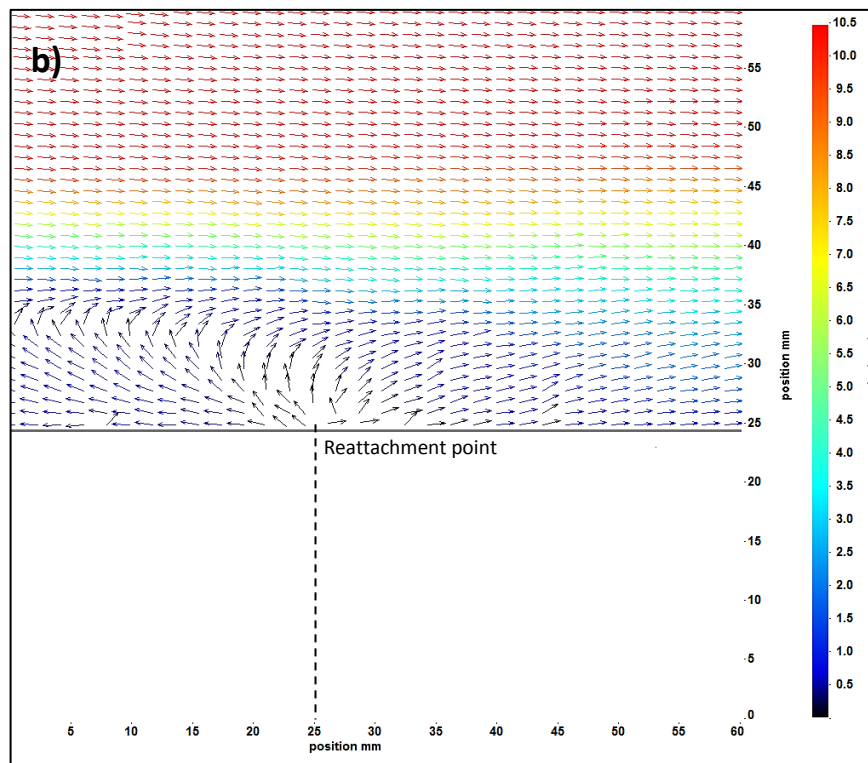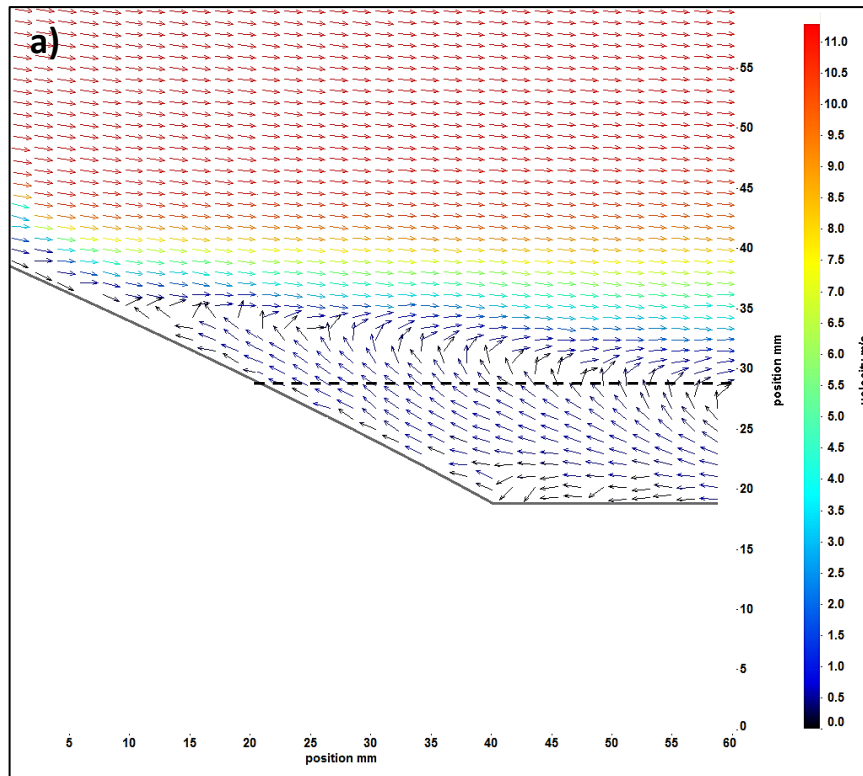
Figure 8.24: Velocity vectors of actuated wake area; a) Recirculation area; b) Reattachment zone ($\beta = 10^o$, $f_e = 1000$ Hz, $Vr = 1.1$, $U_\infty = 10$ m/s).

Furthermore, **Figures 8.25 to 8.27** present the dominant feature of vorticity patterns and velocity streamline under the same operation parameters indicated above ($Vr = 1.1$, $f_e = 1000$ Hz, $\beta = 10^{\circ}$). It appears from the figures that the synthetic jet control effect from the PIV measurement is somewhat similar to 7 m/s freestream velocity. Therefore, better flow control effect is achieved at the maximum velocity ratio ($Vr = 1.1$ here), which is able to push the vorticity shedding towards the hump surface as shown in **Figure 8.25**. **Figures 8.26a and b** support the previous findings in terms of the flow recirculation width and reattachment location for the un-actuated case. However, at the same conditions, the width of the circulation and the reattachment point were also reduced compared to the un-actuated case as shown in **Figure 8.27** due to the vortex rings produced by the synthetic jets. Therefore, similar to 7 m/s, the synthetic jet was able to modify the recirculation bubble size in the wake area to be reduced which is caused by the flow separation delay. However, at higher freestream velocity lower effect was seen compared to 7 m/s velocity due to that at high velocity, an additional momentum can be added to the cross-flow which reduces the actuators effect.
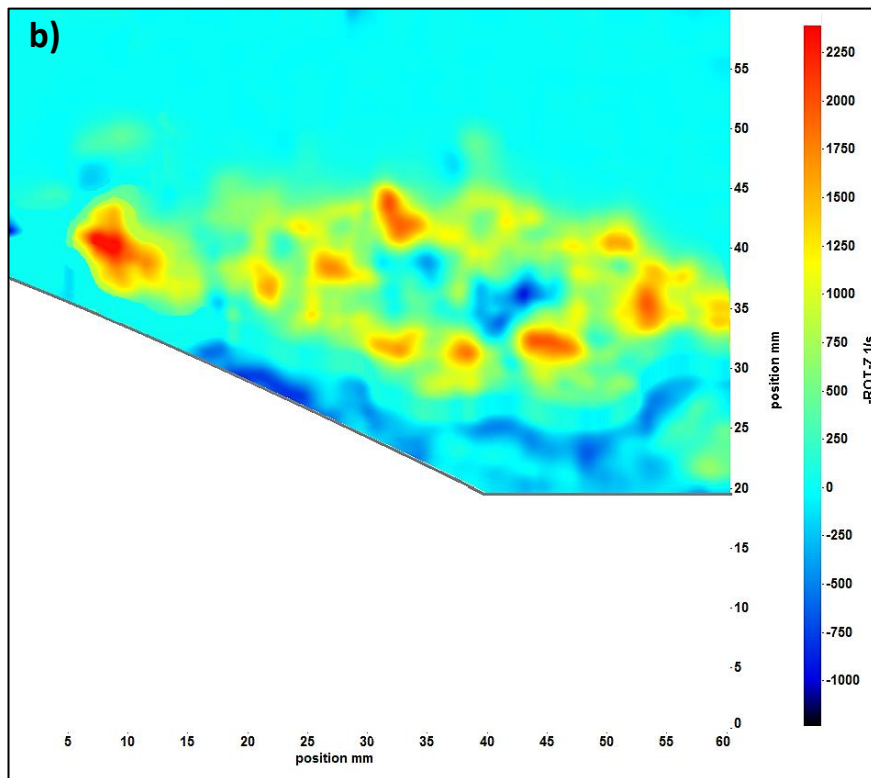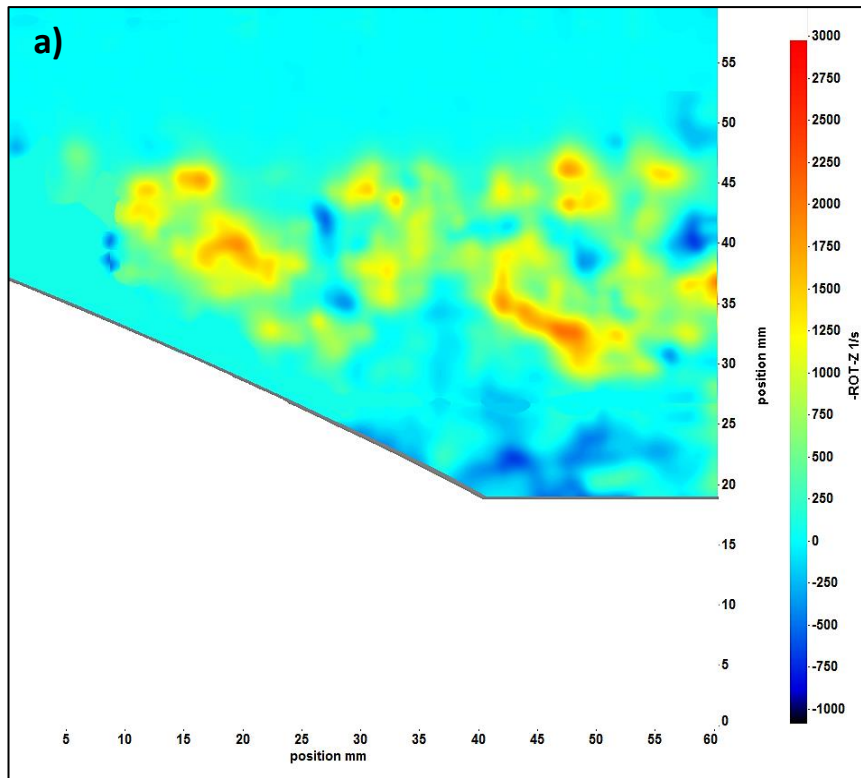
Figure 8.25: The vorticity images of; a) Un-actuated case; b) Actuated case at (Un-modulation excitation, f_e = 1000 Hz, U_∞ = 10 m/s, Vr = 1.1, β = 10°).
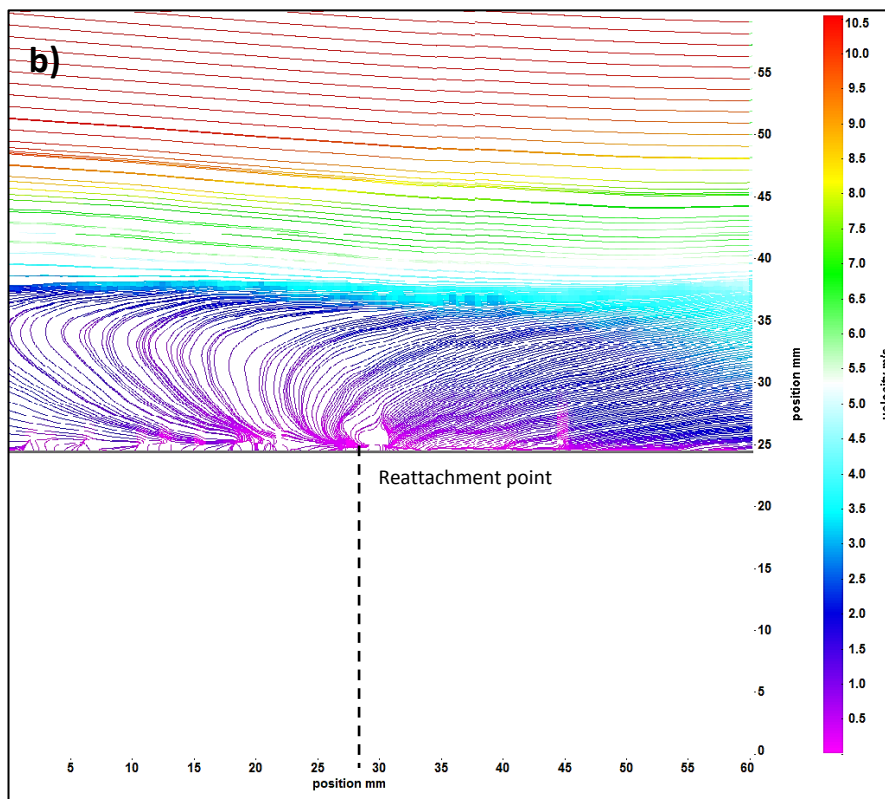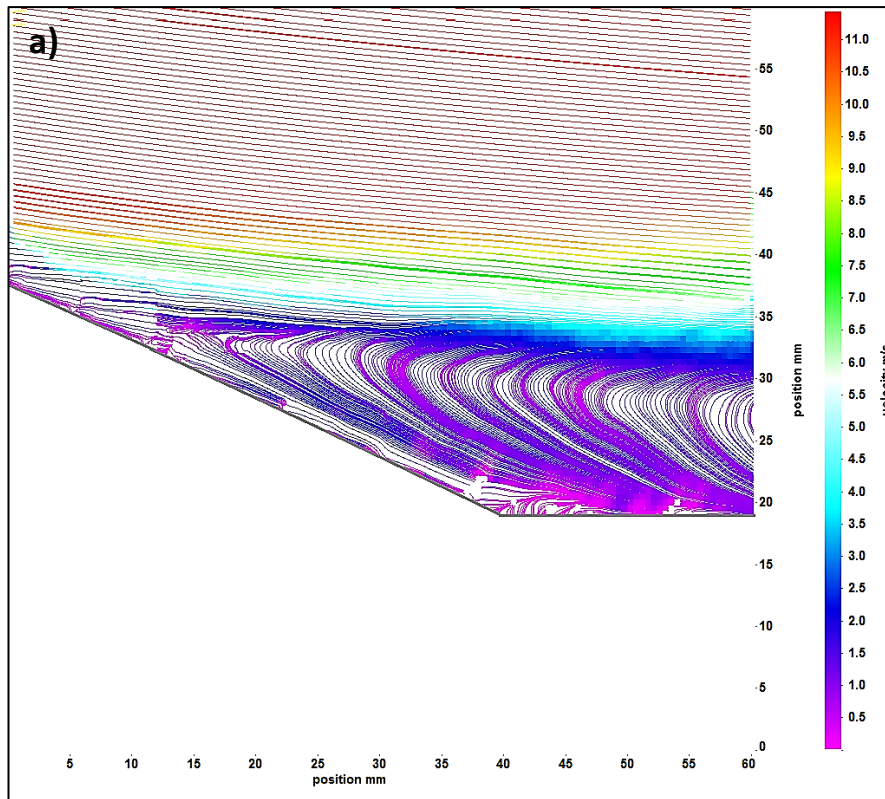
Figure 8.26: The velocity streamline of the un-actuated case showing: a) Recirculation zone; b) Reattachment point at $U_\infty = 10$ m/s.
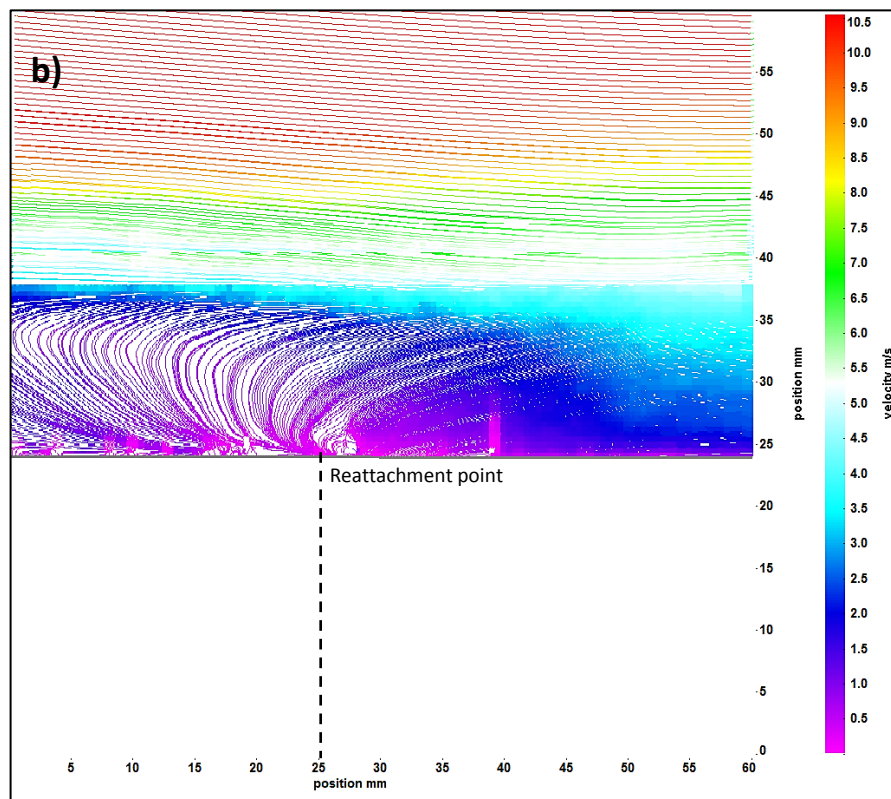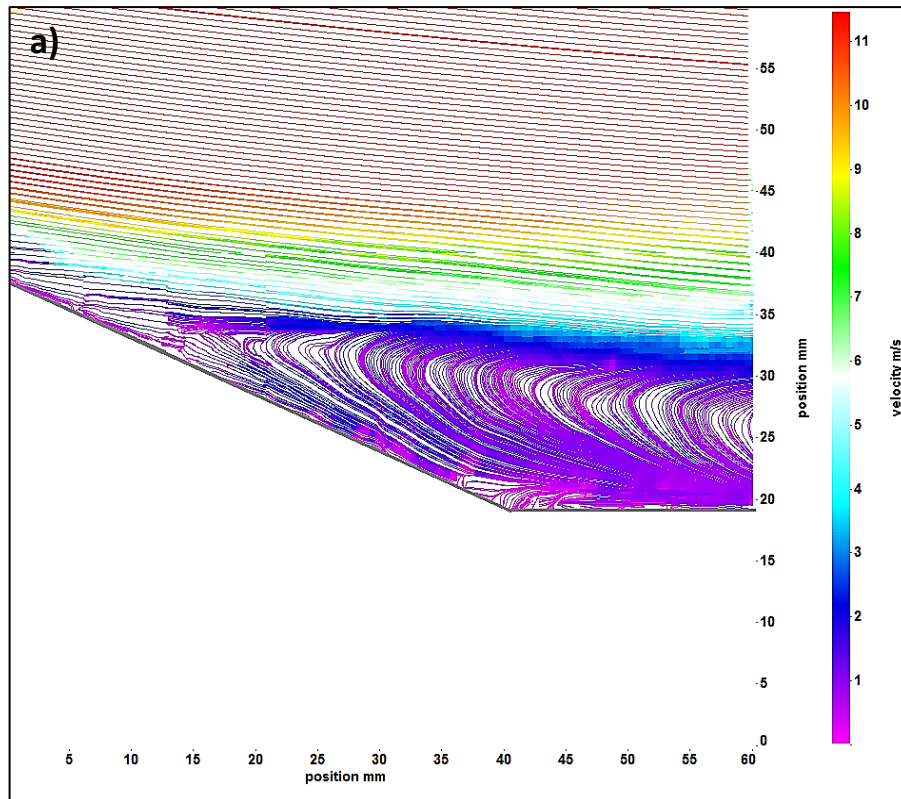
Figure 8.27: The velocity streamline of the un-modulated excitation case showing: a) Recirculation zone; b) Reattachment point at ($U_\infty = 10$ m/s, $Vr = 1.1$, $f_e = 1000$ Hz, $\beta = 10^o$).

8.5. Conclusions

Both HWA and PIV methodologies have been used in this chapter and the results of the flow control experiments outlined show the feasibility of the designed synthetic jet actuators for successfully improving the wake flow behind the hump model. Using the suite of experiments with freestream velocities of $U_\infty = 7$ m/s and 10 m/s it can be shown that both the recirculation width and the reattachment point can be affected by an array of surface mounted synthetic jet actuators along the hump span length. Employing modulated and un-modulated excitation signals to operate the actuators in a uniform manner significantly decreased the size of the recirculation bubble and hence dallying floe separation as a result the associated vorticity is pulled nearer the surface of the hump.

When the actuation takes place using either modulated or un-modulated excitation then a velocity ratio of greater than one will cause a higher decrease in the dominant spectral peak, recirculation thickness and reattachment length compared to a lower jet-to-freestream velocity ratio. Amplitude modulation signal used to actuate the wake flow-field behind the hump can be seen to create some resemblance effects to those seen for single sine wave actuation in that the dominant spectral peak is decreased. There are however, small differences between the effects seen for modulated and un-modulated excitations, mainly, in terms of peak changes in the reverse flow width and reattachment point movement.

In general, the results in the table clearly showed how the onset of reattachment location is moved by about 2 mm in x direction and the recirculation width is also decrease to 11 mm when the velocity increased from 7 m/s to 10 m/s which confirm the flow separation delay. Additionally, the results showed that as expected for the un-actuated case, the reverse flow width is reduced by 14% when the synthetic jet was activated and this reduction in the recirculation area is seen to be significantly lower compared to 7 m/s velocity, suggesting that at higher freestream velocity more momentum was added to the cross-flow and hence the synthetic jet is more likely to be buried inside the boundary layer. **Table 8.2** summarises the PIV actuation findings for both modulated and un-modulated excitation signals under the three velocity ratios 0.5, 1 and 1.5 at the freestream velocity 7 m/s

Table 8.1: Summary of PIV results for both modulated and un-modulated excitation signals at freestream velocity of 7 m/s.

Un-actuated case at U_∞ = 7 m/s	Actuated case using un-modulated excitation signal			Actuated case using amplitude modulated excitation signals		
	Vr =0.5	Vr = 1	Vr = 1.5	Vr = 0.5	Vr = 1	Vr = 1.5
Location of reattachment from the rear of the hump (30 mm)	Almost same	3 mm (reduction)	8 mm (reduction)	Almost same	2 mm (reduction)	6.5 mm (reduction)
Reverse flow width (13 mm)	Almost same	14% (reduction)	24% (reduction)	Almost same	11% (reduction)	21% (reduction)

Chapter 9: Conclusion and Suggestions for Future Work

A series of experimental and numerical studies have been carried out in order to achieve the aims and objectives given in the first chapter. The results of the flow control experiments presented in this study clearly demonstrate the feasibility of the synthetic jet actuator technique for effective control of the wake flow behind a convex hump model. In particular, a set of experiments at $U_\infty = 7$ m/s using HWA and PIV techniques demonstrated that an array of surface mounted synthetic jet actuators can affect the PSD, recirculation area and separation length and hence reduce the velocity deficit in the wake area behind the hump. Steady operation of the actuators is shown to significantly reduce the degree of flow separation bubble area and the associated shear layer vortex shedding. As a consequence, both the separation length and recirculation width area in the wake are reduced. Moreover, as the velocity ratio increased from 0.5 to 1.5 at the optimum angular position of the actuation angle of 10º, a large reduction of power spectral density, recirculation width and separation length was seen and this was achieved using either un-modulated or modulated excitation signals.

This body of work has resulted in several conclusions and has identified several areas that would benefit from further investigations. These are presented below:

➢ To evaluate the effectiveness of using an array of synthetic jet actuators (SJAs) in a wake flow as an active flow control behind a convex hump model, a new sub-sonic blower wind tunnel was developed and constructed at the University of Leeds using both numerical and experimental studies, it is also referred to as an "open-circuit" wind tunnel. The results showed that flow quality was significantly affected by boundary layer controllers (honeycomb and mesh screens) in the settling chamber and wide angle diffuser and the flow turbulent intensity was reduced by more than 50% compared to the CFD model.

➢ Flow visualization techniques such as tufts flow visualization and surface flow visualization as well as CFD results are accurately shown at the beginning of the separation and recirculating zone on both models (200 mm and 300 mm). However, there was greater clarity in the case of

the 200 mm model compared to 300 mm model, which is therefore was employed in active flow control experimental tests. PIV results showed that the exact locations of the separation and reattachment are relatively close to what is seen in the flow visualization results, which is slightly further downstream than that indicated in CFD analysis.

➢   For the SJA developed in quiescent flow conditions, results showed that metal to metal clamping produced the best uniformity of deformation compared to the other two clamping methods (Neoprene rubber and O-rings). Moreover, the results showed that cavity height, orifice diameter and number of orifices and space between the orifices had an effect on the jet velocity and jet strength. Additionally, it has been noticed by utilizing the Helmholtz resonance of the cavity and amplitude modulation excitation, that the actuator can exhibit more significant blowing velocity with a diminished power input thus demonstrating that these excitation parameters could introduce a useful function in flow control application.

➢ For the flow control study, when the actuation was carried out using either modulated or un-modulated excitation signals then as the velocity ratio increased from 0.5 to 1.5, a larger reduction of the dominant spectral peak, recirculation width and separation length was seen. There are however, small differences between the effects seen for modulated and un-modulated excitations. Mainly, in terms of highest changes in the reverse flow width and separation length, it was seen that the peak decrease in reverse flow thickness was decreased from 24% in the un-modulated actuation case to 21% in the modulated case. Moreover, the maximum reduction in the separation length was slightly lower compared to the modulated actuation case. This difference between un-modulated and modulated actuation is presented for all tests.

➢   The flow control results at a higher free stream velocity of 10 m/s and single sine wave excitation showed that as expected for the un-actuated case, the onset of separation location is delayed compared to 7 m/s velocity and the separation length reduced from 75 mm at 7 m/s to 68 mm at 10 m/s. Moreover,

the reverse flow width is reduced by 14% when the synthetic jet activated and this reduction in the recirculation area is seen to be significantly lower compared to 7 m/s velocity.

Although this research has had a considerable success in demonstrating that an array of SJAs are promising means for flow separation control, yet as with any research, some of the valuable recommendations and unanswered issues provide the grounds for future work.

- An additional investigation to represent the mesh screens and honeycomb inside a wide angle diffuser and settling chamber as a porous domain in CFD may further improve the predicting of turbulent intensity in the open-circuit wind tunnel test section.

- In the synthetic jet actuator study in quiescent flow condition in this thesis, the future research needs to extend the investigation to identify a universal jet formation constant, the separation, size, and trajectory of the expelled vortex rings, at additional dimensionless parameters such as stroke length, Stokes number and Reynolds number using flow visualisation and PIV techniques.

- In order to obtain more details about the drag and lift forces as well as the coefficient of pressure, further research may need to be carried out. This can be achieved by measuring the pressure distribution over the hump surface in the wake area behind the hump.

- As the interaction between SJAs developed here and the separated boundary layer in the wake area and their effectiveness in flow control was a function of velocity ratio, Vr, an optimization of this actuator to achieve a higher velocity ratio ($Vr > 1.5$) through either modifying the piezo-ceramic actuator used here or using different types of actuators, such as a pulsed jet actuator or plasma jet actuator.

Appendix-A

List of Publications

Azzawi, I, Mao, X and Jaworski, AJ (2016) *Design, Fabrication and Characterization of Low Speed Open-jet Wind Tunnel.* In: Proceedings of World Congress on Engineering 2016. World Congress on Engineering 2016, 29 Jun - 01 Jul 2016, London. IAENG. ISBN 978-988-19253-0-5 (In Press)

Appendix -B

Matlab Program to Calculate the Power Spectral Density (PSD) and Mean Velocity:

```
t= x (:,1); % to read the data for time from Ty1 (first coloumn)
u= y (:,2); % to read the data for speed from Ty1 (second coloumn)
Fs=4000;
[Pxx,F] = periodogram(u,[],length(u),Fs);
figure(1)
hold on
plot(t,u);xlabel('Time t');ylabel('Speed u');title('Speed vs Time');
hold off
figure(2)
hold on
plot(F,10*log10(Pxx));xlabel('F');ylabel('PSD');title('PSD vs Frequency');
hold off
```

=

Appendix C

Figures C1a to e present the PSD under the un-actuated and actuated flow over the hump at *Vr* = 1.5 and β varied from 0° to ± 15° over *X/L* = 1 and *Y/h* = 0.5. For example, by rotating the hump from 0° to +15°, a downstream actuation is established, while an upstream actuation can be achieved by rotating the hump from 0° to -15°. The results clearly showed that at β = +10°, the dominant peak frequency was significantly affected by the synthetic jet actuation compared to the other actuation angles. Therefore, it can be conclude that the optimum angular position of actuation angle was β = 10° in the downstream flow direction.
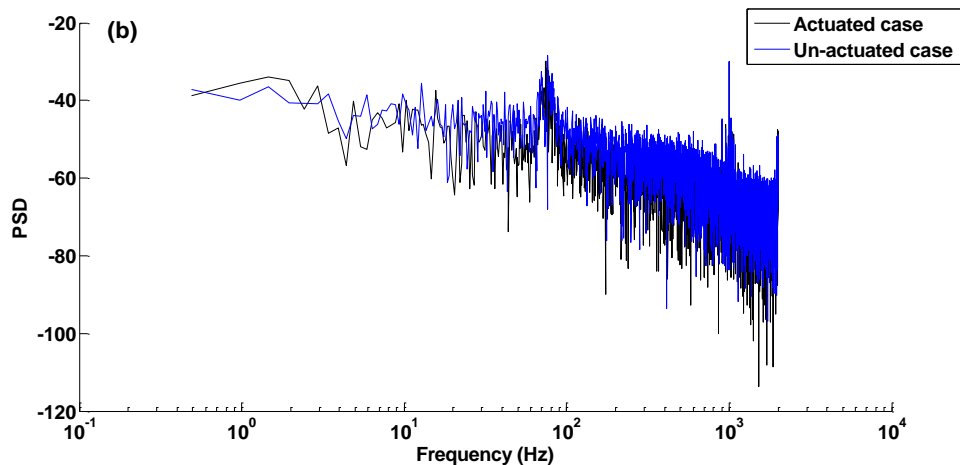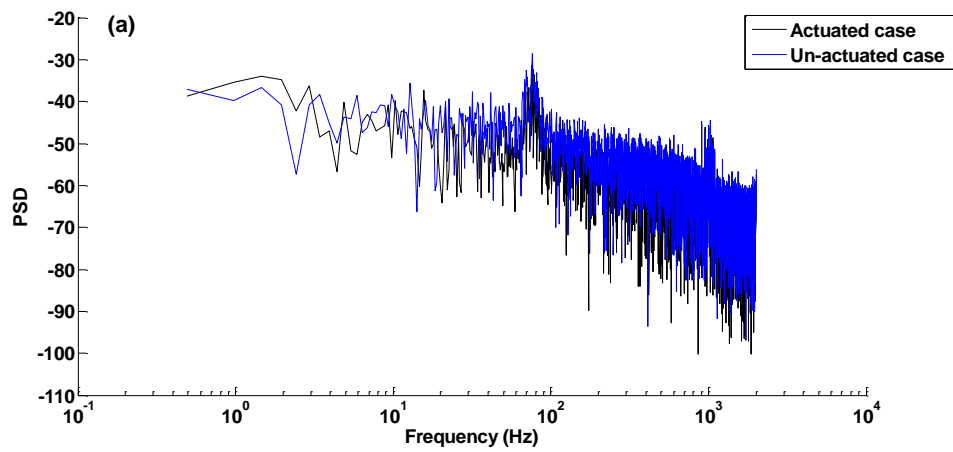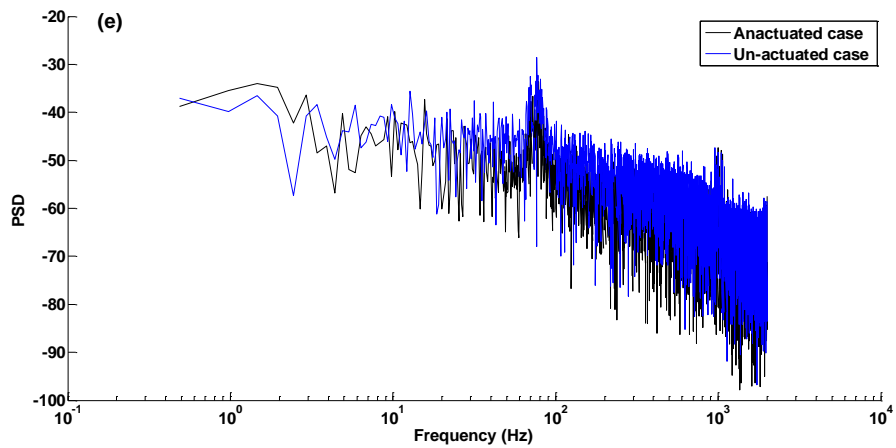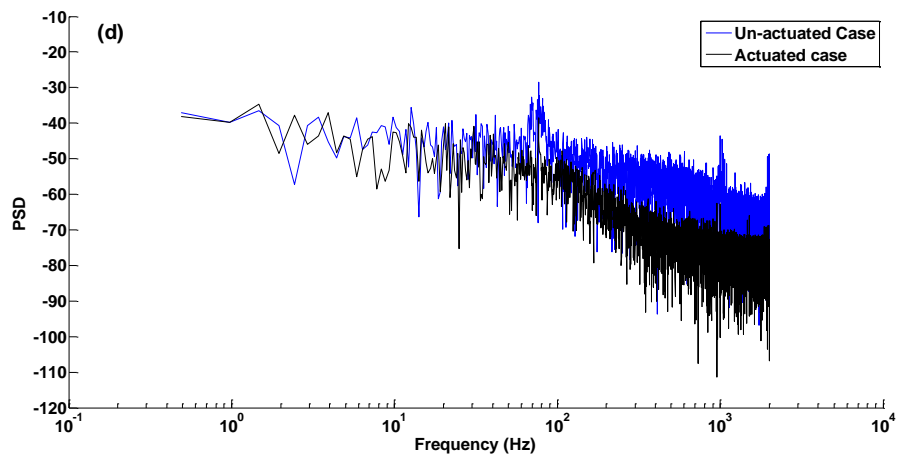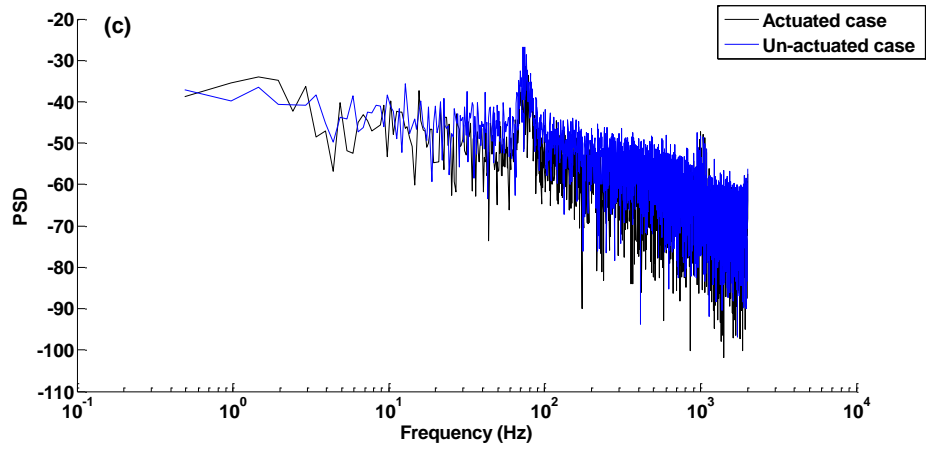
Figure C1: Power spectral density of, a) β = 0°; b) β = -10°; c) β = -15°; d) β = +10°; e) β = +15° at (*Vr* = 1.5, Unmodulated excitation).

Bibliography

Arwatz G, Fono I, Seifert A. Suction and oscillatory blowing actuator modeling and validation. AIAA journal. 2008 May; 46(5):1107-17.

Amitay M, Smith DR, Kibens V, Parekh DE, Glezer A. Aerodynamic flow control over an unconventional airfoil using synthetic jet actuators. AIAA journal. 2001 Mar; 39(3):361-70.

Amitay M, Honohan A, Trautman M, Glezer A. Modification of the aerodynamic characteristics of bluff bodies using fluidic actuators. AIAA paper. 1997 Jun; 2004.

Amitay M, Smith BL, Glezer A. Aerodynamic flow control using synthetic jet technology. AIAA paper. 1998 Jan 12; 208:1998.

Azzawi I, Mao X, Jaworski AJ. Design, Fabrication and Characterization of Low Speed Open-jet Wind Tunnel. In Proceedings of World Congress on Engineering 2016 2016 Apr 16. IAENG.

Broučková Z, Trávníček Z, Šafařík P. Visualization of synthetic jets at higher Stokes numbers. In: EPJ Web of Conferences 2012 (Vol. 25, p. 01007). EDP Sciences.

Buchmann NA, Atkinson C, Soria J. Influence of ZNMF jet flow control on the spatio-temporal flow structure over a NACA-0015 airfoil. Experiments in fluids. 2013 Mar 1; 54(3):1-4.

Barlow, J. B., W. H. Rae, and A. Pope. "Low-speed wind tunnel testing, 1999." Jhon Wiley & Sons, Canada.

Chaudhari, M., Verma, G., Puranik, B. and Agrawal, A. Frequency response of a synthetic jet cavity. Experimental Thermal and Fluid Science, 33(3), pp.439-448, (2009).

Crook A., Wood N. Measurements and Visualizations of Synthetic Jets. AIAA Paper 2001-0145.

Crook A, Wood NJ. A parametric investigation of a synthetic jet in quiescent conditions. In Proceedings, 9th Millennium International Symposium on Flow Visualization 2000.

Cater JE, Soria J. The evolution of round zero-net-mass-flux jets. Journal of Fluid Mechanics. 2002 Dec 10; 472:167-200.

Crook A, Crowther WJ, Wood NJ. A parametric study of a synthetic jet in a cross flow. In Proceedings of the 22nd International Congress of Aeronautical Sciences 2000.

Clauser, F., "Turbulent boundary layers in adverse pressure gradients." Journal of the Aeronautical Sciences (2012).

Choi CK, Kwon DK. Wind tunnel blockage effects on aerodynamic behavior of bluff body. WIND STRUCT INT J. 1998 Dec; 1(4):351-64.

Calautit, J. K., Hassam N., Ch., Ben R. H., Lik F. S., "A validated design methodology for a closed-loop subsonic wind tunnel." Journal of Wind Engineering and Industrial Aerodynamics 125 (2014): 180-194.

Curle. N "The Laminar Boundary Layer Equations" Oxford at the Clarendon Press, 1962.

Cebeci, G. J. Monsinskis and A.M.O. Smith. "Calculation of Separation Points in Compressible Turbulent Flows" Journal of Aircraft Vo1.9, No.9 1972

Didden N. On the formation of vortex rings: rolling-up and production of circulation. Zeitschrift für angewandte Mathematik und Physik ZAMP. 1979 Jan 1; 30(1):101-16.

Donovan JF, Kral LD, Cary AW. Active flow control applied to an airfoil. AIAA paper. 1998 Jan 12; 210.

DeMauro EP, Leong CM, Amitay M. Modification of the near wake behind a finite-span cylinder by a single synthetic jet. Experiments in fluids. 2012 Dec 1; 53(6):1963-78.

Feero MA, Lavoie P, Sullivan PE. Influence of cavity shape on synthetic jet performance. Sensors and Actuators A: Physical. 2015 Mar 1; 223:1-0.

Fujisawa N, Takeda G. Flow control around a circular cylinder by internal acoustic excitation. Journal of Fluids and Structures. 2003 Jun 30; 17(7):903-13.

Feng LH, Wang JJ, Pan C. Effect of novel synthetic jet on wake vortex shedding modes of a circular cylinder. Journal of Fluids and Structures. 2010 Aug 31; 26(6):900-17.

Feng LH, Wang JJ. Synthetic jet control of separation in the flow over a circular cylinder. Experiments in fluids. 2012 Aug 1; 53(2):467-80.

Feng LH, Wang JJ. Modification of a circular cylinder wake with synthetic jet: Vortex shedding modes and mechanism. European Journal of Mechanics-B/Fluids. 2014 Feb 28; 43:14-32.

FLUENT Incorporated: FLUENT user guide [online] 2006. Available from: www1. ansys.com (accessed 01.02.12).

Gallas Q, Holman R, Raju R, Mittal R, Sheplak M, Cattafesta L. Low dimensional modeling of zero-net mass-flux actuators. AIAA paper. 2004 Jul 1; 2413(2).

Gad-el-Hak, M. Flow Control: Passive, Active and Reactive Flow Management. Cambridge University Press, 2000.

Greenblatt D, Wygnanski IJ. The control of flow separation by periodic excitation. Progress in Aerospace Sciences. 2000 Oct 31; 36(7):487-545.

Gilarranz, J. L., L. W. Traub, and O. K. Rediniotis. A new class of synthetic jet actuators—part II: application to flow separation control in: Journal of fluids engineering 127.2 (2005): 377-387.

Glezer A, Amitay M, Honohan AM. Aspects of low-and high-frequency actuation for aerodynamic flow control. AIAA journal. 2005 Jul; 43(7):1501-11.

Gue, F. Experimental study of the behaviour of the synthetic jets for effective flow separation control. PhD Thesis. University of Manchester, 2010.

Glezer, A. Amitay M. "Synthetic jets" Annual Review of Fluid Mechanics 34.1, 503-529, 2002.

Glezer A. The formation of vortex rings. Physics of Fluids (1958-1988). 1988 Dec 1; 31(12):3532-42.

Gharib M, Rambod E, Shariff K. A universal time scale for vortex ring formation. Journal of Fluid Mechanics. 1998 Apr 10; 360:121-40.

Gordon M, Cater JE, Soria J. Investigation of the mean passive scalar field in zero-net-mass-flux jets in cross-flow using planar-laser-induced fluorescence. Physics of Fluids (1994-present). 2004 Mar 1; 16(3):794-808.

Garcillan L, Liddle S, Sunneechurra K, Crowther B, Zhong S, Wood N. PIV measurements of the effect of pitch and skew on a circular orifice synthetic jet in a turbulent boundary layer. AIAA paper. 2006 Jan; 318:2006.

Ghani, S., Aroussi A., Rice E., "Simulation of road vehicle natural environment in a climatic wind tunnel." simulation practice and theory8.6 (2001): 359-375.

Gartmann, A., Wolfgang F., Wolfgang S., and Mathias D., "CFD modelling and validation of measured wind field data in a portable wind tunnel." Aeolian Research 3, no. 3 (2011): 315-325.

Goldschmeid, F. R.: An Approach to Turbulent Incompressible Separation under Adverse Pressure Gradients. J. Aircraft, vol. 2, no. 2, Mar. -Apr. 1965, pp. 108-115.

Holman, R. Y. Utturkar, R. Mittal, Barton L. Smith, L. Cattafesta. Formation criterion for synthetic jets. AIAA journal 43, no. 10 (2005): 2110-2116.

Hong, G. Effectiveness of micro synthetic jet actuator enhanced by flow instability in controlling laminar separation caused by adverse pressure gradient. Sensors and Actuators 132 (2006) 607–615.

Hashiehbaf A, Romano GP. Experimental investigation on circular and non-circular synthetic jets issuing from sharp edge orifices. In Proceedings of 17th International Symposium on Applications of Laser Techniques to Fluid Mechanics. Lisbon, Portugal 2014 Jul.

Head, R., "Entrapment Turbulent Boundary Layer," Rep. R and M 3152, 1960, Aeronautical Research Council, England.
Ishtiaq A. C. The Interaction of Synthetic Jets with Attached and Separating Turbulent Boundary Layer. PhD Thesis, University of Manchester, 2013.

Ishtiaq A. C, Zhong S. Understanding the interaction of synthetic jet with the flat plate boundary layer. ICARME, Trivandrum, India. 2012 May.

Ishtiaq A. C, Zhong S. A single circular synthetic jet issued into turbulent boundary layer. Journal of Visualization. 2014 May 1; 17(2):101-11.

Ingård, U., Labate S. Acoustic circulation effects and the nonlinear impedance of orifices. The Journal of the Acoustical Society of America 22.2, 211-218, 1950.

Ilori OM, Mao X, Jaworski AJ. CFD study of oscillatory flow through 90° bends of thermoacoustic devices. Proceedings of ICR2015. 2015 Aug 21.

Jain M, Puranik B, Agrawal A. A numerical investigation of effects of cavity and orifice parameters on the characteristics of a synthetic jet flow. Sensors and Actuators A: Physical. 2011 Feb 28; 165(2):351-66.

Jabbal M, Wu J, Zhong S. The performance of round synthetic jets in quiescent flow. Aeronautical Journal. 2006 Jun 1; 110(1108):385-93.

Jabbal M, Zhong S. Measurements of synthetic jets in a boundary layer. InIUTAM Symposium on Flow Control and MEMS 2008 (pp. 119-125). Springer Netherlands.

Jabbal M, Zhong S. The near wall effect of synthetic jets in a boundary layer. International Journal of Heat and Fluid Flow. 2008 Feb 29; 29(1):119-30.

Koopmans E, Hoeijmakers HW. Experimental research on flow separation control using synthetic jet actuators.

Kai T. Survey of Separation Prediction Methods Applied to Potential Flow Solutions for an Airfoil (1995).

Lawrence P. Meeting the challenge of aviation emissions: an aircraft industry perspective. Technology Analysis & Strategic Management. 2009 Jan 1; 21(1):79-92.

Lee S, Kim KJ, Park HC. Modelling of an IPMC actuator-driven zero-net-mass-flux pump for flow control. Journal of intelligent material systems and structures. 2006 Jun 1; 17(6):533-41.

Liu H. Wind engineering: a handbook for structural engineering. Pearson Education; 1990 Oct 1.

Liang, Y., Y. Kuga, M. Taya. Design of membrane actuator based on ferromagnetic shape memory alloy composite for synthetic jet applications in: Sensors and Actuators A, Vol. 125, 2006, pp. 512.–518.

Liddle SC, Wood NJ. Investigation into clustering of synthetic jet actuators for flow separation control applications. Aeronautical Journal. 2005; 109(1091):35-44.

Launder, B., Brian D., "Lectures in mathematical models of turbulence." (1972), Academic Press, London, UK.

Morgan, P.E., Rizzetta, D.P. and Visbal, M.R., 2007. Large-eddy simulation of separation control for flow over a wall-mounted hump. AIAA journal, 45(11), pp.2643-2660.

Magill JC, McManus KR. Exploring the feasibility of pulsed jet separation control for aircraft configurations. Journal of Aircraft. 2001 Jan; 38(1):48-56.

McCormick D. C. Boundary Layer Separation Control with Directed Synthetic Jets. AIAA 2000-0519, United Technologies Research Center East Hartford, CT 06108.

Mossi, K., P. Mane, R. Bryant. Velocity Profiles of Synthetic Jets using Piezoelectric Circular Actuators. AIAA Paper 2005-2341, Proceedings of 46th AIAA/ASME/ASCE/AHS/ASC Structures, Structural Dynamics & Materials Conference, Austin, TX, 18-21 April, 2005.

Mane P. Experimental Design and Analysis of Piezoelectric Synthetic Jets in Quiescent Air. Master Dissertation. School of engineering Virginia Commonwealth University, 2005.

Mane, P., Mossi, K., Rostami, A., Bryant, R. G., Castro, N. Piezoelectric actuators as synthetic jets: Cavity dimension effects. Journal of Intelligent Material Systems and Structures, (2007).

Milanovic I, Zaman KB. Synthetic Jets in Cross-Flow, Part II: Jets from Orifices of Different Geometry. AIAA Paper. 2002; 3715:23-6.

Milanovic IM, Zaman KB, Rumsey CL. An isolated circular synthetic jet in cross-flow at low momentum-flux ratio. AIAA paper. 2005 Jan 1; 1110:2005.

Mittal R, Rampunggoon P, Udaykumar HS. Interaction of a synthetic jet with a flat plate boundary layer. AIAA paper. 2001 Jun 11; 2773(200):1.

Ma L, Feng L. Experimental investigation on control of vortex shedding mode of a circular cylinder using synthetic jets placed at stagnation points. Science China Technological Sciences. 2013 Jan 1; 56(1):158-70.

Mehta, R., Bradshaw P., "Design rules for small low-speed wind tunnels." Aeronautical Journal 83.827 (1979): 443-449.

Moonen, P., Bert B., Staf R., and Jan C., "Numerical modeling of the flow conditions in a closed-circuit low-speed wind tunnel", Journal of Wind Engineering and Industrial Aerodynamics 94, no. 10 (2006): 699-723.

Nader, G., Dos Santos, C., Jabardo, P., Cardoso, M., Taira, N., Pereira, M., 2006. Characterization of low turbulence wind tunnel, Metrol. Sustain. Dev. Rio de Janeiro, Brazil, pp. 17–22. (September).

Ong, M.C., Utnes, T., Holmedal, L.E., Myrhaug, D. and Pettersen, B., 2009. Numerical simulation of flow around a smooth circular cylinder at very high Reynolds numbers. Marine Structures, 22(2), pp.142-153.

Ohanian, O. J., P. A. Gelhausen, D. J. Inman. Evaluation of Macro Fiber Composite (MFC) Synthetic Jet Actuators. AIAA Paper 2008-6405, 26th AIAA Applied Aerodynamics Conference, Honolulu, HI, 18 - 21 August 2008.

Ohanian, O. J. Ducted fan aerodynamics and modeling, with applications of steady and synthetic jet flow control. PhD Thesis. Virginia Polytechnic Institute and State University, 2011.

Oren L, Gutmark E, Muragappan S, Khosla S. Flow characteristics of non-circular synthetic jets. In47th AIAA Aerospace Sciences Meeting, Orlando, Florida 2009 Jan (pp. 5-8).

Prandtl, L.; Über Flüssigkeitsbewegung bei sehr kleiner Reibung "On the motion of fluid with very small viscosity", Proceedings of the 3rd International Mathematical Congress, Heidelberg, Germany, pp. 484-491, 1904.

Pratte BD, Baines WD. Profiles of the round turbulent jet in a cross flow. Journal of the Hydraulics Division. 1967 Nov; 93(6):53-64.

Qayoum A, Gupta V, Panigrahi PK, Muralidhar K. Influence of amplitude and frequency modulation on flow created by a synthetic jet actuator. Sensors and Actuators A: Physical. 2010 Jul 31; 162(1):36-50.

Qayoum A, Gupta V, Panigrahi P. Turbulent Boundary Layer Manipulation using Synthetic Jet Actuation. In Proceeding of the World Congress in Engineering (WCE) 2009 Jul 1 (Vol. 2).

Rajasekaran, J., 2011. On the flow characteristics behind a backward-facing step and the design of a new axisymmetric model for their study. Doctoral dissertation, University of Toronto.

Reneaux J. Overview on drag reduction technologies for civil transport aircraft. ONERA: Tire a Part. 2004 Jul; 153:1-8.

Rizzetta, Donald P., Miguel R. Visbal, Michael J. Stanek. Numerical investigation of synthetic-jet flowfields. AIAA journal 37.8 (1999): 919-927.

Razi, H. Circulation enhancement of synthetic jet actuators via multiple orifices. Msc Thesis, University of New South Wales, Sydney, Australia, 2012.

Rosenfeld M, Rambod E, Gharib M. Circulation and formation number of laminar vortex rings. Journal of Fluid Mechanics. 1998 Dec 10; 376:297-318.

Rumsey, C. L. Computation of a synthetic jet in a turbulent cross-flow boundary layer. NASA TM 213273 (2004).

Spazzini, P.G., Iuso, G., Onorato, M., Zurlo, N. and Di Cicca, G.M., 2001. Unsteady behavior of back-facing step flow. Experiments in fluids, 30(5), pp.551-561.

Schlichting H., Gersten K. Boundary Layer Theory. 2000, Book, Germany.

Smith, D. Perturbation of Vortex Wakes for Amelioration of the Vortex Wake Hazard. PhD Thesis, University of Imperial College, London, UK, 2003.

Smith, B. L., and A. Glezer. Jet vectoring using synthetic jets in: Journal of Fluid Mechanics 458 (2002): 1-34.

Smith DA. Perturbation of vortex wakes for amelioration of the vortex wake hazard (Doctoral dissertation, 2003, Imperial College London (University of London)).

Smith BL, Glezer A. The formation and evolution of synthetic jets. Physics of Fluids (1994-present). 1998 Sep 1; 10(9):2281-97.

Smith BL, Glezer A. Jet vectoring using synthetic jets. Journal of Fluid Mechanics. 2002 May 10; 458:1-34.

Schwarz WR, Bradshawt P. Measurements in a pressure-driven three-dimensional turbulent boundary layer during development and decay. AIAA, journal. 1993 Jul; 31(7):1207-14.

Shuster JM, Smith DR. Experimental study of the formation and scaling of a round synthetic jet. Physics of Fluids (1994-present). 2007 Apr 1; 19(4):045109.

Smith, B.L. and Swift, G.W., 2001. Synthetic jets at large Reynolds number and comparison to continuous jets. AIAA paper, 3030, p.2001.

Sathapornnanon, S., Aryut W., Somchai T., Monchai L., Alongkorn Pimpin, and Asi B., The Design and Development of The FMRL 60x18 cm2 Wide-Angle Screened-Diffuser Blower Tunnel, Part II: The Screened Diffuser. In Proceedings of The

Thirteenth National Mechanical Engineering Conference, Pattaya, Chonburi, Thailand, vol. 2, pp. 27-37. 1999.

Schwarz, W., and Peter B., "Measurements in a pressure-driven three-dimensional turbulent boundary layer during development and decay." AIAA journal 31, no. 7 (1993): 1207-1214.

Schaeffler NW. The interaction of a synthetic jet and a turbulent boundary layer. AIAA paper. 2003 Jan 6; 643:2003.

Sassoon, A., Parametric study of synthetic jet actuators on a backward facing step. (2013), (Doctoral dissertation).

Stratford. B. S. "The Prediction of separation of the turbulent boundary layer" Journal of Fluid Mechanics, Vol. 5, 1959.

Tang, H., Salunkhe, P., Zheng, Y., Du, J. and Wu, Y. On the use of synthetic jet actuator arrays for active flow separation control. Experimental Thermal and Fluid Science, 57, pp.1-10, (2014).

Tang H. Performance modelling of synthetic jet actuators for flow separation control (Doctoral dissertation, University of Manchester, 2006).

Tuck A. Soria J. Separation Control On A NACA 0015 Airfoil Using A 2D Micro ZNMF Jet. Aircraft Engineering and Aerospace Technology in: An International Journal 80/2 (2008) 175–180.

Tensi J, Boué I, Paillé F, Dury G. Modification of the wake behind a circular cylinder by using synthetic jets. Journal of Visualization. 2002 Mar 1; 5(1):37-44.

The Engineering Toolbox: Roughness and Surface Coefficients of Ventilation Ducts [Online] 2012. Available from: ⟨http://www.engineeringtoolbox.com⟩ (accessed 01.02.2012).

Utturkar Y, Holman R, Mittal R, Carroll B, Sheplak M, Cattafesta L. A jet formation criterion for synthetic jet actuators. AIAA paper. 2003 Jan; 636:2003.

Ugrina S. Experimental analysis and analytical modeling of synthetic jet cross flow interaction. PhD Thesis. Maryland: University of Maryland, USA, 2007.

Vlajinac, M., "Design, construction and evaluation of a subsonic wind tunnel." PhD diss., Massachusetts Institute of Technology, 1970.

Watson, M., Jaworski, A.J. and Wood, N.J., 2007. Application of synthetic jet actuators for the modification of the characteristics of separated shear layers on slender wings. Aeronautical Journal, 111(1122), pp.519-529.

Watson, M. The Use of Synthetic Jet Actuators for the Enhanced Control of Separated Flows. PhD Thesis, University of Mnachester, 2004.

Watson M, Jaworski AJ, Wood NJ. Contribution to the understanding of flow interactions between multiple synthetic jets. AIAA journal. 2003 Apr; 41(4):747-9.

Watson, M., Jaworski, A. J. and Wood, N. J. A Study of Synthetic Jets from Rectangular and Dual-Circular Orifices. Aeronautical Journal, vol. 107, pp 427-434, 2003a.

Wu KE, Breuer KS. Dynamics of synthetic jet actuator arrays for flow control. AIAA paper. 2003 Jun 23; 4257:2003.

Wu JZ, Lu XY, Denny AG, Fan M, Wu JM. Post-stall flow control on an airfoil by local unsteady forcing. Journal of Fluid Mechanics. 1998 Sep 25; 371:21-58.

Williamson CH. Vortex dynamics in the cylinder wake. Annual review of fluid mechanics. 1996 Jan; 28(1):477-539.

Wang J, Feng L, Xu C. Experimental investigations on separation control and flow structure around a circular cylinder with synthetic jet. Science in China Series E: Technological Sciences. 2007 Oct 1; 50(5):550-9.

Westphal, R., Eaton J.,Pauley W., "Interaction between a vortex and a turbulent boundary layer in a streamwise pressure gradient."Turbulent Shear Flows 5. Springer Berlin Heidelberg, 1987. 266-277.

Xia Q, Zhong S. An experimental study on the behaviours of circular synthetic jets at low Reynolds numbers. Proceedings of the Institution of Mechanical Engineers, Part C: Journal of Mechanical Engineering Science. 2012 Nov 1; 226(11):2686-700.

You D, Moin P. Active control of flow separation over an airfoil using synthetic jets. Journal of Fluids and Structures. 2008 Nov 30; 24(8):1349-57.

Yamada, S., Okamoto, K., Nitta, T., Motosuke, M., and Honmami, S. "Flow Structures by Synthetic Jets Over a Backward Facing Step in Low Reynolds Number." (2009), 47th AIAA Aerospace Sciences Meeting

Zhou, Jue, and Shan Zhong. Numerical simulation of the interaction of a circular synthetic jet with a boundary layer in: Computers & Fluids 38.2 (2009): 393-405.

Zhong S, Garcillan L, Wood NJ. Dye visualisation of inclined and skewed synthetic jets in a cross flow. Aeronautical Journal. 2005; 109(1093):147-55.

Zhong S, Jabbal M, Tang H, Garcillan L, Guo F, Wood N, Warsop C. Towards the design of synthetic-jet actuators for full-scale flight conditions. Flow, turbulence and combustion. 2007 Jun 1; 78(3-4):283-307.

Zhou J. Numerical investigation of the behaviour of circular synthetic jets for effective flow separation control. Ph.D Dissertation. University of Manchester, 2010.

Zhong S, Garcillan L, Wood NJ. Dye visualisation of inclined and skewed synthetic jets in a cross flow. Aeronautical Journal. 2005; 109(1093):147-55.

Zdravkovich MM. Flow around Circular Cylinders: Volume 2: Applications. Oxford university press; 2003 Jan 16.

Zhang S, Zhong S. Turbulent flow separation control over a two-dimensional ramp using synthetic jets. AIAA journal. 2011 Dec; 49(12):2637-49.

Zhong S, Zhang S. Further examination of the mechanism of round synthetic jets in delaying turbulent flow separation. Flow, turbulence and combustion. 2013 Jul 1; 91(1):177-208.